3D flow organization and dynamics in subsonic jets

Aeroacoustic source analysis by tomographic PIV

Daniele Violato

3D flow organization and dynamics in subsonic jets
Aeroacoustic source analysis by tomographic PIV

PROEFSCHRIFT

ter verkrijging van de graad van doctor
aan de Technische Universiteit Delft,
op gezag van de Rector Magnificus Prof. ir. K. Ch. A. M. Luyben,
voorzitter van het College voor Promoties,
in het openbaar te verdedigen op woensdag 6 maart 2013 om 12.30 uur

door

Daniele VIOLATO

Master of Science in Aerospace Engineering,
geboren te Pinerolo, Italy

Dit proefschrift is goedgekeurd door de promotor:
Prof. Dr. Ing. F. Scarano.

Samenstelling promotiecommissie:

Rector Magnificus	Technische Universiteit Delft	voorzitter
Prof. Dr. Ing. F. Scarano	Technische Universiteit Delft	promotor
Prof. Dr. Ir. B.J. Boersma	Technische Universiteit Delft	
Prof. Dr. Ing. R. Camussi	Università degli Studi Roma Tre	
Dr. P. Jordan	Université de Poitiers, Institut Pprime	
Prof. Dr. J. Katz	Johns Hopkins University	
Prof. Dr. Ir. C. Schram	Von Karman Institute for Fluid Dynamics	
Dr. Ir. M. Tummers	Technische Universiteit Delft	
Prof. Dr. D. Simons	Technische Universiteit Delft, reservelid	

This research has been conducted as part of the FLOVIST project, which is funded by the European Research Council (ERC, grant nº 202887).

Copyright © 2013, D. Violato. All rights reserved.
Cover image: “Turbulence drawings on foreshore sand”, photograph by D.Violato (2012). Cover editing by C. Migliori.

In life, we are alone.
However, friendship helps forget it.

Summary

To reap the economic benefits of an ever-growing air transportation system and to meet the increasingly stringent noise regulation, aircraft manufacturers are continuously searching for solutions to aircraft noise. A significant amount of the noise emission is constituted by jet noise, which is generated by the mixing processes between the exhaust flow leaving the jet engines and the atmosphere. A detailed understanding of the jet flow mechanics is of paramount importance to identify the processes responsible for noise production, i.e. the *acoustic source*, and, ultimately, to develop noise control strategies.

This thesis proposes a novel experimental-based methodology to investigate jet aeroacoustics. Firstly, time-resolved tomographic particle image velocimetry (TR-TOMO PIV) is employed to have a time-dependent three-dimensional (3D) description of the turbulent patterns of the jet flow. Secondly, the relation between such patterns and the instantaneous acoustic source is explored using Powell's aeroacoustic analogy.

When the complexity of turbulent flow phenomena surpasses the capability of observation, such as in the case of planar PIV technique, the number of dimensions of the observation space is smaller than the natural dimensions of the phenomenon, leading to ambiguities in the interpretation of the data. Therefore, without a 3D time-dependent (4D) description flow, an accurate evaluation of the instantaneous acoustic noise source may become very difficult if not impossible. In this context, 3D time-dependent measurements are a necessary milestone in the path to the development of experimental aeroacoustics methods based on PIV.

Time-resolved tomographic PIV experiments are conducted at *Re*=5,000, based on the jet diameter and the jet exit velocity, in a tailored-water jet facility. Measurements are performed on jets issued through circular and 6-chevron nozzles, with the latter configuration that is nowadays used on civil aircraft jet engines to reduce acoustic emissions. The attention is placed upon the 3D organization and dynamics of flow transition, where coherent flow structures play a role in the generation of acoustic noise. A full 3D approach enables unambiguous descriptions of the vortex topology, for example by the full vorticity vector or the λ_2-criterion, while the temporal resolution allows addressing the growth and development of the coherent flow structures along with their mutual interaction.

In the circular jet, shedding and pairing of vortices are the most pronounced phenomena observed in the near field of the circular jet. The first and second pairing amplify the axial pulsatile motion in the jet column and lead to the growth of in-plane and out-of-plane azimuthal waves. Typically, 4 main streamwise pairs are distributed around the vortex rings at an angle of 30-40 degrees to the jet axis and move with a characteristic inward-outward radial motion induced by the passage of the vortex rings. The spatial mode analysis shows that the preferred mode of influence of streamwise vortices on vortex rings has wave number

k=4, with the axial vorticity induced by streamwise pairs on the vortex ring that is staggered in phase opposition at the regions of interaction, where primary instabilities grow. With the growth of in-plane azimuthal instabilities, vortex ring humps are tilted and ejected along the axial direction as they are subjected to higher axial velocities. By the end of the potential core, this process culminates in the breakdown of the toroidal shape into streamwise filaments oriented at 30-45 degrees to the jet axis and peripheral structures of "C" shape. The formation of "C" structures and the ejection of vortex humps are characterized by maximum activity of stretching and tilting fields.

The analysis of the 3D patterns in the region of transition from the axisymmetric to the three-dimensional regime is aided by applying proper orthogonal decomposition (POD) to velocity, vorticity and Lamb-vector fields, with the latter that accounts for the flow state in Powell's aeroacoustic analogy. The first 10 modes are analyzed. In all decompositions, the presence of vortex rings travelling after pairing is described by the first pair of modes. In the velocity modes, the axial component identifies an helical motion in the region across the end of the potential core, while it describes flapping and precession motions further downstream. In the vorticity decomposition, the first pair of modes shows that travelling vortex rings are accompanied by the radial and axial vorticity fields developing across the end of the potential core with a 40-45 degree inclination to the jet axis. This pattern, also observed in mode pairs at lower energy, is ascribed to the process of vortex ring breakdown. Analogous patterns are observed in the Lamb vector modes.

In the jet with chevrons, the axisymmetric ring-like coherence of the circular jet is not encountered. Instead, streamwise flow structures of azimuthal vorticity emanate from the chevron apices, and counter-rotating streamwise vortices of axial and radial vorticity develop from the chevron notches. The decay of streamwise vortices is accompanied by the formation of C-shaped structures. This processes are associated with peak activity of stretching and tilting fields.

The relation between coherent flow structures and the instantaneous acoustic source is investigated recalling Powell's aeroacoustic analogy, with the acoustic source that is identified by the second time derivative of the Lamb vector. The spatio-temporal evolution of the source is mapped and is compared to that of the vortices, to visually detect flow events involved in the acoustic generation. In the circular jet, pronounced source activity is observed in correspondence to vortex pairing, azimuthal instabilities and streamwise filaments, with the largest generation by the end of the potential core during the vortex ring breakdown process. In the region near to the nozzle, the POD analysis of the acoustic source shows a characteristic toroidal coherence that is related to vortex ring shedding and pairing, whereas, in the region by the end of the potential core, where the vortex rings breakdown, it describes the development of three-dimensional disturbances at 40-45 degree to the jet axis. Such disturbances are associated with Strouhal number $1.05 \leq St \leq 1.9$, which are higher than those found for the velocity, vorticity and Lamb vector modes (typically $St \leq 0.9$). In the chevron jet, instead, evident peak activity is reported during the process of streamwise vortex decay and C structure formation.

Performing unbiased acoustic predictions of the jet noise with TR-TOMO PIV measurements is a challenging task due to the constraints on the extent of the instantaneous measurement domain and on the required spatial and temporal resolutions. This work

attempts to meet this challenge with measurements performed at spatial and temporal resolution (up to Strouhal of 4) that enables to appreciate not only the details of the vortex interactions but also their connection to the local pattern of acoustic source. Moreover, measurements are conducted over a jet axial extent that is sufficiently long (10 jet diameters) to capture the large-scale events from the nozzle to 4 jet diameters beyond the end of the potential core. Far-field acoustic predictions are performed by direct evaluation of Powell's analogy using TR-TOMO PIV data. The spectrum of the acoustic pressure shows peaks at the pairing and the shedding frequencies and a broader hump ($1 \leq St \leq 2.25$). This is ascribed to the breakdown of ring vortices, after visually inspecting the acoustic source dynamics and having found that the frequencies ($1.05 \leq St \leq 1.9$) associated with the 3D waves of the source modes lie within the range of the spectral hump.

Samenvatting

Om de economische voordelen van een alsmaar groeiend luchttransportsysteem te kunnen oogsten en om aan steeds strenger wordende geluidsoverlastregelgeving te kunnen voldoen, zijn vliegtuigfabrikanten continu op zoek naar innovaties voor het reduceren van vliegtuiglawaai. Een groot deel van het lawaai wordt veroorzaakt door het mengproces tussen de uitlaatstroom van de straalmotor en de atmosfeer. Het doorgronden van de mechanica van de straalmotoruitstroming is van groot belang voor het identificeren van de processen die lawaai produceren (de akoestische bron) en, uiteindelijk, lawaai reducerende strategieën te ontwerpen.

Dit proefschrift introduceert een nieuwe, op experimenten gebaseerde, methodologie voor het onderzoeken van de aero-akoestiek van straalmotoren. Ten eerste wordt Time-Resolved Tomographic Particle Image Velocimetry (TR-TOMO PIV) toegepast om een tijdsafhankelijke driedimensionale beschrijving van de turbulente patronen van de straalstroming te verkrijgen. Ten tweede is de relatie tussen zulke patronen en de directe akoestische bron verkend met behulp van Powells aero-akoestische analogie.

Als de complexiteit van de turbulente stromingsfenomenen de mogelijkheden tot observatie te boven gaat, zoals bij de planaire PIV-techniek het geval is, is het aantal dimensies van de observatieruimte kleiner dan de natuurlijke dimensie van het fenomeen, wat leidt tot dubbelzinnigheden in de interpretatie van de data. Daarom is zonder een 3D tijdsafhankelijke (4D) beschrijving van de stroming een accurate evaluatie van de directe akoestische bron bijzonder lastig. In deze context zijn 3D tijdsafhankelijke metingen een noodzakelijke mijlpaal op de weg van de ontwikkeling van experimentele aero-akoestische methodes gebaseerd op PIV.

TR-TOMO PIV experimenten zijn uitgevoerd bij Re=5,000, gebaseerd op de straaldiameter en uitstroomsnelheid, in een speciaal ontworpen waterstraal opstelling. Metingen zijn uitgevoerd op stralen uit cirkelvormige en 6-voudig gekartelde straaltuiten; de laatstgenoemde configuratie wordt tegenwoordig bij straalmotoren van verkeersvliegtuigen toegepast om akoestische emissies te reduceren. De aandacht is gericht op de 3D organisatie en dynamica van stromingstransitie, waarbij coherente stromingsstructuren een rol spelen bij het genereren van lawaai. Een volledige 3D benadering maakt een ondubbelzinnige beschrijving van de werveltopologie mogelijk, bijvoorbeeld met behulp van de volledige vorticiteitsvector of het λ_2-criterium, terwijl de tijdsresolutie het mogelijk maakt de groei en ontwikkeling van de coherente stromingsstructuren te onderzoeken samen met hun onderlinge interactie.

In de cirkelvormige straalstroming zijn het ontstaan en het paren van wervels het meest uitgesproken fenomeen dat optreedt in het nabije veld. De eerste en tweede paringen versterken de axiale pulserende beweging in de straal en leiden tot de groei van in-het-vlak en buiten-het-vlak gelegen azimuthale golven. Doorgaans zijn 4 stroomsgewijze hoofdparen verdeeld rond de wervelring onder een hoek van 30 tot 40 graden ten opzichte van de straalas en vertonen een karakteristieke buitenwaarts gerichte radiale beweging, veroorzaakt door de passerende wervelringen. De ruimtelijke modaalanalyse laat zien dat de voorkeursmodus van invloed van stroomsgewijze wervels op wervelringen een golfgetal k=4 heeft, met de axiale vorticiteit geïnduceerd door stroomwijze paren op de wervelring, die is versprongen in fase-oppositie in de interactiegebieden, waar primaire instabiliteiten toenemen. Met de groei van in het vlak gelegen azimuthale instabiliteiten, worden uitstulpingen van de wervelring gekanteld en naar buiten gedrukt langs de axiale richting, terwijl ze blootgesteld worden aan hogere axiale snelheden. Tegen het einde van de potentiaalkern leidt dit proces tot de afbraak van de toroïdale vorm en de creatie van stroomsgewijze filamenten die onder een hoek van 30-45 graden georiënteerd staan ten opzichte van de straalas en perifere structuren met een C-vorm. The formatie van C-vormen en de uitstoting van wervelbulten worden gekarakteriseerd door maximale activiteit van strekkende en kantelende velden.

De analyse van de 3D patronen in het gebied waar de overgang optreedt van het asymmetrische naar het 3D-regime wordt ondersteund door het toepassen van “Proper Orthogonal Decomposition” op snelheid, vorticiteit en Lamb-vectorvelden, waarbij laatstgenoemde de stromingseigenschap representeert die van belang is voor Powells aero-akoestitische analogie. De eerste 10 modi zijn geanalyseerd. In alle decomposities wordt de aanwezigheid van wervelringen die na paring stroomafwaarts reizen beschreven door het eerste paar modi. In de snelheidsmodi identificeert de axiale component een helixbeweging in het gebied voorbij het einde van de potentiaalkern, terwijl het flappende en precessie bewegingen verder stroomafwaarts beschrijft. In de vorticiteitsdecompositie laat het eerste paar modi zien dat de getransporteerde wervelringen vergezeld worden door de radiale en axiale vorticiteitsvelden die zich ontwikkelen voorbij het einde van de potentiaalkern onder een hoek van 40-45 graden ten opzichte van de straalas. Dit patroon, dat ook waargenomen wordt in modusparen bij lagere energie, wordt toegeschreven aan het afbraakproces van de wervelring. Analoge patronen worden waargenomen in de Lamb-vectormodi.

In de straal met kartels wordt de axiaal-symmetrische ringachtige coherentie van de cirkelvormige straal niet waargenomen. In plaats daarvan komen stroomsgewijze stromingsstructuren van azimuthale vorticiteit van de karteluiteinden en contraroterende stroomsgewijze wervels van axiale en radiale vorticiteit ontwikkelen zich vanuit de inkeping van de kartel. Het geleidelijk verzwakken van stroomsgewijze wervels gaat gepaard met de formatie van C-vormige structuren. Deze processen worden geassocieerd met piekactiviteit van strekkende en kantelende velden.

De relatie tussen coherente stromingsstructuren en de instantane akoestische bron is onderzocht met Powells aero-akoestische analogie, met de akoestische bron die wordt geïdentificeerd door de tweede afgeleide van de Lamb-vector. The ruimte-tijd evolutie van de bron is in kaart gebracht en vergeleken met die van de wervels, voor de visuele detectie van stromingsgebeurtenissen die betrokken zijn bij akoestische generatie. In de cirkelvormige straal wordt uitgesproken bronactiviteit waargenomen in overeenkomst met wervelparing, azimuthale instabiliteiten en stroomsgewijze filamenten, waarbij de grootste generatie plaatsvindt bij het einde van de potentiaalkern tijdens het afbraakproces van de wervelring. In het gebied nabij de straaluitlaat laat de POD analyse van de akoestische bron een karakteristieke toroïdale coherentie zien, die gerelateerd is aan de wervelring die afschudt en paart, terwijl in het gebied bij het einde van de potentiaalkern, waar de wervelringen opbreken, het de ontwikkeling van 3D storingen onder een hoek van 40-45 graden ten opzichte van de straalas beschrijft. Zulke storingen worden geassocieerd met een Strouhal getal $1.05 \leq \mathrm{St} \leq 1.9$, hetgeen hoger is dan wat gevonden werd voor de snelheid, vorticiteit en Lamb-vectormodi (typisch $\mathrm{St} \leq 0.9$). In de kartelstraal werd daarentegen evidente piekactiviteit geregistreerd, tijdens het proces van stroomwijze wervelafbraak and C-vorm formatie.

Het uitvoeren van eenduidige akoestische voorspellingen van het straallawaai met TR-TOMO PIV metingen is een uitdagende onderneming door de beperkingen op de grootte van het directe meetgebied en de vereiste ruimtelijke en tijdsresoluties. Dit werk probeert de uitdaging aan te gaan met metingen die zijn uitgevoerd op een ruimtelijke en tijdsresolutie (tot een Strouhal van 4) die het mogelijk maakt om niet alleen de details van de wervelinteracties weer te geven, maar ook hun relatie tot het lokale patroon van de akoestische bron. Daarbovenop zijn metingen uitgevoerd over een axiale lengte die genoeg is (10 straaldiameters) om de grootschalige gebeurtenissen van de straal tot 4 straaldiameters voorbij het einde van de potentiaalkern vast te leggen. Verre-veld akoestische voorspellingen zijn uitgevoerd door directe evaluatie van Powells analogie op basis van TR-TOMO PIV data. Het spectrum van de geluidsdruk laat pieken zien bij de frequenties van het vormen en paren van de wervels, alsmede een bredere bult ($1 \leq \mathrm{St} \leq 2.25$). Deze wordt toegeschreven aan de afbraak van ringwervels, nadat op basis van een visuele inspectie van de akoestische brondynamica is vastgesteld dat de frequenties ($1.05 \leq \mathrm{St} \leq 1.9$) die geassocieerd zijn met 3D golven van de bron modi binnen het bereik van de spectrale bult liggen.

Acknowledgements

This thesis summarizes the activities conducted in my PhD research between October 2008 and October 2012. During these years, I had the pleasure to meet several people who, one way or another, have contributed to the realization of my PhD research.

I am grateful to my supervisor Prof. Fulvio Scarano for guiding me along the journey of my PhD research. I have very much appreciated the collaboration with Fulvio, who, with enthusiasm and constant dedication, offered me time for discussion and encouragement.

I want to thank my friend and colleague Dr. Andrea Ianiro for collaborating to the realization of the jet experiments and for his valuable criticism during our scientific discussions. I would like to acknowledge Andrea's expertise and enthusiasm in times where trustful results were hardly obtainable. I very much enjoyed his company in and out of the lab. I believe, we will never forget the moments in which we listened to "Simply the best" to find the right determination for concluding the experiments.

I am grateful to the secretaries and technicians of the Aerodynamics group of TU Delft: Bettie, Colette, Frits, Nico, Peter, Eric, Leo and Stefan; it is because of their assistance that I could conduct and conclude the work described in this thesis.

Special thanks go to my PhD fellows Matteo Novara, Artur Palha and (Dr.) Daniele Ragni with whom I worked and I wandered around the world. With you, dear friends, I have shared science and life in their ups and downs. With you, I have shared the most-enriching never-ending philosophical discussions about politics, future, capitalism, food, love, revolution, science, freedom, women, technology, knowledge, dreams and fears. I hope we keep on travelling and philosophizing until we die, no matter if do it together or separately.

I would also like to thank my PhD-student colleagues for the good company during the long days at the office. In particular, thank you Sina Ghaemi, Andrea Sciacchitano (my desk-mate), Vahid Kazemi and Kyle Lynch.

I am grateful to Giuseppe Ceglia who, with enthusiasm and commitment, contributed to the challenging experiments of the ORINOCO project.

In the Netherlands, I was lucky to meet some special people. With them, year by year, I have built a tight community of friends. We have enjoyed staying together, partying, eating, laughing, as well as helping each other. In particular, I would like to thank Marilia Fourlaki, Samuele Oliviero, Antonio Tedesco, Jan Talsma, Nelly Bonelli, Andrea Di Matteo, Diana Brandao, Laura Vitale, Jacopo Serpieri, Efrén Fernández Abeledo and Alessandro Testa. I hope, my dear friends, we can continue on this path for years to come.

I would like to thank some friends back in Italy for always accepting me for what I am. Thank you Matteo Puttilli, Simone Pavan, Paola Damiani, Peppo (needless to mention his surname!), Andrea Linarello, Eliana Mancin, Stefano Casale, Lorena Frairia, Susanna Ricci, Giulia Beux and Francesco Melillo. I would also like to thank my good friend Franco Barbero, who has been a man of inspiration during my entire life.

My greatest gratitude goes to my family. To my grandmother Maria, my grandfather Guerrino, my father Giorgio, my mother Maria Grazia and my “little” brother Francesco for constantly offering me unconditional love, support and encouragement throughout my life.

Finally, I want to thank you, Camilla, for making me smile anywhere, anytime.
An important *era* of my life is ending. I am very curious to live the next one.

Delft, February 5, 2013

We can do only few life-changing things in our life.
Like changing a 165-70-R13 tire
along the unpaved Ruta 40.

[Somewhere between Los Antiguos and Bajo Caracoles, Ruta 40,
Argentina, December 29, 2011]

Contents

Summary .... *v*

Samenvatting .... *xi*

Acknowledgements .... *xv*

Contents .... *xvii*

Chapter 1 .... **21**

Introduction *21*

1.1 The noise-issue in civil aviation 22
1.2 Aircraft jet noise 23
1.3 Aeroacoustics 23
  1.3.1 Investigation of aeroacoustic sound generation 24
1.4 Computational aeroacoustics (CAA) 25
1.5 Experimental aeroacoustics 26
  1.5.1 Pressure sensors and microphone beam-forming 26
  1.5.2 The challenge of the flow visualization approach 27
  1.5.3 Towards 4D-PIV for aeroacoustics 28
1.6 Pressure from 4D PIV 31
1.7 Research framework 33
1.8 Objectives of the thesis 34
1.9 Outline of the thesis 34

Chapter 2 .... **37**

Theoretical background *37*

2.1 Free jets 37
  2.1.1 Governing flow equations 38
  2.1.2 Non-dimensional parameters 39
  2.1.3 Laminar and turbulent jets 40
  2.1.4 Coherent structures in jets 41
2.2 Jet aeroacoustics 46
  2.2.1 The role of coherent structures in sound generation 47
  2.2.2 Jet noise control strategies 49
2.3 Aeroacoustic analogies 52
  2.3.1 Lighthill’s analogy 53
  2.3.2 Powell’s analogy 56

Chapter 3 .... **61**

From planar to 4D PIV *61*
- 3.1 Planar PIV 61
  - 3.1.1 Working principles 61
  - 3.1.2 Seeding particles 62
  - 3.1.3 Particle imaging 63
  - 3.1.4 Image analysis 64
- 3.2 Tomographic PIV 65
  - 3.2.1 Illumination and imaging system 66
  - 3.2.2 Calibration 68
  - 3.2.3 Tomographic reconstruction 68
  - 3.2.4 Motion analysis 72
  - 3.2.5 4D PIV 73
  - 3.2.6 Computational cost 75
- 3.3 Data reduction 76
  - 3.3.1 Vortex identification methods 76
  - 3.3.2 The Lamb vector 78
  - 3.3.3 Aeroacoustic source characterization 78
  - 3.3.4 Proper orthogonal decomposition 78

Chapter 4 .... **83**

Experimental instrumentation and arrangements *83*
- 4.1 Jet tomographic facility 83
- 4.2 Time resolved tomographic PIV 86
  - 4.2.1 Tomographic reconstruction 89
  - 4.2.2 Vector-field computation 92
- 4.3 Time resolved planar PIV 93
- 4.4 Uncertainty analysis for TOMO PIV 95
- 4.5 Statistical flow properties in circular and chevron jets 97

Chapter 5 .... **105**

3D organization and dynamics of turbulent jets *105*
- 5.1 Introduction 105
- 5.2 Objectives 107
- 5.3 Unsteady behavior of the circular jet 108
  - 5.3.1 Axisymmetric regime 108
  - 5.3.2 Azimuthal instabilities and streamwise vortices 112
  - 5.3.3 The influence between azimuthal instabilities and streamwise vortices .. 119
  - 5.3.4 The process of vortex ring breakdown 120
  - 5.3.5 Large-scale coherence beyond the potential core 122
- 5.4 3D POD analysis of circular jet 123
  - 5.4.1 Decomposition based on velocity 125

5.4.2 Decomposition based on vorticity 128
5.4.3 Decomposition based on Lamb vector 129
5.5 The chevron jet 133
5.5.1 Streamwise vortices 135
5.5.2 Flow coherence organization at transition 139
5.6 Statistical distribution of vorticity components 140
5.7 Stretching and tilting of flow structures 142
5.7.1 The circular jet 143
5.7.2 The chevron jet 144
5.7.3 Statistical characterization 145
5.8 Conclusions 146

Chapter 6 149

3D aeroacoustic source characterization and jet noise prediction 149
6.1 Introduction 149
6.2 Objectives 150
6.3 Instantaneous patterns of the acoustic source 150
6.3.1 Vortex ring breakdown as main acoustic source event 153
6.3.2 The chevron jet 153
6.3.3 Statistical characterization of the acoustic source 154
6.4 3D modal decomposition 155
6.5 Noise prediction based on 4D PIV measurements 158
6.6 Conclusions 163

Chapter 7 165

Lagrangian and Eulerian evaluation of pressure field 165
7.1 Introduction 165
7.2 Objectives 167
7.3 Theoretical background 167
7.3.1 Pressure field evaluation 167
7.3.2 Material derivative evaluation 169
7.4 Experimental set up 175
7.4.1 Tomographic reconstruction 177
7.4.2 3D-Vector field computation 177
7.4.3 Pressure field determination 179
7.5 Results 179
7.5.1 Velocity field 179
7.5.2 Material velocity derivative 180
7.5.3 Pressure field determination 184
7.5.4 3-D flow effects 188
7.6 Conclusions 189

Chapter 8 191

Conclusions *191*
8.1 3D organization and dynamics of subsonic jets 191
  8.1.1 Circular jet 191
  8.1.2 Chevron jet 193
8.2 The implication of coherent structures in the aeroacoustic generation 193
  8.2.1 Noise prediction based on 4D PIV measurements 194
8.3 Lagrangian and Eulerian evaluation of pressure field 194

Chapter 9 197

Outlook on 3D organization of compressible jets *197*
9.1 The ORINOCO project 197
  9.1.1 Jet flow facility 198
  9.1.2 Tomographic PIV measurements 199
  9.1.3 3D organization by modal decomposition 201
9.2 Towards time-resolved TOMO PIV for high speed flows 202

Appendix A *205*
High resolution PIV measurements on compressible jets 205
Instantaneous velocity fields 205

Appendix B *211*
Sound and its human perception 211

Bibliography *213*

List of publications *229*
Journal articles 229
Conference proceedings 229
Talks 230

Curriculum Vitae *233*

Chapter 1

Introduction

Noise is one of the most important sources of environmental annoyance in urban communities. Noise is an *unwanted sound* that is the by-product of operating mechanical devices such as motorized vehicles, industrial machineries, computers, air-conditioning systems, among others. Such sound constitutes a form of environmental pollution that disturbs communication and speech intelligibility and interferes with sleep and mental tasks. Besides creating discomfort, a prolonged exposure to noise can have detrimental consequences on human health, such as cardiovascular hazard, hearing impairment and abnormal endocrine reactions (Ising and Kruppa, 2004). Also, it can affect social behavior and workplace safety (Kryter, 1994). To limit the consequences on public health and safety, governmental legislation on acoustic emissions has become increasingly restrictive, especially in matter of ground and air transports, which are the major causes of noise pollution in nowadays cities (Smith, 1989). A solution to noise exposition often lies in the use of acoustically insulating materials, which, for example, are used for the construction of buildings located in proximity of highways, train stations and airports. Such solution, however, can be very expensive and applicable only to confined environments. Alternative strategies, instead, aim at abating the noise at the source itself. In this prospective, understanding the sound generation process is essential to design quieter devices.

Noise can be generated by structural vibrations, thermal phenomena, electric discharges or unsteady flows. The latter can generate sound either by themselves (e.g. in a high-speed jet) or by interacting with a surface such as over cavities. The largest part of the sound produced in civil aviation has aerodynamic nature. To comply with today increasingly stringent noise regulations, aircraft manufacturers are seeking for design solutions that reduce noise emissions. Evidently, the development of such technologies requires a better knowledge of the noise generation mechanism, which, is not yet well understood for a number of cases, which become the objective of investigation of several scientific studies. A contribution to the above topic is offered within the present thesis.

1.1 The noise-issue in civil aviation

After the Second World War, the rapid growth of civil aviation has brought much greater intrusion of noise on community life due to increasing air traffic and growing populated areas nearby airports. The increasing number of public complaints, as well as the evidence of health hazard from noise exposure (Franssen et *al.*, 2002; Eriksson et *al.*, 2007), has led the aeronautical authorities to impose ever-increasingly stringent noise certifications standards on aircrafts. On the other hand, in response to local communities' concern, airports have adopted severe restrictions on night operations. In 2011, for example, the night traffic at Amsterdam Schiphol Airport was reduced to only 7% of the day-traffic (Traffic review 2011). Moreover, to discourage airlines from keeping noisy aircrafts, many airports apply extra charges, which can even result in a 100% increase in take-off/landing fees, depending on the noise certifications of the airplane.

The need for noise damping technologies and research in jet noise became more pressing in the early 1950s, when the first commercial jet-powered aircrafts entered into service. Although, in general, jet powered aircrafts have become progressively quieter with the introduction of turbofan engines in the 1960s and 1970s (Figure 1.1), the reduction in the noise level has not been sufficient to allow increased operations without affecting the community peacefulness. Therefore, the design of quieter aircrafts is today a key strategy to enjoy the economic benefits of an ever-growing air transportation system.

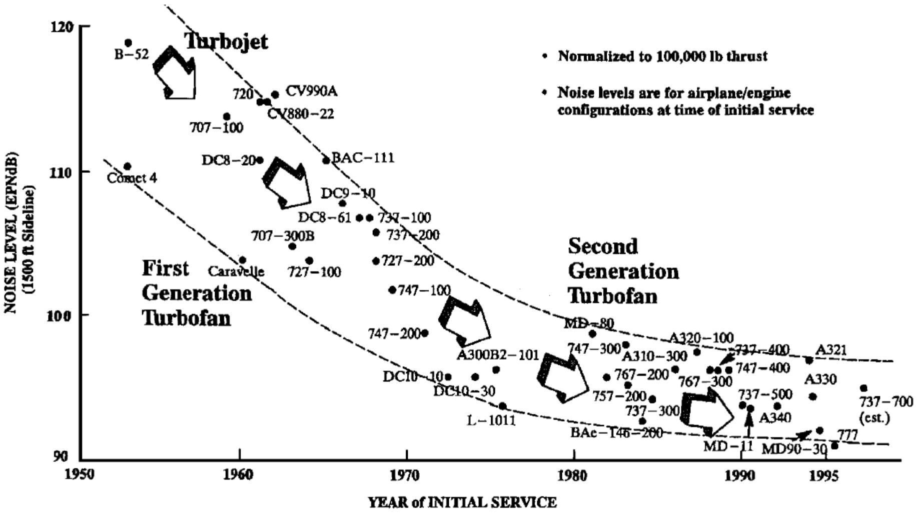

Figure 1.1 Progress in aircraft noise reduction (Clarke, 2003)

1.2 Aircraft jet noise

A significant amount of the total noise emissions of a civil aircraft is associated with the mixing process between the exhaust flow leaving the jet engines and the atmosphere. Such noise, commonly referred to as jet noise (Smith, 1989), which is a low pitched rumble that is particularly pronounced at take-off, when full trust is required. The rest of the aircraft noise is instead generated by the air interacting with the airframe (undercarriage, high lift devices, fuselage) and the rotors (fan, compressor, turbine, jet exhaust), and, in general, is more dominant at approach (Figure 1.2).

Jet noise is substantially reduced by turbofan systems and, more recently, by nozzle geometry configurations, such as the chevron nozzle (more details are given in section 2.2.2). Nowadays, the on-going development of such technologies continuously requires a deeper knowledge of the jet flow mechanics to understand which processes are responsible for noise production.

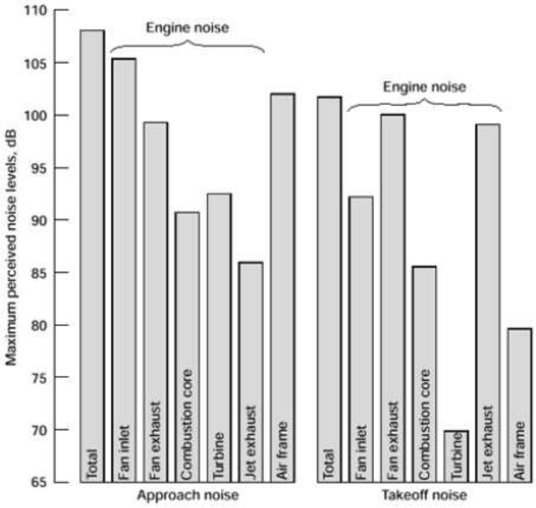

Figure 1.2 Breakdown of the noise sources of a modern commercial aircraft (Kroo, 2003)

1.3 Aeroacoustics

In 1952, the pioneering work on sound generated aerodynamically was published by Sir James Lighthill, who, in the context of attempting to predict the intensity of the noise produced by turbulent jets, proposed a theoretical approach “…for estimating the intensity of the sound produced in terms of the details of the fluid flow…”. Lighthill showed that the noise intensity of turbulent iso-thermal jets is proportional to approximately the eighth power of a characteristic jet velocity. Lighthill’s theory established the foundation of *aeroacoustics*, an area of science that blends together fluid mechanics and acoustics, with particular emphasis on the process of sound production by unsteady flow phenomena. Advances in aeroacoustics are regularly reported in literature and many reviews are available as well as textbooks (Goldstein 1976; Howe 2003). A review on the aeroacoustic problem in aeronautics is given by Ffowcs Williams (1977).

Initial efforts have been taken in the direction of a mathematical reformulation of the governing flow equations. Lighthill obtained a result in the form of a wave equation, commonly referred to as Lighthill’s aeroacoustic analogy (see section 2.3.1), where the source term takes into account of the pressure fluctuations produced by the flow turbulence. The main idea behind the approach is separating the sound generation mechanism from that of pure sound propagation.

Lighthill’s analogy, which is valid only for the aeroacoustics of unbounded turbulent flows, such as free jets, was followed by further generalizations. Curle (1955) and Ffowcs Williams and Hawkings (1969) extended the Lighthill’s theory into new formulations that also account for the aeroacoustic production by turbulence interacting with solid bodies, such as in the case of propellers-wing interactions and airframe noise. The aeroacoustic analogies of Phillips (1960), Lilley (1974) and Goldstein (2003) included the effect of interaction between the flow and the acoustic waves, whereas others highlighted the role of flow vorticity, such as those by Powell (1964), Howe (1975) and Moehring (1978). In all the formulations, the generated sound is assumed to be such a small, therefore negligible pressure disturbance compared with the dynamic pressure fluctuations in the flow. The latter assumption is not valid when flow compressibility arises at values of the Mach number approaching unity.

1.3.1 Investigation of aeroacoustic sound generation

Although the aeroacoustic analogies are appropriate to associate the turbulent flow motions and the generation of acoustic waves and, they do not provide explicit clarification about the flow properties that are most involved in the generation of noise. Details on the controversial discussion on jet noise are given in the reviews by Tam (1998), Jordan and Gervais (2008), and Jordan and Colonius (2013). This is mostly due to their integral formulation of the sound source, which makes it difficult to associate acoustic noise generation to a specific flow event isolated from the others. Nevertheless, the solution of the problem still requires the complex flow behavior to be known or extensively measured in order to properly define the *acoustic source*, which makes the understanding of the flow organization and dynamics of extreme importance.

Acoustic perturbations are generally much smaller (threshold of hearing 2 10^{-5} Pa compared to 10^{5} of the atmospheric pressure) compared to the disturbances present in the flow where they are generated, which include turbulent disturbances, related to pressure and velocity gradients and entropic disturbances. While these disturbances move with the flow and have a little effect away from the flow region, acoustic disturbances can efficiently propagate over long distances. These characteristics make aeroacoustics a challenging field of research.

1.4 Computational aeroacoustics (CAA)

While for several decades after their first introduction, acoustic analogies were only applied to simplified analytical flow models, or were used as a dimensional tool, and predictions were based on empirical methods (Bailly and Bogey, 2004), nowadays, with the exponential growth of computer power and with the development of fast and accurate methods for computational fluid dynamics (CFD), acoustic analysis of more complex flow configurations can be afforded by numerical methods, that are commonly referred to as computational aeroacoustics (CAA, a complete review on several approaches is given by Wang *et al.*, 2006). These methods combine unsteady flow simulations of the noise-producing region by direct numerical simulation (DNS), large eddy simulation (LES, Figure 1.3) or unsteady Reynolds averaged Navier-Stokes equations (URANS) simulation, with one of the aeroacoustic analogies (Lighthill, 1952; Powell,1964; Ffowcs Williams and Hawkings 1969; Howe 1975; Moehring, 1978).

While acoustic investigations with the DNS approach have mostly focused on the fundamental aspects of circular jets at low Reynolds number (Freund, 2001) due to the high computational cost, flow regimes of actual industrial application ($Re \sim 10^5$) can be afforded by LES (Bogey et al., 2003; Boersma, 2005), mixed LES-URANS approaches (Colonius and Lele, 2004) and unsteady RANS simulations (Wright *et al.*, 2004). It is well known that the disturbances associated to the acoustic phenomena are of some order of magnitude smaller than ambient pressure (in case of loud turbojet noise of 114dB at the sideline point of certification, the radiated pressure fluctuation is less than 10^{-4} of the ambient pressure), which challenges these methods in terms of required accuracy (Colonius and Lele, 2004). Despite the limitations of the current tools, important results have been recently achieved in the field. Recently, for example, high Reynolds number jets issued through more complex geometries, such as lobed and chevron nozzles, have been recently afforded with LES (Xia *et al.*, 2009; Uzun and Hussaini, 2009).

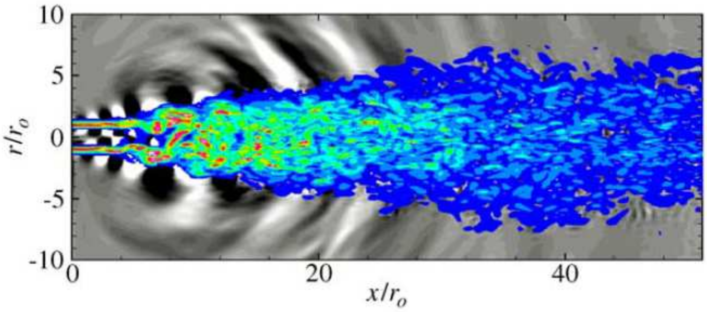

Figure 1.3 A composite visualization of an unheated turbulent jet at M= 0.9 and its sound radiation obtained by LES from Bodony and Lele (2004). Colored contours show the vorticity magnitude and highlight the jet turbulence. The grey scale contours represent dilatation and show the radiation pattern of acoustic waves

1.5 Experimental aeroacoustics

1.5.1 Pressure sensors and microphone beam-forming

Current standard experimental investigations in aeroacoustics rely on the localization of the acoustic source by surface pressure measurements or phased microphone beam-forming technique (Dougherty, 2002; Brooks and Humphreys, 2006), a 2D source imaging technique which was originally introduced by Maynard *et al.* (1985) and is nowadays also applicable to moving sources (Sijtsma, 2006; Figure 1.4). This experimental approach has the advantage to deal directly with the acoustic field, enabling the characterization of the spectral properties and the determination of the sound pressure level with good precision, thus not requiring any accurate solution of the flow field. Clearly, the drawback lies in the lack of information about the flow phenomena at the origin of sound emission, i.e. the *source*. As a result, the measurements require much scrutiny if the researcher is to identify the physical causes behind the noise emission.

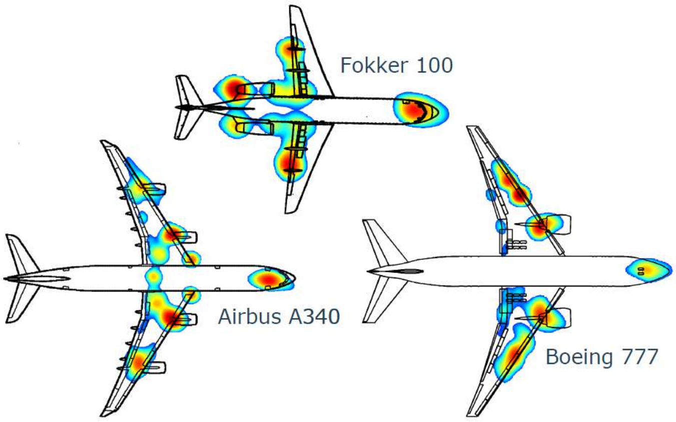

Figure 1.4 Noise source map of civil aircraft obtained by beam forming technique (Sijtsma, 2006)

To supply local information on the fluctuating pressure, surface-mounted pressure sensors are placed on the test models. This allows obtaining very accurate and well localized information complementary to the remote measurement by phased microphone arrays. However, the integration of instruments onto the model surface is rather complex and, often, only a limited number of sensors can be installed, which limits this approach to the verification of other techniques. In addition, when a free shear flow is concerned, the pressure sensors are positioned by means of designed supports, which, if located not sufficiently far away, affect the flow itself.

1.5.2 The challenge of the flow visualization approach

Since 1960s the experimental descriptions of jet flow topology were based on flow visualization techniques, such as Schlieren photography (Bradshaw *et al.* 1964; Crow and Champagne, 1971; Paschereit, 1992), smoke visualization (Becker and Massaro, 1968), hydrogen bubble visualization (Yule 1978), laser induced fluorescence (LIF, Dimotakis *et al.*, 1983), while the information on the related velocity field was retrieved by single-point measurement techniques, such as laser-Doppler anemometry (LDA, Dimotakis *et al.*, 1983) and hot-wire anemometry HWA in single (Crow and Champagne, 1971; Lau *et al.* 1972; Moore, 1977) and multiple probe configurations (Cintriniti and George, 2000).

In the last decades, the advent of particle image velocimetry PIV (Willert and Gharib 1991; Raffel *et al.*, 2007) and its developments (stereo-PIV, Arroyo and Greated 1991; dual-plane stereo-PIV, Kähler and Kompenhans 2000) have led to a better quantitative understanding of several problems in fluid mechanics. Reviews on this topic are given by Adrian (1991, 2005) and Westerweel *et al.*, (2013). In jet flows, PIV measurements were typically performed along streamwise or cross-sectional planes to investigate, quantitatively, the properties of shear layer and the transition patterns. Liepmann and Gharib (1992) used velocity information to evaluate the out-of-plane vorticity associated with streamwise structures, whereas Ganapathisubramani *et al.* (2002) also showed the related patterns by velocity gradient and Q-criterion (Jeong and Hussain, 1995). For a high speed jet, Tinney *et al.* (2008a) extracted the POD modes from stereo PIV cross-sectional realizations and showed the mechanism of fluid entrainment with low-order reconstructions of the velocity field.

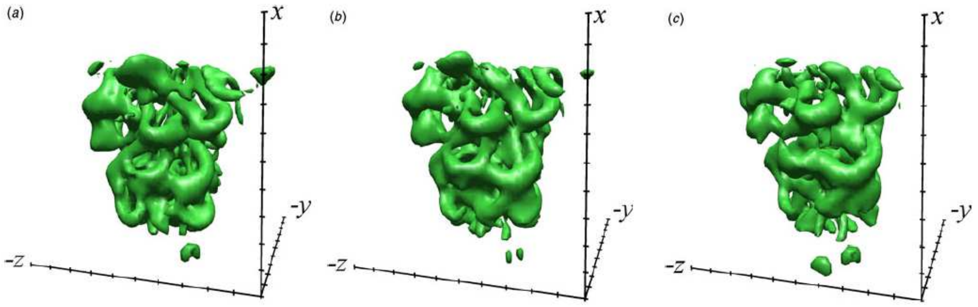

Figure 1.5 Iso-surface of vorticity magnitude $|\boldsymbol{\omega}| = 2.5\ \mathrm{s}^{-1}$. (a) $t = t_0$, (b) $t = t_0 + 0.330$ s, (c) $t = t_0 + 0.660$ s (Hori and Sakakibara, 2004).

The successful development of PIV systems performing at high-repetition rate enabled time-resolved measurements of more realistic flow configurations (Schroeder *et al.* 2004). In high-speed cold and hot jets at 0.5 to 0.9 Mach numbers, Wernet (2007) applied time-resolved PIV (TR PIV) at a sampling rate up to 25 kHz, reporting that TR PIV measurements captured the major features and most of the spectral energy. More recently, time-resolved stereo PIV was successfully used to study the instantaneous entrainment in relation with the transition patterns in circular and daisy-shaped orifice jets at *Re*= 3,600 (El Hassan and Meslem, 2010) and, with a similar approach, to discuss the influence of K-H vortex rings on the instantaneous entrainment and net volume flux in the near field of a cross-shaped orifice jet (El Hassan *et al*., 2011).

The flow turbulence is characterized by temporally evolving, highly complex three-dimensional patterns, resulting in a complex structure of the flow fluctuations, with broad spectrum of both temporal and spatial scales. Therefore, time-resolved volume-based measurements are of great interest to describe the three-dimensional flow evolution, especially in configurations where the flow does not exhibit symmetry along a plane or an axis. In most cases several planar measurements are necessary for a global characterization.

High speed scanning stereo PIV system (Bruecker, 1995) was applied by Hori and Sakakibara (2004) on a jet at *Re* = 1,000 to reconstruct, in a 3D domain, temporal sequences of velocity fields. These where used to map sequences of iso-surfaces of vorticity magnitude which illustrated the convection of elongated coherent structures in the region between 35 and 55 jet diameters downstream the nozzle exit (Figure 1.5). A scanning stereo PIV was used by Wu *et al.* (2011) to study the three-dimensional flow structures in the tip region of a water pump rotor blade. Other methods to obtain three-dimensional three-components (3D3C) flow measurements that have been later developed are 3D particle tracking velocimetry (3D PTV, Maas *et al.*, 1993), holographic particle image velocimetry (HPIV, Hinsch, 2002) and, recently the most assessed, Tomographic Particle Image Velocimetry (TOMO PIV, Elsinga *et al.*, 2006). Staack *et al.* (2010) compared TOMO PIV measurements and volumetric velocity fields reconstructed by scanning light sheet technique (Bruecker, 1995). They concluded that the former approach complies better with the mass conservation principle (for an incompressible flow) compared to the latter. Later, Khashehchi *et al.* (2010) showed the applicability of TOMO PIV to investigate the turbulent interface by the invariants of the velocity gradient tensor.

Successfully applied to the diagnostic of complex three-dimensional flows (turbulent boundary layers by Schroeder *et al.*, 2008 and Humble *et al.*, 2009, wake flows Scarano and Poelma, 2009), TOMO PIV technique opens a way to more advanced flow diagnostic possibilities, with advantage to map the complete velocity, vorticity and pressure fields (Violato *et al.*, 2011; Ghaemi *et al.*, 2012) that are well suited for the application of the acoustic analogies (Scarano 2013).

1.5.3 Towards 4D-PIV for aeroacoustics

The developments in the area of high-speed PIV, have led to its utilization as an experimental quantitative flow visualization tool. PIV has been recently used to investigate the aeroacoustic properties of transitional and turbulent flows in the incompressible regime. A broader prospective on this methodology has been acknowledged in the recent review article by Morris, 2011. Such a novel approach, if successfully deployed, can be complementary to numerical techniques, because it is able to investigate higher Reynolds number flows and, in addition to the microphone array methods, it allows the study the properties of the flow fluctuations that are associated to the sound generation and emission.

The main idea is to establish a direct connection between the aero-acoustics problem and the flow phenomena at the origin of noise generation (see review article by Jordan and Gervais, 2008), similarly to what is done by CAA when based on the solution of the fully 3D unsteady Navier-Stokes equations. It is necessary to rely on quantitative field measurement techniques able to describe the unsteady flow behavior in order to apply the aeroacoustic analogies. Time-resolved PIV (TR-PIV) based on high repetition rate systems (in the range of 1-10 kHz) is suited for such task. Wernet contributed much to this research direction (1998, 2005). In 2007 he stated that TR PIV, "…is the newest and most exciting tool recently developed to support our continuing efforts to characterize and improve our understanding of the decay of turbulence in jet flows a critical element for understanding the acoustic properties of the flow."

The approach is based on the use of PIV to measure the velocity fluctuations in the source region. The local hydrodynamic pressure fluctuations can be evaluated by use of the momentum equation and are subsequently used as input of an acoustic analogy. Other approaches, discussed in the present thesis, are based on analogies that do not require the explicit evaluation of the pressure (e.g. Powell analogy, 1964).

Preliminary studies showed that already the standard PIV approach (planar measurements at low repetition-rate) can be employed to perform aero-acoustic investigations by two-point turbulence statistics to evaluate the Lighthill turbulent stress tensor (Seiner *et al.*, 1998). In a transitional jet, where flow periodicity was imposed by a periodic forcing, Schram *et al.* (2005) investigated the mechanism of sound generation by vortex pairing with phase-locked planar PIV and a conservative formulation of vortex sound theory (Powell, 1964; Howe, 1975). It was found good agreement between the sound prediction and the microphone measurements. Based on dual-system PIV measurements, Fleury *et al.* (2008) statistically modeled the Lighthill stress tensor of a compressible jet (Mach number 0.6 and 0.9) by space-time second-order velocity correlations obtained from a dual-PIV system.

PIV has been also applied to investigate the sound produced by flows interacting with a body surface. Henning *et al.* (2008) performed planar PIV and phased-microphone-array measurements and investigated the acoustic source in the vicinity of a circular cylinder and an airfoil leading-edge slat by cross-correlation function between the acoustic pressure and velocity/vorticity fluctuations. A similar approach was later applied to a rod-airfoil flow configuration (Henning *et al.*, 2009) and a compressible cold jet (Henning *et al.*, 2010). However, analyses comprising stationary measurements of statistically independent flow realizations do not allow investigating the dynamical characteristics of the flow events, which are important to comprehend the mechanism by which the turbulent kinetic energy of the flow is converted into sound energy (Tinney *et al.*, 2008a).

Generally, the complexity of turbulent flow phenomena surpasses the capability of observation of planar PIV technique. The number of dimensions of the observation space is smaller than the natural dimensions of the phenomenon, leading to ambiguities in the interpretation of the data. Without a 3D time-dependent (4D) description of the turbulent flow pattern, accurate evaluations of the acoustic noise generation may become very difficult if not impossible. In this context, 3D time-dependent information of the flow is an important milestone in the path to the development of an experimental aeroacoustics methods based on PIV (Scarano 2013).

The key role of 4D flow descriptions for aeroacoustics is clearly stated by Tinney *et al.* (2008b), who, based on simultaneous cross-sectional stereo PIV and near-field pressure measurements on a high speed jet, presented a time-resolved low-order reconstruction of the velocity field (Figure 1.6) to develop an intuition for the time-resolved 3D low-order behavior. The authors obtained this result combining POD technique and an extension of linear stochastic estimation (LSE, Adrian 1977) to distributed space-time sampling (Tinney *et al.*, 2006) which permits conditional analysis of a given field (e.g., the turbulent velocity field) with respect to the complete space-time structure of another field (e.g., the near-field pressure). Furthermore, using the time-resolved low-order reconstruction of the velocity field, Tinney *et al.* (2008b) evaluated the Lighthill source term (Figure 1.6) and predicted the far-field acoustic, finding energy attenuation in the acoustic spectrum and good agreement in the acoustic directivity compared to microphone measurements.

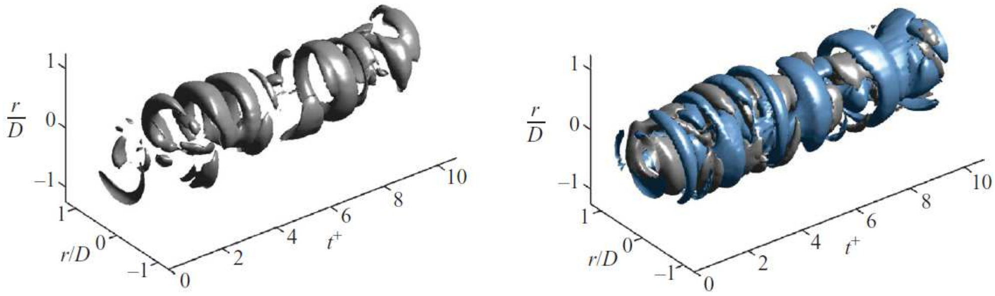

Figure 1.6 Time-resolved low-order reconstruction of a transonic jet at 3 jet diameters off the nozzle; (left) iso-surface of *Q*-criterion; (right) corresponding Lighthill source term (Tinney *et al.*, 2008b)

With TR-TOMO PIV (4D-PIV, Scarano 2007), Violato and Scarano (2011, 2013) investigated the dynamical evolution of shear layer instabilities in circular (Figure 1.7) and chevron jets at *Re*=5,000 (chapter 5 of this thesis). The authors reported detailed and quantitative descriptions of the instantaneous vortex topology based on the vorticity field and the λ_2-*criterion* (Jeong and Hussain, 1995) and showed the need of 4D measurements to explore the relation between the coherent structures and the instantaneous acoustic source (Figure 1.7) based on Powell's aeroacoustic analogy (chapter 6 of this thesis). The use of 4D PIV measurements to perform acoustic predictions of the jet noise still remains a challenging task, especially due to the constraints on the extent of the instantaneous measurement domain (see section 2.3.1 and 6.5) and on the required spatial and temporal resolution. For this reason, acoustic analyses have been so far afforded using direct numerical simulations (DNS; Freund, 2001) and large eddy simulations (LES; Bogey et *al*., 2003) techniques to obtain accurate descriptions of the flow field.

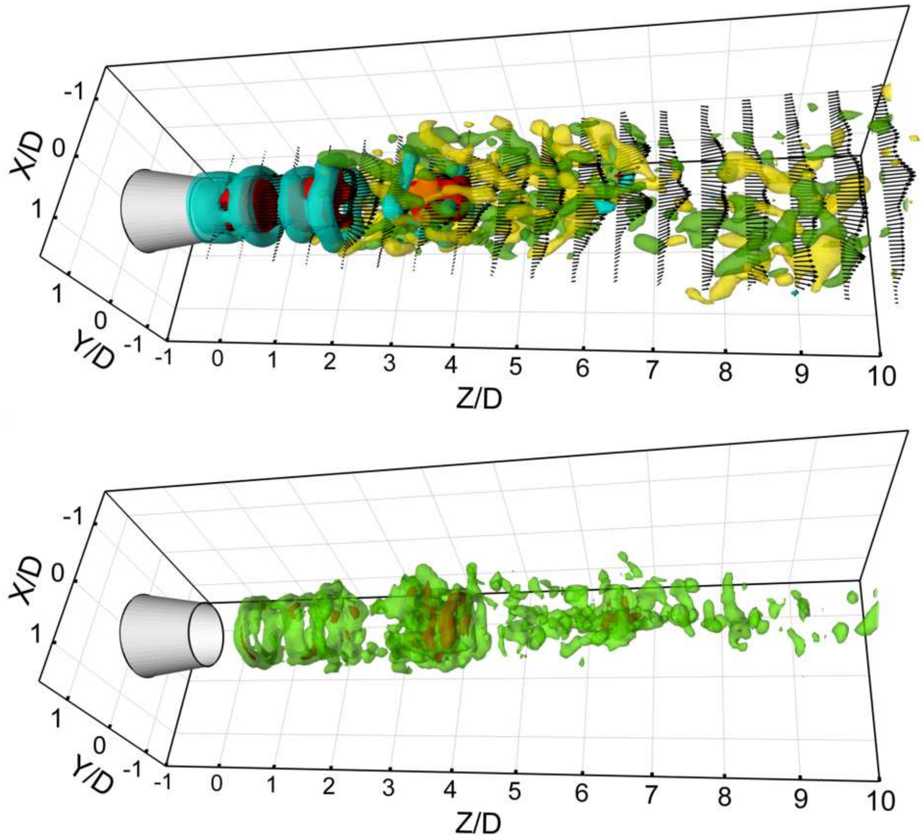

Figure 1.7 Transitional jet at *Re*=5,000; (top) instantaneous vortex pattern and (bottom) corresponding acoustic source identified by the second time derivative of the Lamb vector (Violato and Scarano, 2013, from chapter 5 and 6)

1.6 Pressure from 4D PIV

In the recent years, particular attention has been given to the use of PIV as non-intrusive method to measure the pressure field in the flow. Pressure fields from PIV measurements have been used to infer aerodynamic loads (van Oudheusden, 2007) and aeroacoustic predictions of flows interacting with body surfaces (Haigermoser, 2009). An extensive discussion on the state-of-the-art of PIV-based pressure measurement is given by van Oudheusden (2013).

For aeroacoustic analysis, as described by Haigermoser (2009), Koschatzky *et al.* (2010, 2011) and Lorenzoni *et al.* (2009, 2012), time-resolved planar PIV measurements are used to extract the body-surface pressure distribution, which is used to predict the instantaneous far-field acoustic pressure by means of Curle’s analogy (1955). Figure 1.8 shows the instantaneous velocity and pressure fields of a rod-airfoil flow and the comparison between the related far-field acoustic prediction (Lorenzoni *et al.*, 2009 and 2012) based on Curle's analogy and microphone measurements.

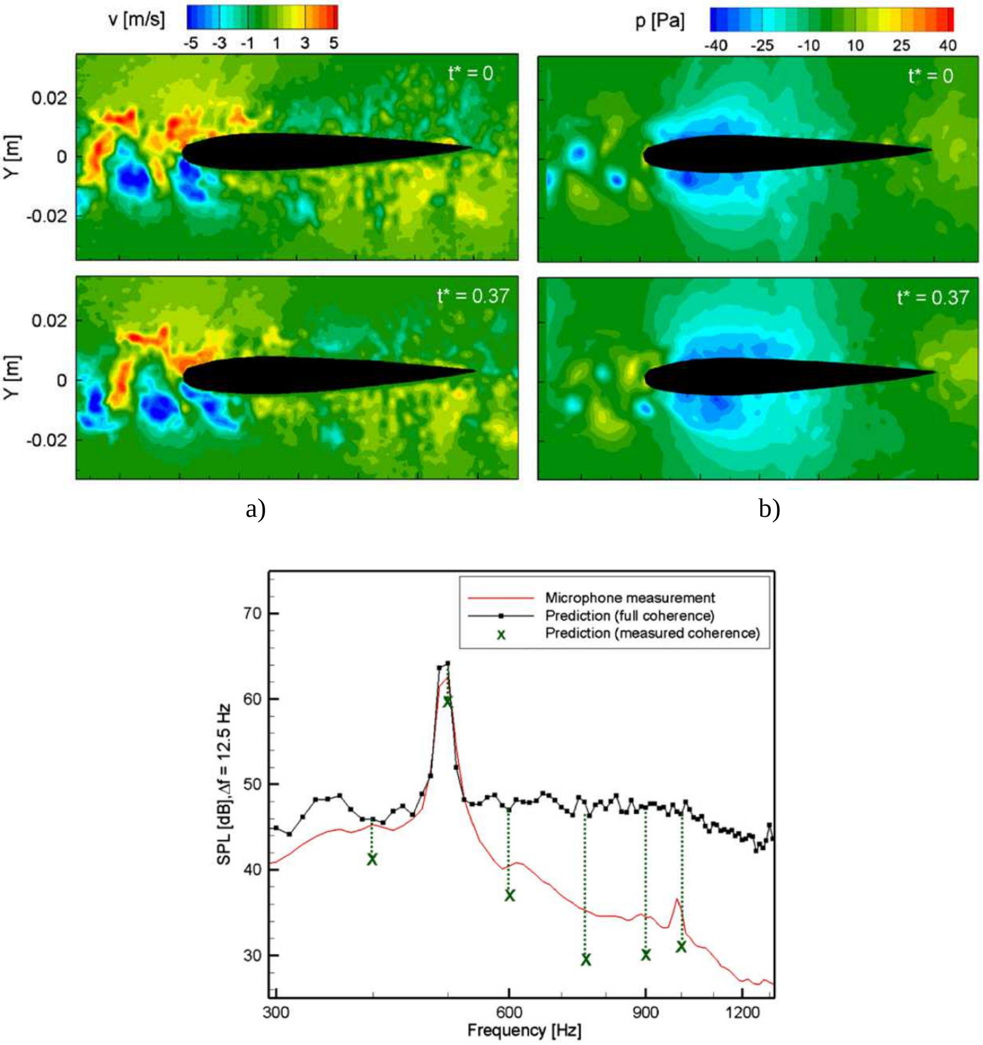

a) b)

c)

Figure 1.8 NACA0012 airfoil embedded in the Karman wake of a rod. Time sequence visualization of the instantaneous vertical velocity (a) and pressure; c) comparison between acoustic spectra obtained from microphone measurements and acoustic prediction by Curle's analogy (Lorenzoni *et al.* 2012)

Higher accuracy in the pressure evaluation from PIV would lead to more reliable PIV-based sound predictions to be used together with computational aeroacoustics CAA (Crighton, 1993), sensors and microphone arrays (Brooks and Humphreys, 2003). The accuracy of pressure measurements strongly depends on the accuracy of the material acceleration, which can be obtained from time-resolved velocity measurements either by an Eulerian (Baur and Kongeter, 1999) or a Lagrangian (Liu and Katz, 2006) approach. Violato *et al.* (2011) compared these two approaches using time-resolved TOMO PIV measurements of the rod-airfoil flow studied by Lorenzoni *et al.* (2009). They found that the Lagrangian approach allows larger time separations, thus lower precision error, whereas the Eulerian is restricted to shorter time separations and is found not applicable to evaluate pressure gradient field if a relative precision error lower than 10% is required (chapter 7 of this thesis). For the above reasons, the Lagrangian approach has been recently used by Ghaemi *et al.* (2012) and Proebsting *et al.* (2012) for the evaluation of the 3D instantaneous pressure field in turbulent boundary layers.

Violato *et al.* (2011) also compared the pressure evaluated from 3D measurements to that obtained from synchronous planar ones to discuss the effect of 3D flow phenomena on the accuracy of the Lagrangian technique (chapter 7 of this thesis).

1.7 Research framework

The research presented in this thesis is part of the FLOVIST project (Flow Visualization Inspired Aeroacoustics with Time-Resolved Tomographic Particle Image Velocimetry), funded by the European Research Council (ERC) between 2008 and 2012.

The FLOVIST project aims at the development of an innovative experimental approach based on time-resolved TOMO-PIV technique to investigate the 3D organization and dynamics of flows of aeronautical interest and their role in the production of acoustic noise.

Although large-scale problems typical of industrial applications are not at reach for the proposed method because of physical limitations in the optical components and energy sources for illumination, the main field of application is that of wind-tunnel scaled experiments that, however, still constitute a consistent part of the aerodynamic fundamental research related to aircraft design.

The project aims to demonstrate that through the application of this methodology a new investigation approach can be followed by scientists and researchers for the study of complex three-dimensional flows and related aeroacoustic properties. On the other hand, from the point of view of fundamental research the project opens new scientific horizons in the sense that it offers the unprecedented possibility to perform observations of fluid flow phenomena in a non-reduced number of dimensions (4D flow visualization) at a quantitative level.

Still, a non-negligible side-product is the capability to validate CFD turbulence models used for RANS and LES calculations on a three-dimensional basis. It also offers a unique complementary experimental tool to the array microphone analysis, which at present is the state-of-the-art concerning field measurements and complex aerodynamic systems analysis.

Finally, considerable and broad impact is expected on fundamental research in fluid flows and turbulence, given the general applicability of the experimental approach to the study of vortex dynamics, unsteady flows and turbulent coherent structures.

Four Ph.D. students and one Post-Doc are contributing to FLOVIST research. The topics cover

- advanced developments of Tomographic PIV;
- developments of non-intrusive surface pressure analysis by TR-TOMO PIV and application to turbulent boundary layers and trailing edge flows;
- application to jets aeroacoustics (discussed in this thesis);
- benchmarking with respect to DNS.

The research conducted within the FLOVIST project yields physical insights into jet flows (Violato and Scarano 2011 and 2013), turbulent boundary layers (Ghaemi and Scarano, 2011; Ghaemi *et al.*, 2012) and wake flows (Violato *et al.*, 2011; Lorenzoni *et al.*, 2009 and 2012), as well as improvements to the PIV technique (Novara *et al.*, 2010; Ghaemi and Scarano, 2010; Moore *et al.*, 2011; Scarano and Moore 2011; Novara and Scarano, 2012; Sciacchitano *et al.*; 2012).

1.8 Objectives of the thesis

Two objectives are pursued in this thesis. The first one is to investigate the 3D evolution of large-scale structures in subsonic jets at moderate Reynolds number using time-resolved tomographic PIV. Circular and six-chevron jets are compared. The focus is placed upon the process of transition from the laminar to the turbulent regime, which features 3D patterns not accessible by single-point or planar measurement approaches.

The second objective is to study the relation between the large-scale flow events and the aeroacoustic source evoking Powell's analogy, with acoustic predictions that are performed by direct integration of the analogy using TR-TOMO PIV data.

1.9 Outline of the thesis

Chapter 2 outlines the fundamental concepts of jet flows and jet aeroacoustics and introduces the relevant flow equations.

Chapter 3 describes the working principle of planar and tomographic PIV, as well as time-resolved tomographic PIV. This is followed by the description of the data reduction approaches used in this thesis.

Chapter 4 is devoted to the description of the facility, the experimental instrumentation and the arrangements adopted to perform time-resolved tomographic PIV experiments on jet flows. This is followed by an uncertainty analysis for tomographic PIV measurements and by a statistical flow characterization for circular and chevron jets.

Chapter 5 describes of the 3D large-scale organization and dynamics in incompressible turbulent jets at Reynolds number 5,000, with a comparison between the circular and six-chevron jet configurations. Coherent structures are described using instantaneous velocity and vorticity fields, as well as by vortex identification criterions (e.g. λ_2-criterion). For the circular jet, 3D proper orthogonal decomposition of the velocity, vorticity and Lamb vector fields is employed to identify more clearly some aspects of the flow 3D organization in the region of transition to the turbulent regime. This is followed by a survey on the stretching-tilting fields of the flow structures.

Chapter 6 describes the relation between large-scale events and acoustic source, which, evoking Powell’s aeroacoustic analogy, is associated with the second time derivative of the Lamb vector. For the circular jet, the analysis of the source in the transition region is aided by 3D proper orthogonal decompositions. Finally, acoustic predictions are performed by direct integration of Powell’s analogy using TR-TOMO PIV data and conjectures on the events most producing noise are proposed.

Chapter 7 presents a time-resolved tomographic PIV investigation on a rod-airfoil flow configuration. The 3D velocity field is used to evaluate the instantaneous pressure field by integration of the pressure gradient field. A Lagrangian approach in the material derivative evaluation is compared to an Eulerian one in terms of precision error at different values of the time interval and the criticality of measurement temporal resolution on pressure field evaluation is discussed. Moreover, the instantaneous planar pressure evaluated from tomographic velocity fields is compared to that obtained from synchronous planar PIV velocity fields to discuss 3-D flow effects on the accuracy of the Lagrangian approach.

Chapter 8 summarizes the major conclusions of this thesis, whereas future directions are proposed in chapter 9, which presents a tomographic PIV investigation on compressible jets that was conducted within the ORINOCO project in September 2012.

Chapter 2

Theoretical background

This chapter introduces the definitions and terminology used in the remainder of the thesis for the discussion of the physical concepts of jet flows. The discussion includes background and fundamental aspects of jet aeroacoustics.

2.1 Free jets

Jet flows are produced by a pressure drop through a nozzle, or an orifice. Velocity profile and the turbulent properties at the nozzle exit vary greatly depending on the nozzle shape (Schetz and Fush, 1999) and upon the upstream flow characteristics. For instance, in the laminar regime, pipe-shaped nozzles produce parabolic velocity profiles, whereas convergent nozzles produce a uniform (top-hat) velocity profile at the exit. A comprehensive overview of jet flows is given by Rajaratnam (1976), while in this section, only the salient concepts are introduced.

Jet flows can be initially laminar or turbulent, while the ambient flow can be stationary with respect to the nozzle exit, or moving, in which case it is said to be a co-flow. As shown in the schematic of Figure 2.1, the interface separating the jet from the ambient fluid is referred to as the free shear layer. In the turbulent regime, mass entrainment and momentum transfer occurs through this region. As a result, the jet increases its radius (spreading) and its mass rate. While becoming thicker, the shear layer penetrates towards the jet axis in the potential flow region (also referred to as potential core), where the flow velocity is equal to that at the nozzle exit. The length of the potential core varies upon how the shear layer develops. It has been reported to extend up to 6.5 jet diameters (Hussain and Zaman, 1981), depending on the velocity profiles and the turbulence levels at the nozzle exit.

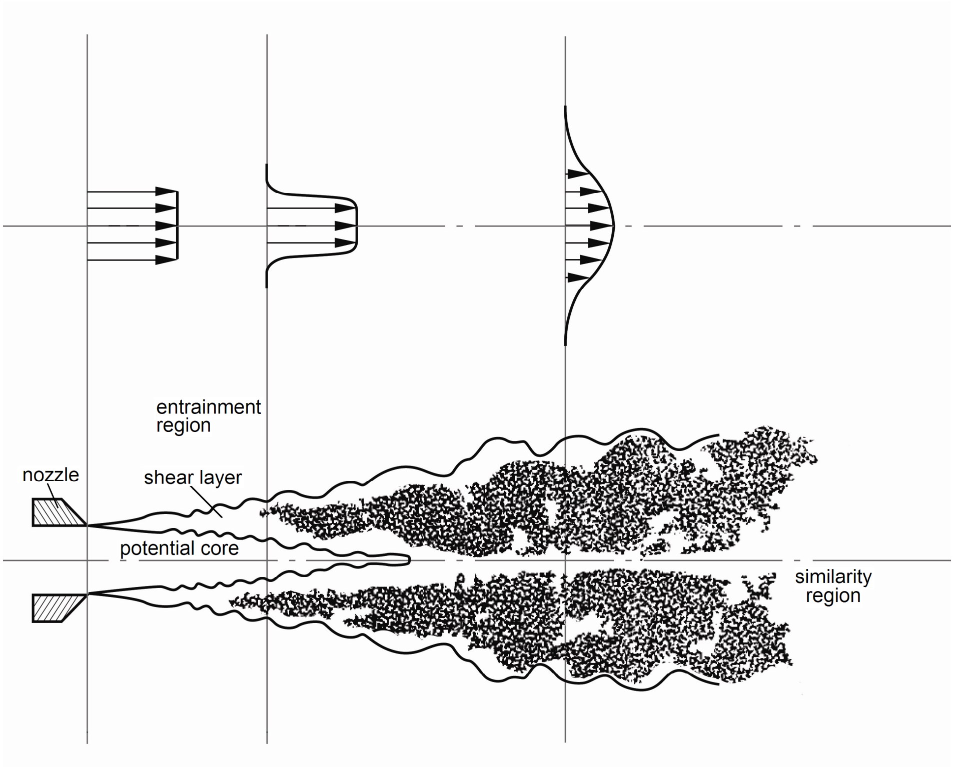

Figure 2.1 Jet flow sketch (bottom) with mean axial velocity profiles (top)

The region beyond the end of the potential core where mean velocity profile is self-preserving is commonly referred to as the similarity region. This, according to Tennekes and Lumley (1972), is located beyond 8 jet diameters from the nozzle exit, while the turbulence quantities are still evolving at 40 diameters.

2.1.1 Governing flow equations

The equations governing the flow motion are derived by considerations of conservation of mass, momentum and energy in an infinitesimal control volume. At a given time instant, these three conservations laws together with the thermodynamic constitutive relations (including the equation of state, in this case the ideal gas law) relate the velocity vector field **V** with the thermodynamic variables (pressure *p*, density *ρ* and temperature *T*).

The mass conservation is expressed by the continuity equation, which using Einstein's summation convention reads as

$$\frac{\partial \rho}{\partial t}+\frac{\partial\left(\rho V_i\right)}{\partial x_i}=0 \; . \tag{2.1}$$

For incompressible flows, the velocity field is divergence-free:

$$\frac{\partial V_i}{\partial x_i} = 0 . \tag{2.2}$$

The conservation of momentum is described by the Navier-Stokes equations

$$\frac{\partial \rho V_i}{\partial t} + \frac{\partial}{\partial x_j}\left[\rho V_i V_j + p\delta_{ij}\right] = \frac{\partial \tau_{ij}}{\partial x_j} + f_i . \tag{2.3}$$

where f_i are the body forces, τ_{ij} is the viscous tensor that, for a Newtonian fluid with constant viscosity μ, is given by

$$\tau_{ij} = \mu\left(\frac{\partial V_i}{\partial x_j} + \frac{\partial V_j}{\partial x_i} - \frac{2}{3}\delta_{ij}\frac{\partial V_k}{\partial x_k}\right). \tag{2.4}$$

The viscosity of the flow depends on the flow temperature and can be determined by the Sutherland's law

$$\frac{\mu}{\mu_\infty} = \left(\frac{T}{T_\infty}\right)^{3/2} \frac{1.4T_\infty}{T + 0.4T_\infty} . \tag{2.5}$$

If conductive and viscous effects are neglected and external forces are absent, which is the case of the flow regime considered in this thesis, and the entropy is uniform. Then we can consider the homo-entropic flow condition

$$\frac{\partial s}{\partial x_i} = 0 . \tag{2.6}$$

The motion of the flow can be finally determined from equations (2.1) and (2.3), using the equation of state for an ideal gas

$$p = \rho RT , \tag{2.7}$$

which relate the thermodynamic quantities p, ρ and T with each other (R is the gas constant).

The speed of sound is defined as

$$c^2 = \left(\frac{\partial p}{\partial \rho}\right)_s , \tag{2.8}$$

where the subscript s indicates an isentropic process. For an ideal gas, the speed of sound is given by

$$c = \sqrt{\gamma RT} , \tag{2.9}$$

where γ is the specific heat ratio.

2.1.2 Non-dimensional parameters

In this study, the Reynolds number *Re* is based on the nozzle diameter and the axial velocity at the jet exit W_j:

$$Re = \frac{W_j D}{\nu}, \tag{2.10}$$

where $\nu = \mu / \rho$ is the kinematic viscosity.

The Mach number M is defined as the ratio between the velocity W_j and the speed of sound c:

$$M = \frac{W_j}{c}, \tag{2.11}$$

while the frequency in non-dimensional form is obtained dividing the dimensional frequency f by a reference velocity V_{ref} and multiplying by a length scale L, resulting in the Strouhal number St:

$$St = \frac{fL}{V_{ref}}. \tag{2.12}$$

2.1.3 Laminar and turbulent jets

Circular free jets can be classified according to the value of the Reynolds number into four different categories (Viskanta, 1993)

- dissipated laminar jet, $Re < 300$
- fully laminar jet, $300 < Re < 1000$
- transitional or semi-turbulent jet, $1000 < Re < 3000$
- fully turbulent jet, $Re > 3000$.

However, factors such as the Reynolds number and the exit velocity profile affect the mixing process at the outer jet boundaries that transforms a jet with a laminar exit into a turbulent jet. For a more details on turbulent jets the reader is referred to the review article by List (1982).

Jets are employed in many engineering processes such as aircraft propulsion (Bridges and Brown, 2004; Alkislar, *et al.* 2007), surface cooling (Tummers *et al.*, 2011; Geers *et al.*, 2008) and fuel mixing (Tummers *et al.*, 2009; Oldenhof *et al.*, 2010). In aircraft jet engines, jet flows are characterized by a Reynolds number larger than 10^5, meaning that the device operated in turbulent regime. Several studies have been conducted on high speed jets to investigate the flow patterns (Lau *et al.* 1972 and 1979; Camussi and Guj, 1999; Jung *et al.* 2004; Ukeiley *et al.*, 2007) and the acoustic generation (Bridges and Brown, 2004; Hileman *et al.*, 2005; Alkislar, *et al.* 2007; Grizzi and Camussi, 2012).

On the other hand, jets at low Reynolds numbers with laminar exit still remain of fundamental interest because of their reduced range of turbulent scales. In aeroacoustics this allows the study of the jet dynamics and sound radiation in simplified settings where the flow is dominated by coherent structures (section 2.1.4 and 2.2.1). Additionally, at low-Reynolds number jets it is possible to calculate the flow field using direct numerical simulation (Verzicco and Orlandi, 1994; Freund, 2001).

2.1.4 Coherent structures in jets

In the 1960s and 1970s, the turbulent flow motions in high-Reynolds jets and, in other turbulent flows, were observed to be more ordered than previously hypothesized and scientists started referring to a new conceptual flow entity, namely coherent structure (Cantwell 1981; Lumley 1981). Mollo-Christensen (1967) reported such orderly nature in turbulent round jets: "… although the velocity signal is random, one should expect to see intermittently a rather regular spatial structure in the shear layer". A large body of studies later provided detailed descriptions of orderly motions in jet flows, such as Crow and Champagne (1971), Yule (1978), Hussain (1986) and Liepmann and Gharib (1992) to cite just a few.

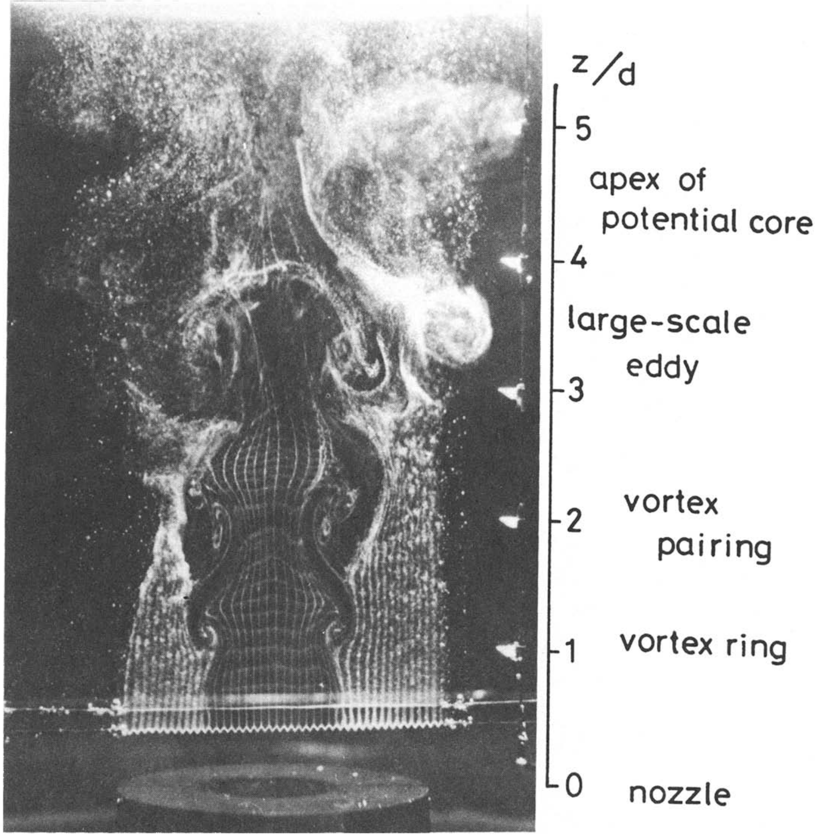

Figure 2.2 Free jet flow patterns during laminar to turbulent transition; visualization by the hydrogen bubble method (Kataoka *et al.*, 1987)

In the region near the nozzle exit of initially laminar round jets (Figure 2.2), the shear layer develops wave-like instabilities of Kelvin-Helmholtz type that grow as flow structures of ring-like shape (Bradshaw, 1963; Becker and Massaro 1968; Kataoka *et al.*, 1987; Camussi and Guj, 1999). At moderate Reynolds number, such structures grow maintaining axial symmetry and undergo pairing (Figure 2.3) due to the mutual flow induction (Crow and Champagne, 1971; Winant and Browand 1974; Schram 2003). The vortex ring pattern, as well as the shedding and pairing frequencies depends on the initial state of the shear layer (i.e., the initial condition) which must include details of the mean and turbulence measures of the jet exit flow (Bridges and Hussain, 1987). For example, a jet with a small boundary layer thickness has more "room" for several successive vortex pairings to occur (such as in Laufer and Yen, 1983), compared to a jet with a thick boundary layer (Violato and Scarano, 2011). Vortex pairing is largely absent in initially fully turbulent jets, instead (Hussain, 1983).

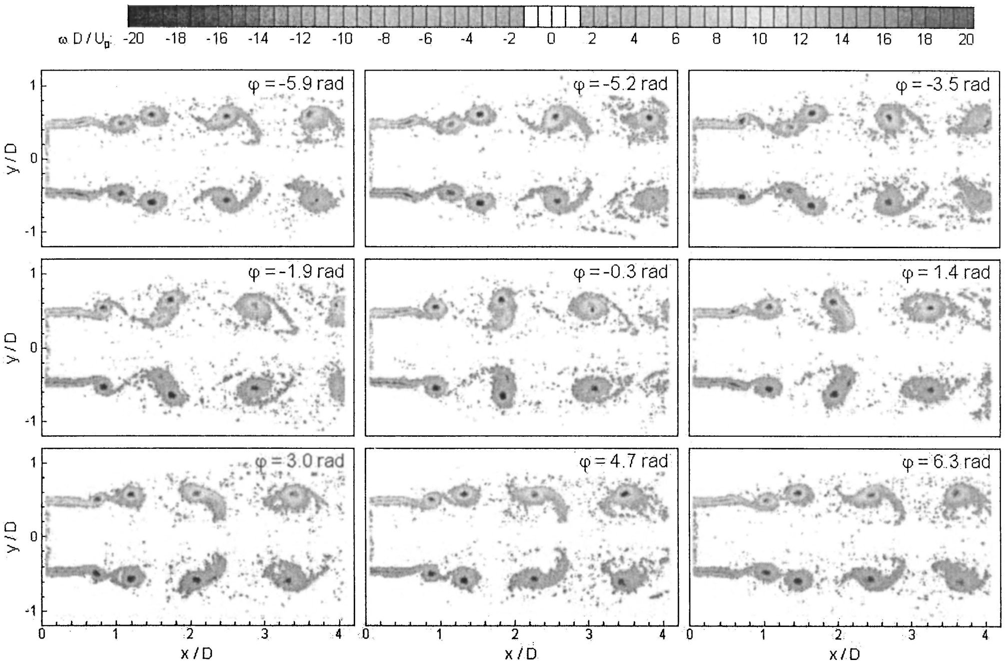

Figure 2.3 Sequence of vortex pairing by PIV; iso-contour of vorticity field (Schram et al., 2004)

The mechanism of flow transition from laminar to turbulent regime is characterized by the formation of streamwise vortices (Dimotakis *et al.* 1983, Paschereit *et al.* 1992, Ganapathisubramani *et al.*, 2002) and the growth of vortex ring azimuthal waves (Widnall and Sullivan, 1973; Yule, 1978). In Figure 2.4a, the cross-sectional LIF visualizations by

Liepmann and Gharib (1992) illustrate the azimuthal instabilities of a vortex ring that is surrounded by counter-rotating pairs of streamwise vortices. These, instead, are initially formed in the region between vortex rings, commonly referred to as the braid region (Figure 2.4b). According to Hussain (1986), streamwise vortices induce the deformation of the vortex rings and cause mixing and dissipation. Ganapathisubramani *et al.*, (2002) used the *Q*-criterion to inspect the patterns of streamwise vortices (Figure 2.5). However, being based on stereo-PIV, such patterns should be verified quantitatively with volume based techniques (see chapter 5).

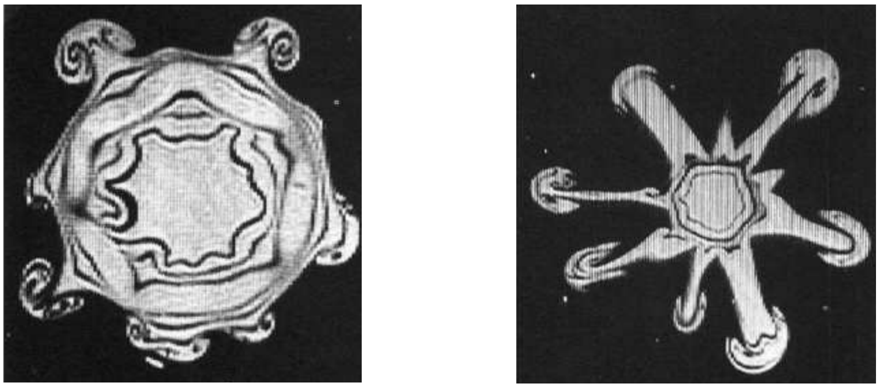

a) b)

Figure 2.4 Cross-sectional LIF visualization of jet flow at *Re*=5,500 (Liepmann and Gharib, 1992); (a) vortex ring with azimuthal instabilities surrounded by pairs of streamwise vortices; (b) streamwise vortices in the braid region

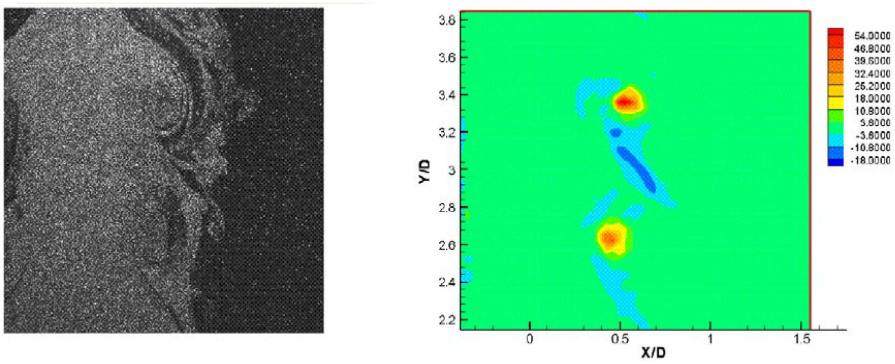

Figure 2.5 Streamwise vortices in circular jet Re=19,000; (left) flow visualization and (right) corresponding iso-contour of Q-criterion from stereo-PIV(Ganapathisubramani et al., 2002)

With hydrogen bubble visualizations, Yule (1978) found that the region of transition, which is located by the end of the potential core, is characterized by loss of circumferential coherence and the formation of smaller scales that ejects bursts of fluids (Figure 2.6). Hussain and Zaman (1981) identified toroidal structures developing azimuthal lobes, which by the end of the potential core split into coherent substructures.the process also involves a cut-and-connect mechanism by which substructures result from the initial vortex ring (Figure 2.7, Hussain, 1986). The same authors argued that the formation of these lobes and the breakdown of the vortices are more important in the production of aerodynamic noise (see section 2.2.1). Using hot-wire measurements, Juvé *et al.* (1980) observed that sudden decelerations occur frequently near the end of the potential core, whereas Kyle and Shreenivasan (1993) reported that energetic and highly regular pairing leads to the early and abrupt breakdown of the potential core.

In the region beyond the end of the potential core the vortex ring coherence vanishes (Yule, 1978; Hussain and Zaman, 1981) and the flow is mainly organized into streamwise vortex filaments. Based on planar PIV and flow visualizations, Liepmann and Gharib (1992) reported that the streamwise vorticity is the main factor controlling the entrainment process downstream the potential core.

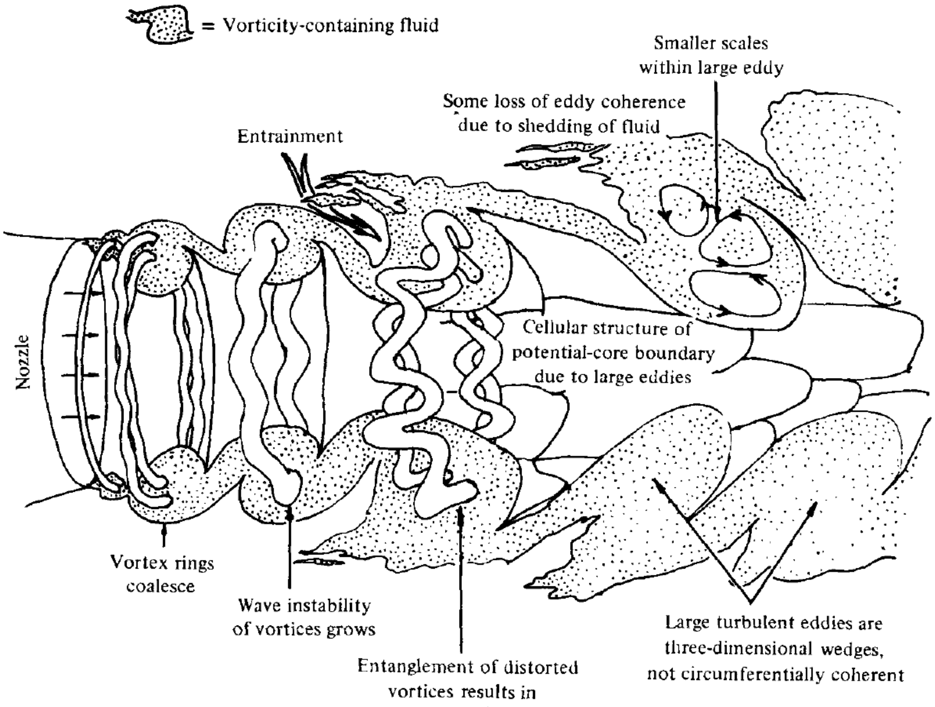
= Vorticity-containing fluid
Smaller scales within large eddy
Some loss of eddy coherence due to shedding of fluid
Entrainment
Nozzle
Cellular structure of potential-core boundary due to large eddies
Vortex rings coalesce
Wave instability of vortices grows
Entanglement of distorted vortices results in turbulent flow
Large turbulent eddies are three-dimensional wedges, not circumferentially coherent

Figure 2.6 Physical structure of transitional jet (Yule, 1978)

Quantitative descriptions of the 3D vortex dynamics in the region beyond that of axisymmetric coherence cannot be accurate if based on single point or planar measurements. The fully understanding of the 3D vortex pattern evolution requires time-resolved, volume based measurements, as proposed in chapter 5 of this thesis, where the process of vortex ring breakdown is described quantitatively based on velocity and vorticity vectors, as well as the λ_2-*criterion* (Jeong and Hussain, 1995).

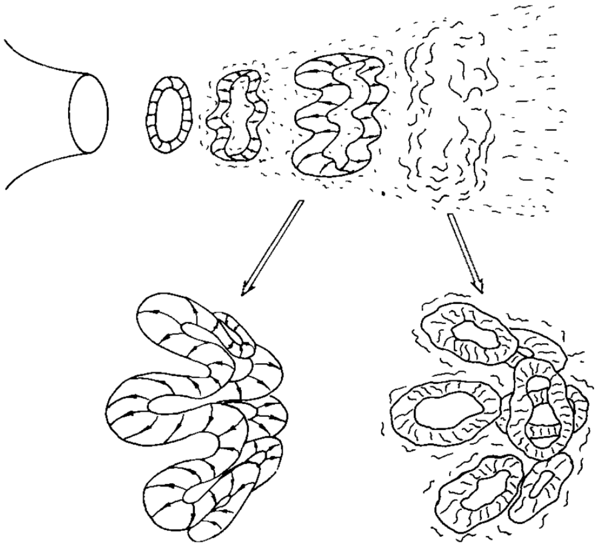

Figure 2.7 Schematic of the vortex ring breakdown process (Hussain, 1986)

Further experiments focused on the region downstream of the axisymmetric regime where specific strategies were adopted to reconstruct three-dimensional flow features from point-wise planar measurements. Matsuda and Sakakibara (2005) produced a 3D representation of the turbulent coherent structures combining stereo-PIV measurements perpendicular to the jet axis and assuming Taylor's hypothesis. They visualized groups of hairpin vortex structures in the fully developed turbulent region of jets in the range $1{,}500<Re<5{,}000$.

Following the approach of Cintriniti and George (2000), Jung *et al.* (2004) scanned the first 6 diameters of a turbulent axisymmetric jet at high Reynolds number with a polar array of 138 synchronized straight hot wire probes and showed a low-dimensional time-dependent reconstruction of the streamwise velocity using the dominant POD modes. Reconstruction of the full-field streamwise velocity component using the dominant POD modes shows clearly the evolution of the flow with downstream position, from 'volcano-type' eruptions to a 'propeller-like' pattern. In a later study, Iqbal and Thomas (2007) achieved a three-component implementation of the POD and reported a helical vortex structure beyond the tip of the potential core.

When applied to velocity fields, such as PIV data or numerical simulations, POD analysis enables the identification of the coherent structures in terms of global eigenmodes. By POD technique and PIV, Shinneeb *et al*. (2008) investigated the vortex organization in the far-field region of a turbulent jet based on PIV measurements along the streamwise plane. With a vortex identification algorithm applied to velocity fields reconstructed by a number of modes such to recover 40% of the turbulent kinetic energy, the authors observed that the number of vortices decreases in the axial direction. The occurrence of the vortex pairing and tearing processes was mentioned by the authors, although without a description of the modal patterns.

Lynch and Thurow (2009) applied a novel three-dimensional light intensity visualization technique developed by Thurow and Satija (2007) to study the large-scale vortices in a jet at *Re*=10,000 (Figure 2.8). Instantaneous visualization of the transition region showed the rupture of jet centerline axial-symmetry, while POD analysis of the image intensity identified *flapping* motion and the combination between *flapping* and *helical* modes.

The 3D features of the velocity modes extracted from hot wire measurements (Jung *et al*., 2004; Iqbal and Thomas, 2007), PIV (Shinneeb *et al*., 2008) and three-dimensional light intensity visualization (Lynch and Thurow, 2009;) remain to be ascertained with a fully 3D kinematic analysis. This is proposed in chapter 5, where POD decomposition is applied to 3D velocity, vorticity and Lamb vector fields and the modes are described and commented in relation with the above literature.

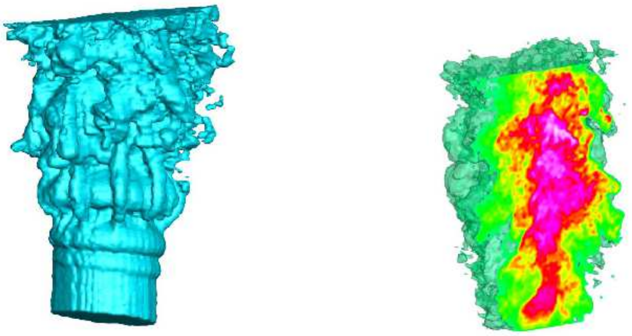

Figure 2.8 Instantaneous 3D flow visualization by light intensity iso-surface: (left) near and (right) transition regions. (Lynch and Thurow, 2009).

2.2 Jet aeroacoustics

Jet aeroacoustics is a branch of aeroacoustic that deals with sound generation from jet flows. It was firstly investigated by Lighthill (1952), who clearly stated its focus : "…it is concerned with uncovering the mechanism of conversion of energy between two of its forms, namely, the kinetic energy of fluctuating shear motions and the acoustic energy of fluctuating longitudinal motions". Lighthill was to formulate a theory that mathematically unified the before separated fields of acoustic and aerodynamics. He reformulated the equations of fluid motion as a wave equation, the Lighthill's acoustic analogy (section 2.3.1), and showed that this was an appropriate tool to describe the acoustic wave generated by the turbulent motions of the jet, namely the source term.

2.2.1 The role of coherent structures in sound generation

The jet flows were known to comprise random turbulent fluctuations, correlated over a spatiotemporal extent defined by the integral scales of the turbulence. The double spatial derivative in Lighthill's source term implied a quadrupole behavior, and so the sources of jet noise were understood as quadrupole elemental deformations associated with a system of randomly distributed eddies, convected with and radiating into the mean-flow. This view changed radically over the course the 1960s and 1970s, when it was recognized the existence of a more organized underlying structure in free shear-flows. Early observations of organized eddies in the near-nozzle region were reported in the experimental works by Bradshaw *et al.* (1964) and Mollo-Christensen (1967), while, later, Crow and Champagne (1971) reported the presence of ring-like structures and conjectured their implications with sound generation. Since then several investigations have focused on the role of coherent structures in the generation of sound. Michalke and Fuchs (1975) and Juvé *et al.* (1979) discussed the strong azimuthal coherence in the sound field radiated by the round jet as evidence of a source mechanism involving vortex rings. Lau *et al.* (1972) and Moore (1977) also related microphone measurements to the presence of large scale vortices, whereas Dahan *et al.* (1978) experimentally showed that 50% of the sound radiation of hot jets could be attributed to the dynamics of coherent flow structures (Gui *et al.*, 2003). A complete review of coherent structures in jet noise is given in Jordan and Gervais (2008) and Jordan and Colonius (2013).

In subsonic jets, which are concerned in this thesis, there are three different mechanisms through which vortex rings can generate sound: the pairing of vortex rings, the oscillation of vortex rings and the breakdown of vortex rings. Vortex pairing mechanism was studied with microphones measurements by Bridges and Hussain (1987), who reported significant sound generation in jets with laminar exit. The experimental work by Laufer and Yen (1983) showed that acoustic sources are associated with the nonlinear saturation of the unstable wave amplitudes of the shear layer occurring at the vortex-pairing locations and that the radiation intensity varies nonlinearly with the source strength and is highly directional, exponential in character. More recently, Coiffet et al. (2006) gave experimental evidence supporting the existence vortex-pairing and/or wavy-wall type instabilities mechanism in the region upstream of the end of the potential core, and demonstrate that the production mechanism is linear. Vortex ring oscillations were shown to efficiently produce sound in the analytical study by Kopiev and Chernyshev (1997) and in the experimental investigation by Kopiev *et al.* (1999). The breakdown of ring structures in the region by the end of the potential core was argued to be a source mechanism (Hussain and Zaman, 1981) more efficient than vortex pairing, in contrast with Laufer and Yen (1983). Hussain (1986) specifically described the noise generation as the result of the cut-and connect interaction of coherent structures.

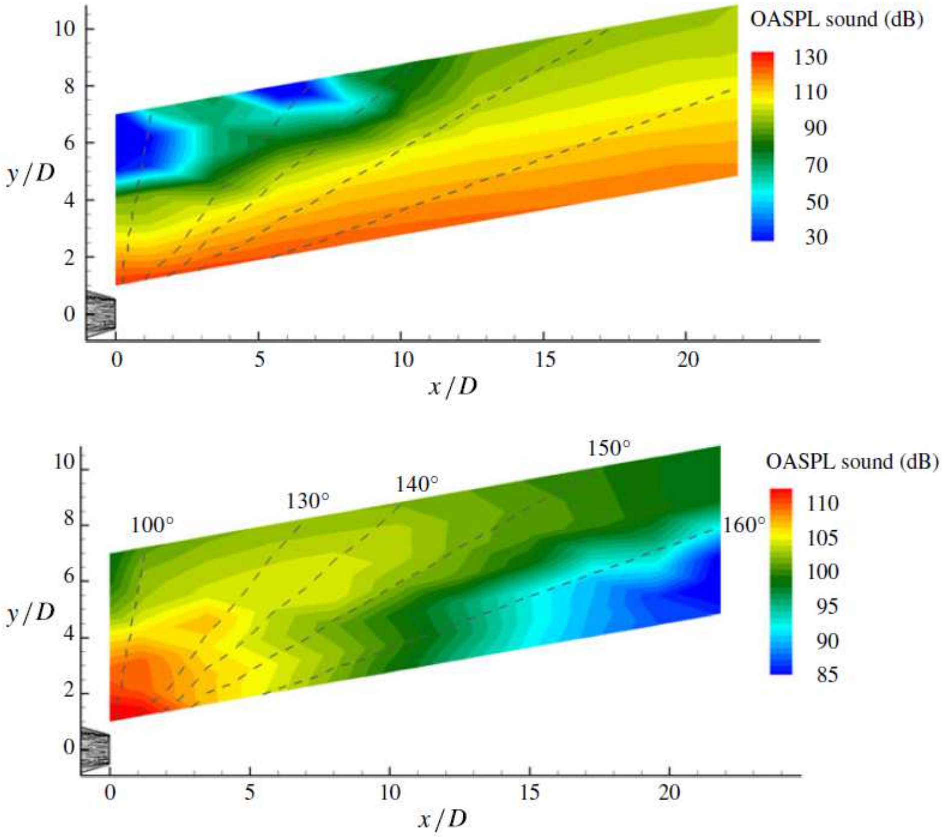

Figure 2.9 OASPL of the hydrodynamic (top) and acoustic (bottom) components in a high-speed jet at Mach 0.5 (Grizzi and Camussi, 2012)

Other studies suggested that events associated with the collapse of the annular mixing-layer at the end of the potential core may constitute the dominant sound production mechanism (Hileman *et al.* 2005; Jordan and Gervais, 2008). Juvé et al. (1980) experimentally observed intermittent noise emissions of the region near the end of the potential core, where sudden decelerations are due to the engulfment of fluid by toroidal structures. With aeroacoustic predictions based on large eddy simulation, Bogey *et al*. (2003) discussed the acoustic generation in relation with the acceleration and stretch of vortical structures when moving towards the jet axial region at the end of the potential core.

In a recent investigation, Grizzi and Camussi (2012) proposed a wavelet based analysis to distinguish the hydrodynamic and the acoustic components in near-field pressure measurements (Figure 2.9). With simultaneous velocity–pressure measurements they also determined the flow regions exhibiting maximum correlation levels with the acoustic or hydrodynamic components of the pressure signals. In the acoustic case, the largest correlations were obtained at the end of the potential core, whereas the largest hydrodynamic pressure–velocity correlations are located close to the nozzle exit and in the far region, beyond the end of the potential core, where turbulence is known to be strongly intermittent (Figure 2.10). The intimate nature of the hydrodynamic and acoustic sources, the authors said, remains unclear and should be the topic addressed in future studies.

The mechanism by which coherent structures are active as sound source suggests that a convected wave packet may constitute a pertinent model for the organized component of the flow. Stability theory was evoked as possible theoretical framework for the modeling of such flow behavior. Kinematical and dynamical models for coherent structures were proposed in the work by Michalke (1971), Tam and Morris (1980), among others. Coherent turbulent structures are modeled by means of a hydrodynamic stability analysis of the mean flow; for slowly spreading mean flows solutions comprise waves which amplify spatially and then decay. From the point of view of sound production, the salient features of such flow organization, as identified by the said modeling efforts, are the process of amplification and decay, and the high level of axial coherence. While model refinements are often aided by CAA (Cavalieri *et al.*, 2011a), more recently, TR-TOMO PIV data have been also used (Cavalieri *et al*. 2012).

The intermittent nature of the flow structures responsible of the hydrodynamic pressure fluctuations has been demonstrated in several papers, starting from the early observations of Mollo-Christensen (1967), to the very recent paper by Cavalieri *et al.* (2011b) (see also the review papers by Jordan and Gervais 2008 and Jordan and Colonius 2013 for a comprehensive review on this subject). More specifically, Cavalieri et al. (2011b) introduced an acoustic model that accounts for wave packets having time-dependent amplitudes and spatial extents (the so called jittering) and is able to reproduce typical intermittency observed in subsonic jets at the end of the potential core.

2.2.2 Jet noise control strategies

Early noise abatement strategies for jet engines were developed based on the Lighthill's theory saying that the noise emission is proportional to the exhaust speeds with power eight. In the 1960s and 1970s, for example, jet engines were designed with turbofan systems which enabled lower exhaust speeds and higher mass flow to guarantee the same trust performances. The implication of coherent flow structures in noise generation suggested that lower acoustic emissions could be achieved by reducing the azimuthal flow coherence with modification of the nozzle exit geometry (Bradshaw *et al.* 1964). This idea lead to the design of chevron nozzle geometries (Bridges and Brown, 2004) that have been recently applied to jet-engines as noise damping solution (Figure 2.11). Tabbed nozzles (Tam and Zaman, 2000), distributed nozzles (Kinzie *et al.* 2002) and nozzles with micro-jets (Alkislar, *et al*. 2007) are other examples of noise reducing configurations under investigation.

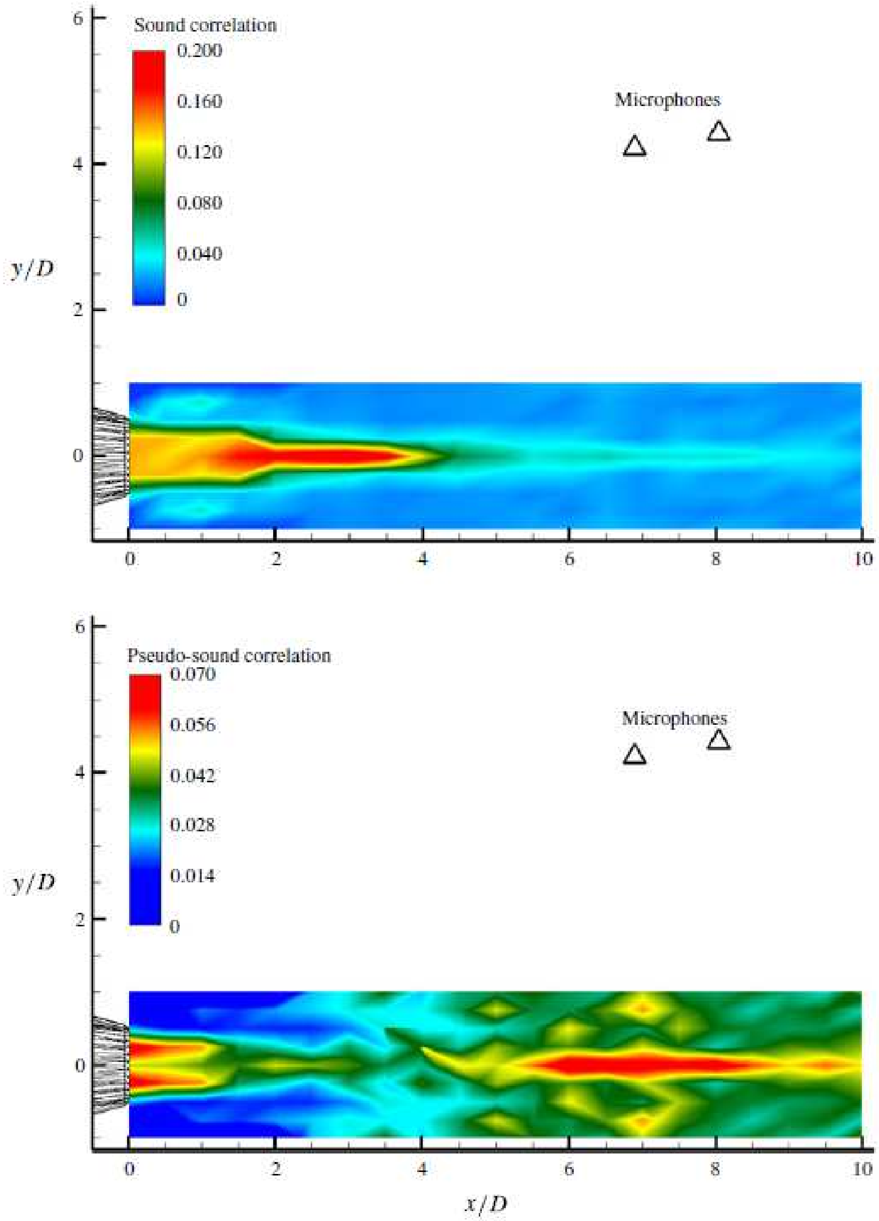

Figure 2.10 Spatial distribution of the velocity cross-correlations with acoustic signal (top) and with the hydrodynamic signal (bottom) in a high-speed jet at Mach 0.5 (Grizzi and Camussi, 2012)

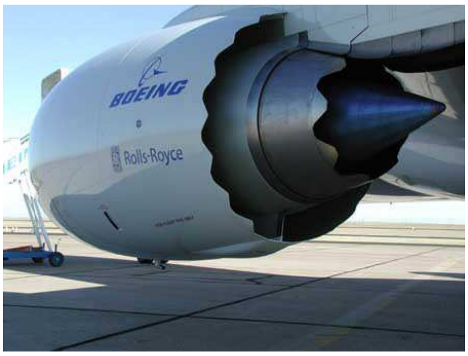

Figure 2.11 Chevron geometry of Rolls Royce engine on Boeing 777-200ER

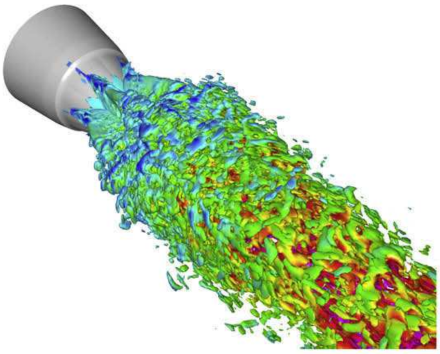

Figure 2.12 Large-eddy simulation of a chevron jet (Xia *et al.*, 2009)

An extensive investigation on chevron jets (Figure 2.12) was conducted by Bridges and Brown (2004), who, using PIV and microphone measurements, focused on the impact of chevron geometric parameters on the mean flow properties and the far field noise emissions. From the time-averaged properties, they showed that the penetration of the chevron into the jet flow influences the axial vorticity of the shear layer and leads to increased noise at high frequency and decreased noise at low frequency. For the six chevron configuration, for example they show a reduction of the sound pressure level at low frequencies (approximately 3 dB). Using stereoscopic PIV, Opalski et al. (2005) reported that the presence of well-defined streamwise vortices in the shear layer of both cold and hot jets with Mach numbers ranging between 0.9 and 1.5. With Navier-Stokes (RANS) calculations, Birch *et al.* (2006) showed that the chevrons generate axial vortices increase the mixing layer growth rate. The acoustic signature of streamwise structures was investigated by Alkislar *et al.* (2007) in a 9-chevron jet configuration using stereoscopic PIV and microphone measurements (Mach 0.9, Re=1.3x10^6), reporting a noise reduction at low-frequencies (Figure 2.13).

The experimental investigations of chevron jets that are available in the literature have mostly focused on flow statistics with larger emphasis on the acoustic emissions rather than the description of instantaneous flow patterns. However, as the acoustic production is highly related to the motion and the interaction of the coherent structures, the reason why chevron jets are characterized by reduced of noise emissions still remains unclear and requires better fundamental physical understanding.

In chapter 5 and 6, this thesis will discuss the 3D organization the aeroacoustic source of chevron jets at low Reynolds number. However, the phenomenology hereby studied cannot be quantitatively compared with Bridges and Brown (2004), in view of the different nature of high Reynolds number jets (see section 2.2.3). Nevertheless, low-Re regimes remain of fundamental interest as allows the study of the dynamics and the related acoustics in simplified settings, where the number of turbulent scales is reduced.

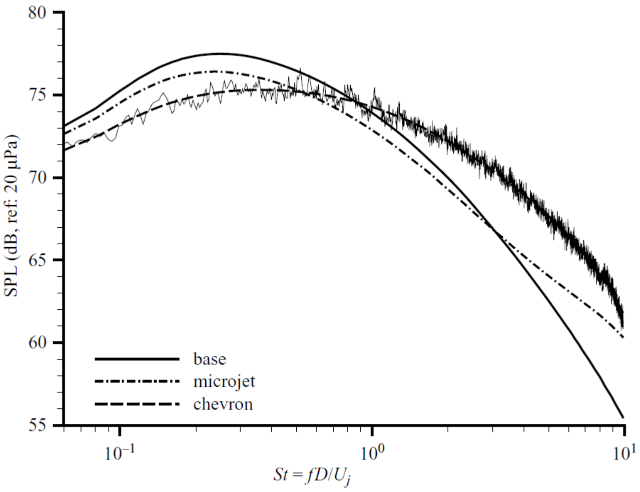

Figure 2.13 Sound pressure level spectra of jets with different nozzle configurations (Alkislar *et al.*, 2007).

2.2.3 High-Reynolds number jets

Despite the large body of numerical and experimental investigations, it remains not clear whether the studies performed to date apply to high Reynolds number, fully turbulent jets. *There is a room for doubt*, as Jordan and Colonius (2013) stressed in a recent review article on turbulent jet noise.

It is under discussion whether the turbulence and the radiated noise can be considered independent of *Re*, beyond a certain threshold ($Re > 4 \times 10^5$, Viswanathan, 2004). Moreover, studies (Harper-Bourne, 2010; Zaman, 2011) observed that the far-field is also sensitive to the contraction ratio of the nozzle, even when the nozzle boundary layer is turbulent. Current research projects (e.g. the ORINOCO project, see section 9.1) have the intent to understand such sensitivity in terms of the influence of jet parameters and the inlet disturbances on coherent structures in prospective of control strategies (Jordan and Colonius, 2013).

2.3 Aeroacoustic analogies

An aeroacoustic analogy is a reformulation of the fluid dynamics equations that allows to evaluate the acoustic perturbation from the intense and vortical flow motion. The part of the flow in which sound production is expected is called the source region. The part of the flow in which the listener is standing defines the reference flow. The difference between the actual flow and an extrapolation of the reference flow into the source region is identified as the source of sound. However, the distinction between sound production and sound propagation mechanisms can be delicate and it may require a certain knowledge of the flow (Morris and Farassat, 2002) for the prediction of jet noise. In the present study, nevertheless, it is not a major problem. The source region is in fact the near field of a subsonic jet in which vortex structures are formed and developed, whereas the listener is located in the quiet medium that surrounds the jet. In a Cartesian coordinate system, the acoustic source will be identified by the position vector **y**, whereas the location where the acoustic pressure is predicted will be referred as listener position and will be identified by the position vector **x**.

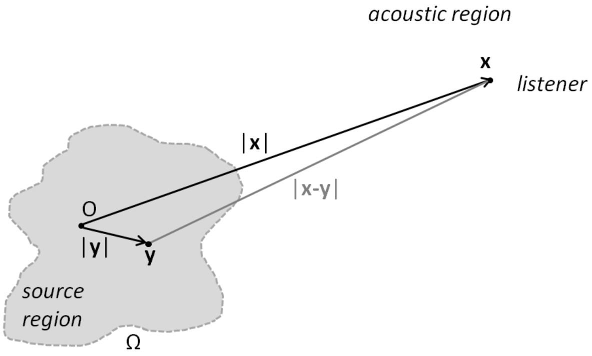

Figure 2.14 Source and listener position vectors in the analogies of Lighthill and Powell.

2.3.1 Lighthill’s analogy

Lighthill’s aeroacoustic analogy is derived to predict the sound produced by a finite region of turbulent flow in an unbounded field. The continuity and momentum equations (2.1) and (2.3) are reformulated into an inhomogeneous wave equation, by subtracting the divergence of the latter from the time derivative of the former. It is then obtained

$$\frac{\partial^2 \rho}{\partial t^2} = \frac{\partial^2 \left(\rho V_i V_j - \tau_{ij}\right)}{\partial x_i \partial x_j} + \frac{\partial^2 p}{\partial x_i^2} - \frac{\partial f_i}{\partial x_j}. \tag{2.13}$$

It is now subtracted the term $c_0^2 \left(\partial^2 \rho / \partial x_i^2\right)$ from both sides of the above equation (c_0 is the speed of sound)

$$\frac{\partial^2 \rho}{\partial t^2} - c_0^2 \frac{\partial^2 \rho}{\partial x_i^2} = \frac{\partial^2 \left(\rho V_i V_j - \tau_{ij}\right)}{\partial x_i \partial x_j} + \frac{\partial^2 \left(p - c_0^2 \rho\right)}{\partial x_i^2} - \frac{\partial f_i}{\partial x_j}. \tag{2.14}$$

One can note that the above equation has the structure of a wave equation with a source term on the right hand side. Considering the acoustic propagation in a uniform and stagnant fluid, where ρ_0, p_0 and V_{i0} are the reference density, pressure and velocity in the acoustic region, the perturbations can be written as

$$\begin{aligned} \rho' &= \rho - \rho_0 \\ p' &= p - p_0 \ , \\ V_i' &= V_i - V_{i0} \end{aligned} \tag{2.15}$$

where it is assumed that $\rho' \ll \rho$, $p' \ll p$ and $V_i' \ll V_i$.

In the specific case, as the flow surrounding the jet is stagnant ($V_{i0} = 0$) and ρ_0 and p_0 are constants, the Lighthill's analogy can be written as

$$\frac{\partial^2 \rho'}{\partial t^2} - c_0^2 \frac{\partial^2 \rho'}{\partial x_i^2} = \frac{\partial^2 T_{ij}}{\partial x_i \partial x_j} - \frac{\partial f_i}{\partial x_j}, \tag{2.16}$$

where T_{ij} is the Lighthill stress tensor defined as

$$T_{ij} = \rho V_i V_j + \left(p' - c_0^2 \rho' \right) \delta_{ij} - \tau_{ij}, \tag{2.17}$$

In the acoustic field where the listener is located the source term on the right hand side of (2.16) vanishes: external forces f_i are absent, $\rho V_i V$ is in linear approximation negligible, viscous contributions τ_{ij} are negligible for distances comparable to the wavelength and the term $\left(p' - c_0^2 \rho' \right)$ vanishes in linear approximation if c_0 is identified as the isentropic speed of sound.

In the case of the jet flow investigated in this thesis, no external forces are applied to the source region. Here the viscous contribution τ_{ij} can also be neglected when the Reynolds number is high (>10^3). By numerical simulations of vortex pairing in a jet flow at Reynolds number ranging between 1,000 and 4,000, Verzicco *et al.* (1997) showed that the sound production related to the viscous effects was at least three orders of magnitude smaller than the contribution of the Reynolds stresses. Moreover, as the investigated jet is isothermal, the non-isentropic contribution $\left(p' - c_0^2 \rho' \right)$ to the acoustic source is also neglected (Morfey, 1984; Obermeier, 1985). Under the above conditions the density fluctuations ρ' in the source region are of order M^2, which means $\rho V_i V_j \simeq \rho_0 V_i V_j$ in the source region of incompressible flows (M<0.3). It follows that Lighthill's analogy reads as

$$\frac{\partial^2 \rho'}{\partial t^2} - c_0^2 \frac{\partial^2 \rho'}{\partial x_i^2} = \frac{\partial^2 \rho_0 V_i V_j}{\partial x_i \partial x_j}, \tag{2.18}$$

which describes the conversion of the kinetic energy due to the rotational motion into the acoustic waves. The source term, involving a second spatial derivative, has a quadrupolar behavior. This means that the solution for the sound generated by turbulence is equivalent to the solution for the radiation into an ideal, stationary acoustic medium, produced by a distribution of quadrupoles whose strength per unit volume is $\rho_0 V_i V_j$. The solution of (2.18) is obtained with the integral formulation

$$p'(\mathbf{x},t) \equiv c_o \rho'(\mathbf{x},t) = c_o \int_{-\infty}^{t} \iiint_{\Omega} G_0(t,\mathbf{x} \mid \tau,\mathbf{y}) \frac{\partial^2 \rho_0 V_i V_j}{\partial y_i \partial y_j} d^3 y d\tau , \tag{2.19}$$

where Ω is the source region domain, while $G_0(t,\mathbf{x} \mid \tau,\mathbf{y})$ is the free space Green's function, which is the solution to the equation generated by an impulsive point source $\delta(\mathbf{x}-\mathbf{y})\delta(t-\tau)$:

$$\left(\frac{1}{c_0^2} \frac{\partial^2}{\partial t^2} - \frac{\partial^2}{\partial x_i^2} \right) G = \delta(\mathbf{x}-\mathbf{y})\delta(t-\tau) , \tag{2.20}$$

Note that $(t,\mathbf{x})$ are the listener coordinate, while $(\tau,\mathbf{y})$ are the source coordinate (Figure 2.14). As shown by Abramowitz and Stegun (1965), the solution of eq. (2.20) is

$$G_0(t,\mathbf{x} \mid \tau,\mathbf{y}) = \frac{1}{4\pi |\mathbf{x}-\mathbf{y}|} \delta \left(t - \tau - \frac{|\mathbf{x}-\mathbf{y}|}{c_0} \right), \tag{2.21}$$

which represents a an impulsive spherical and symmetric wave expanding from the source at **y** at a speed of sound c_0. The free space Green's function has the elementary property of symmetry for differentiation with respect to the source coordinate **y** and the observer **x**

$$\frac{\partial G_0}{\partial x_i} = - \frac{\partial G_0}{\partial y_i} \tag{2.22}$$

It follows that the integrand spatial derivatives of (2.19) can be moved out of the integral to obtain

$$p'(\mathbf{x},t) = \frac{\partial^2}{\partial x_i \partial x_j} \int_{-\infty}^{t} \iiint_{\Omega} \frac{\delta(t - \tau - |\mathbf{x}-\mathbf{y}| / c_o)}{4\pi |\mathbf{x}-\mathbf{y}|} \rho_0 V_i V_j d^3 \mathbf{y} d\tau , \tag{2.23}$$

which integrated in time using the properties of the Dirac function reads as

$$p'(\mathbf{x},t) = \frac{\partial^2}{\partial x_i \partial x_j} \iiint_{\Omega} \left. \frac{\rho_0 V_i V_j}{4\pi |\mathbf{x}-\mathbf{y}|} \right|_{t^*} d^3 \mathbf{y} . \tag{2.24}$$

The above equation has to be evaluated at the retarded time $t^* = t - |\mathbf{x}-\mathbf{y}| / c_0$

The use of Lighthill's analogy predict the acoustic field of a low-Mach number jet based on PIV data has some difficulties, as discussed by Schram (2003) in the study of vortex paring noise. First of all, errors in the description of the flow field are not likely to respect the conservation of momentum, thus inducing fictitious external forces. These, which radiate as spurious dipolar sources, can even have an efficiency higher than the actual source. In other words, inaccuracies in the evaluation of the spatial derivative (eq. (2.24)) result in spurious dipolar or monopolar sources.

Another issue, which was discussed by Schram and Hirschberg (2003), is related to the integration boundaries of the term $\rho V_i V_j$. The velocity field associated vortex structure is typically much more extended than the corresponding vorticity field, making the definition of the integration limits not trivial (Crow, 1970). In fact, the spatial domain truncation of the acoustic source results in spurious dipolar field which can completely overreach the expected quadrupole. Such issue was faced by Mitchell *et al.* (1999) in a direct numerical simulation of vortex paring sound (*Re*=2,500). As the axial extent of the Lighthill source term was larger than the numerical domain, they had model the source beyond the downstream boundary of the domain to avoid the generation of spurious waves.

2.3.2 Powell’s analogy

An alternative formulation of the Lighthill analogy was elaborated by Powell (1964) in the Vortex Sound Theory, in which the analogy is expressed as a function of the vorticity field. This, being typically more confined in space than the corresponding velocity field, makes the integration of the acoustic source term considerably simpler than applying Lighthill’s analogy.

Schram and Hirschberg (2003) and, later, Schram *et al.* (2005), evidenced that Vortex Sound Theory offers the advantage of a powerful formalism to compensate for inaccuracies in the flow data. The conservation of momentum and the kinetic energy, in fact, appear explicitly in the derivation of the analogy, thus allowing to impose their invariance even if the data do not respect such conservation laws. This has triggered many ideas developed by Schram and co-workers leading to the derivation of a so-called conservative formulation of the vortex sound theory for axisymmetric flows.

The derivation of Powell’s analogy consists in arranging the governing equations in a single inhomogeneous wave equation, where the vorticity vector $\boldsymbol{\omega} \equiv \nabla \times \mathbf{V}$ appears in the source term. Assuming the absence of external forces and negligible viscous effects, as done for Lighthill’ analogy (Lighthill’s analogy 2.3.1), and considering the identity

$$\nabla\left(\frac{|\mathbf{V}|^2}{2}\right) = \mathbf{V}\times\boldsymbol{\omega} + \mathbf{V}\cdot\nabla\,, \tag{2.25}$$

the momentum equation can be written as (Powell, 1964)

$$\frac{\partial\rho\mathbf{V}}{\partial t} + \nabla\left(\rho\frac{|\mathbf{V}|^2}{2}\right) + \rho\left(\mathbf{V}\times\boldsymbol{\omega}\right) + \nabla p = 0\,. \tag{2.26}$$

Substituting the time derivative of the continuity equation (2.1) into the divergence of the momentum equation (2.26), the following wave equation is obtained

$$\frac{\partial^2\rho}{\partial t^2} - \frac{\partial^2 p}{\partial x_i^2} = \nabla\cdot\left[\rho\left(\mathbf{V}\times\boldsymbol{\omega}\right) + \nabla\left(\rho\frac{|\mathbf{V}|^2}{2}\right) - \mathbf{V}\frac{\partial\rho}{\partial t} - \frac{1}{2}|\mathbf{V}|^2\,\nabla\rho\right]. \tag{2.27}$$

In the acoustic region, it is applied the decomposition (2.15) and it is added the term $1\big/c_0^2\,\partial^2 p'\big/\partial t^2$ to both sides of equation (2.27), which now reads as

$$\frac{1}{c_0^2}\frac{\partial^2 p'}{\partial t^2}-\frac{\partial^2 p'}{\partial x_i^2}=\nabla\cdot\left[\rho\left(\mathbf{V}\times\boldsymbol{\omega}\right)+\nabla\left(\rho\frac{\left|\mathbf{V}\right|^2}{2}\right)-\mathbf{V}\frac{\partial\rho}{\partial t}-\frac{1}{2}\left|\mathbf{V}\right|^2\nabla\rho\right]+\frac{\partial^2}{\partial t^2}\left(\frac{p'}{c_0^2}-\rho'\right) \tag{2.28}$$

where the last term on the right hand side is neglected assuming isentropic sound speed in the acoustic region (similarly to Lighthill's analogy derivation eq. (2.16)).

For homo-entropic flows, densities variations are only kinetic, so that the four terms under the divergence operator respectively scale as 1, 1, StM^2, M^2. For low-Mach number flows ($\rho=\rho_0$) and Strouhal numbers $St=O(1)$, which is the case of the jet investigated in this thesis, the terms proportional to M^2 can be then neglected, it is obtained

$$\frac{1}{c_0^2}\frac{\partial^2 p'}{\partial t^2}-\frac{\partial^2 p'}{\partial x_i^2}=\nabla\cdot\left[\rho_0\left(\mathbf{V}\times\boldsymbol{\omega}\right)\right]+\nabla^2\left(\rho_0\frac{\left|\mathbf{V}\right|^2}{2}\right). \tag{2.29}$$

The solution of eq. (2.29) is obtained with the integral formulation using free space Green's function eq. (2.21)

$$p'(\mathbf{x},t)=\frac{\rho_0}{4\pi}\frac{\partial}{\partial x_i}\iiint\limits_{\Omega}\left.\frac{\left(\mathbf{V}\times\boldsymbol{\omega}\right)_i}{\left|\mathbf{x}-\mathbf{y}\right|}\right|_{t^*}d^3\mathbf{y}+\frac{\rho_0}{4\pi}\frac{\partial^2}{\partial x_i^2}\iiint\limits_{\Omega}\left.\frac{\left|\mathbf{V}\right|^2/2}{\left|\mathbf{x}-\mathbf{y}\right|}\right|_{t^*}d^3\mathbf{y}\,. \tag{2.30}$$

Following the discussion by Schram and Hirschberg (2003), the assumptions of compact source region $d/\lambda\ll 1$ (d is the characteristic source size and λ is the radiated wavelength) enables the expression of the retarded time by a Taylor expansion, which, with the far field approximation $\lambda/\left|\mathbf{x}\right|\ll 1$, leads to

$$\frac{\partial}{\partial x_i}\simeq\frac{x_i}{c_0\left|\mathbf{x}\right|}\frac{\partial}{\partial t}\,. \tag{2.31}$$

The first integral of (2.30) now reads as

$$\begin{aligned}\frac{\rho_0}{4\pi}\frac{\partial}{\partial x_i}\iiint\limits_{\Omega}\left.\frac{\left(\mathbf{V}\times\boldsymbol{\omega}\right)_i}{\left|\mathbf{x}-\mathbf{y}\right|}\right|_{t^*}d^3\mathbf{y}\simeq&-\frac{\rho_0}{4\pi c_0}\frac{x_i}{\left|\mathbf{x}\right|^2}\frac{\partial}{\partial t}\iiint\limits_{\Omega}\left(\mathbf{V}\times\boldsymbol{\omega}\right)_i\Big|_{t^*}d^3\mathbf{y}\\&-\frac{\rho_0}{4\pi c_0^2}\frac{x_ix_j}{\left|\mathbf{x}\right|^3}\frac{\partial^2}{\partial t^2}\iiint\limits_{\Omega}y_i\left(\mathbf{V}\times\boldsymbol{\omega}\right)_i\Big|_{t^*}d^3\mathbf{y}\end{aligned} \tag{2.32}$$

in which the integrands on the right hand side are evaluated at $t^*\simeq t-\left|\mathbf{x}\right|/c_0$.

It can be demonstrated (Batchelor, 1967; Saffman, 1992) that, due to the absence of external forces which implies the conservation of impulse

$$\mathbf{I}=\frac{1}{2}\rho_0\iiint\limits_{\Omega}\mathbf{y}\times\boldsymbol{\omega}\;d^3\mathbf{y}\,, \tag{2.33}$$

the first term of eq. (2.32) is equal to zero. Similarly, the second integral of (2.30) can be written as

$$\frac{\rho_0}{4\pi}\frac{\partial^2}{\partial x_i^2}\iiint_\Omega \left.\frac{|\mathbf{V}|^2/2}{|\mathbf{x}-\mathbf{y}|}\right|_{t^*} d^3\mathbf{y} \simeq \frac{\rho_0}{4\pi c_0}\frac{1}{|\mathbf{x}|}\frac{\partial^2}{\partial t^2}\iiint_\Omega \left.\frac{|\mathbf{V}|^2}{2}\right|_{t^*} d^3\mathbf{y} + \frac{\rho_0}{4\pi c_0^2}\frac{x_j}{|\mathbf{x}|^2}\frac{\partial^3}{\partial t^3}\iiint_\Omega y_j \left.\frac{|\mathbf{V}|^2}{2}\right|_{t^*} d^3\mathbf{y} \tag{2.34}$$

in which, assuming inviscid and incompressible flow (Batchelor, 1967; Saffman, 1992), the term on the left side vanishes due to the conservation of the kinetic energy

$$T = \rho_0 \iiint_\Omega \mathbf{y}\cdot(\boldsymbol{\omega}\times\mathbf{V})\, d^3\mathbf{y}\,. \tag{2.35}$$

Moreover, Powell showed that the second term on the right hand side is negligible for low Mach numbers and the integral solution of Powell’s analogy reads as

$$p'(\mathbf{x},t) = -\frac{\rho_0}{4\pi c_0^2 |\mathbf{x}|^3}\frac{\partial^2}{\partial t^2}\iiint_\Omega (\mathbf{x}\cdot\mathbf{y})\,\mathbf{x}\cdot\left.(\boldsymbol{\omega}\times\mathbf{V})\right|_{t^*} d^3\mathbf{y}\,. \tag{2.36}$$

where the vector $(\boldsymbol{\omega}\times\mathbf{V})$ is defined as Lamb vector **L** (section 3.3.2). Note that eq. (2.36) is obtained imposing the conservation of the flow impulse (eq. (2.33)) and the kinetic energy (eq. (2.35)), as no external forces are applied and the flow is assumed inviscid and incompressible. This holds even if the data of the flow field, such as PIV data, do not respect the two conservation laws.

For low Mach number jet with no external force field and negligible viscous-thermal effects, assuming compact source region, the far-field solution of Powell’s analogy reads as

$$p'(\mathbf{x},t) = -\frac{\rho_0}{4\pi c_0^2 |\mathbf{x}|^3}\frac{\partial^2}{\partial t^2}\iiint_\Omega (\mathbf{x}\cdot\mathbf{y})\,\mathbf{x}\cdot\left.\mathbf{L}\right|_{t^*} d^3\mathbf{y}\,. \tag{2.37}$$

Note that Powell’s analogy (eq. (2.37)) contains a volumetric integral and a second time derivative, which means that the source term is correctly evaluated if three dimensional time-resolved data are available.

In this study, it will be considered a system of cylindrical coordinates (R,θ,Z) where R, θ and Z are respectively the radial, the azimuthal and the axial coordinate, which is a more convenient when dealing with jet flow predictions. The listener's and the source position vectors are then written as

$$\begin{aligned}\mathbf{y} &= \{y_r, y_\theta, y_z\}\\ \mathbf{x} &= \{x_r, x_\theta, x_z\}\end{aligned} \tag{2.38}$$

whereas the Lamb vector reads as

$$\mathbf{L} = \{L_r, L_\theta, L_z\}\,. \tag{2.39}$$

By substituting (2.38) and (2.39) into (2.37), it is obtained the expression of Powell’s analogy in cylindrical coordinates, which reads as

$$p'(\mathbf{x},t) = -\frac{\rho_0}{4\pi c_0^2 |\mathbf{x}|^3}\frac{\partial^2}{\partial t^2}\int_{Z_1}^{Z_2}\int_0^{2\pi}\int_0^{R_1} (\mathbf{x}\cdot\mathbf{y})\,\mathbf{x}\cdot\left.\mathbf{L}\right|_{t^*} \det(\mathbf{J})\, dR\, d\theta\, dZ\,. \tag{2.40}$$

where Z_1 and Z_2 are the axial positions of the inflow and outflow boundaries, R_1 is the location of the radial boundary and

$$\mathbf{J} = \begin{bmatrix} \frac{dx}{dR} & \frac{dx}{d\theta} & \frac{dx}{dZ} \\ \frac{dy}{dR} & \frac{dy}{d\theta} & \frac{dy}{dZ} \\ \frac{dz}{dR} & \frac{dz}{d\theta} & \frac{dz}{dZ} \end{bmatrix} = \begin{bmatrix} \cos\theta & -R\sin\theta & 0 \\ \sin\theta & R\cos\theta & 0 \\ 0 & 0 & 1 \end{bmatrix}. \tag{2.41}$$

is the Jacobian matrix.

Chapter 3

From planar to 4D PIV

This chapter is devoted to the description of the working principle of planar and tomographic PIV and discusses the features of high-speed tomographic PIV systems used for time resolved tomographic PIV (4D PIV). The chapter also includes a discussion of the data reduction methods used in the present work, including vortex identification methods, aeroacoustic source characterization and proper orthogonal decomposition.

3.1 Planar PIV

3.1.1 Working principles

Particle image velocimetry (PIV) is an optical, non-intrusive, technique for the measurement of the instantaneous velocity at several points within a fluid. A complete overview on the technique and its impact in fluid mechanic research is given in the contributions by Adrian (1991, 2005), Westerweel (1993, 1997), Willert and Gharib (1999) and Raffel *et al.* (1998, 2007).

A schematic of a typical PIV experimental set up is illustrated in Figure 3.1. The fluid is seeded with micrometric tracer particles, which are illuminated by thin laser light sheet (1-2 mm of thickness). The light scattered by the particle tracers is recorded with a digital camera, either charged-couple device (CCD) or complementary metal-oxide-semiconductor (CMOS), at two subsequent time instants onto two separate image frames. The motion of the particles is then obtained by measuring the displacement of the particle image and, in first approximation, the velocity is inferred as:

$$\mathbf{V} = \frac{\mathbf{x}_2(x,y,t+\Delta t) - \mathbf{x}_1(x,y,t)}{\Delta t} + o(\Delta t^2)\,, \tag{3.1}$$

where $\mathbf{V}$ is the particle velocity vector, $\mathbf{x}_1$ and $\mathbf{x}_2$ the particle position vectors, respectively at time instants *t* and *t+Δt*.

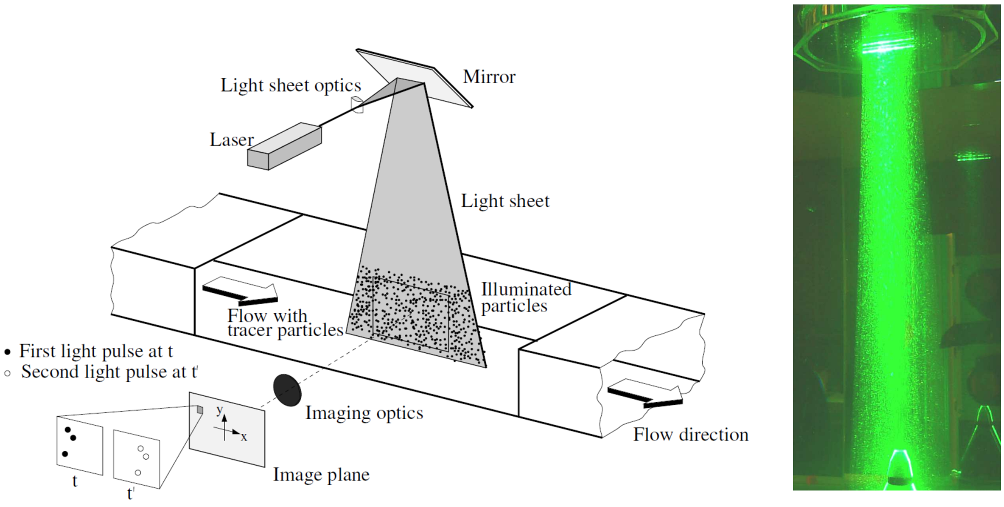
Light sheet optics
Mirror
Laser
Light sheet
Illuminated particles
Flow with tracer particles
• First light pulse at t
○ Second light pulse at t'
Imaging optics
y
x
Image plane
Flow direction
t
t'

Figure 3.1 Schematic of a typical PIV experimental set up (Raffel *et al.*, 2007) and a detail of laser illumination on a airfoil (Violato and Scarano, 2011)

Due to the abundance of the particles and their complex motion, it is generally difficult to distinguish them in the two frames (as typically done in particle tracking velocimetry, PTV). Instead, the evaluation of the particle displacement ($\mathbf{x}_2$-$\mathbf{x}_1$) is conducted statistically by means of the 2D spatial cross-correlation function (see section 3.1.4).

3.1.2 Seeding particles

The choice of the seeding particles is a crucial aspect of every velocimetry technique based on particle imaging. The velocity of the flow is obtained indirectly from the measured displacement of the tracers; moreover their concentration determines the spatial resolution. Tracer particles must be accurately follow the fluid motion without inducing any alteration and they must be of a relatively high scattering material, so that they can be easily detectable on the camera images (Westerweel, 1993). Criteria for the choice of the particle for different PIV application were proposed in Adrian and Yao (1985), whereas an overview of particle dynamic response is given by Emrich (1981).

Based on the difference between the fluid and particle densities, ρ and ρ_p respectively, Raffel *et al.* (1998) used the Stokes flow interaction around a sphere to estimate the relative velocity $\mathbf{V}_S$ between the particle tracer and the surrounding flow as

$$\mathbf{V}_S = d_p^2 \frac{\rho_p - \rho}{18\mu} \mathbf{a}, \tag{3.2}$$

where d_p is the particle diameter, μ is the dynamic viscosity of the fluid and **a** is the acceleration. Considering the gravitational forces **g** acting on the particle, **a** can be written as

$$\mathbf{a} = \frac{d\mathbf{V}}{dt} + \mathbf{g}. \tag{3.3}$$

From eq. (3.2), it results that the ideal tracer particle must have the same density of the fluid in which it is immersed (neutral buoyancy condition). This condition is easily satisfied in liquid flows, and is impossible to meet for gas flows, such as air. In this case, very small particles have to be adopted. Melling (1997) theoretically estimated that for a frequency response of 10 kHz in air, the particle diameter should be 1μm maximum. The response of particle tracers is most critical in high-speed flows especially in the supersonic regime where shock waves occur. The application of PIV in these regimes has been discussed by Scarano (2008). Further experimental research has shown that the particle tracers used in aerodynamic experiments can have a temporal response of less than 2 microseconds (500kHz, Ragni *et al.* 2010).

3.1.3 Particle imaging

Images of tracer particles are formed on the camera sensor plane using photographic lenses. Since these are limited in their aperture, the imaged tracer particles appear as a diffraction pattern which consists of Airy disk and rings (Raffel *et al.*, 2007).

Considering the Gauss's relation of optics

$$\frac{1}{f} = \frac{1}{z_0} + \frac{1}{Z_0}, \tag{3.4}$$

where f is the focal length, z_0 is the distance between the image plane and the lens, and Z_0 is the distance between the lens and the object plane. Defining the magnification factor M as

$$M = \frac{z_0}{Z_0}, \tag{3.5}$$

for a given aperture D_a and laser wave-length λ, the diameter of the Airy disk d_{diff} is given by

$$d_{diff} = 2.44 f_{\#}(M+1)\lambda, \tag{3.6}$$

where $f_{\#}=f/D_a$ is the f-number. Note that eq. (3.6) is valid for the imagining of small particles at small magnifications.

For larger particles and larger magnifications, the imaged particle diameter d_τ reads as (Adrian, 1991)

$$d_\tau = \sqrt{d_g^2 + d_{diff}^2 + d_{ab}^2}\ , \tag{3.7}$$

where the geometrical diameter d_g is proportional to the particle diameters d_p

$$d_g = M d_p\ , \tag{3.8}$$

and d_{ab} is the aberration term that is mainly a function of $f_\#$ and of the lens quality through its modulation transfer function (Raffel *et al.*, 2007). Note that d_τ must be sufficiently large (>2 pixels) to prevent the *peak-locking* effect, where subpixel estimation leads to a displacement bias error (Westerweel, 1997).

In an aberration-free lens, the particles are considered to be sharp in focus when the geometrical particle blur is equal to the diffraction diameter d_{diff}. Note that this condition holds within the region in viewing direction called the depth of field δ_z (Raffel *et al.*, 2007), which reads as

$$\delta_z = 4.88\lambda f_\#^2 \left(1 + \frac{1}{M^2}\right). \tag{3.9}$$

Note that, once M and λ are set by the experimental parameters, the depth of field δ_z becomes a function of $f_\#$, meaning that an increase in the δ_z can be obtain at the expenses of the amount of light passing through the objective.

3.1.4 Image analysis

Consider the schematic of Figure 3.2. Two particle images with light intensity distributions are $I_1(i,j)$ and $I_2(i,j)$, respectively, for the *i*th and *j*th pixels, are subsequently recorded with a separation time Δt. They are divided into smaller regions, called interrogation windows, where the normalized cross-correlation function (Willert and Gharib, 1991) is evaluated as

$$R(\Delta x, \Delta y) = \frac{\sum_i \sum_j [I_1(i,j) - \overline{I}_1][I_2(i+\Delta x, j+\Delta y) - \overline{I}_2]}{\sqrt{\sum_i \sum_j [I_1(i,j) - \overline{I}_1]^2 \sum_i \sum_j [I_2(i+\Delta x, j+\Delta y) - \overline{I}_2]^2}} \tag{3.10}$$

where $\overline{I}_1$ and $\overline{I}_2$ that are the average intensities in the interrogation window and Δx and Δy the image pixel shifts. Adrian (1991) proposed that at least 10 particles must be present in the correlation window for a statistically robust measurement.

The position of the largest peak in the correlation map $R(\Delta x, \Delta y)$ is, in linear approximation, the displacement ($\mathbf{x}_2$-$\mathbf{x}_1$) within each interrogation window. The velocity vector is then determined knowing the time separation Δt. The signal to noise ratio is defined as the ratio between the first and second largest correlation peaks.

Several studies focused on the characterization of the response function associated with the cross-correlation approach. Westerweel (1993) observed that the uncertainty on the velocity measurement depends on the accuracy in detecting the location of the correlation peak (typically 0.1 pixel).

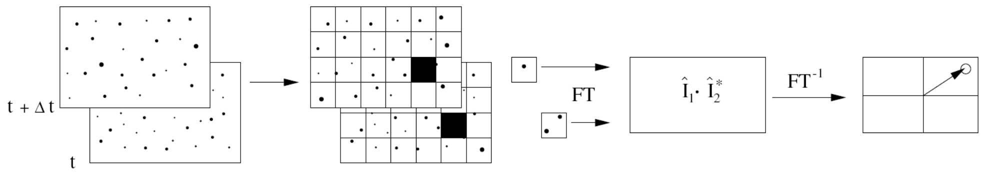

Figure 3.2 Schematic of digital PIV cross-correlation process (Raffel *et al.*, 2007)

Over the last 20 years, the image analysis approach by Willert and Gharib (1991) have been improved by a multi-grid iterative approach (Soria 1996; Westerweel, 1997, Scarano and Riethmuller, 1999) allowing a larger measurement dynamic range. Image deformation (Huang *et al*., 1993a and 1993b) is conventionally applied in the iterative loop to improve the measurement confidence of in-plane velocity gradients where flow exhibits motions other than translational, such as vortex flows and shear flows (Nogueira *et al.*, 1999; Scarano 2002). Moreover, a reduction of the window size along the direction of the velocity gradient leads to a visible improvement of the spatial resolution in highly sheared regions. Although Scarano (2003) states that, since the velocity gradient is taken into account by window deformation the interrogation regions should be adapted according to the curvature of the velocity field, the improvement shown by the above mentioned techniques can be due to a combination of two factors. On one hand, in regions of strong shear, the gradient is not completely compensated for by the deformation technique, therefore a reduction of the window size along that direction results in a more robust measurement. On the other hand, when a high value of the first derivative of the velocity also corresponds to high curvature, the adaptive approach implicitly takes care of the issue of the second derivative indicated by Scarano (2003). Regarding adaptive window correlation, the reader is also referred to Di Florio *et al*., 2002 and Theunissen *et al*. (2007 and 2010).

For steady flow phenomena, Meinhart *et al.* (2000) proposed the ensemble average correlation approach by which coincident correlation planes are averaged from a sequence of images instead of coincident velocity fields (Raffel *et al.*, 2007). If the position of the peak is the same in the correlation map sequence, such as in stationary flows, the random noise is reduced by the averaging. As a result average velocity fields can be evaluated with increased resolution (smaller interrogation windows) depending on the number of recordings in the sequence. Despite losing information on the flow unsteadiness (*rms* value is not computed), the ensemble correlation approach is computationally more efficient and increases the increase the robustness of the measurements.

3.2 Tomographic PIV

Tomographic PIV was introduced as an extension of the PIV method to measurements in three-dimensional space, (TOMO PIV, Elsinga *et al.*, 2006). The technique is able to access the three-components of the velocity vector within a volumetric measurement domain (3D-3C). The principle of optical tomography is followed to reconstruct the 3D distribution of tracers from its projections (images) taken simultaneously by multiple cameras (typically 3 to 6) oriented along different viewing directions. Enabling the visualization and quantification of the instantaneous 3D velocity field, TOMO PIV is a powerful tool to understand the intrinsic organization of complex flows, with turbulence being a prominent example, which, often, cannot be fully comprehended based on planar two and three components techniques. Moreover, the recent development of high-speed cameras has led to the development of time-resolved TOMO-PIV (4D PIV, Schroeder *et al.*, 2008), which is advantageous in the investigation of unsteady flows (Ghaemi and Scarano, 2011) and the related aeroacoustic implications (Violato and Scarano, 2013). A comprehensive discussion on the principles and applications of TOMO PIV is given in the review article by Scarano (2013), and only the salient details are discussed in this section.

Since its introduction, TOMO PIV has been successfully applied to study a large variety of flow configurations, such as jet flows (Violato and Scarano 2011; Khashehchi et al. 2010; Staack *et al.* 2010), turbulent boundary layers (Schroeder *et al*., 2010; Humble *et al*., 2009; Ghaemi *et al.*, 2012) and wake flows (Scarano and Poelma 2009, Hain *et al.*, 2010, Violato *et al*., 2011), with the intention to explore the instantaneous 3D and 4D (3D time-resolved) organization of coherent structures in turbulence.

Among other techniques aiming at the measurement of the velocity distribution in a three-dimensional domain Scarano (2013) can distinguished three categories: three-dimensional particle tracking velocimetry (3D PTV; Maas *et al.*, 1993), scanning light-sheet (SLS; Bruecker, 1995) and holographic PIV (H-PIV; Hinsch, 2002). While the first one has been mostly employed for the study of Lagrangian particle motion in turbulence (Moroni *et al.*, 2003), the scanning light sheet technique has demonstrated a great potential in flows at moderate speed, being able to describe the complex flow pattern of transitional and turbulent flows (Bruecker 1995; Hori and Sakakibara, 2004). However, it cannot be easily extended to flows with a velocity higher than approximately 1 m/s. Holography PIV has been largely used for the instantaneous description of three-dimensional flows (Hinsch, 2002; Katz and Sheng, 2010), with the drawback, however, that its use is limited by several technical limitations. In contrast, several applications the digital holographic PIV have been achieved, such as in the study of wall-bounded turbulence (Sheng *et al.*, 2008). However its use is limited to measurement volumes of few cubic millimeters.

As shown in the schematic of Figure 3.3, TOMO PIV consists in three main steps: image recording, tomographic reconstruction and motion analysis by cross-correlation function. Accurate tomographic reconstructions are obtained by means of a calibration procedure that is similar to that used for stereo-PIV (Willert, 1997).

3.2.1 Illumination and imaging system

Tracer particles are illuminated within a measurement volume by a pulsed laser light which is expanded in depth by means of optical lenses, which involve less complex arrangement since the laser beam diameter of most of lasers (e.g. Nd:Yag lasers) is large enough that a single cylindrical lens, or beam expander, can be sufficient to achieved the desired light volume.

The scattered light is simultaneously recorded from different viewing directions by digital cameras (CCD or CMOS), typically in a number of 3 or 4. Compared with planar PIV, the constrains on the orientation of the 3D illuminated domain with respect to the imaging system are more relaxed, as the particle tracers are imaged even if they move along the viewing direction and there is no need to align the light sheet such to reduce out-of-plane motion.

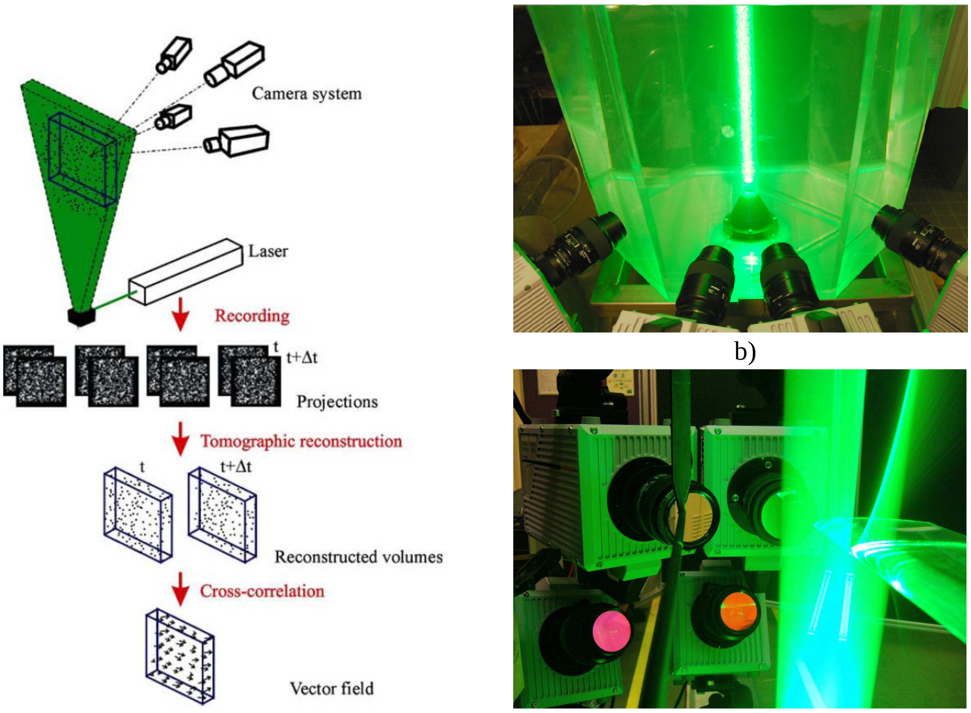

b)

a)

c)

Figure 3.3 a) Schematic of the working principle of TOMO-PIV (Elsinga *et al.*, 2006); examples of TOMO-PIV set up for b) jet flow and c) rod-airfoil flow investigations (Violato *et al.*, 2011; chapter 7)

Lens tilting systems are set on the cameras to comply with the Scheimpflug condition, by which the focal plane has to be aligned with the mid-plane of the 3D domain. In order to focus the particles across the depth of the laser light volume (see eq. (3.9)), the lens aperture is reduced by increasing f-number $f_{\#}$, consequently resulting in a reduced amount of the light reaching the camera sensor. The situation is even more critical for time-resolved Tomo-PIV (Schroeder *et al.*, 2008) experiments where more powerful illumination is needed to provide the proper light intensity within the pulse duration. It is therefore clear that the level of light intensity is an important constraint on the measurement domain thickness, which can be enlarged only if a stronger illumination system is available. The amount of light from a given laser source can be maximized using methods such as the double-pass light amplification system (Scarano and Poelma 2009, Schroeder *et al.*, 2011) and the multi-pass light amplification (Schroeder *et al.*, 2008; Ghaemi and Scarano, 2010). Favorable experimental conditions can be obtained in water (as in the study discussed within this thesis), where a relatively large measurement domain can be accessed (Scarano and Poelma, 2009; Violato and Scarano, 2011 and 2013). Also other type light sources were employed, such as computer beamers (Percin *et al.*, 2011) and light emitting diodes (Willert *et al.*, 2010).

3.2.2 Calibration

Since the tomographic reconstruction relies on the triangulation of the cameras views in the three-dimensional space, the image coordinate (x,y) are mapped onto those of the reconstructed volume (X,Y,Z) by means of a calibration procedure. A calibration target containing markers of known size and position is simultaneously imaged by the cameras at several positions (with steps of 5 to 10 mm) along the depth of the illuminated volume (Figure 3.4). The position of the markers are used to determine the coefficients of the function which maps the physical coordinates (X_i,Y_i,Z_i) onto the pixel coordinates (x_i,y_i). The chosen mapping function is a third order polynomial in X and Y, whereas linear interpolation is used to find the corresponding image coordinated between the available Z positions.

A substantial improvement in the accuracy of the reconstructed volumes, as well as in the robustness velocity field, is obtained by the *volume self-calibration* procedure proposed by Wieneke (2008), who found inspired from the self-calibration method used for stereo-PIV to correct misalignment between the laser sheet and the calibration plane. The self-calibration technique allows to refine the manual calibration by minimizing the disparity between the images of the same particle onto the camera images. As the technique relies on the identification of individual particle, volume self-calibration is preferably performed on multiple recordings at low density images, where imaged particles are easily detectable by eye (particle image density *ppp* below 0.02). An iterative application of such procedure allows to reduce the disparity value to values smaller than 0.1 pixels.

3.2.3 Tomographic reconstruction

Two-dimensional images, in the schematic of Figure 3.3 each recording is formed by a quadruplet of images, are reconstructed into three-dimensional light intensity distributions (reconstructed objects) by means of the Multiplicative Algebraic Reconstruction Technique algorithm (MART, Herman and Lent, 1976). In this method, the reconstructed intensity, $E(X,Y,Z)$, is discretized in 3D array of cubic voxel elements having approximately the same linear size as the pixels composing the camera images. The reconstruction technique makes use of the projection equation linking the image intensity distribution, $I\ (x,\ y)$ to the 3D object intensity distribution $E(X,Y,Z)$ as

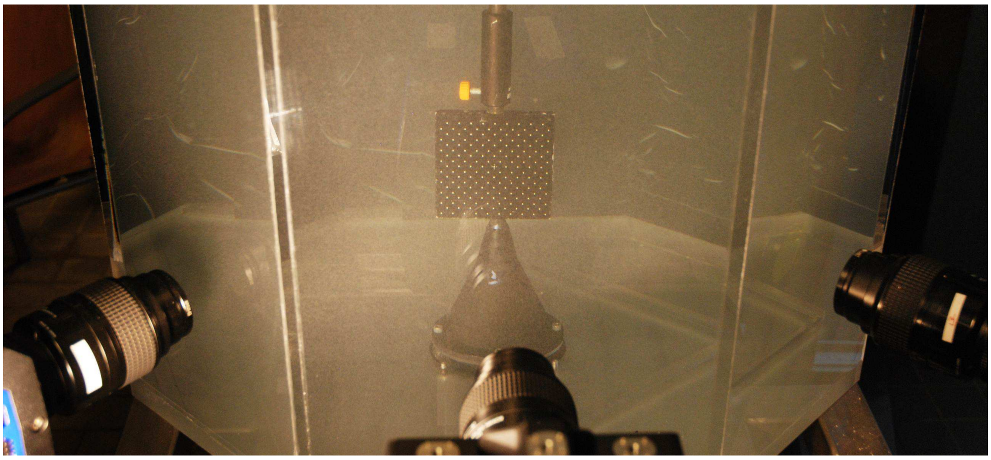

Figure 3.4 Double layered calibration target is employed for the tomographic jet experiment

$$\sum_{j\in N_i} w_{i,j} E(X_j, Y_j, Z_j) = I(x_i, x_i) \tag{3.11}$$

where the value $w_{i,j}$ defines the weight of the contribution of the *j*th voxel intensity $E(X_j,Y_j,Z_j)$ to the *i*th pixel's intensity $I(x_i, y_i)$ and depends from the distance between the voxel and the line-of-sight. N_i is the total number of voxels in the line-of-sight corresponding to the *i*th pixel (x_i, y_i). A schematic representation of the imaging model is illustrated in Figure 3.5, showing top-view representation of the reconstructed domain where the levels of grey indicate the value of $w_{i,j}$ in each voxel with respect to the pixel $I(x_i, y_i)$.

The MART algorithm is implemented as an iterative technique, with the update of the system of equations based on the ratio between the measured pixel intensity and the projection of the object through an relaxation parameter $0 \le \mu \le 1$. The iterative update is as follows

$$E^{k+1}(X_j, Y_j, Z_j) = E^k(X_j, Y_j, Z_j)\left[I(x_i, y_i) \Big/ \sum_{j\in N_i} w_{i,j} E^k(X_j, Y_j, Z_j) \right]^{\mu w_{i,j}} \tag{3.12}$$

The term of update, which is the second addendum in the above equation, is defined by the ratio of the pixel intensity $I(x_i, y_i)$ with the projection of the object $E^k(X_j,Y_j,Z_j)$. It is required that $I(x_i, y_i)$ and $E^k(X_j,Y_j,Z_j)$ are positive definite. To quantify the accuracy of the reconstruction process, Elsinga *et al.*, (2006) used the quality factor Q, which is the normalized correlation coefficient computed between the actual particle field E_{actual} (known for numerical simulations) and the reconstructed one E_{rec}:

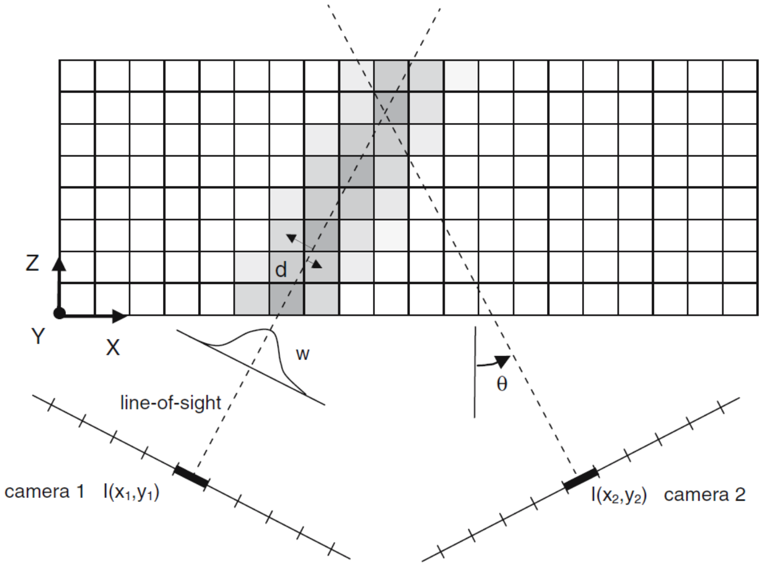

Figure 3.5 Schematic of the imaging model used for for tomographic reconstruction; in this top view the image plane is shown as a line of pixel elements and the measurement volume is a 2D array of voxels; dashed lines indicate the pixels lines of sight and voxels are colorcoded depending on the value of the weghting coefficient w_{ij} in each of the voxels with respect to the pixel $I(x_1,y_1)$; voxel distance from the line of sight is indicated with d (Elsinga *et al.*, 2006).

$$Q = \frac{\sum E_{actual} \cdot E_{rec}}{\sqrt{\sum E_{actual}^2 \sum E_{rec}^2}} \tag{3.13}$$

For iterative MART, in any real experiment the factor Q typically does not change appreciably after 5 iterations (Elsinga *et al.*, 2006).

The reconstruction quality is affected by several types of error, which are classified in three categories: discretization errors, shape errors and *ghost particles* (Maas *et al.*, 1993). Discretization errors are due to the voxel representation of the intensity field and become important when the imaged particle diameter d_τ (eq. (3.7)) is smaller than 2 pixels. Shape errors arise when the solid angle subtended by the camera system is low (an optimum angle is approximately 30º, Figure 3.6); this results in reconstructed particles that are elongated along the viewing direction, which reduces the accuracy of the velocity component along the depth (Scarano, 2013). When the optical arrangement is such that the particle diameter on the image is sufficiently large and that the angle between cameras is within the optimal range, then the quality of the reconstruction depends mostly on the *ghost particles*. These consist of spurious intensity peaks in the reconstructed objects arising from the non-unique solution to the under-determined algebraic problem of eq. (3.11). In the motion analysis, the ghost particles lead to a less robust cross-correlation signal, as their intensity is subtracted from the actual field, and can affect the motion analysis since they do not necessarily follow the displacement of the actual particles. A detailed description of the *ghost particles* behavior is given by Elsinga *et al.* (2011).

Being formed at the intersections of lines-of-sight correspondent to non-zero pixels, the number of *ghost particles* depends on the image seeding density, imaged particle diameter and the number of cameras. Figure 3.7 summarizes the influence of these three factors on the reconstruction quality Q, where ppp is the particle image density (in pixel unit) and N_S is the source density (Keane and Adrian, 1990), which reads as

$$N_S = ppp\,\frac{\pi d_\tau^*}{4} \tag{3.14}$$

with $d_\tau^* = d_\tau/\Delta x$ (Δx is the pixel size).

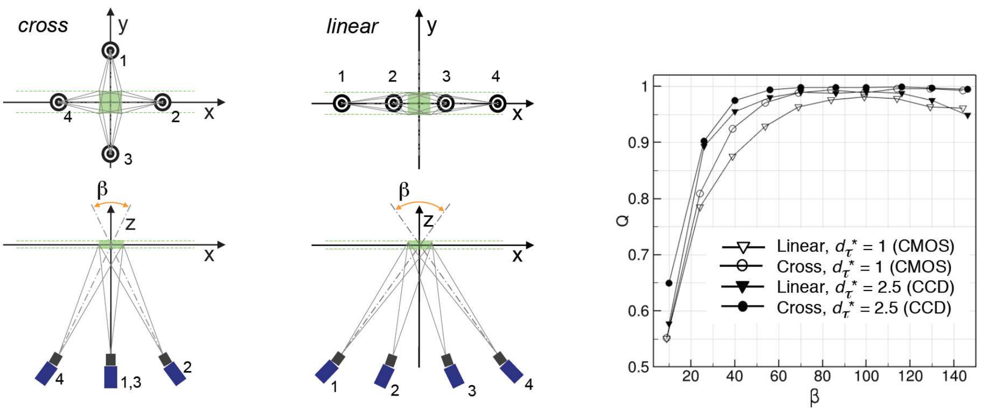

Figure 3.6 (left) Cross-like and linear imaging configurations of tomographic PIV systems with four cameras; (right) reconstruction quality factor Q versus system aperture angle β where $d_\tau^* = d_\tau/\Delta x$, Δx is the pixel size (Scarano, 2013)

Acceptable accuracy for the velocity measurement can be obtained for value of Q larger than 0.75 (Elsinga *et al.* 2006), which, in four camera system means that the source density is limited to a value of 0.3 (Scarano, 2013).

Improvements in the reconstruction accuracy can be obtained combining the MART algorithm with the Motion Tracking Enhancement technique (MTE, Novara *et al.* 2010). This method, which is based on the use of multiple recording, allows the reduction of ghost particles in the 3D objects, and, therefore, it can be used to overcome the current limitations in seeding density, thus spatial resolution, of the TOMO PIV (Novara and Scarano, 2012).

The quality of the PIV images has a large impact on the reconstruction quality because spurious intensity, such as background noise, is back-projected into the 3D domain through the MART algorithm (Elsinga *et al.*, 2006). Recently, Scarano (2013) said that an effective background removal technique is obtained combining the subtraction of a pixel-wise time history minimum intensity and a local minimum subtraction within a spatial kernel of size ranging between 11 to 31 pixels depending on the case. Moreover, the particle intensity reconstruction can be affected, or even be impossible, due to laser light reflections from solid walls or particle agglomerates in the proximity of the surface, which may be region of research interest. In such situations, dark paintings applied to the surface or a different illumination angle can help solving the issue. However, in case reflections still affect the recorded images, improvements can be obtained with a cautious image pre-processing. Scarano and Sciacchitano (2011) proposed a method to reduce light reflections from stationary or moving surfaces based on the availability of a time-resolved sequence of recording if the frequency of the reflection vibration is separated by the one proper of the tracers by at least a factor three.

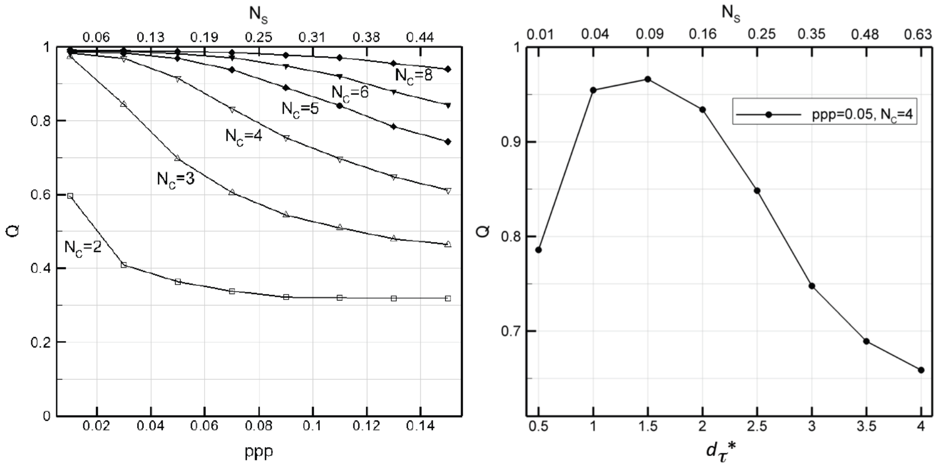

Figure 3.7 (left) Reconstruction quality factor Q as a function of image source density N_S or particle image number density *ppp* (results obtained at a fixed particle image diameter of 2 pixels); results are parameterized as a function of the number of viewing cameras N_C. (right) reconstruction quality factor dependence upon the particle image diameter at a given value of the particle image number density (Scarano, 2013)

3.2.4 Motion analysis

The velocity field is evaluated by cross-correlation of two reconstructed intensity fields, knowing their time separation Δt. The reconstructed volume is divided into sub-domains, typically of cubic geometry, where the particle displacement is evaluated by means of three-dimensional cross-correlation function. The size of the interrogation volume should be large enough to include at least 5 to 10 particles, which are less than in planar PIV since TOMO PIV technique does not suffer of out-of-plane motion.

In this work the 3D cross-correlation is performed with a multi-grid volume deformation approach (VODIM, Scarano and Poelma, 2009), which is based on the multi-grid window deformation (WIDIM) approach proposed by Scarano and Riethmuller (2000) for planar PIV. The universal outlier detection method (Westerweel and Scarano, 2005) is applied to detect erroneous vectors resulting from correlation of noise or artifacts of particle tracers. This method is based on setting a unique threshold value (typically 2) for the median test which is valid for a wide range of flows and Reynolds number. The detected vectors are then replaced with the result of a regression function performed among the neighboring values.

Novara *et al.* (2012) have recently proposed an adaptive 3D correlation strategy to increase the local spatial resolution in complex 3D and vortex-dominated flows that exhibit high vorticity in confined regions like shear layers and vortex filaments. The adaptive criterion is based on the analysis of the components of the local velocity gradient tensor, which returns the level of anisotropy of velocity spatial fluctuations. The principle to increase the local spatial resolution is based on the deformation of spherical isotropic interrogation regions, obtained by means of Gaussian weighting, into ellipsoids, with free choice of the principal axes and their directions. As shown in Figure 3.8 for the jet flow studied within this thesis, the interrogation region is contracted in the direction of the maximum velocity variation and elongated in the minimum one in order to maintain a constant interrogation volume.

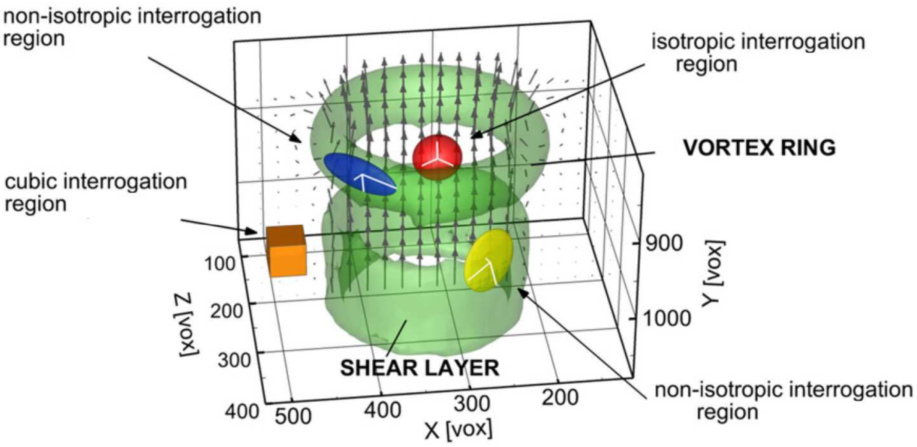
non-isotropic interrogation region
isotropic interrogation region
VORTEX RING
cubic interrogation region
100
200
300
400
Z [vox]
900
1000
Y [vox]
SHEAR LAYER
500
400
300
200
X [vox]
non-isotropic interrogation region

Figure 3.8 Adaptive 3D correlation in a jet flow (adapted from Novara *et al*., 2012)

3.2.5 4D PIV

Similar to the case of planar PIV, the time-resolved analysis of tomographic PIV recordings offers some advantages. First, the object reconstruction for time series can be based on more than two exposures (MTE, Novara *et al.* 2010), which further enhance the accuracy of the reconstruction. Secondly, the sequence of objects can be analyzed by a 3D sliding-average-correlation (Scarano *et al.*, 2010), or by a 3D extension of the *pyramid correlation* (Sciacchitano *et al.*, 2011). These methods have shown to be very effective in reducing the amount of spurious vectors and the level of random noise for data acquired in continuous single-frame mode.

Considering N exposures (N-1 object pairs), the sliding-average-correlation technique, which is employed in this thesis (section 4.2.2), reads as:

$$R = \sum_{n=1}^{N} E_n \otimes E_{n-1} \tag{3.15}$$

where the symbol $\otimes$ is the cross-correlation function. The choice of the appropriate value for the temporal kernel (number of exposures) must be based on considerations on the time-scales of the flow and on the interrogation box size. A practical approach is to limit the maximum length of *fluid sweep* to the length of the interrogation box. Therefore, if the typical particle displacement is 8 voxels and the interrogation box is taken of 40x40x40 voxels, the temporal kernel should not exceed 5 objects (4 object pairs). The beneficial effect of this technique on the measurement accuracy is described in section 4.2.2.

The availability of 4D (3D time-resolved) data enables more advanced flow diagnostic possibilities compared to the planar ones. 3D measurement allows the simultaneous evaluation the velocity vector and the velocity gradient tensor within a volumetric domain. As a result, the organization of turbulent motions can be inspected less ambiguously making use of vortex detection methods (vorticity and λ_2-criterion, see section 3.3.1) and 3D proper orthogonal decomposition (section 3.3.4), including the characteristic time evolution when measurements with temporal resolution are available.

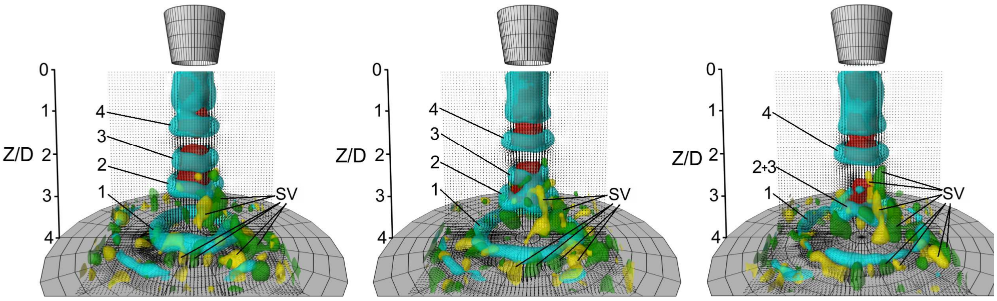

Figure 3.9 Impinging jet at *Re*=5,000 studied by TR-TOMO PIV; temporal sequence of instantaneous iso-surface axial velocity (red) azimuthal vorticity (cyan), axial vorticity (negative in green and positive in yellow); (adapted from Violato *et al.*, 2012)

The time-resolved measurement of the velocity field enables the simultaneous determination of the velocity and pressure spatial distribution, which is important in unsteady aerodynamics and aeroacoustics. The introduction of 4D measurements yields a consistent treatment of the governing equation for the pressure evaluation for incompressible flows (see chapter 7; Violato *et al.*, 2011), where all the variables of the momentum equation can be measured and the pressure gradient remains the sole unknown. The evaluation of the flow field pressure requires a numerical integration technique for the above equation, provided of the Neumann and Dirichlet boundary conditions. In case of jet flows, the use of Powell's analogy offers a more feasible approach to the study of noise generation process (section 3.3.4).

3.2.6 Computational cost

Ever since the introduction, several studies have been devoted to increase the computational efficiency of the reconstruction and volume cross-correlation techniques, which, in the early times (2005-2007), required total of an hour or more. Besides affecting the data processing, when such a long time is needed to obtain a single velocity field, the experimental setup optimization becomes significantly more difficult as no feedback is rapidly available to guide the experimentalist in the choice of different configurations (e.g. illumination, seeding concentration, calibration verification).

Several advanced techniques have been developed to reduce the computational cost of the MART reconstruction procedure, such as the multiplicative line-of-sight technique (MLOS, Atkinson and Soria, 2009), which exploits the sparseness of the reconstructed domain, and the multi-grid approach (MG, Discetti and Astarita, 2010), which reduces of approximately 5 times the computational time required for reconstruction (7 times if coupled with a MLOS approach) and reduces of around 40 times the memory load. An acceleration over more than one order of magnitude compared to standard MART is obtained combining MLOS technique with the simultaneous correction of the solution (Simultaneous Multiplicative Algebraic Reconstruction Technique, SMART; used in the investigation described in section 9.1)

The computational challenges involved in the motion analysis of 3D objects led to several studies focused of the acceleration of the cross-correlation technique. As indicated by Scarano (2013), in fact, the computational cost for cross-correlation analysis in tomographic PIV is 4 to 5 orders of magnitude higher than in planar PIV. A faster volume cross-correlation can be obtained by exploiting the sparsity of the intensity field (Atkinson and Soria, 2009; Discetti and Astarita, 2010) and voxel binning to reduce the size of the volume in the first step of the iterative interrogation (Discetti and Astarita, 2012).

Thanks to the advances in the hardware (multi-core processors) and in the processing algorithms, the computational time to calculate a single 3D velocity field from 1 Mpixel images by a 4 camera tomographic system could be reduced from 1 hour to approximately 5 minutes.

The use of 3D sliding-average-correlation technique results in an increased computational cost by a factor of (*N-1*), with *N* that is the number of exposures (Sciacchitano et al., 2011).

3.3 Data reduction

3.3.1 Vortex identification methods

Vortex structures will be identified considering the components by the vorticity vector field $\boldsymbol{\omega} \equiv \nabla \times \mathbf{V}$ or the norm $\left|\boldsymbol{\omega}\right|$ (Figure 3.10a). Alternatively, vortices will be detected by a more general criterion that was introduced by Jeong and Hussain (1995) for incompressible flows, commonly referred to as λ_2-criterion. This states that the geometry of the vortex structure is correctly represented by identifying the negative region of the second largest eigenvalue of

$$\mathbf{S}^2 + \boldsymbol{\Omega}^2 \tag{3.16}$$

where

$$\mathbf{S} = \begin{bmatrix} \frac{dU}{dx} & \frac{1}{2}\left(\frac{dV}{dx}+\frac{dU}{dy}\right) & \frac{1}{2}\left(\frac{dW}{dx}+\frac{dU}{dz}\right) \\ \frac{1}{2}\left(\frac{dU}{dy}+\frac{dV}{dx}\right) & \frac{dV}{dy} & \frac{1}{2}\left(\frac{dW}{dy}+\frac{dV}{dz}\right) \\ \frac{1}{2}\left(\frac{dU}{dz}+\frac{dW}{dx}\right) & \frac{1}{2}\left(\frac{dV}{dz}+\frac{dW}{dy}\right) & \frac{dW}{dz} \end{bmatrix} \tag{3.17}$$

and

$$\boldsymbol{\Omega} = \begin{bmatrix} 0 & \frac{1}{2}\left(\frac{dV}{dx}-\frac{dU}{dy}\right) & \frac{1}{2}\left(\frac{dW}{dx}-\frac{dU}{dz}\right) \\ \frac{1}{2}\left(\frac{dU}{dy}-\frac{dV}{dx}\right) & 0 & \frac{1}{2}\left(\frac{dW}{dy}-\frac{dV}{dz}\right) \\ \frac{1}{2}\left(\frac{dU}{dz}-\frac{dW}{dx}\right) & \frac{1}{2}\left(\frac{dV}{dz}-\frac{dW}{dy}\right) & 0 \end{bmatrix} \tag{3.18}$$

are respectively the symmetric and antisymmetric parts of the velocity gradient tensor $\nabla \mathbf{V}$.

The λ_2 definition corresponds to the pressure minimum in a plane, when contributions of unsteady irrotational straining and viscous terms in the Navier-Stokes equations are discarded (Figure 3.10b). This definition captures the pressure minimum in a plane perpendicular to the vortex axis at high Reynolds numbers, and accurately defines vortex cores at low Reynolds numbers, unlike a pressure-minimum criterion such as the Q-criterion. Moreover, Jeong and Hussain (1995) observed that a vortex boundaries based on $\left|\boldsymbol{\omega}\right|$ are ambiguous and that for vortex cores embedded in a surrounding flow with a shear comparable to the vorticity within the core, such as wall bounded and homogeneous shear flows, the maximum $\left|\boldsymbol{\omega}\right|$ may be located outside the vortex core.

The velocity gradient terms, which are employed both in the vorticity based criterion and the λ_2-criterion, are evaluated from TOMO PIV data by centered difference scheme. Raffel *et al.* (2007) gives a broader discussion on differentiation schemes employed with PIV.

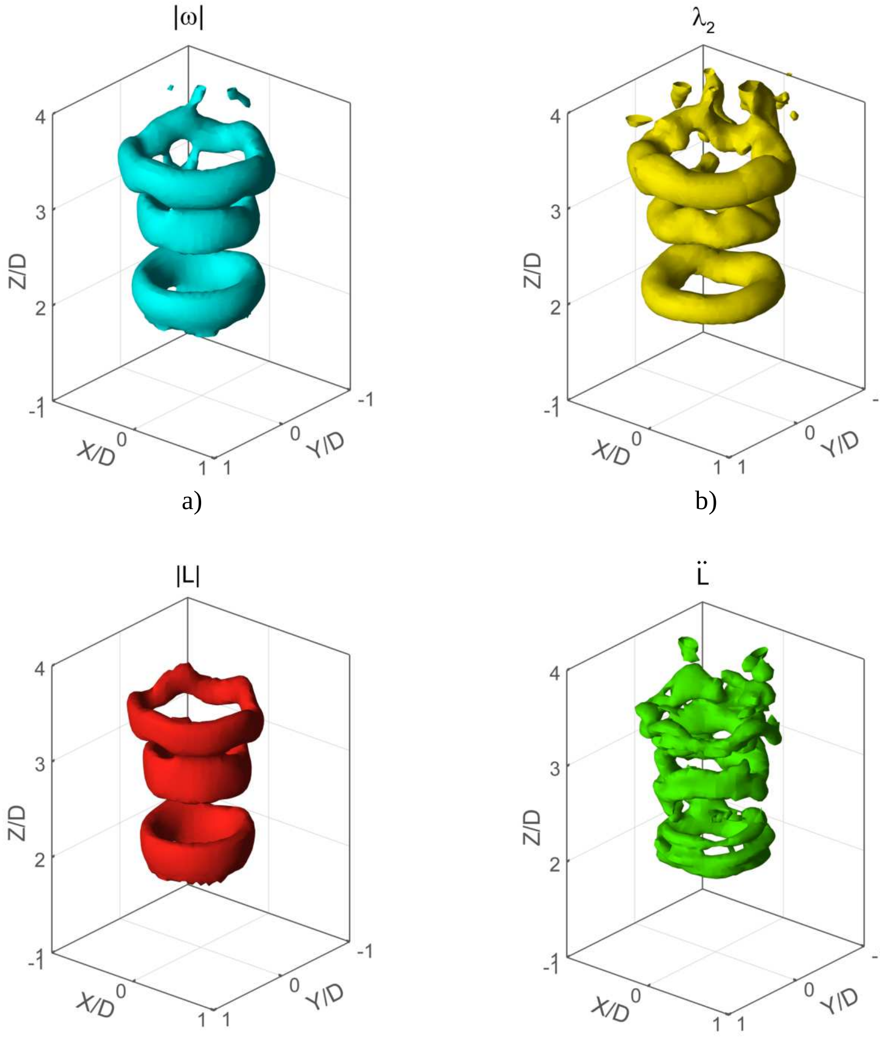

a) b)

c) d)

Figure 3.10 Vortex ring structures; iso-surface of absolute vorticity $|\boldsymbol{\omega}|$ (a), λ_2-criterion (b), absolute Lamb vector $|\mathbf{L}|$ (c) and acoustic source $\ddot{L}$ (d).

3.3.2 The Lamb vector

The Navier Stokes equation for incompressible flow (eq. (2.2)) can be written in a form that was given, among others, by Lamb (1878):

$$\frac{\partial \mathbf{V}}{\partial t} = -\nabla\left(\frac{p}{\rho}+\frac{\mathbf{V}^2}{2}\right) - \boldsymbol{\omega}\times\mathbf{V} - \nu\nabla\times\boldsymbol{\omega} \,. \tag{3.19}$$

where $\boldsymbol{\omega}\times\mathbf{V}$ is the Lamb vector **L** (Figure 3.10c) that represents the Coriolis acceleration of a velocity field under the effect of its own rotation. In literature, this vector is also referred to as “vortex force”. Usually for solid body rotation, the Coriolis force is built with a rotation vector which is independent of the velocity. A more detailed discussion on the Lamb vector is given by Rousseaux *et al.* (2006).

3.3.3 Aeroacoustic source characterization

In Powell’s analogy (eq. (2.40)), the Lamb vector is part of the source term and accounts for the flow state. Exploiting the linear property of the integral function, Powell’s analogy (see eq. (2.40)) can be rewritten as

$$p'(\mathbf{x},t) = -\frac{\rho_0}{4\pi c_0^2 \left|\mathbf{x}\right|^3} \int_{Z_1}^{Z_2}\int_{0}^{2\pi}\int_{0}^{R_1} \left(\mathbf{x}\cdot\mathbf{y}\right)\mathbf{x}\cdot\left.\left(\frac{\partial^2}{\partial t^2}\mathbf{L}\right)\right|_{t^*} \det(\mathbf{J})\, dR\, d\theta\, dZ \,. \tag{3.20}$$

Based on the above equation, the acoustic source can be mapped using

$$\ddot{L} = \left|\left(d^2\mathbf{L}/dt^2\right)\right| = \left[\left(d^2L_r/dt^2\right)^2 + \left(d^2L_\theta/dt^2\right)^2 + \left(d^2L_z/dt^2\right)^2\right]^{1/2} . \tag{3.21}$$

Note that this property clearly requires three-dimensional and time-resolved information, which, except for the current experimental investigation, may only be considered available from numerical simulations (DNS or LES). In sections 6.3 and 6.4 of this thesis, a survey on the spatio-temporal pattern of $\ddot{L}$, not yet available in literature, will be discussed in relation with large-scale structures that are identified by the λ_2-*criterion* (see section 3.3.1).

Care is however necessary when a source term from an acoustic analogy (see eq. (3.21)) is used to analyze a turbulent flow, because high level of source fluctuation do not necessarily imply high levels of sound radiation. The sound radiation capability of a source must be view in terms of the convolution integral, with an appropriate Green function, that describes the process of sound radiation (Crighton, 1975; Freund, 2001; Cabana *et al.,* 2008).

3.3.4 Proper orthogonal decomposition

Proper Orthogonal Decomposition (POD, Berkooz *et al.*, 1993) is a statistical technique to objectively classifying and describing turbulent flows in terms of most energetic coherent motions that can be used to produce of a low-order reconstruction of the flow field. When applied to velocity fields, such as PIV data or numerical simulations, POD analysis enables the identification of the coherent structures in terms of global eigenmodes. POD was applied to planar PIV data to describe a large variety of jet flow configurations: annular jets (Patte-Rouland *et al.*, 2001), normally impinging jets (Geers *et al.*, 2005) turbulent jets in crossflow (Meyer et al., 2007), daisy- and cross-shaped orifice jets (El Hassan and Meslem, 2010; El Hassan *et al.*, 2011). More recently, Schmid *et al.* (2012) have investigated the use of dynamical mode decomposition (DMD; Schmid, 2010) for the analysis of TR-TOMO PIV data of the same jet. Although, the results show that DMD is a suitable technique to infer the dynamical features of the velocity fluctuations, the present work will be based on POD also for reasons of comparison with the more abundant literature available.

The POD principles are briefly introduced here following the method of snapshots (Sirovic, 1987). Consider a set of data $u(\mathbf{x},t_n)$ that are simultaneously taken at N time instants such that the samples are uncorrelated and linearly independent. The corresponding fluctuating component is defined as

$$u'(\mathbf{x},t_n)=u(\mathbf{x},t_n)-\overline{u}(\mathbf{x}), \tag{3.22}$$

where $\overline{u}(\mathbf{x})$ is the temporal average

$$\overline{u}(\mathbf{x})=\frac{1}{N}\sum_{n=1}^{N}u(\mathbf{x},t_n)\,. \tag{3.23}$$

The POD method extracts orthonormal eigenmodes $\psi(\mathbf{x})$ and orthonormal amplitude coefficients $a_k(t)$ such that the reconstruction

$$u'(\mathbf{x},t_n)=\sum_{k=1}^{\infty}a_k(t)\psi_k(\mathbf{x}) \tag{3.24}$$

is optimal, in the sense that the functions ψ maximize the normalized average projection of ψ onto u'

$$\max_{\psi}\frac{\left\langle\left(\psi(\mathbf{x}),u'\left(\mathbf{x},t\right)\right)^2\right\rangle}{\left(\psi(\mathbf{x}),\psi(\mathbf{x})\right)}\,. \tag{3.25}$$

The time coefficients $a_k(t)$ are determined by the projection of the flow-fields on the global modes

$$a_k(t)=\left(u'\left(\mathbf{x},t\right),\psi_k(\mathbf{x})\right)\,. \tag{3.26}$$

The snapshot method introduced by Sirovich (1987) is less computationally demanding and the above maximization problem corresponds to solve a degenerate integral equation, in which the solutions are linear combinations of the snapshots

$$\psi_k(\mathbf{x})=\sum_{n=1}^{N}\Phi_n^k u'(\mathbf{x},t_n) \quad k=1,...,N \tag{3.27}$$

where Φ_n^k is the n^{th} component of the k^{th} eigenvector. The eigenmodes can then be found by solving the following eigenvalue problem

$$C_u\Phi=\lambda\Phi \tag{3.28}$$

where C is the L_2-norm matrix,

$$C_u = \frac{1}{N}\left(u'(\mathbf{x}), u'(\mathbf{x})\right). \tag{3.29}$$

The cumulative sum of the eigenvalues λ_k corresponds to the total energy and each eigenmode is associated with an energy percentage e_k :

$$e_k = \lambda_k \Big/ \sum_{i=1}^{N} \lambda_i . \tag{3.30}$$

POD descriptions of PIV data are commonly produced choosing the mean square fluctuating velocity as norm, which represents the kinetic energy of the flow. However, a more efficient identification of the coherent structures in PIV data can be obtained by the vorticity decomposition, as proposed by Kostas *et al.* (2005), who applied POD on the velocity and the magnitude of the out-of-plane vorticity. Such quantity, as explained by the authors, is a *quasi-enstrophy*, since only one component of the vorticity was considered.

In this investigation, POD analysis is first conducted on three-dimensional velocity data sets based on the mean square fluctuating energy, which, for the fluctuating velocity vector $\mathbf{V}'$ can be written as

$$C_V = \frac{1}{N}\left(\mathbf{V}'(\mathbf{x}), \mathbf{V}'(\mathbf{x})\right) \tag{3.31}$$

Then, by centered difference scheme, the velocity information is used to evaluate the three-dimensional vorticity field (Raffel *et al.*, 2007). This is analyzed by POD using, as norm, the mean square fluctuating *enstrophy*

$$C_\omega = \frac{1}{N}\left(\boldsymbol{\omega}'(\mathbf{x}), \boldsymbol{\omega}'(\mathbf{x})\right) \tag{3.32}$$

where $\boldsymbol{\omega}'$ is the fluctuating vorticity vector.

Moreover, the velocity and the vorticity vectors are used to evaluate the Lamb vector $\mathbf{L} = \boldsymbol{\omega} \times \mathbf{V}$, which is a relevant quantity in aeroacoustics as it accounts for the flow state in Powell's aeroacoustic analogy (Section 2.3.2). The modal analysis of the Lamb vector field is conducted by POD based on the norm of the fluctuating Lamb vector $\mathbf{L}'$

$$C_L = \frac{1}{N}\left(\mathbf{L}'(\mathbf{x}), \mathbf{L}'(\mathbf{x})\right) \tag{3.33}$$

which will be referred to as mean square fluctuating *Lamb energy*. Finally, following Powell's aeroacoustic analogy, the acoustic source is related to the second time derivative of the Lamb vector $d^2\mathbf{L}/dt^2$ (Section 3.3.3), which is analyzed with the POD technique based on the norm of the fluctuating component $d^2\mathbf{L}/dt^2\,'$

$$C_{d^2\mathbf{L}/dt^2} = \frac{1}{N}\left(d^2\mathbf{L}/dt^2\,'(\mathbf{x}), d^2\mathbf{L}/dt^2\,'(\mathbf{x})\right) \tag{3.34}$$

The above norm will be referred to as mean square fluctuating *acoustic source energy*.

Chapter 4

Experimental instrumentation and arrangements

This chapter is devoted to the description of the facility, the experimental instrumentation and the arrangements used for the experimental investigation. This is followed by the uncertainty analysis for tomographic PIV experiments. The chapter also includes a presentation of the overall flow characterization on a statistical basis for circular and chevron jets.

4.1 Jet tomographic facility

Experiments are conducted in a water facility at the Aerodynamic Laboratories of TU Delft in the Aerospace Engineering Department. The Jet Tomography Facility (JTF) facility has been specifically designed for tomographic experiments on water jets. However, given its versatility, JTF has also been used for experiments on flapping wings (Percin *et al.*, 2011) and high-speed air jets (see Chapter 9). A round nozzle of exit diameter D=10 mm and contraction ratio of 56:1, is installed at bottom wall of a tank. Following the work of Schram *et al.* (2003; 2005), the nozzle contraction shape is a symmetric 7th order polynomial profile (Figure 4.1):

$$\eta(\xi) = (-20\xi^3 + 70\xi^2 - 84\xi + 35)\xi^4 \tag{4.1}$$

with $\xi = \left(L - x\right)/L$ and $\eta = \left(r - r_2\right)/\left(r_1 - r_2\right)$. The chosen profile yields a uniform laminar flow at the exit.

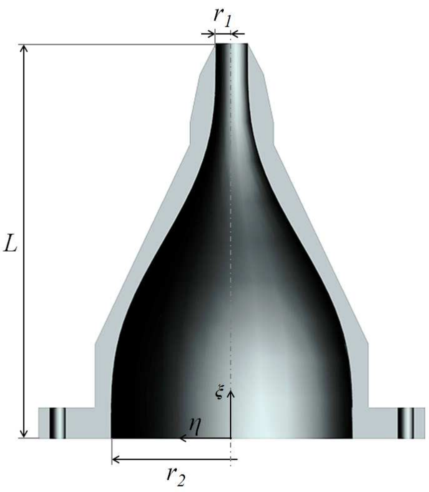

Figure 4.1 Cross section of nozzle contraction

Table 4.1 Nozzle contraction dimensions

Inlet radius	r_1	37.5 mm
Outlet radius	r_2	5 mm
length	L	125 mm

The jet is enclosed in an octagonal water tank of 600 mm diameter and 800 mm height built in Plexiglas to enable extensive optical access for illumination and tomographic imaging. The schematic of Figure 4.2 shows a cross-section of the jet tomographic facility. When the facility is completely filled with water, the pump (1) forces the fluid out of the water reservoir (2) into the hydrostatic pressure tank (3). The water flow rate is set by a valve (4) with the help of a flow meter (5). An impact plate (6) is placed at the inlet of the settling chamber (7) to promote the mixing with the seeding particles. Honeycomb (8) and grids (9) are fitted in the duct upstream of the nozzle contraction (10) to reduce the flow turbulence into the octagonal shaped test section (11), which is equipped with a laser window (12). Water is drained though an outlet (13) back to the water reservoir (2).

The system is hydrostatically driven and provides a stable supply in a range of exit velocity W_j from 0.1 to 2m/s, corresponding to Reynolds numbers ranging between 1,000 and 20,000. The water temperature is 20ºC.

The 6-chevrons jet exit is applied on top of the circular nozzle profile, with chevrons 7 mm high and inclined towards the jet axis by an angle to the jet axis of 12 degrees, as shown in Figure 4.3, thus resulting in a penetration depth of 1.5 mm.

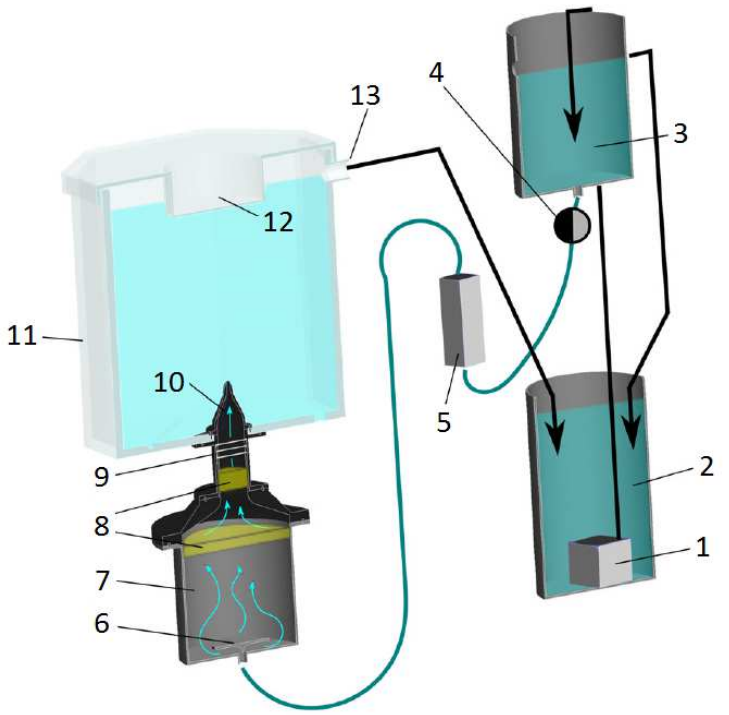

Figure 4.2 Cross-section of jet tomographic facility. Pump (1), water reservoir (2), hydrostatic pressure tank (3), valve (4), flow meter (5), impact plate (6), settling chamber (7), honeycomb (8), grid (9), nozzle contraction (10), octagonal shaped test section (11), a laser window (12), outlet (13).

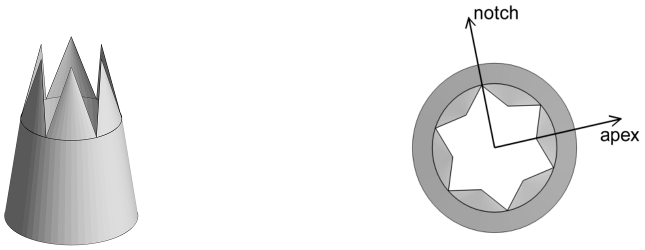

Figure 4.3 Chevron nozzle (left); azimuthal position of chevron notch and apex (right).

4.2 Time resolved tomographic PIV

Tomographic experiments are performed for a nominal axial velocity at the jet exit of 0.5 m/s yielding a Reynolds number *Re*= 5,000 based on the jet diameter *D*.

Neutrally buoyant polyamide particles of 56 μm of diameter are dispersed homogeneously, achieving a uniform concentration of 0.65 particles/mm^3. The illumination is provided by a Quantronix *Darwin-Duo* solid-state diode-pumped Nd:YLF laser (2x25 mJ/pulse at 1 kHz).

After a transmission distance of 1.5 m, the laser beam features a diameter of 6 mm and is further expanded through a diverging lens to a diameter of 80 mm and then focused with a converging lens to obtain a conical illumination domain (Figure 4.4). The light scattered by the particles is recorded by a tomographic system composed of three 3 *Imager pro* HS 4M cameras (12 bits, 2048x2048 pixels, pixel pitch of 11 μm) arranged horizontally with azimuthal aperture of 90 degrees. The choice of conical, or cylindrical (Figure 4.5), illuminated volume eliminates the need for camera-lens tilt mechanism to comply with the Scheimpflug condition. Nikon objectives of 105 mm focal length are set with a numerical aperture $f_{\#}$= 22 to allow focused imaging of the illuminated particles. For the chosen illumination and imaging configuration the particle image density (*ppp*) decreases from the axis towards the edge of the illuminated volume and, at the jet axis, increases along the axial coordinate from 0.037 (at the jet exit) to 0.043 (10 diameters above the exit) particles/pixel. Table 4.2 summarizes the details of the settings of the experiments conducted by Violato and Scarano in 2011 and 2013.

The choice of a conical (Violato and Scarano, 2013) or cylindrical (Violato and Scarano, 2011) domain of illumination also results in a more favorable an accurate reconstruction of the particle field, as the particle image density does not change with the viewing angle along the azimuth and decreases moving from the axis to the periphery of the jet (Figure 4.4). Moreover, the extent of uniform flow velocity in the region outside the jet is minimized, which mitigates the effect of ghost particles velocity (Elsinga *et al.*, 2011) in turn biasing the measurement in the shear layer and jet core (Novara and Scarano, 2012).

Sequences of images of tracer particles (Figure 4.6) are recorded at 1 kHz resulting in a temporal resolution that yields 35 samples for the fastest expected events (vortex shedding). The imaged-particle displacement at the exit is approximately 10 pixels along the jet axis.

The field of view is of 50 x 100 mm with a digital resolution of 18.5 pixels/mm. Sequences of 500 images are also recorded at 20 Hz in frame-straddling mode (pulse separation time 1 ms) for a total time of 25 s to produce a statistically significant data ensemble.

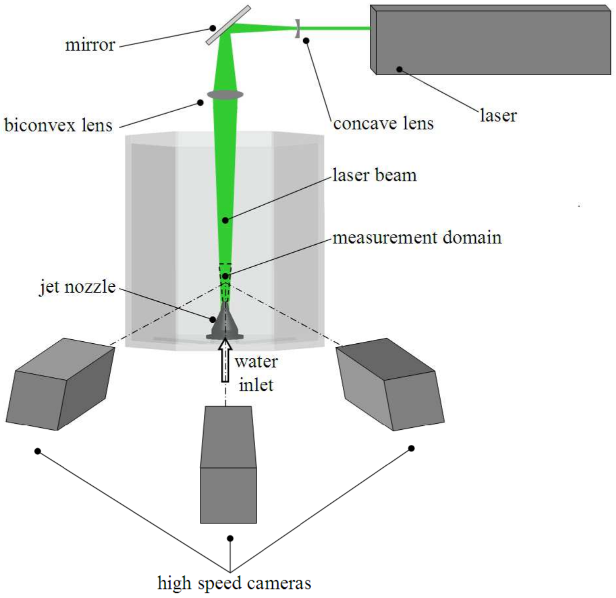
mirror
biconvex lens
concave lens
laser
laser beam
measurement domain
jet nozzle
water inlet
high speed cameras

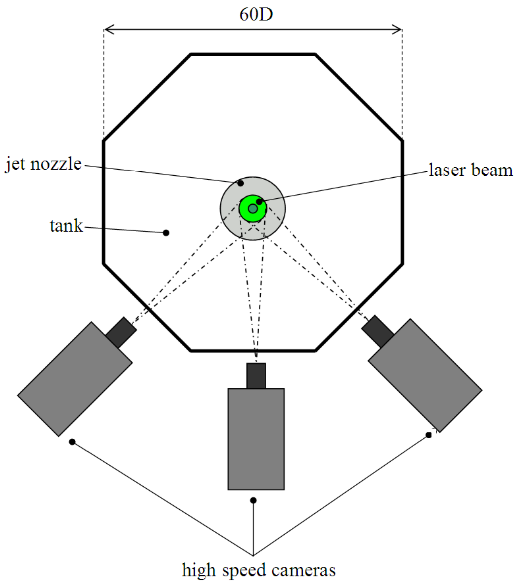
60D
jet nozzle
laser beam
tank
high speed cameras

Figure 4.4 (top) Schematic view of conical illumination and imaging in the tomographic experiment; (bottom) view of the system; (Violato and Scarano, 2013)

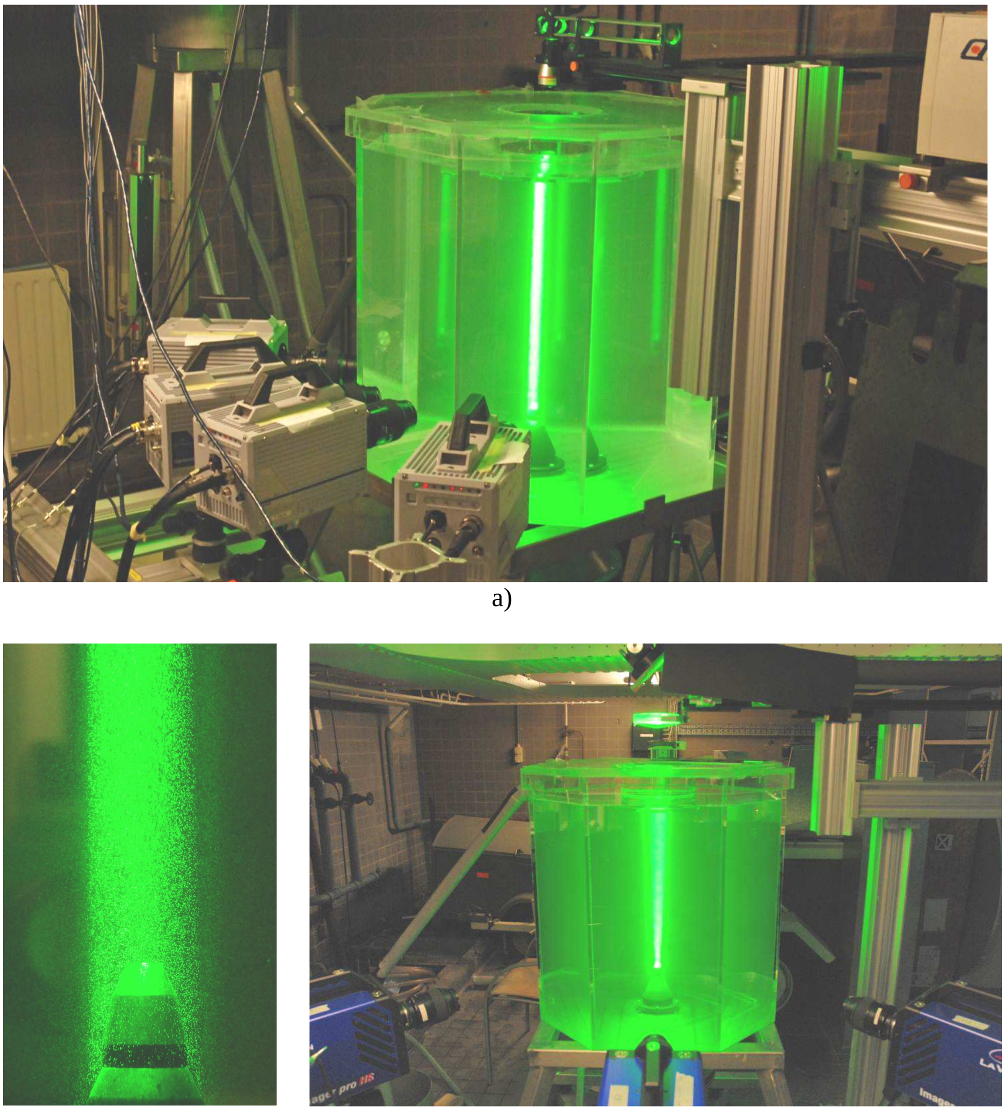

a)

b) c)

Figure 4.5 Imaging and illumination configurations in the tomographic experiments; a) 4 camera system with cylindrical illumination; b) detail of the cylindrical beam; c) 3 camera system with conical illumination

4.2.1 Tomographic reconstruction

The volumetric light intensity reconstruction is performed following the of Multiplicative Algebraic Reconstruction Technique algorithm (MART, Hermann and Lent, 1976) by the LaVision software *Davis* 8. A three-dimensional mapping function from image-space to physical object-space is generated by imaging a calibration target. The initial experimental errors due to system calibration are approximately 0.5 pixels as estimated from the disparity vector field. The misalignment is reduced to less than 0.05 pixels making use of the *3D self-calibration* technique (Wieneke, 2008). The raw images are pre-processed with subtraction of the minimum intensity at each pixel for the entire sequence, followed by a subtraction of the local minimum over a kernel of 31x31 pixels. The MART algorithm is applied with four iterations.

At the given particle image density, despite the radial decrease and axial increase, the use of 3-camera tomographic system leads to rather accurate 3D object reconstructions with a reconstruction quality Q estimated above 0.75 (Elsinga *et al*., 2006).

The illuminated volume is discretized with 660 x 660 x 2000 voxels resulting in a digital resolution of 20 voxels/mm (voxel pitch of 50 μm). Following Elsinga *et al*. (2006), the accuracy of the reconstruction is evaluated *a-posteriori* comparing the intensity of reconstructed particles in the illuminated region with that of *ghost particles* produced in the immediate surroundings of the illuminated domain. A signal-to-noise ratio may be defined as the reconstructed particles intensity inside the illuminated area versus that reconstructed outside. The laser light intensity follows a Gaussian distribution along the radius and the light is concentrated in a circular region. In Violato and Scarano (2011), this is found approximately 550 voxels of diameter (Figure 4.7), corresponding to 27.5mm. The peak intensity profile along the radial direction r shows that the intensity outside of the illuminate region is negligible. The reconstruction signal-to-noise ratio as defined above is higher than 4.

Figure 4.8 shows the coordinate system and the measurement domains for the chevron and circular jets in the experiments conducted by Violato and Scarano (2011, 2013).

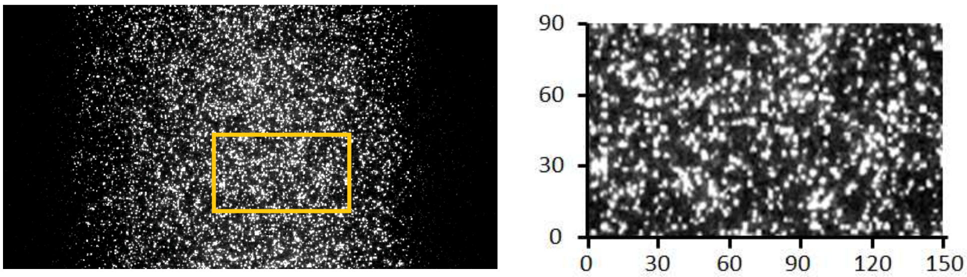

Figure 4.6 (left) Particle image recording after subtraction of the local minimum over a 31x31 pixels kernel; (right) sample extracted from yellow window

Table 4.2 Experimental settings for time-resolved TOMO PIV measurements conducted by Violato and Scarano (2011, 2013)

	(2011)	(2013)
Seeding	particle diameter 56 µm concentration 0.65 part/mm^3	particle diameter 56 µm concentration 0.65 part/mm^3
Illumination	Quantronix *Darwin-Duo* Nd-YLF laser (2 x 25mJ@1 kHz) Cylindrical beam (diameter 3*D*)	Quantronix *Darwin-Duo* Nd-YLF laser (2 x 25mJ@1 kHz) Conical beam (min diameter 2*D*, max diameter 3.3*D*)
Recording device	4 Photron Fast CAM SA1 cameras (1024 x 1024 pixels@ 5.4kHz) 20 µm pixel pitch	3 Imager pro HS 4M cameras (2016 x 2016 pixels@ 1.3 kHz) 11 µm pixel pitch
Optical arrangement	Nikon objectives *f*=105mm; *f#*=32 field of view: 5*D* x 5*D*	Nikon objectives *f*=105mm; *f#*=22 field of view: 5*D* x 10*D*
Acquisition frequency	1kHz	1kHz
Time of acquisition	0.5 s	2 s
Nozzle geometry	circular; chevron	circular
Measurement domain	3D x 3D x 5D	3.3D x 3.3D x 10D

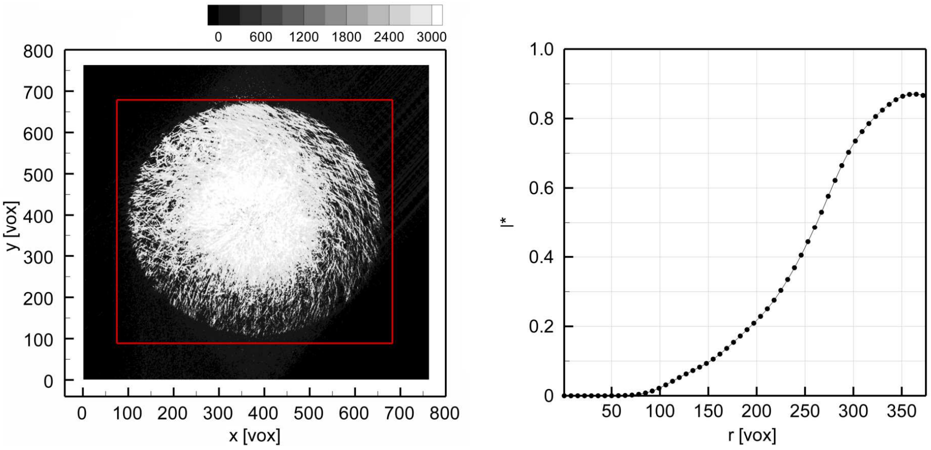

Figure 4.7 (left) Reconstructed particle peak intensity distribution averaged along *z*-axis (the red box indicates the reconstructed region); streaks are visible wich correspond to particles reconstructed over a sequence of recordings; (right) normalized particle peak intensity profile along the radial direction (azimuthal average)

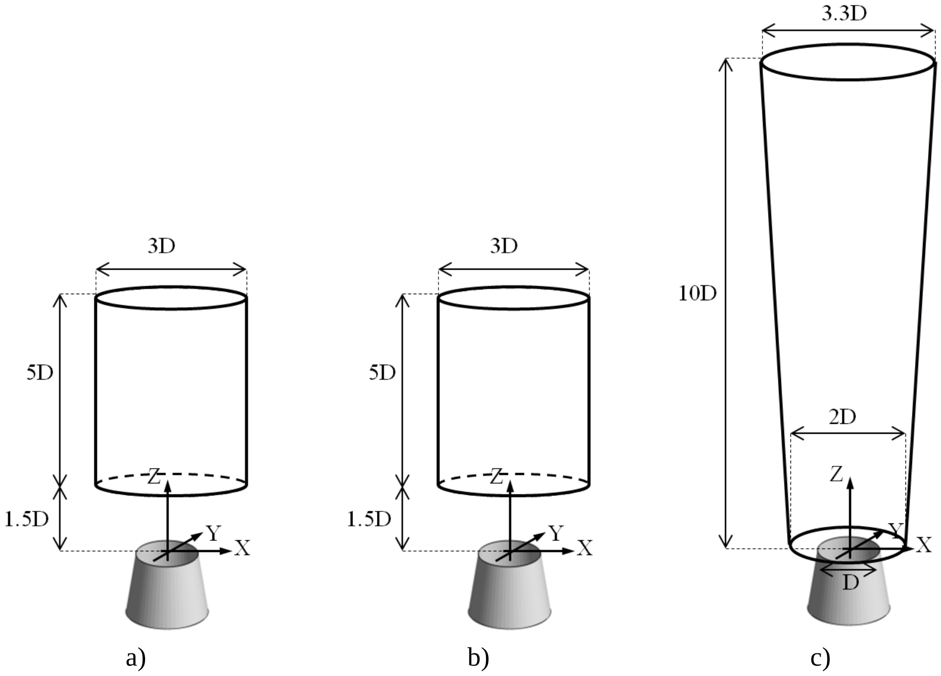

Figure 4.8 Measurement domains and coordinate system; a-b) circular and chevron jets (Violato and Scarano, 2011); c) circular jet (Violato and Scarano, 2013)

4.2.2 Vector-field computation

The three-dimensional particle field motion is computed by Volume Deformation Iterative Multigrid (VODIM) technique (Scarano and Poelma, 2009) with a final interrogation volume of 40x40x40 voxels (2x2x2 mm^3) with an overlap between adjacent interrogation boxes of 75%, leading to a vector pitch of 0.5 mm. At the given particle concentration, 6.5 particles are counted, on average, within the interrogation box.

A further refinement of the analysis is obtained by using the Sliding Average Correlation technique (SAC, Scarano *et al.*, 2010), whereby the cross-correlation map, obtained over three subsequent object-pairs, is averaged yielding higher signal-to-noise ratio and higher measurement precision. Such approach is an extension of the method proposed by Meinhart *et al.* (2000) that is here extended to unsteady velocity fields, when the sampling rate exceeds that strictly needed for temporally resolving the flow. As discussed in section 3.2.5, correlation averaging technique over three subsequent object-pairs is applied to have higher signal-to-noise ratio and higher measurement precision in time-resolved measurements. The use of such averaging technique involves a longer measurement time interval corresponding to the separation of four exposures (3 ms). The use of four subsequent objects results in a reduction of the displacement rms error from approximately 0.12 to 0.05 voxels, as it is shown in the velocity time-history plotted in Figure 4.9.

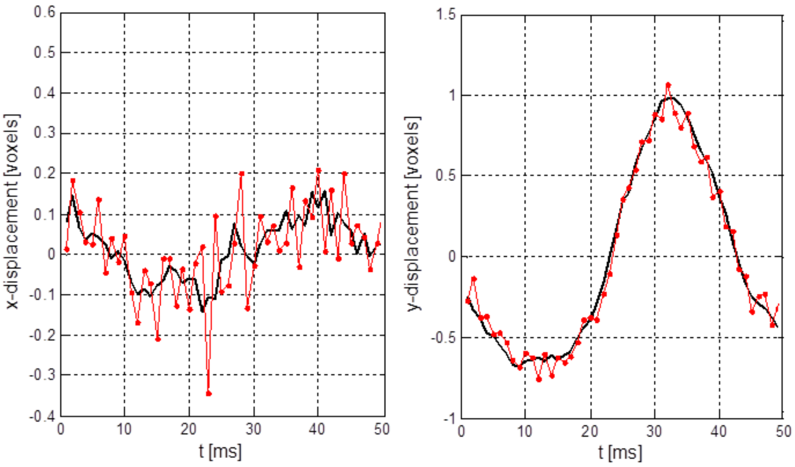

Figure 4.9 Time-resolved velocity components in the jet. Comparison of velocity time-history obtained by single-pair correlation (solid red line and dots) and averaged correlation over three pairs (black line). (Scarano *et al.*, 2010)

Data processing is performed on a dual quad-core Intel *Xeon* processor at 2.83 GHz with 8 GB RAM memory. Reconstruction of a pair of objects and the 3D cross-correlation requires 1 hours and 20 minute for the small measurement domain (Figure 4.8 a-b, Violato and Scarano, 2011) and 3 hours and 40 minute for the large domain (Figure 4.8 c, Violato and Scarano, 2013).

When needed, data post-processing is applied that consists of a space-time least-squares regression. Spatio-temporal noisy fluctuations are significantly suppressed by applying the second order polynomial least squares regression (Scarano and Poelma, 2009) with a kernel of 5x5x5 grid nodes in space (2 mm^3), corresponding to the interrogation box size. Given the high repetition rate of the measurement a temporal kernel that encompasses 7 time steps (6 ms) is used without affecting the temporal resolution of the measurement in the range of time scales of interest (up to a value of the Strouhal number of 4). Further details on the measurement uncertainty are discussed in section 4.4.

4.3 Time resolved planar PIV

Planar PIV experiments are conducted on the circular jet for statistical characterization of the flow.

Neutrally buoyant polyamide particles of 10μm diameter are employed with a concentration of approximately 6 particles/mm^3. The illumination and imaging is provided by the same equipment as used for the tomographic experiments. A laser-light sheet of 1.5 mm is formed applying a knife-edge slit-filter to the expanded beam.

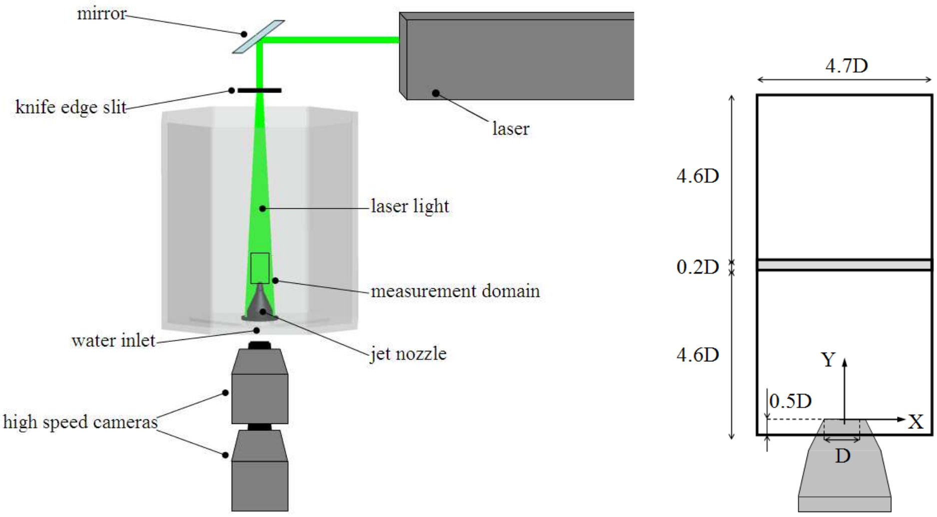

a) b)

Figure 4.10 Planar PIV experiments; (left) schematic of the recording and the illumination system; (right) field of view

Two cameras are combined to cover a measurement region extending from the exit up to 10 diameters (Figure 4.10 and Figure 4.11). The cameras are equipped with objectives of 105 mm focal length set at numerical aperture $f_{\#}$=2.8 to maximize light intensity. To avoid the phenomenon of peak-locking (Westerweel, 2000) the focal plane is slightly offset from the illumination plane (*defocussing*) and the particle images are blurred over an area of approximately 2x2 pixels. Sequences of images of tracer particles are recorded at frequency of 1.2 kHz yielding a particle image displacement of approximately 7 pixels at the jet exit.

The field of view (FOV) of each camera is 47 mm x 47 mm, with a digital resolution of 20.7 pixels/mm. The two FOVs overlap of 2 mm and, when combined, form a measurement domain of 47 mm x 92 mm. The experimental settings are summarized in Table 4.3.

The time-averaged velocity profile at the exit, where the flow regime is steady and laminar, is computed by ensemble-averaging the correlation signal along the measurement sequence (Meinhart *et al.* 2000). As a result, the interrogation window can be decreased down to 6 x 6 pixels (0.29 x 0.29 mm^2) with an overlap factor of 50% leading to a vector pitch of 0.13mm.

Table 4.3 Experimental settings for planar PIV measurements

Seeding	particle diameter 10 μm concentration 6 part/mm^3
Illumination	Quantronix *Darwin-Duo* Nd-YLF laser (2 x 25mJ@1 kHz) sheet thickness 1.5 mm
Recording device	2 Photron Fast CAM SA1 cameras (1024 x 1024 pixels@ 5.4kHz) 20 μm pixel pitch
Optical arrangement	Nikon objectives *f*=105mm; *f#*=2.8 field of view: 4.7*D* x 9.2*D*
Acquisition frequency	1.2kHz
Time of acquisition	3.5 s
Nozzle geometry	circular

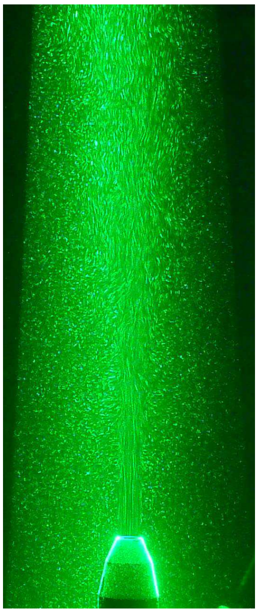

Figure 4.11 Laser sheet for planar PIV

4.4 Uncertainty analysis for TOMO PIV

A reliable estimate of the measurement uncertainty of three-dimensional time resolved measurements can be performed by several *a posteriori* approaches based on physical criteria (Sheng *et al.*, 2008; Scarano and Poelma, 2009). At the present measurement rate, temporal fluctuations are sampled by a large number of snapshots, where the measurement error is expected to be uncorrelated. The measurement precision error can be evaluated by comparing the velocity time history to a filtered version obtained with a kernel length smaller than the flow scales. Such a comparison is shown in Figure 4.12, in which the raw and the filtered data are plotted at a given point in the shear layer (x=0.5D, y=0, z=3D), where the flow unsteady behavior is dominated by the passage of laminar vortex rings. Each velocity component is filtered with a second order polynomial least squares regression (Schrijer and Scarano, 2008) over a kernel of size L in space and duration T. In order to avoid significant amplitude modulation, which would mean a distortion of large-scale flow structure characteristics, the kernel size must satisfy the following relations: $L<d_V$ and $T<d_V/W_V$, where d_V is the core diameter of a vortex moving with a velocity W_V. An estimate of the characteristic kernel size, for instance, can be based on laminar vortex rings (d_V=4x10^{-3} m and W_V=0.2 m/s) leading to L<4x10^{-3} m and T <20ms. In this investigation, a significant suppression of the spatio-temporal noisy fluctuations is obtained by applying the second order polynomial least squares (Scarano and Poelma, 2009) with a kernel size of 5 grid nodes in space (2 mm^3), corresponding to the interrogation box size, and 7 time steps (6 ms). The residual of the velocity can be referred to as measurement error, which is estimated to 0.15 voxels for all the velocity components, based on standard deviation over the entire data ensemble. The relative error on the velocity measurement is approximately 2% with respect to the particle displacement at the jet exit of 8 voxels.

The applied filter does not lead to any reduction in spatial resolution, which remains equal to 2 mm. On the other hand, it reduces the temporal resolution to 6 ms. In such a condition, for example, the maximum number of azimuthal modes that can be detected along the nozzle circumference is 15, whereas the minimum temporal variation that can be observed is 12 times smaller than the pairing period (72 ms).

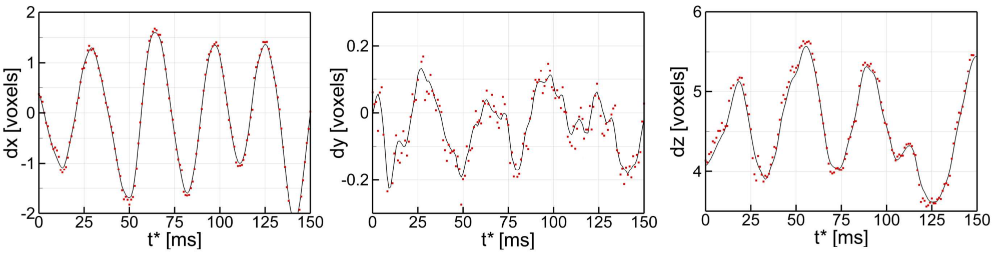

Figure 4.12 Time history of the velocity components at (x=0.5D, y=0, z=3D). Raw data (red dots) and second order time-space filtered data (solid black line)

Furthermore, the measurement error on the components of the velocity gradient can be estimated invoking the principle of local mass conservation (Zhang *et al.*, 1997). Although the flow divergence $\nabla \cdot \mathbf{V}$ is a flow property of little interest when dealing with incompressible flows, it is a suitable quantity to estimate the measurement error on the spatial derivatives of the flow. In the entire domain, the condition

$$\nabla \cdot \mathbf{V} = \frac{\partial u}{\partial x} + \frac{\partial v}{\partial y} + \frac{\partial w}{\partial z} = 0 , \tag{4.2}$$

must be satisfied at all-time instants. The numerical evaluation of $\nabla \cdot \mathbf{V}$ from experimental data may differ from zero due to measurement error on the velocity and the numerical truncation in the spatial discretization. As discussed in Scarano and Poelma (2009), the relatively large overlap factor between neighboring interrogation boxes ensures that truncation errors are negligible with respect to the finite size of the interrogation. Hence, the standard deviation of the velocity divergence over the entire measurement domain and during the whole observation time $\langle |\nabla \cdot \mathbf{V}| \rangle$ can be used as statistical estimate of the measurement precision for the velocity gradient tensor components. Figure 4.13 illustrates the probability density function of $\nabla \cdot \mathbf{V}$. The dotted and solid lines correspond to the raw and the filtered data. The error shows a Gaussian distribution symmetrical around zero with a standard deviation $\langle |\nabla \cdot \mathbf{V}| \rangle$ of 0.012 and 0.007 voxels/voxel for the raw and the filtered data, respectively. The measurement of the terms on the *trace* of the velocity gradient tensor $\partial u / \partial x$, $\partial v / \partial y$ and $\partial w / \partial z$ is usually less accurate than that of the non-diagonal terms, therefore the above values may be considered as conservative estimates for the uncertainty of all the velocity gradient components. Considering the particular case of the vorticity, dividing the absolute error by the typical value measured in the core of the shed vortex (0.25 voxels/voxel), the resulting relative precision error on the vorticity field is estimated to be less than 3%.

In the region where the fluctuations are dominated by laminar vortex rings, the vorticity residual evaluated as the difference between the filtered and raw data exhibits a standard deviation of 0.01 voxels/voxel, which is comparable to the above estimate of the measurement uncertainty.

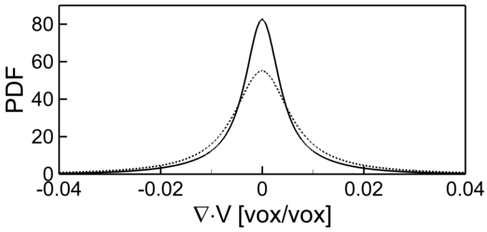

Figure 4.13 Probability density of measurement error estimated by velocity divergence. Raw data (dotted line) and filtered (solid line)

4.5 Statistical flow properties in circular and chevron jets

The mean velocity profile of the circular jet at the nozzle exit was obtained through the ensemble average technique (section 3.1.4) leading to a 77 vectors along the diameter (Figure 4.14). The profile is taken at *Z/D*=0.1 to avoid using data corrupted by laser light reflections from the nozzle surface. Following Alkislar *et al.* (2007), the normalized displacement thickness

$$\delta_e / D = \int_{(R/D)_{0.1}}^{(R/D)_{0.9}} \left(1 - W / W_j\right) dR \big/ D , \tag{4.3}$$

and the normalized momentum thickness

$$\theta_e / D = \int_{(R/D)_{0.1}}^{(R/D)_{0.9}} \left[W / W_j (1 - W / W_j)\right] dR \big/ D \tag{4.4}$$

are measured between $(R/D)_{0.1}$ and $(R/D)_{0.9}$, which correspond to the radial position where $W/\ W_j$ =0.1 and W/W_j=0.9,with W_j jet exit velocity. It is found normalized displacement thickness δ_e / D of 0.078 and normalized momentum thickness θ_e / D of 0.028. Their ratio δ_e / D = 2.78 agrees well with the theoretical value for the Blasius solution of 2.59 (Zaman and Hussain, 1980). Moreover, θ_e / D satisfies the relation for laminar shear layers

$$\theta_e / D = c\left(\frac{W_j D}{\nu}\right)^{-0.5} \tag{4.5}$$

with c=1.2 (Schram *et al*., 2003). The level of axial velocity fluctuation w'/W_j in the jet core is less than 0.5% (Petersen, 1978; Zaman and Hussain, 1980; Liepman and Gharib, 1992).

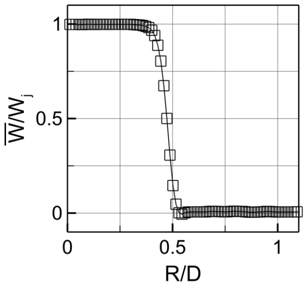

Figure 4.14 Cross-sectional profile of mean-axial velocity at Z/D = 0.1

The spatial distribution of the mean axial velocity is illustrated in Figure 4.15 as iso-contours on a radial plane on the cylindrical domain. The potential core, which is identified by the contour line $\overline{W}/W_j$ = 0.95, shows an axial penetration of 6.25 diameters. Further downstream, the mean axial velocity decreases to 0.55 at Z/D=10 (Crow and Champagne, 1971; Hussain and Zaman, 1981).

The peak activity of the turbulent fluctuations is concentrated between Z/D=2.5 and Z/D=8.5, as depicted by the iso-contour plots of Figure 4.16. For 3<Z/D<4.5, axial and radial fluctuations w'/W_j and v_r'/W_j reach peaks of 0.18. For a circular jet at Re=12,000, Zaman and Hussain (1980) associated the peak activity w'/W_j =0.11 at Z/D=3 to the pairing of vortex ring structures. At higher Reynolds (Re=55,000), the same authors (Hussain and Zaman, 1981) found w'/W_j >0.15 between Z/D=2.5 and 7 and observed that, when the jet was acoustically excited at the vortex pairing frequency, the axial fluctuation showed again a peak at the pairing position (Z/D=3). Also Ganapathisubramani *et al.* (2002) reported peak values of axial velocity fluctuations associated to the pairing phenomenon. Further downstream w'/W_j and v_r'/W_j gradually decreases reaching 0.15 at Z/D=4.5. Similar observation was reported by Yule (1978) who found that all the fluctuating velocity components of jet flows ranging between Re=9,000 to 2x10^5.

The azimuthal fluctuations v_θ'/W_j , instead, are dominant in the region by the end of the potential core. For low Reynolds number jets, Yule (1978) reported that circumferential fluctuations intensify as the flow three-dimensionality develops and the axisymmetric regime vanishes rapidly.

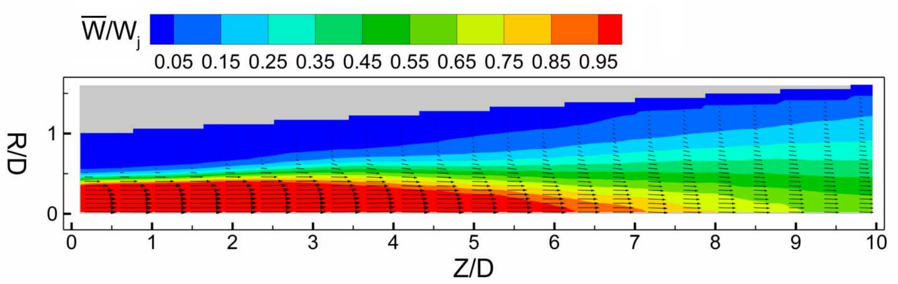

Figure 4.15 Iso-contours of mean-axial velocity on a radial plane

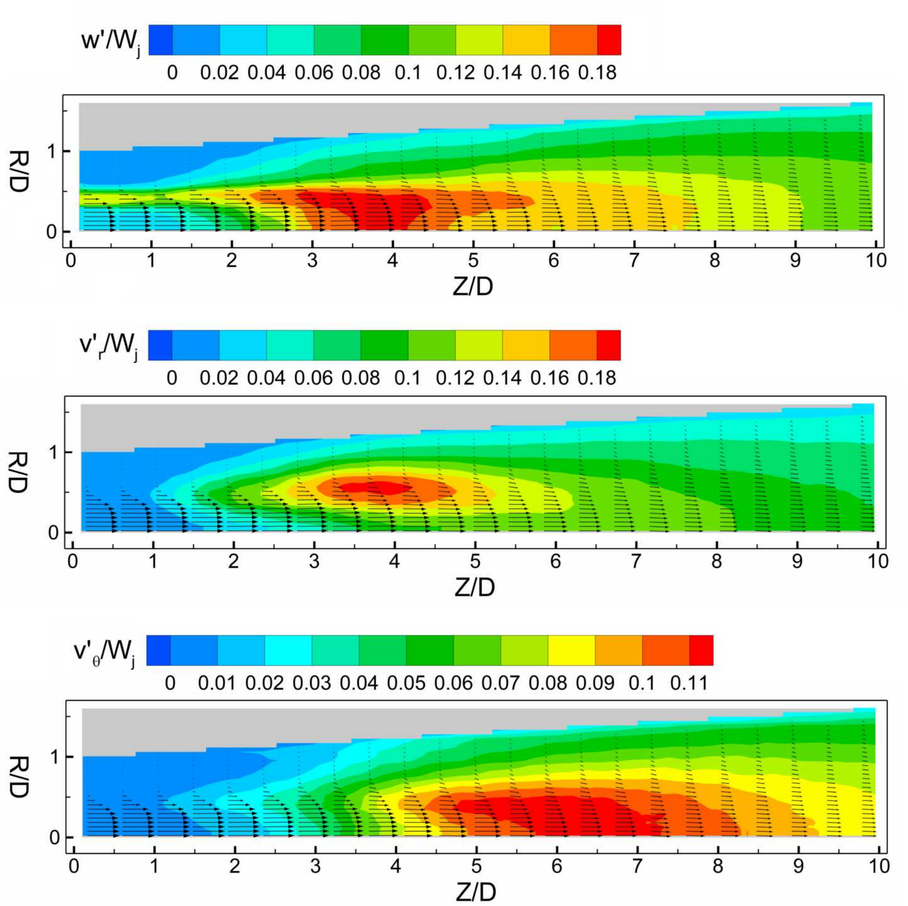

Figure 4.16 Iso-contours of velocity fluctuations on a radial plane: axial w'/W_j, radial v_r'/W_j and tangential v_θ'/W_j components

The spatial development of the jet is illustrated by contours of mean axial velocity on several cross-sectional planes, as illustrated in Figure 4.17, which showing that 95% of the axial velocity is still maintained beyond *Z/D*=4 (Bridges and Brown, 2004; Opalski *et al.*, 2005; Alkislar et al. 2007). Compared to the axisymmetric development of the circular case (Figure 4.15), the shear layer of the chevron is shaped from the nozzle exit with a star-like pattern as a result of the chevron geometry (Bridges and Brown, 2004; Opalski *et al.,* 2005; Alkislar et al. 2007). Most evident between *Z/D*=1 and 2, a secondary flow pattern of higher axial velocity is installed in correspondence to the notch where the radial outflow, approximately $0.1W_j$, rolls-up into a circulatory motion slightly staggered with respect to the chevron apex. The secondary flow develops either on the left or on the right side of the valley and does not occur with fully regular organization, which is ascribed to small imperfections of the boundary conditions. Although being conducted at higher values of the Reynolds number, the investigations by Bridges and Brown (2004), Opalski et al. (2005) and Alkislar et al. (2007) showed lobed patterns centered at the chevron notch, which suggests the tendency of secondary rollers to be aligned with the notch as *Re* increases. On the other hand, similarly to what reported by Opalski et al. (2005) and Alkislar et al. (2007), the flow loses the characteristic lobed pattern and gradually gains axisymmetric coherence between *Z/D*=3 and 4.

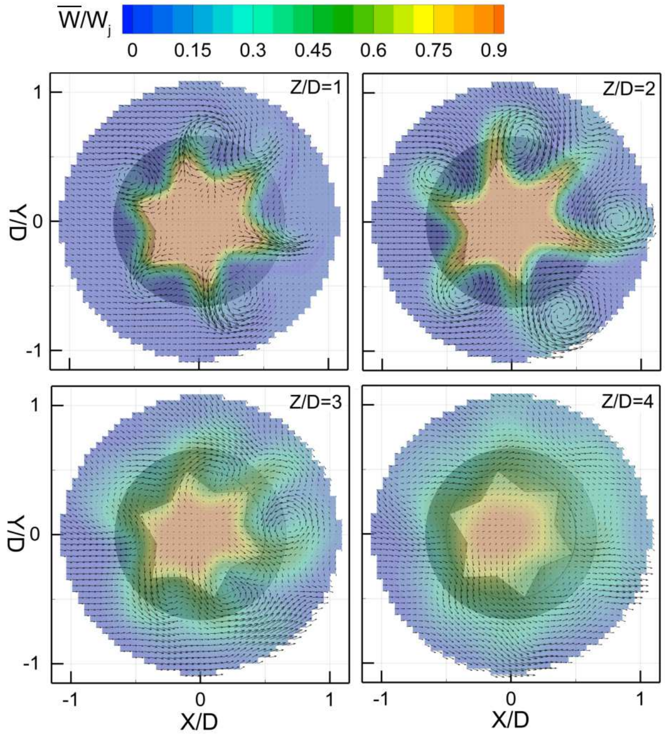

Figure 4.17 Chevron jet: contours of mean-axial velocity at different cross-sectional *Z*-planes; X-Y projection of velocity vectors

To observe the effect of chevrons on the development of the shear layer, mean axial velocity profiles corresponding to the chevron apex and notch (Figure 4.3) are compared to the circular case in the radial direction (Figure 4.18). The velocity profile at the notch and apex are obtained by averaging the velocity from the six azimuthal locations. The normalized shear layer thickness δ/D is defined as the distance between the radial locations where W/W_j=0.1 and 0.9, at Z/D=1 (Figure 4.18). The profile extracted at the notch is characterized by a thicker shear layer (δ/D=0.28) compared to that at the apex (δ/D=0.14) and the circular case (δ/D=0.17). In fact, the chevrons induce a stretching of the shear layer (Alkislar *et al*. 2007) with a 15% smaller thickness at the apex and an increase up to 50% at the notch, when compared to the circular case. More downstream, at Z/D=3 (Figure 4.18), the time-averaged profiles of axial velocity show a much closer trend. At the apex, the shear layer thickness δ/D (0.3) becomes 10% smaller than in the circular case, while it is 17% larger at the notch.

The turbulent fluctuations also exhibit marked differences between the circular and the chevron jet exit. In Figure 4.19 axial and radial velocity fluctuations, respectively w'/W_j and v'_r/W_j, are compared along the jet axis. In the circular jet, the axial fluctuation increases rapidly, reaching a peak of 0.17 at Z/D=3.2. For a circular jet at *Re*=12,000, Zaman and Hussain (1980) associated the peak activity w'/W_j =0.11 at Z/D=3 to the pairing of vortex ring structures. At higher Reynolds (*Re*=55,000), the same authors (Hussain and Zaman, 1981) found w'/W_j >0.15 between Z=2.5 and 7 and observed that, when the jet was acoustically excited at the vortex pairing frequency, the axial fluctuation showed again a peak at the pairing position (Z/D=3). Also Ganapathisubramani *et al.* (2002) reported peak values of axial velocity fluctuations associated to the pairing phenomenon. Further downstream (Z/D>4, Figure 4.19), w'/W_j decreases to 0.11. Similar observation was reported by Yule (1978) who found that all the fluctuating velocity components of jet flows ranging between *Re*=9,000 to $2\text{x}10^5$ tend to a constant value of 0.15.

In the chevron case, the axial velocity fluctuation increases to 0.07 in the first three jet diameters and then it remains nearly constant, which means that, compared to the circular case, at *Re*=5,000, chevrons are responsible for a considerable reduction of axial fluctuations (up to 40%). For a compressible chevron jet at *Re*=$1.3\text{x}10^6$, Alkislar *et al* (2007) reported the tendency of the peak value of w' to an asymptotic value of 0.12, which, for Z/D>3, was 25% smaller than that of the circular jet.

In the circular jet, the radial turbulence intensity v'_r/W_j gradually increases along the jet axis reaching a nearly constant value of 0.09 between Z/D=6 and 7, which is in agreement with experiments at higher Reynolds number by Yule (1978), Hussain and Zaman (1981) and Alkislar *et al* (2007). In the chevron configuration, v'_r/W_j increases with the same rate of the circular jet until Z/D=3.5 and then levels out to 0.05 meaning of a radial turbulence suppression up to 25%.

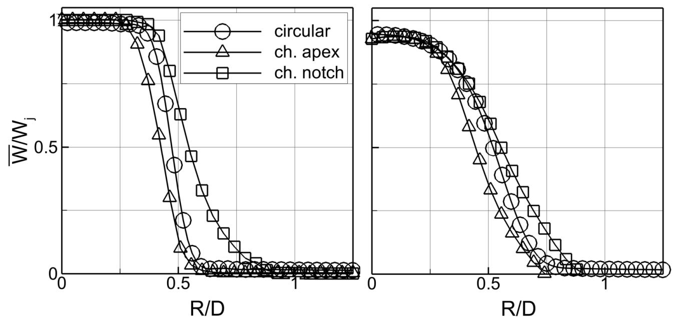

Figure 4.18 Mean axial velocity profiles at *Z/D*=1 (left) and *Z/D*=3 (right)

Cross-sectional profiles of w'/W_j, v'_r/W_j and transverse Reynolds stress $(w'v'_r)\ /W_j^2$ of the circular and chevron jet are compared in Figure 4.20. At *Z/D*=1 the turbulent fluctuations peak along the position of the shear layer. Axial velocity fluctuation w'/W_j is approximately 50% higher in the chevron nozzle than the circular, with peaks of 0.11, indicating a more rapid onset of the turbulent regime. In contrast, the radial fluctuation v'_r/W_j, is higher in the circular jet with peak value of 0.08, which is 8 times smaller at the chevron apex and 3 times at the notch. The presence of axisymmetric vortex structures causes radial fluctuations of amplitude comparable to those in the axial direction. At the notch axial and radial turbulence reach peaks of 0.1 and 0.03, respectively, at radial coordinate *R/D*=0.45. At the apex, peak values are observed at *R/D*=0.35, which also correspond to the radial position of maximum w'/W_j and v'_r/W_j in the circular jet. In the chevron jet, the transverse Reynolds stress $(w'v'_r)/W_j^2$ at the apex is one order of magnitude smaller than the peak activity at the notch (0.0033). Maximum of $(w'v'_r)/W_j^2$ =0.0012 is observed for the circular configuration.

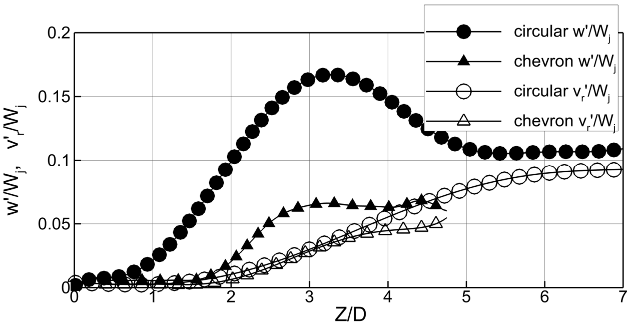

Figure 4.19 Axial and radial velocity fluctuations along the jet axis

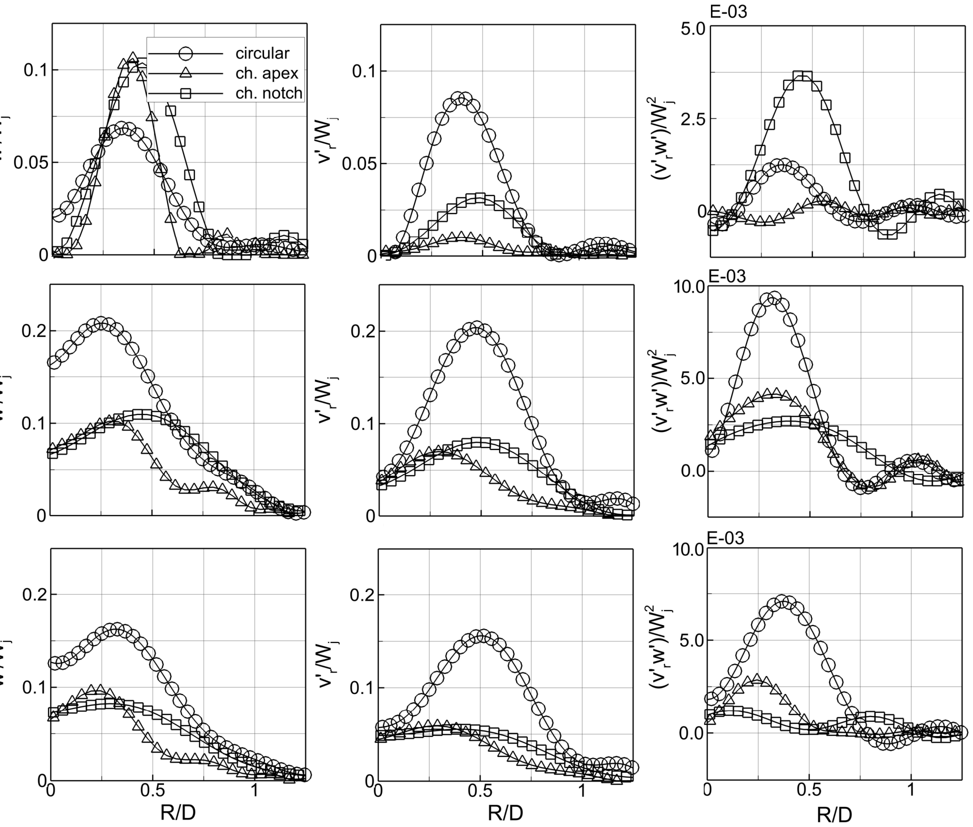

Figure 4.20 Axial and radial velocity fluctuation and transverse Reynolds stress at cross section *Z/D*=1 (top), *Z/D*=3 (centre), *Z/D*=4.5 (bottom)

An overall increase of the turbulent fluctuations is observed at *Z/D*=3 for both configurations. In the circular jet, axial turbulence shows a maximum (0.21) at *R/D*=0.25, 50% larger than in the chevron case. Profiles of w'/W_j along the apex and the notch directions show a similar trend reaching 0.1 at *R/D*=0.25. Further away from the axis the apex profile drops to 0.03 at *R/D*=0.6, whereas the notch profile reaches a peak (0.11) on the side of lower speed (*R/D*=0.4) and gradually decreases with a rate comparable to that of the circular case. For the radial velocity fluctuations v'_r/W_j, the circular configuration shows peak activity (0.2 at *R/D*=0.5) of intensity comparable to the axial peak turbulence. In the chevron case the maximum values of v'_r/W_j correspond to those of w'/W_j, although reduced by 60% with respect to peak activity found in the circular jet. Peaks in axial and radial turbulent intensity are associated with the vortex pairing process (Bradshaw *et al.*, 1963). The chevron apex profile shows a peak $(w'v'_r)/W_j^2=0.004$ in the region of higher velocity (*R/D*=0.3) that is 40% larger than that in the notch direction ($(w'v'_r)/W_j^2$ at *R/D*=0.4). However, when compared to the circular configuration, the apex and notch profiles feature maximum 50% and 70% smaller, respectively. Despite an overall increase of 30%, profiles of w'/W_j, v'_r/W_j and $(w'v'_r)/W_j^2$ shown in this investigation are in agreement with Hussain and Zaman (1981). On the other hand, no similarity is found with the cross-sectional profile at Z/D=2 shown in the investigation by Alkislar *et al*. (2007), which is ascribed to the considerable difference in Reynolds number.

At Z/D=4.5, axial and radial turbulence and Reynolds stress $(w'v'_r)/W_j^2$ of both configurations show a reduced peak activity when compared to what observed at Z/D=3. In the circular jet, turbulence peak activity is observed at R/D=0.3 for w' (0.17) and at R/D=0.5 for v'_r/W_j (0.16), corresponding to a 20% reduction compared to the absolute peaks at Z/D=3. A similar decrease is also found for the transverse Reynolds stress $(w'v'_r)/W_j^2$. Bradshaw *et al*. (1963) reported a similar shear stress profile at Z/D=4 with peak activity of 0.009 at R/D=0.5. In the chevron configuration, peaks of w'/W_j reduces of 5% at the apex and 20% at the notch in comparison to the values at Z/D=3. Radial turbulence, instead, drops of 25% at the apex and 45% at notch. The Reynolds stress $(w'v'_r)/W_j^2$ is attenuated too: at the apex, its peak decreases to 0.003 and is shifted towards the jet axis (R/D=0.25), while $(w'v'_r)/W_j^2$ globally drops of approximately 50%.

Chapter 5

3D organization and dynamics of turbulent jets

Violato D and Scarano F (2011) Three-dimensional evolution of flow structures in transitional circular and chevron jets. *Physics of Fluids*, 23, 124104, DOI 10.1063/1.3665141.

5.1 Introduction

The process of flow transition occurring in jets with laminar exit is governed by the growth of unstable modes introducing large-scale coherent flow structures. The transition pattern is reported to largely depend upon the geometry of the nozzle exit, Reynolds number and the nozzle exit velocity profile. In many engineering applications, passive mixing- and acoustic-control strategies are based on the alterations of the jet exit geometry. Compared to the circular jet, the mean entrainment rate increases in elliptic (Ho and Gutmark, 1987) and lobed jets (El Hassan and Meslem, 2010), while reduced acoustic emissions are characteristic of chevron jets (Bridges and Brown, 2004). The dynamical behavior of large-scale structures and their interactions in jets in the compressible regime is particularly relevant to aeroacoustics. However, the fundamental physical processes at the origin of sound generation are associated with the flow turbulence and its complex three-dimensional nature with energy distributed over a wide spectrum.

The role of large-scale flow structures in circular jet flows (see section 2.1.4 for a complete overview) can be studied with the direct numerical simulation (DNS) and large eddy simulation (LES) techniques (Freund, 2001; Boersma, 2005), which offer a formidable tool for the detailed analysis of unsteady flow behavior. More complex geometries such as lobed and chevron nozzles at high Reynolds numbers have been recently afforded with LES

(Xia *et al.*, 2009; Uzun and Hussaini, 2009), whereas investigations with DNS have mostly focused on the fundamental aspects of circular jets at low Reynolds number (Freund, 2001).

Experimental investigations on the organization of coherent flow structures require field measurement techniques such as flow visualization (Becker and Massaro, 1968; Crow and Champagne, 1971; Dimotakis *et al.*, 1983; Paschereit *et al.* 1992) and, in the last decades, particle image velocimetry (PIV). PIV measurements are typically conducted along streamwise or cross-sectional planes to investigate the unsteady behavior of the shear layer and the transition patterns (Liepmann and Gharib 1992; Ganapathisubramani *et al.*, 2002). Cross sectional measurements perpendicular to the jet axis enabled a quasi-3D representation of the turbulent coherent structures invoking Taylor's hypothesis in the fully developed turbulent region (Matsuda and Sakakibara, 2005). With high speed three-dimensional flow visualization technique and proper orthogonal decomposition, Lynch and Thurow (2009) showed vortex rings, azimuthal ring waves and streamwise vortex structure circular jets at *Re*=10,000. However, the corresponding vorticity pattern still remains to be ascertained by 3D velocimetry techniques.

Modifying the shape of the jet exit geometry has dramatic effects on the organization and stability of the shear layer with consequences on the entrainment rate, the spectral characteristics and the related acoustic emissions. Early investigations from Paterson (1984) showed that nozzles with a lobed exit generate coherent streamwise vortices emanating from the exit. Ho and Gutmark (1987) observed that an elliptic nozzle sheds vortices with pre-defined azimuthal distortion, producing an enhancement of the mean entrainment rate. Zaman and Raman (1997) placed tabs at the exit of turbulent circular jet reporting a marked loss of azimuthal coherence and the generation of pairs of streamwise vortices, which contribute to the increase of the lateral spreading of the jet along the direction orthogonal to the plane of the tabs. Streamwise structures are also formed in rectangular jets, as shown by the phased-locked stereo PIV measurements by Alkislar *et al.* (2003). More recently, El Hassan and Meslem (2010) studied the entrainment of circular and daisy-shaped orifice jets at *Re*= 3,600 using time-resolved stereo PIV and snapshot POD analysis. They concluded that, the daisy-shaped orifice jet undergoes earlier transition due to the generation of streamwise vortices, with a significant enhancement of the entrainment process. A similar methodology was adopted by El Hassan *et al.* (2011) who reported the influence of K-H structures on the instantaneous entrainment and net volume flux.

The idea that coherent flow structures of the jet near region are involved in the sound generation mechanism (Crow and Champagne, 1971; Michalke and Fuchs, 1975; Moore, 1977; Hileman *et al*, 2005; review article by Jordan and Gervais, 2008) suggests that a reduction of the flow azimuthal coherence, for instance by using chevrons, could promote local cancellation of large-scale acoustic fluctuations, thus leading to far-field acoustic suppression (Bradshaw *et al.* 1963). In a survey on chevron nozzles, Bridges and Brown (2004) used PIV and microphone measurements to investigate the relationship between flow-field patterns, far field noise and chevron geometric parameters. From the time-averaged properties, it emerged clearly that the chevron penetration depth influences the axial vorticity acting on the shear layer and, ultimately, leading to a faster decay of the core velocity. Furthermore, Opalski *et al.* (2005) investigated the relationship between the chevron geometry and flow characteristics, reporting extensive flow statistics at Mach numbers ranging between 0.9 and 1.5, for both cold and hot jets. Stereoscopic PIV was used to measure the three components of the mean and fluctuating velocity, as well as the axial vorticity and turbulent kinetic energy, over a region extending beyond 20 nozzle diameters downstream the nozzle, reporting the presence of well-defined streamwise vortices. The relation between the latter and the reduction of low-frequency acoustic emissions of 9-chevron configuration (Mach 0.9, Re=1.3x10^6) was investigated by Alkislar *et al.* (2007) who used stereoscopic PIV and microphone measurements. Numerical studies, making use of Reynolds-averaged Navier-Stokes (RANS) calculations in the near field have been performed by Thomas *et al.* (2001) and Birch *et al.* (2006). The latter showed that the chevrons generate axial vortices increase the mixing layer growth rate.

The experimental investigations of chevron jets have mostly focused on flow statistics with larger emphasis on the acoustic emissions rather than the description of instantaneous flow patterns. Nevertheless, as the acoustic production is strongly related to the large-scale flow motion (Michalke and Fuchs, 1975; Moore, 1977; Coiffet *et al.*, 2006), the observation of the temporal evolution of large-scales structures is of major importance to understand the physical mechanism behind the production of acoustic noise.

5.2 Objectives

In this chapter, it is investigated the impact of three-dimensional disturbances on the entire transition pattern in a jet at Re=5,000, with a comparative analysis between the circular and chevron configurations. The focus is placed upon the three-dimensional organization and dynamics of large-scale structures.

The main questions driving the need for time resolved 3D measurements (3C3D) are to what extent the nozzle geometry affects the instantaneous azimuthal coherence and what is the role of the instantaneous coherent fluctuations exhibited during the transition to the turbulent regime. Given the three-dimensional complex pattern of the flow, the above questions require a full 3D approach to produce an unambiguous description of the vortex topology. Moreover, the temporal resolution of the phenomenon allows addressing the growth and development of the coherent flow structures along with their mutual interaction.

For the circular jet, the focus is placed upon the dynamical evolution of the coherent vortex structures and their interaction in the transition from the axisymmetric to the three-dimensional regime, ultimately leading to the process of breakdown into coherent substructures by the end of the potential core (Hussain and Zaman, 1981). The analysis of the related 3D patterns is aided by proper orthogonal decompositions of velocity, vorticity and Lamb-vector.

The chosen 6-chevron jet configuration (see Figure 4.3) follows that proposed by Bridges and Brown (2004), who performed experiments at considerably higher Reynolds number. Despite not enabling quantitative comparisons with the work of Bridges and Brown (2004), the current investigation is intended to clarify some fundamental processes occurring in the process of transition to turbulence.

5.3 Unsteady behavior of the circular jet

The instantaneous flow organization is depicted in Figure 5.1. Toroidal vortices are clearly identified by iso-surfaces of azimuthal vorticity $\omega_\theta D/W_j$ whereas the three-dimensional flow structures are visualized by the axial and radial vorticity components $\omega_z D/W_\mathrm{j}$ and $\omega_r D/W_j$. The separate visualization of each component of the vorticity vector enables a more direct evaluation of the flow organization. In the region near to the nozzle exit (Z/D=0 and Z/D=5.5), the flow exhibits pulsatile motion (iso-surface W/W_j) driven by the shedding and pairing of toroidal vortices at Strouhal number $St=fD/W_j$=0.72 and 0.36, respectively. Vortex pairing is accompanied by to the growth of azimuthal instabilities and the formation of counter-rotating pairs of streamwise vortices of radial and axial vorticity (Violato and Scarano, 2011) that surround the jet shear layer. In the region beyond the end of the potential core (Z/D>6,Figure 5.1) vortex ring coherence is absent (Yule 1978; Hussain and Zaman, 1981) and the flow is mainly organized into streamwise vortex filaments. Liepmann and Gharib (1992) reported that the streamwise vorticity is the main factor controlling the entrainment process beyond the end of the potential core.

The development towards the three-dimensional regime occurs mostly downstream of the pairing region and is visualized by the normalized axial and radial vorticity components $\omega_z D/W_j$ and $\omega_r D/W_j$, which are plotted separately.

5.3.1 Axisymmetric regime

The most prominent unsteady feature exhibited by the circular jet flow is the shedding of axisymmetric vortices, due to the growth of Kelvin-Helmholtz instabilities. The shedding occurs regularly for a laminar jet exit as reported in previous works (Becker and Massaro 1958, Liepman and Gharib 1992). The instantaneous flow organization of the circular jet is illustrated in the temporal sequence of Figure 5.2 showing the Kelvin-Helmholtz vortices by iso-surfaces of azimuthal vorticity $\omega_\theta D/W_j$. The development towards the three-dimensional regime occurs mostly downstream of the pairing region and is visualized by the axial and radial vorticity components $\omega_z D/W_j$ and $\omega_r D/W_j$, which are plotted separately.

Figure 5.2 illustrates a temporal sequence of the flow field with snapshots separated by a time $\Delta t W_j/D$ =0.61, which corresponds to approximately half the shedding period. The iso-surface of normalized vorticity $\omega_\theta D/W_j$ =4 identifies axisymmetric vortices which are labeled with “3”, “4” and “5”. The formation of vortex ring structures in the near region of circular jets is well known from several studies conducted over a wide range of Reynolds number from 10^3 to 10^5 (Bradshaw *et al.*, 1963; Crow and Champagne, 1971; Winant and Browand, 1974; Yule, 1978; Liepman and Gharib 1992; Ganapathisubramani 2002). In the early investigations (Brown, 1935; Crow and Champagne, 1971) it was hypothesized that acoustical excitation at the natural shedding frequency or at the pairing frequency (Zaman and Hussain 1980) significantly stabilizes the temporal and spatial formation of the ring vortices, as well as the pairing. In later studies, this method enabled an accurate phase-locked analysis of the pairing mechanism (Schram, 2003).

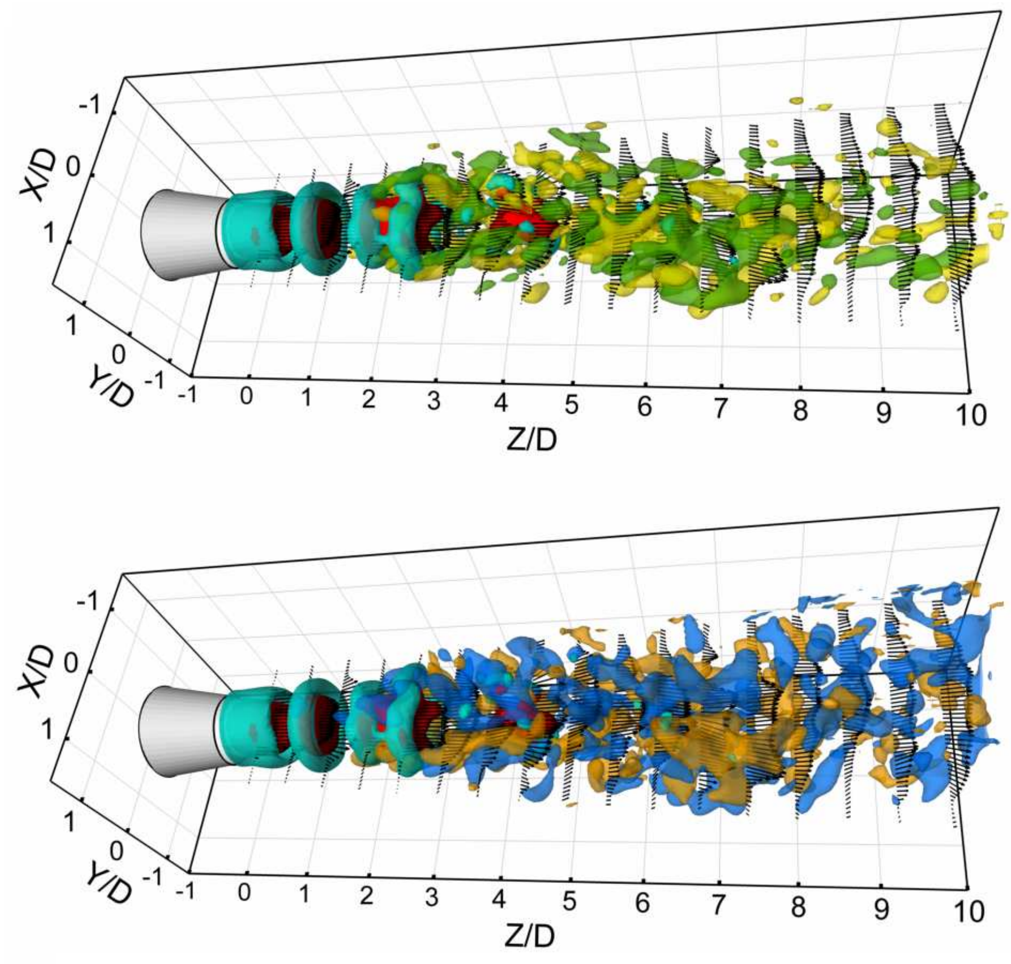

Figure 5.1 Instantaneous vortex pattern in the circular jet. Velocity vectors are shown 1 every 10 along Z on the axial plane $Y/D=0$. Iso-surfaces of axial velocity $W/W_j=1.05$ (red). Top: iso-surfaces $\omega_\theta D/W_j=4$ (cyan), $\omega_z D/W_j=-1.2$ (green) and 1.2 (yellow); bottom: iso-surfaces $\omega_\theta D/W_j=4$ (cyan), $\omega_r D/W_j=-1.2$ (blue) and 1.2 (orange)

In the present experiment, the shedding is observed to occur between $Z/D=2$ and 2.5, which agrees with the findings of Liepmann and Gharib (1992), and occurs at Strouhal number (*St*) of 0.72, which also agrees with the investigation on a non-excited jet at *Re*=5,000 by Becker and Massaro (1968). The spacing between the vortex rings appears to be half of the nozzle diameter. The pattern of dilated and compressed streamlines induced by the ring vortices, which are coplanar to the jet nozzle, is often referred to as varicose mode (Becker and Massaro, 1968). The core induces an outward flow at its leading edge and inward at the trailing one, which increases as the vortex ring grows and is convected downstream. At the leading edge of vortex rings, such as “3”, the radial velocity reaches peaks of 0.3 and the vorticity $|\boldsymbol{\omega}|D/W_j$ at the core is 6. This is shown in Figure 5.3 where the vortex rings are identified by iso-lines of λ_2-criterion.

In the range between 2.7 and 3.5 diameters, where axial and radial fluctuations exhibit maximum amplitude (w'/W_j=0.2 and v'_r/W_j =0.21, Figure 4.20), the vortices undergo pairing (Crow and Champagne, 1971; Hussain and Zaman 1981; Schram 2005) with a frequency *St*=0.36, half of that of shedding. The early study by Petersen (1978) on a circular jet at *Re*=5,000 showed that that vortex pairing takes place at 3 jet diameters downstream the nozzle exit with a frequency of *St*=0.55. With a tracking of the vortex cores in a *Re*=5,500 jet, Liepmann and Gharib (1992) showed that the first pairing usually takes place before *Z/D*=2.5 jet diameters. For acoustically excited jets at low Reynolds number, the phenomenon was studied for different Strouhal numbers ranging from 0.1 to 2. Crow and Champagne (1971) reported that vortices pair can be stabilized at *St*=0.3 for *Re*=10,500 to 100,000, whereas Zaman and Hussain (1980) and Schram (2003) investigated cases with a stronger excitation of the so called ‘jet-column mode’ at *St*=0.85 (*Re*=32,000) and 0.93 (*Re*=14,000), respectively. Based on phase locked PIV measurements, Schram (2003) found that, at *Re*=14,000, vortex pairing, or *leapfrogging*, occurred at *Z/D*≈1.8.

The flow induced by the preceding vortex (“4”) produces axial and inward accelerations in the jet core between vortex “3” and “4”. As a result, the pursuer vortex ("4") is stretched along the axis increasing in convective velocity to peaks of 0.49 and decreasing in diameter. On the other hand, due to the outward motion induced by follower (“4”), the preceding one (“3”) stretches positively while widening in diameter and its convection speed decreases to minima of 0.43. Because of the convective velocity difference, the distance between the two vortices gradually reduces and the pursuer vortex (“4”) pairs with the preceding one (“3”). During pairing, as expected from angular momentum conservation, the peak vorticity at the core of trailing vortex reduces. For the trailing vortex, $|\boldsymbol{\omega}|$ drops from 6 to 4, while it increases to 7.5 at the leading one (Figure 5.3). At the end of the pairing, the resulting vortex (“3+4”) has a convective velocity of 0.45 and induces a strong patch of flow at higher axial velocity of approximately 0.25 in the jet column. Axial velocity is maximum (W/W_j=1.15) within the vortex ("3+4") and it drops to W/W_j=0.7 in the upstream braid region. The induced outward motion, instead, gradually increases during pairing to absolute peak values of 0.35 at *Z/D*=3.

The convective velocity W_V of vortex rings at *Re*=14,000 was reported by Schram (2003) who found W_V/W_j=0.43 for the preceding vortex, W_V/W_j =0.64 for the pursuer and 0.61 for the merged. In this investigation, instead, vortices are detected by λ_2-criterion and convective velocities are evaluated at each time instant.

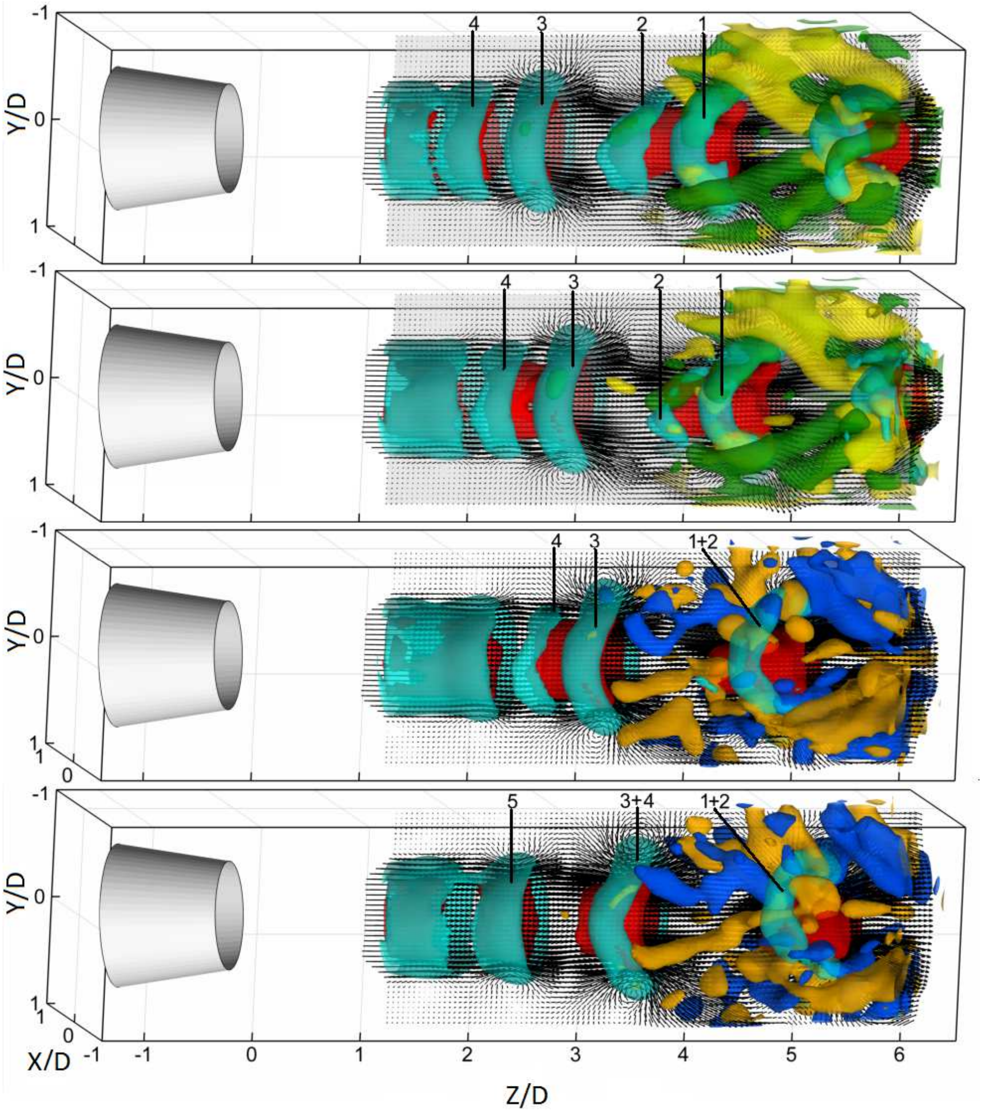

Figure 5.2 Time sequence visualization of the circular jet. Velocity vector slice in the axial plane. Iso-surfaces of axial velocity W/W_j=1.05 (red). In the first two snapshots, iso-surface of vorticity components $\omega_\theta D/W_j$ =4 (cyan), $\omega_z D/W_j$ =-1.2 (green) and 1.2 (yellow); in the last two snapshots: iso-surfaces $\omega_\theta D/W_j$ =4 (cyan), $\omega_r D/W_j$ =-1.2 (blue) and 1.2 (orange). Time separation between displayed images $\Delta t W_j/D$=0.61

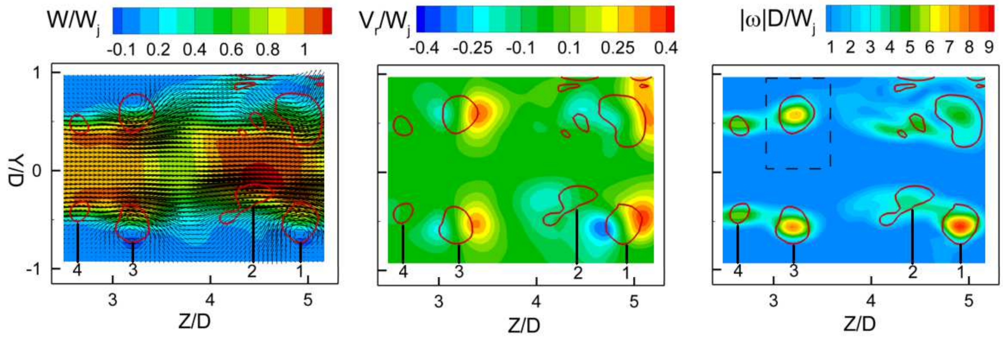

Figure 5.3 Iso-contour of axial W/W_j and radial velocity V_r/W_j (left and centre) and absolute vorticity $|\omega|D/W_j$ (right) on plane X/D=0, iso-line of $\lambda_2 D/W_j$=-0.5, $\Delta tW_j/D$=0.61

5.3.2 Azimuthal instabilities and streamwise vortices

During vortex pairing the flow pattern shows a significant growth of azimuthal instabilities (Widnall and Sullivan, 1973; Yule, 1978; Liepmann Gharib 1992). These may be further amplified during a second pairing event occurring downstream that leads to a further stretching of the distorted vortex. The growth of azimuthal modes of the ring vortices is accompanied by the formation of secondary vortices appearing just outside the region interested by the primary vortices. The secondary vortices develop in the streamwise direction (Bradshaw et al., 1964; Liepmann Gharib, 1992; Ganapatisubramani, 2002). Because only few studies are reported the use of volumetric approaches to investigate the three-dimensional flow behavior, the organization of vortices in the three-dimensional regime is not fully understood. Hori and Sakakibara (2004) reported that, in the self-preserving region of a circular jet at *Re*=1,000, the jet interface is dominated by structures with elongated loop-vortices. Lynch and Thurow (2009), by means of high speed three-dimensional flow visualization and proper orthogonal decomposition, showed azimuthal ring waves and streamwise instabilities in circular jets at *Re*=10,000.

After a vortex pairing event ($Z/D\approx 3$, Figure 5.2), the vortex rings gradually lose their axial symmetry, the azimuthal disturbances become more pronounced (see vortex “1” and “1+2”) and counter-rotating streamwise filaments of radial and axial vorticity are formed. To understand the relation between the growth of azimuthal instabilities and the gradual loss of symmetry, the temporal evolution of vortex “3+4” since its formation from vortex “3” and “4” is shown in Figure 5.4, where the iso-surface $\lambda_2 D/W_j$=-0.5 identifying the vortex is color coded with the radial velocity component V_r/W_j. When approaching the pairing (tW_j/D=0.82), although vortex “3” and “4” are axisymmetric, the radial velocity distribution on vortex “3” shows small irregularities with, respectively, peaks of 0.33 and -0.25 at the leading and trailing edge. After pairing (Z/D=4.25, tW_j/D=2.44), the axial symmetry of the vortex “3+4” begins to decay and V_r/W_j reaches 0.4 at the leading edge on four localized regions, which are labeled with “P”. At tW_j/D=4.08, these regions correspond to the peaks of azimuthal out-of-plane waves, whose amplitude doubles within $\Delta tW_j/D$=1.64. At tW_j/D=5.72, three smaller azimuthal waves “S” deform the vortex ring shape and the flow motion in the azimuthal direction becomes comparable to V_r/W_j (Figure 5.5). Comparatively, Yule (1978) reported the vortex rings gradually lose azimuthal coherence along the jet due to increasing circumferential velocity fluctuations. Vortex rings also undergo in-plane instability, which leads to the formation of 4 primary waves, which further rise between tW_j/D=3.28 and 4.92 (in case of vortex “3+4”), deforming the ring along two directions orthogonal to each other. This is illustrated in the temporal sequence of Figure 5.6 showing a top view of the vortex “3+4” leading edge.

Early observations of vortex azimuthal instabilities were reported by Widnall and Sullivan (1973) who studied the vortex rings formed through acoustical excitation of an air jet and reported that the number of modes increases with *Re*. The same authors observed 6 in-plane modes at Reynolds number (Γ/ν) of 5790, based on the circulation Γ of the primary structures, and found that the number of waves increases with the Reynolds number. In the current experiments, which are conducted at Reynolds number Γ/ν=5000 based on the circulation of the axisymmetric primary structures ($\Gamma = \int_S \omega_x dS$ and surface S defined by the dashed line of Figure 5.3), an average of 4 in-plane waves are observed.

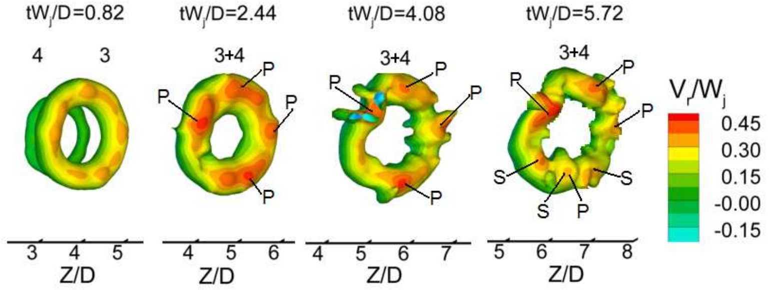

Figure 5.4 Time sequence visualization of vortex “3+4” identified by iso-surface $\lambda_2 D/W_j$=-0.5 color coded with radial velocity component V_r/W_j. Time separation between snapshots $\Delta tW_j/D$=1.64

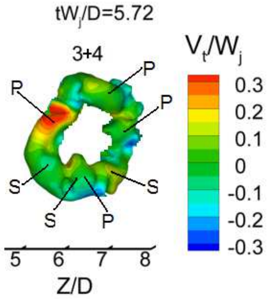

Figure 5.5 Iso-surface $\lambda_2 D/W_j$=-0.5 of vortex “3+4” color coded with tangential velocity V_t/W_j

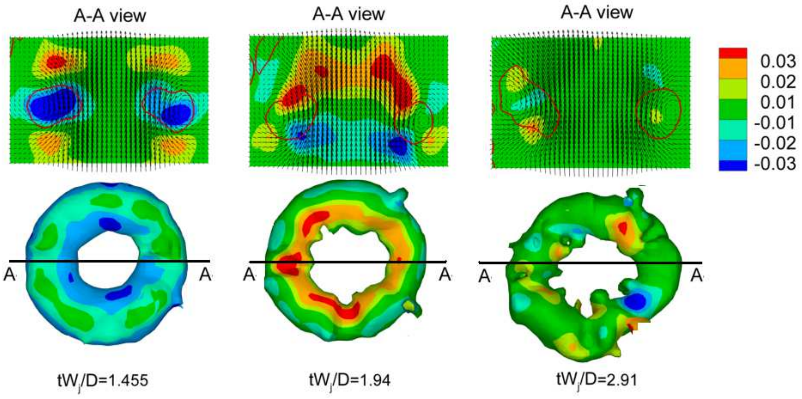

Figure 5.6 Visualization of vortex “3+4” at three subsequent time instants. (bottom) Top view of iso-surface $\lambda_2 D/W_j$=-0.5 color coded with $(dV_r/dt)D/W_j^2$ (left), $(dW/dt)D/W_j^2$ (centre), $(dV_\theta/dt)D/W_j^2$ (right). (top) Corresponding iso-contour on sectional plane A-A with iso-line $\lambda_2 D/W_j$=-0.5

The study of the dynamic flow properties associated with the large-scale structures must be based on data with time resolution satisfying, at least, the Nyquist criterion. With a 30Hz cross-sectional PIV acquisition, Liepmann and Garib (1992) showed the characteristic outward-inward radial motion induced by the passage of a vortex ring and evaluated the temporal evolution of the radial volume flux at different axial position. However, no information could be obtained on the related acceleration field, which is relevant to the decay of axisymmetric coherence of the vortex rings. Figure 5.6 illustrates the spatial distribution of the acceleration field associated with the vortex “3+4”. On the bottom, vortex “3+4” is shown at three subsequent time instants and is color-coded with the axial and radial components of the acceleration, respectively $(dW/dt)D/W_j^2$ $(dV_r/dt)D/W_j^2$, which are also shown as contour plot on the sectional plane A-A. Between the instant of vortex pairing and that at which vortex “3+4” travels outside of the measurement domain, the radial acceleration attains a maximum at tW_j/D=2.44, corresponding to the first instant after the pairing. Despite being smaller than 0.01 on iso-surface $\lambda_2 D/W_j$=-0.5 and negative (-0.03) in correspondence with the core, $(dV_r/dt)D/W_j^2$ reaches values larger than 0.02 on the trailing and leading edge of the vortex cores, with asymmetric pattern. Maximum activity of 0.03 is observed at the leading edge of the left core (see corresponding contour plot). Further downstream, while $(dV_r/dt)D/W_j^2$ shows an overall decrease, at tW_j/D=3.28, the axial acceleration $(dW/dt)D/W_j^2$ reaches peaks of 0.03 on the leading side of the vortex and minima of comparable magnitude at the trailing edge, with asymmetric pattern along the azimuthal direction. Instead, peaks of normalized tangential acceleration are observed when the vortex is very deformed, such as at tW_j/D=4.92 where $|(dV_\theta/dt)D/W_j^2|$ 0.03.

Between Z/D=4 and Z/D =5, a second pairing event is observed between vortex “1”, already resulting from a pairing, and vortex “2” (4<Z/D<5, Figure 5.2). The instabilities grown during the first pairing appear to be further amplified by the second pairing, due to the larger axial and radial velocity fluctuations induced by the preceding vortex (“1”). In the present case, one observes a tilting up to 30 degrees of the trailing vortex (“2”) while moving closer to vortex “1”. Temporal fluctuations at a half the frequency (St=0.16) are observed, which result in further amplification of the pulsating motion. The associated radial velocity reaches peaks of 0.38 and axial velocity shows instantaneous fluctuations ranging from 0.7 in the braid region (3.5<Z/D<4) and 1.25 within “1+2” (4.25< Z/D <4.75) (Figure 5.3). The radial turbulence associated with the region of second pairing (4< Z/D <5) increases to 0.08 along the jet axis (Figure 4.19), although its peak activity decreases to 0.15, corresponding to a 25% drop compared to the first pairing (Z=4.5, Figure 4.20). Here the axial turbulence w'/W_j reduces, without any relative maximum of along the jet axis (Figure 4.19), as it was instead observed for the first pairing. The reduction of the axial and radial turbulence accompanied by instantaneous fluctuation w'/W_j and v'_r/W_j that are comparable or even larger than those found at the first pairing, can be due to the lower temporal periodicity of second pairing. In addition, the flow three-dimensionalities observed in this region tend to turn axial and radial fluctuations into the tangential ones. At Z/D=5, these are associated with tangential turbulence v'_θ/W_j =0.12.

Secondary flow instabilities are organized in counter-rotating pairs of streamwise vortices, similarly to the streamwise structures of mixing layers (Bernal and Roshko, 1986), that contribute to both axial and radial vorticity given their inclination angle relative to the jet axis (iso-surface $\omega_z D/W_j$ and $\omega_r D/W_j$, Figure 5.2) . The temporal sequence of Figure 5.7 illustrates the characteristic motion of the longitudinal filaments of $\omega_z D/W_j$ =-1.2 (green) and 1.2 (yellow) during the passage of vortex ring “3+4”. At Z/D=3.5 (tW_j/D=2.44), the streamwise structures are distributed around the vortex ring with an angle of approximately 30-40 degrees to the jet axis (Bradshaw *et al.*,1963). The formation of streamwise instabilities is however observed further upstream, in the flow region dominated by the primary instabilities (Liepmann and Gharib, 1992). In the braid region at Z/D=2.5, for instance, they reach peaks of absolute axial vorticity of 0.4. Due to the flow motion induced by the ring vortex, streamwise structures move outward at the leading edge of the ring and inward at trailing edge, leading to a configuration where the filaments wrap the vortex ring (tW_j/D=4.92). The presence of longitudinal coherence inclined to the axis was reported in flow visualization investigations in circular jet flows at 2,500<Re<80,000 (Bradshaw *et al.,*1963; Yule, 1978; Dimotakis *et al*. 1983, Lynch and Thurow, 2009). The early study by Bradshaw *et al*. (1963) suggested that the augmentation of streamwise coherence by artificial means, such as lobed nozzle or ejector shroud surrounding the nozzle could be used to increase mixing properties and to reduce the acoustic emission. Yule (1978) and Liepmann and Gharib (1992) observed that such structures develop in the braid region and accompany the pairing of the rings, and the latter authors added that the streamwise structures move in and out following the radial motion induced by the approaching vortex rings.

The distribution and strength of the vortex filaments of $\omega_z D/W_j$ at the leading and trailing edge of the vortex ring, as well as at X-Y ring mid plane, are illustrated in Figure 5.8 showing cross-sectional contours of axial vorticity of vortex “3+4” at tW_j/D=2.44 and tW_j/D=4.92. At tW_j/D=2.44, on the cross-section at the vortex ring trailing edge (Z/D=3.2), a total of 11 streamwise instabilities (Liepmann and Gharib, 1992) with axial vorticity magnitude $0.6<|\omega_z D/W_j|<1.2$ occupy radial distance (R/D=0.6). As shown by the velocity vectors, they are subjected to a rather uniform radial inward motion of 0.3 that is induced by the ring vortex. The difference in the number of waves between the azimuthal instability (4 primary waves) and the streamwise structure (11) suggests that these do not develop from the primary ring instabilities but are rather formed in the braid region (Liepmann and Gharib, 1992). The cross-sectional plot at Z/D=3.5 illustrates the 4 longitudinal pairs (“STP”) located in the vicinity of the external edge of the ring, with magnitude ranging from 0.5 to 1.5. Due to the outward flow induced by the ring, the pairs are ejected towards larger radial distances (R/D=0.8). At leading edge, the same 4 pairs of streamwise structures are immersed in the outward radial motion induced by the ring (V_r/Wj=0.33).

At tW_j/D=4.92, the absolute axial vorticity of the streamwise structures increases up to 3 and remains uniform upstream (Z/D=4.9) and downstream (Z/D =5.5) the ring vortex. Due to the reduced azimuthal coherence of the flow, as it can be noticed comparing the velocity vectors at tW_j/D=4.92 with tW_j/D=2.44, the streamwise filaments no longer occupy a constant radial position and the visual identification of counter-rotating pairs becomes more difficult. The average number of longitudinal structures (“ST”) with a value of $|\omega_z D/W_j| > 1.5$ is 16, which is larger in comparison to the upstream location Z/D = 3.2.

The latter observation does not seem to agree with the findings by Liepmann and Gharib (1992) who, based on LIF images, reported that the number of longitudinal structures decreases with the downstream distance. At Z/D=5.2, the number of axial swirl peaks associated with the primary structures is larger in comparison to what observed at tW_j/D=2.44. On average, a total of 11 peaks with $|\omega_z D/W_j|$>2.5 are found. In addition, compared to the cross sections Z/D=4.9 and 5.2, the activity of $|\omega_z D/W_j|$ shows the tendency to drop at the vortex ring leading edge (Z/D=5.5).

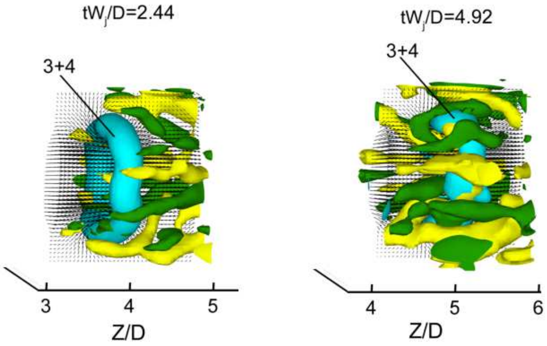

Figure 5.7 Time sequence visualization of iso-surface $\omega_\theta D/W_j$ =4 (cyan), $\omega_z D/W_j$ =-1.2 (green) and 1.2 (yellow)

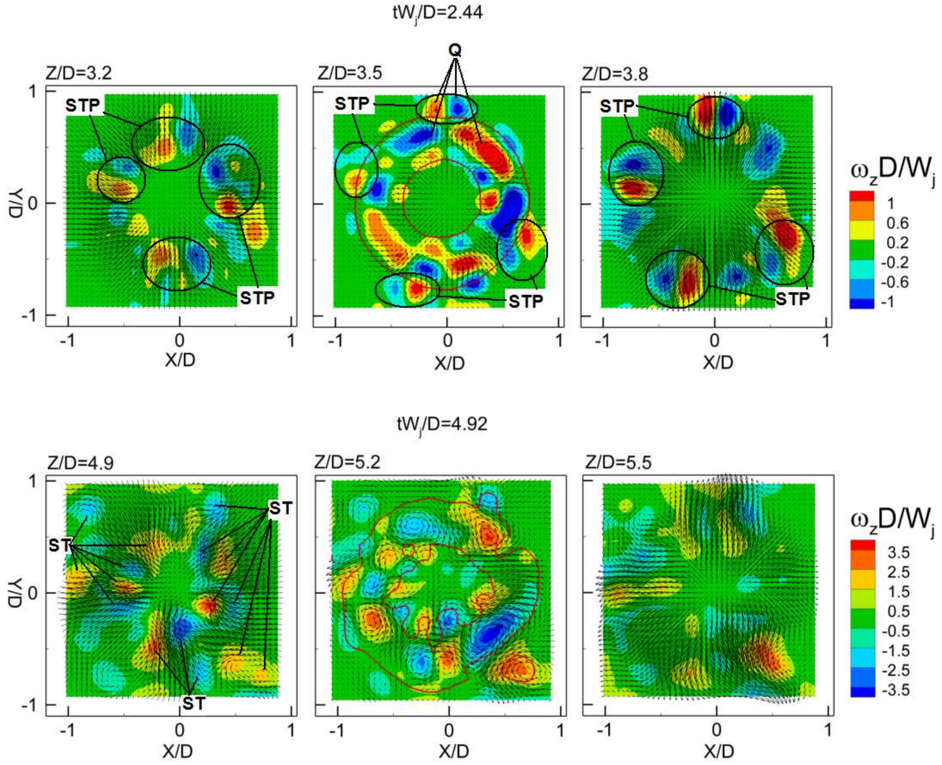

Figure 5.8 Cross-sectional iso-contours of axial vorticity $\omega_z D/W_{j.}$ at t=2.44 (top) and t=4.92 (bottom). X-Y projection of velocity vectors and with iso-line $\lambda_2 D/W_j$ =-0.5

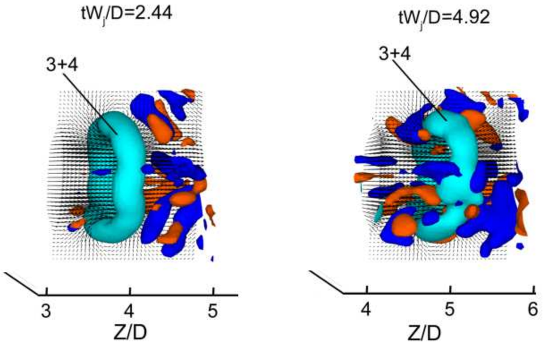

Figure 5.9 Time sequence visualization of iso-surface $\omega_\theta D/W_j$ =4 (cyan), $\omega_r D/W_j$ =-1.2 (blue) and 1.2 (red)

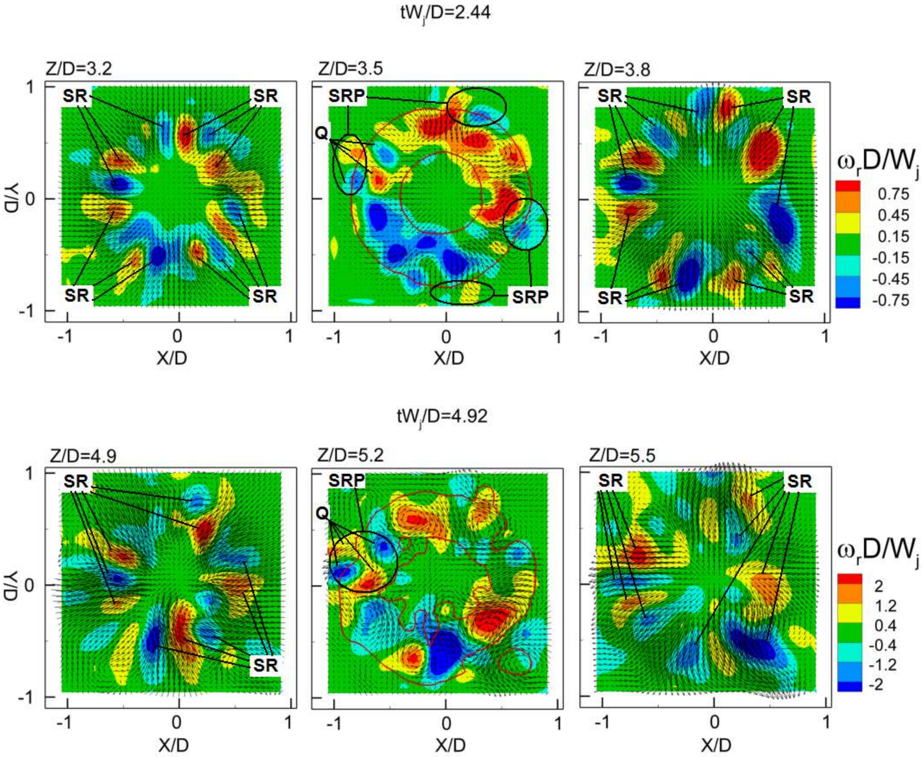

Figure 5.10 Cross-sectional iso-contours of radial vorticity $\omega_r D/W_j$ at tW_j/D=2.44 (top) and tW_j/D=4.92 (bottom). X-Y projection of velocity vectors and with iso-line $\lambda_2 D/W_j$ =-0.5

A detail of the streamwise radial coherence is illustrated in Figure 5.9 where two subsequent snapshots show that, similarly to "ST" vortices, the radial filaments "SR" move in the radial direction under the entrainment of vortex ring "3+4". At the leading edge of vortex "3+4", the filaments are distributed around the ring with an angle of approximately 30-40 degree to the jet axis (Z/D=3.5, tW_j/D=2.44). They are formed in the region of vortex rings, in conjunction with the growth of vortices "ST" (Z/D=2.5), although showing peaks of radial vorticity 50% larger than those of the axial vorticity. The investigations by Yule (1978) and Liepmann and Gharib (1992) reported the presence of streamwise vortices "ST", whereas they did not observe any streamwise coherence of radial vorticity, perhaps because the observations were only based upon cross-sectional measurements.

The organization and strength of the vortex filaments of $\omega_r D/W_j$ ("SR") across "3+4" are illustrated in Figure 5.10. At tW_j/D=2.44, on the cross-section at the vortex ring trailing edge (Z/D=3.2), a total of 13 elements with radial vorticity magnitude $0.45<|\omega_r D/W_j|<0.75$ are located at the same radial position of "STP" vortices (R/D=0.6) and they are subjected to a rather uniform radial inward motion induced by the ring (V_r/W_j=0.3). Unlike "ST", "SR" vortices do not have a clear organization in pairs. The difference in the number of waves between azimuthal instability (4 primary waves) and the number of "SR" vortices (13) suggests that these are formed in the braid region and most likely they do not develop from the primary ring instabilities. At the vortex cross-section (Z/D=3.5), pairs of "SR" ("SRP") are observed around the vortex ring "3+4". This shows regions with alternating sign of ω_r, which may indicate that mode k=1 is energetic. Between Z/D=3.2 and 3.5, the outward radial motion at the ring leading edge leads to the radial displacement of "SR" vortices from R/D=0.6 to R/D=0.8. At tW_j/D=4.92, the absolute axial vorticity of the streamwise structures increases of three times. However, the reduced azimuthal coherence of the flow results in "SR" vortices occupying a scattered position, as observed for the "ST" filaments.

5.3.3 The influence between azimuthal instabilities and streamwise vortices

The presence of 4 primary azimuthal waves and 4 streamwise vortex pairs of axial vorticity suggests a possible influence between the ring vortex and "STP" vortices. At Z/D=3.5 (Figure 5.8), the spatial modes of axial vorticity $\omega_z D/W_j$ in the azimuthal direction are extracted for a radial position corresponding to the vortex ring (R/D=0.6) and to the streamwise structures (R/D=0.85). The corresponding modal spectra and the phase shift response are shown in Figure 5.11. The most energetic modes of the vortex rings are observed at low wave number k, such as k=2 ("saddle" mode), 3 and 4. In the streamwise vortex, the energy is distributed over a larger range with peaks at k= 4, 9, 10 and 12. Nearly constant absolute phase shift $|\Delta\Phi|= \pi$ is found between the ring and streamwise vortices for wave numbers k=2, 3, 4, 5, 6, 7, 8 and 9. The high energy content at k=4 that is observed in both the spectra indicates the preferred mode of influence of streamwise pairs on vortex rings. The axial vorticity that is induced on the vortex ring is staggered in phase opposition, forming quadruplets (“Q”, Figure 5.8). At such locations the vortex is tilted leading to the growth of a primary hump.

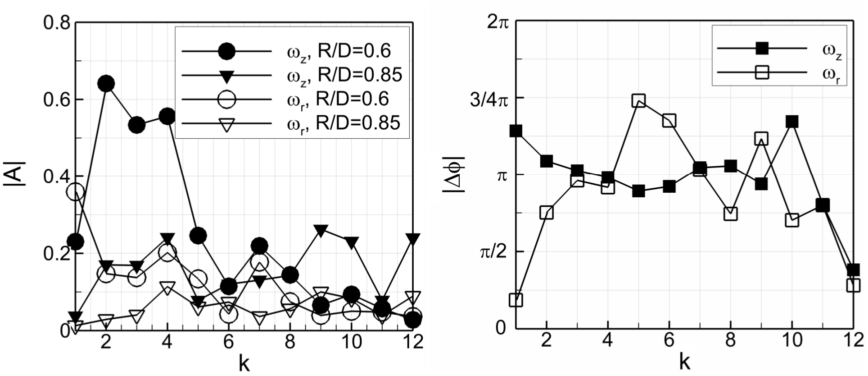

Figure 5.11 Azimuthal modal spectra of axial and radial vorticity (left) and phase shift (right)

5.3.4 The process of vortex ring breakdown

The spatio-temporal evolution of a selected event during the breakdown of a toroidal vortex is shown in the temporal sequence of Figure 5.12 where the iso-surface $\lambda_2 D/W_j$ =-0.8 identifying the vortices are color-coded by the instantaneous axial velocity W/W_j. To facilitate the visualization, iso-surfaces are mapped between R/D=0 and R/D=1. The decay of the azimuthal coherence of toroidal structures begins after pairing (Violato and Scarano, 2011) with the growth of four in-plane (see label “P”, tW_j/D=0) and four out-of-plane azimuthal waves. With the growth of in-plane azimuthal instabilities, portions of the vortex ring (see labels “P”) are tilted inward and stretched towards the jet axis ($0<tW_j/D<1.26$), where the axial velocity is larger (W/W_j=1). Due to the asymmetric distribution of W, regions “P” are then ejected and tilted along the jet axis ($1.68<tW_j/D<2.1$), producing axial stretching and, ultimately, the disruption of the toroidal shape (Z/D=5.8 and 6.5). Bogey *et al.* (2003) associated such transient event to a possible mechanism of acoustic generation. By the end of the potential core, the characteristic axial and radial velocity fluctuations are w'/W_j =0.16 and v_r'/W_j =0.14, 30% smaller than those observed for the pairing process (Figure 4.16). In contrast, azimuthal velocity component reaches peak activity of 0.11, which is about twice that at pairing. Vortex portions originated from low-axial velocity regions gradually disrupt into smaller structure of “C” shape (see label “C”, $1.68<tW_j/D<2.52$), whereas those originated from region “P” form an angle of 30-45 degrees with the jet axis ($2.52<tW_j/D<2.94$).

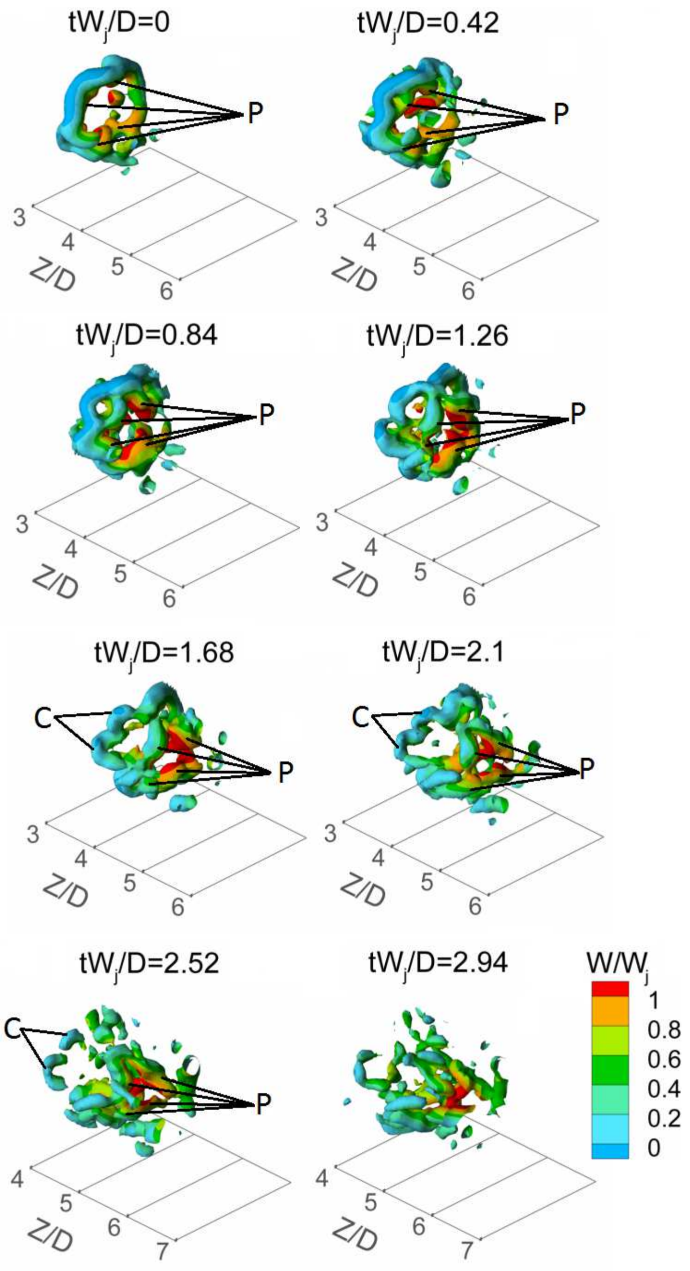
tW$_j$/D=0
tW$_j$/D=0.42
tW$_j$/D=0.84
tW$_j$/D=1.26
tW$_j$/D=1.68
tW$_j$/D=2.1
tW$_j$/D=2.52
tW$_j$/D=2.94
P
C
Z/D
3
4
5
6
7
W/W$_j$
1
0.8
0.6
0.4
0.2
0

a) Azimuthal waves inception

b) Induced axial velocity

c) Breakdown of azimuthal coherence

d) Turbulent engulfment

Figure 5.12 Time sequence visualization of vortex ring breakdown. Iso-surface $\lambda_2 D/W_j$ =-0.8 color coded with axial velocity component W/W_j. Time separation between snapshots $\Delta tW_j/D$=0.42

The evolution of the breakdown hereby reported agrees with the early conjectures by Hussain and Zaman (1981) who described that toroidal vortices develop azimuthal lobes and disrupt into coherent substructures by the end of the potential core.

5.3.5 Large-scale coherence beyond the potential core

Downstream the potential core ($7<Z/D<10$), the three-dimensional regime exhibits, as most recurrent pattern, vortex filaments with scattered orientation (Figure 5.13). The decay of the vortex coherence is faster between $0<R/D<0.8$ where the axial velocity is characterized by flow patches of maximum axial velocity $W/W_j=0.6$ (Figure 4.18), and velocity fluctuations w'/W_j, v_r'/W_j and v_t'/W_j of comparable magnitude (0.1-0.12, Figure 4.16). By contrast, in the periphery of the jet ($0.8<R/D<1.6$), where fluctuations are about 50% smaller, "C" structures ($tW_j/D=0$) tend to re-organize into filaments "VF" ($tW_j/D=1.68$). "VF" structures are typically oriented along the azimuthal direction and have a characteristic length ranging between 1 to 2 jet diameters, based on iso-surface $\lambda_2 D/W_j=-0.5$. The advection velocity along the axial direction is 0.2. As shown in Figure 5.13(c and d), they engulf outer fluid on the trailing side and eject on the leading one, with peaks of instantaneous radial velocity of 0.1 (Yule, 1978). The typical life-time of the "VF" is $\Delta tW_j/D=6$ after which they break-up into sub-structures "VFsub" ($tW_j/D=6.3$) between $Z/D=9$ and 10. Yule (1978) reported the presence of vortices with similar patterns up to 5 jet diameters downstream the transition.

The normalized axial, radial and tangential flux associated with the "VF" structure can be defined as

$$\left\{Q_w, Q_r, Q_\theta\right\} = \frac{1}{D^2}\int_S \left\{W/W_j\,\hat{e}_w, V_r/W_j\,\hat{e}_r, V_\theta/W_j\,\hat{e}_\theta\right\}\cdot\overline{dS}\,, \tag{5.1}$$

where S is the surface of the volume containing the "VF" vortex, $\hat{e}_w$, $\hat{e}_r$, and $\hat{e}_\theta$ denote the unit vector in the axial, radial and tangential direction, $\overline{dS}$ is the vector normal to S. On average, the flux related with "VF" shows that the axial and the radial components have the same magnitude and opposite sign ($Q_w=0.075$; $Q_r=-0.075$), whereas the tangential component is one order magnitude smaller. Compared to Liepmann and Gharib (1992), who ascribed to streamwise vorticity the major role in the entrainment of the flow beyond the end of the potential core, the observations on "VF" filaments hereby reported provide a more specific characterization of the vortex pattern involved in such entrainment.

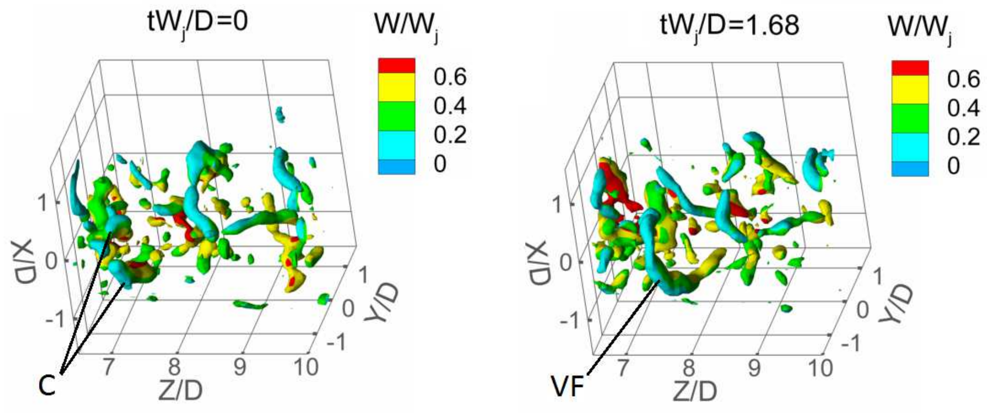
tW_j/D=0
W/W_j
0.6
0.4
0.2
0
X/D
Z/D
Y/D
C
tW_j/D=1.68
W/W_j
VF

a) C-structures

b) Vortex filament formation

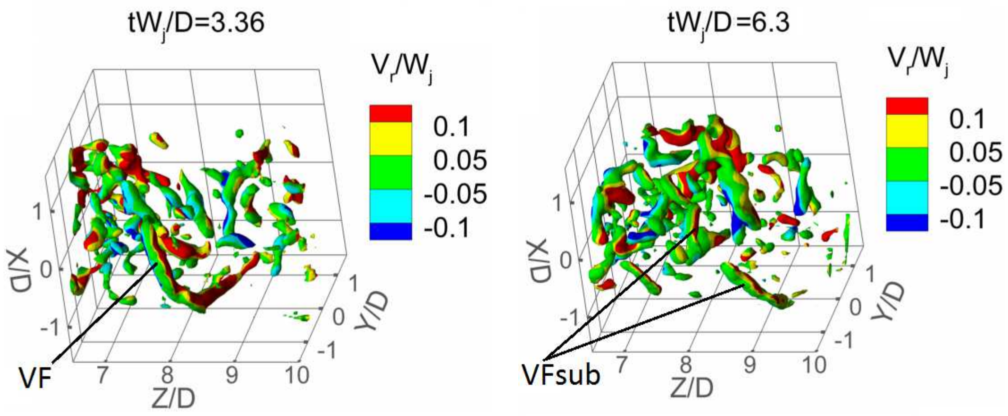
tW_j/D=3.36
V_r/W_j
0.1
0.05
-0.05
-0.1
X/D
Z/D
Y/D
VF
tW_j/D=6.3
V_r/W_j
VFsub

c) Vortex filament advection

d) Vortex filament breakdown

Figure 5.13 Time sequence visualization of vortices after breakdown. Phenomenon of *C-vortex connect* and subsequent *filament tearing*. Iso-surface $\lambda_2 D/W_j$=-0.5 color coded with W/W_j (a and b) and V_r/W_j (c and d)

5.4 3D POD analysis of circular jet

Snapshot-POD (Sirovich, 1987) is applied to inspect the large-scale features developing in the jet with attention to the three-dimensional regime by the end of the potential core. The analysis is conducted on fields of velocity (**V**), vorticity (**ω**) and Lamb vector (**L**) fields as well as second time derivative of the Lamb vector $d^2\mathbf{L}/dt^2$, which will be discussed in the next chapter (Section 6.4). The decomposition of velocity, vorticity and Lamb vector fields is based on a sequence of 500 uncorrelated snapshots, which corresponds to an observation length of 1000 jet diameters.

The distributions of energy across the three-dimensional POD modes of velocity, vorticity, Lamb vector and its second time derivative fields are illustrated in Figure 5.14 together with the cumulative energy distributions. Mode #1 and 2# of the velocity correspond to 7.5% and 7.4% of the total *kinetic energy* (eq. (3.31)), whereas less *enstrophy* (eq. (3.32)) corresponds to vorticity mode #1 and #2 (5.7% and 5.6%). The Lamb vector is decomposed with a slightly higher efficiency, where mode #1 and 2# respectively capture 8.6% and 8.3% of the total *Lamb energy* (eq. (3.33)).

The spatial organization of the first 10 dominant POD modes of velocity (Figure 5.15 and Figure 5.16), vorticity (Figure 5.17 and Figure 5.18), Lamb vector (Figure 5.19 and Figure 5.20) and Lamb vector second time derivative (Figure 6.7) are described and the related information on the characteristic frequencies are extracted from the spectrum of the time coefficients $a_k(t)$ (eq. (3.26)) of the modes. The peak frequencies of velocity, vorticity, Lamb vector are summarized in Figure 5.21 while those of the Lamb vector second time derivative are discussed in section 6.4 (Figure 6.9).

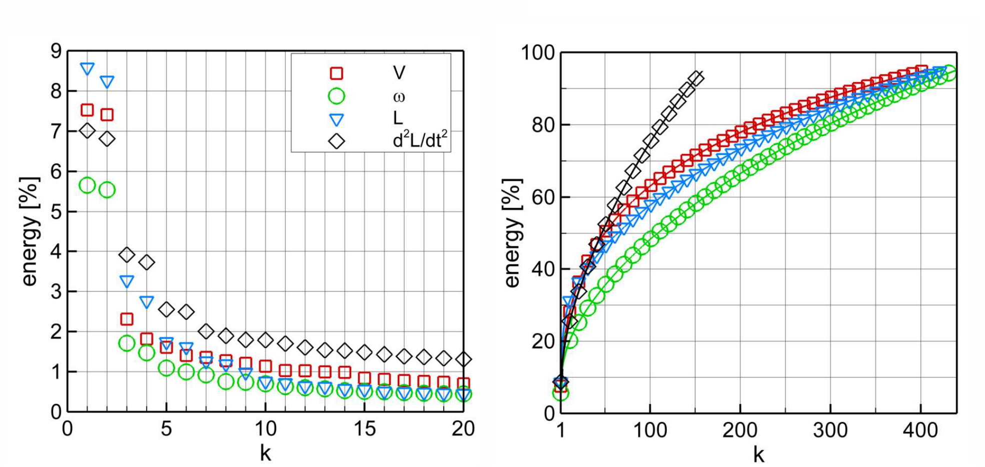

Figure 5.14 Left: energy distributions across first 20 modes of velocity **V**, vorticity **ω**, Lamb vector **L** and second time derivative of the Lamb vector $d^2\mathbf{L}/dt^2$; right: cumulative energy distributions (symbols are shown 1 every 10). Note that the observation length employed for $d^2\mathbf{L}/dt^2$ decomposition is shorter compared to **V**, **ω** and **L** as discussed in section 6.4

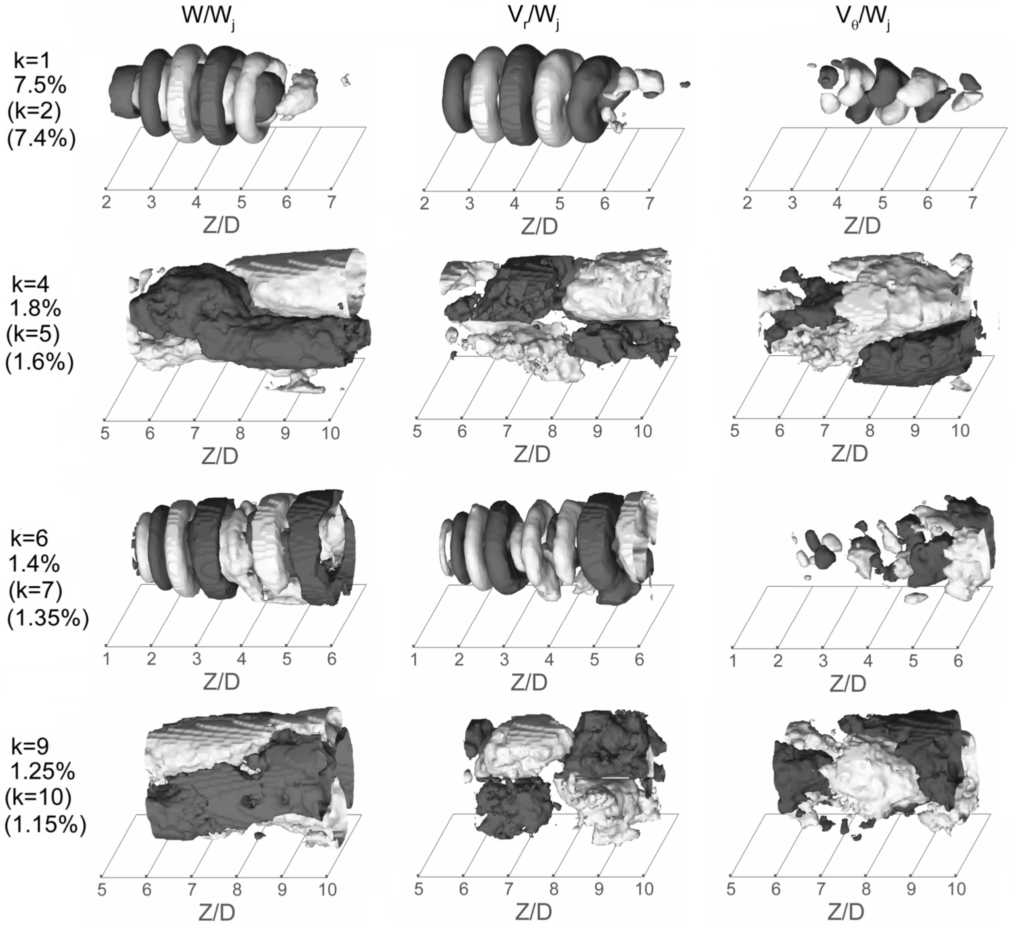

Figure 5.15 POD modes of velocity describing travelling waves. Between brackets mode number and energy of the coupled mode. Positive (light grey) and negative (dark grey) iso-surfaces of W/W_j (left), V_r/Wj (center) and V_θ/Wj (right)

5.4.1 Decomposition based on velocity

The POD method is now applied to the 3D velocity fields. Figure 5.14 shows that about 50% of the kinetic energy is captured by the first 50 modes, which is far less than the 350 modes reported by Jordan *et al.* (2007) for a compressible jet at *Re*=3,600. In the first 10 velocity modes, which correspond to 27.5% of the kinetic energy, there are pairs (#1 and #2, #4 and #5, #6 and #7, #9 and #10) phase shifted of $\pi/2$ in the axial direction describing travelling waves (Figure 5.15). Non-travelling (presumably pulsatile) modes (#3 and #8) are instead illustrated in Figure 5.16. For conciseness, Figure 5.15 shows the iso-surfaces of W/W_j,V_r/W_j, and V_θ/W_j of only one mode for each pair. Mode #1 and #2 describe travelling toroidal vortices (Bi *et al.* 2003; Shinneeb *et al.*, 2008; Jung *et al.* 2004; Lynch and Thurow, 2009) that are formed after pairing and have characteristic Strouhal number *St*=0.36 (Figure 5.21).

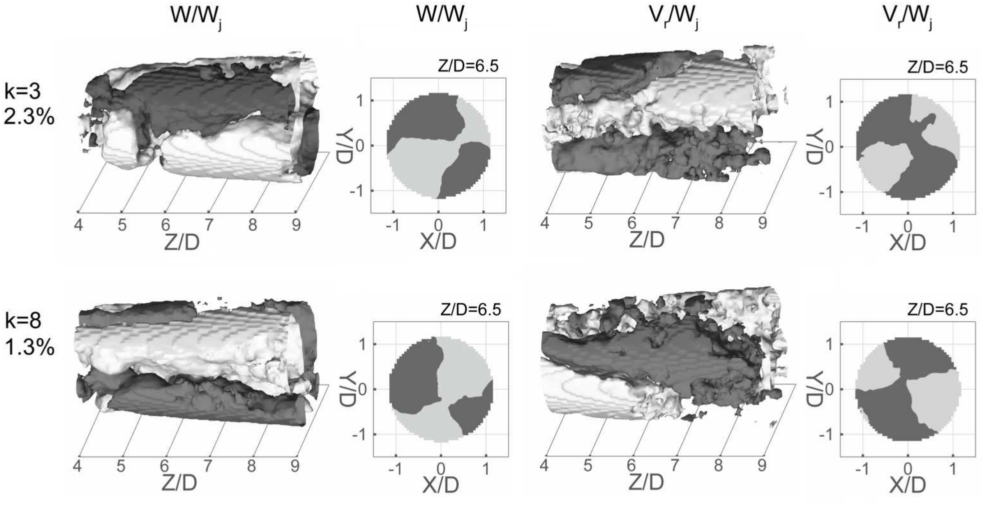

Figure 5.16 POD modes of velocity describing pulsatile motions. Positive (light grey) and negative (dark grey) iso-surfaces of W/W_j (left), Vr/W_j (right) and cross-sectional iso-contours

The axial velocity component shows an pulsatile motion along the axial direction, whereas the azimuthal velocity reveals the presence of “periodic” twisting that develop in the inner region of the vortices. In mode #4 and #5, across the end of the potential core ($6<Z/D<8$), the intertwining between the region of positive and negative W/W_j indicates a *helical* motion. This was previously reported by Iqbal and Thomas (2007) who observed it beyond the end of the potential core. A similar observation was made by Lynch and Thurow (2009). Further downstream ($Z/D>8$), instead, W/W_j describe a *flapping* motion (Lynch and Thurow, 2009). The aforementioned motions are coupled with a *wave-like* motion (V_r/W_j) and a periodic *twisting* (V_θ /W_j) that have 4 jet diameters of spatial wavelength. Mode #4 and #5 are associated with a primary frequency *St*=0.3 and a secondary of 0.7. Mode #6 and #7 describe travelling toroidal vortices after shedding, which are periodically twisted between Z/D=3 and Z/D=6 with a wavelength of 1 jet diameter (*St*=0.72). Mode #9 and #10 show two filaments of positive and two filaments of negative W/W_j, that are phased shifted of π/2 on the plane normal to the jet axis and develop downstream the end of the potential core. They describe a *precession* motion. This is coupled with a *wave-like* motion (V_r/W_j) and a periodic *twisting* (V_θ/W_j) that are similar to those observed in mode #4 and #5. Primary and secondary

Strouhal peaks of pair #9-#10 are 0.36 and 0.7 Mode #3 and mode #8 are characterized by the axial development of four filaments of W/W_j and V_r/W_j, two of positive sign and two of negative sign. They describe axial and radial pulsatile motions ($4<Z/D<9$) with a phase shift of about 45 degrees in the azimuthal direction (Figure 5.16) and a discrepancy in the associated energy of about 1%. Moreover, while they are characterized by similar secondary Strouhal peak (0.7), they differ for the primary one.

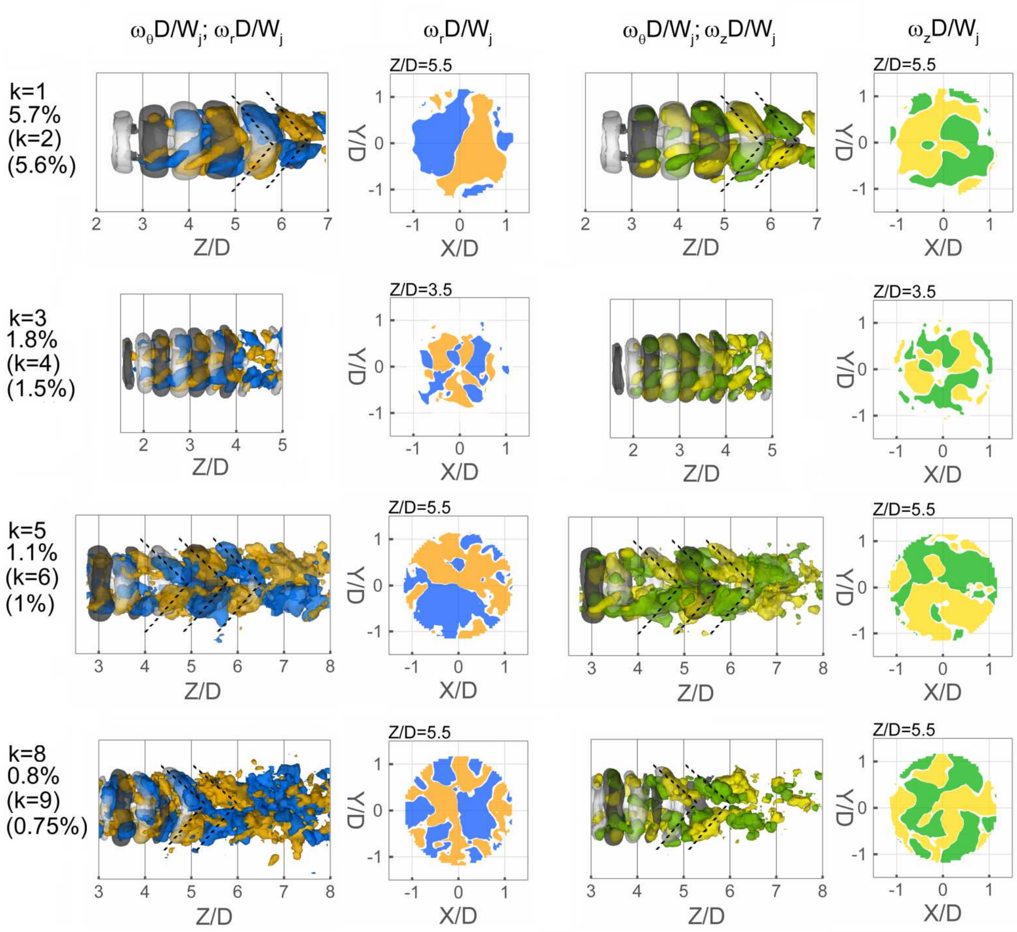

Figure 5.17 POD modes of vorticity describing travelling waves. Between brackets mode number and energy of the coupled mode. Left: iso-surfaces of $\omega_\theta D/W_j$ (positive in light grey; negative in dark grey) and $\omega_r D/W_j$ (positive in orange and negative in blue) and cross-sectional iso-contour of $\omega_r D/W_j$. Right: iso-surfaces of $\omega_\theta D/W_j$ (positive in light grey; negative in dark grey) and $\omega_z D/W_j$ (positive in yellow and negative in green) and cross-sectional iso-contour of $\omega_z D/W_j$ with iso-line $\omega_\theta D/W_j$

5.4.2 Decomposition based on vorticity

The POD method applied to the vorticity fields highlights the dynamical organization of coherent vortices. In the first 10 vorticity modes, which correspond to 20% of the flow enstrophy, there are pairs (#1 and #2, #3 and #4, #5 and #6, #8 and #9) phase shifted of $\pi/2$ in the axial direction describing travelling waves. For conciseness, only one mode for each pair is reported in Figure 5.17. Pulsatile modes (#7 and #10) are instead illustrated in Figure 5.18.

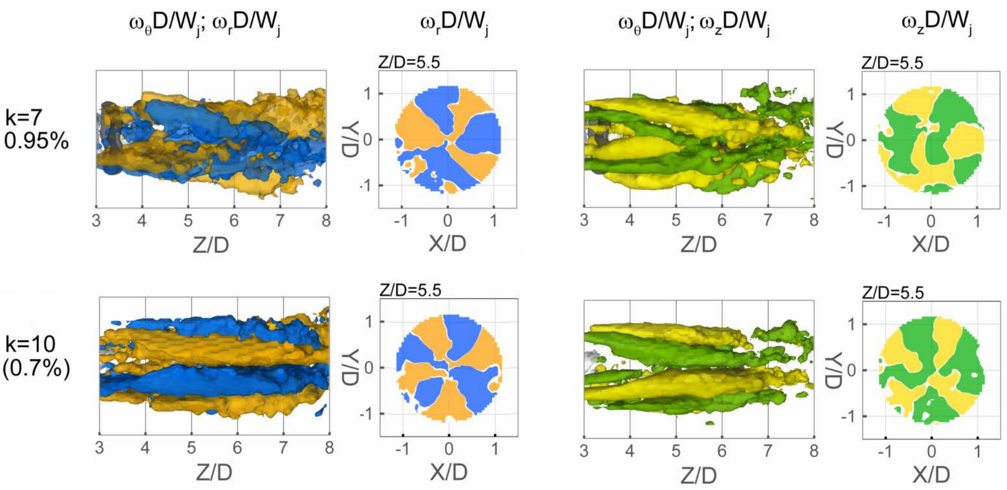
$\omega_\theta D/W_j$; $\omega_r D/W_j$
$\omega_r D/W_j$
$\omega_\theta D/W_j$; $\omega_z D/W_j$
$\omega_z D/W_j$
k=7
0.95%
k=10
(0.7%)
Z/D=5.5
Z/D
X/D
Y/D
3
4
5
6
7
8
-1
0
1

Figure 5.18 POD modes of vorticity describing pulsatile motions (refer to caption of Figure 5.17 for the legend)

Travelling ring vortices after pairing are described by mode #1 and mode #2, which are the most energetic (5.7% and 5.6% of the total energy), as found from the velocity decomposition. The same type of motion is also associated with mode #5 and #6 with lower energy content. The three-dimensional pattern that evolves in conjunction travelling vortex rings and that, ultimately, leads to the breakdown, is illustrated by iso-surfaces of radial and axial components of the vorticity modes, $\omega_r D/W_j$ and $\omega_z D/W_j$ as well as by cross-sectional iso-contours plots of the same quantities. Characterized by peak Strouhal St=0.36 (Figure 5.21), mode #1 and 2# show that the motion of vortex rings after pairing (see iso-surfaces of $\omega_\theta D/W_j$) is accompanied by travelling waves of $\omega_r D/W_j$ and $\omega_z D/W_j$ that develop across the end of the potential core. For Z/D>4.5, they show a characteristic inclination of 40-45 degrees to the jet axis (see dashed lines). Phase opposition on the plane normal to the jet axis (see iso-contour plots at Z/D=5.5) is observed for $\omega_r D/W_j$ and $\omega_z D/W_j$, indicating that while one half of the ring structure is subjected to inward radial swirl and positive axial swirl, the other half undergo outward radial swirl and negative axial swirl. Mode #3 and #4 describe travelling ring vortices after shedding (see iso-surface of $\omega_\theta D/W_j$, *St*=0.72) with spatial wavelength of 0.75, half that of pairing mode (mode #1 and #2), in the region between *Z/D*=1.5 and 4. The motion is combined with travelling waves of $\omega_r D/W_j$ and $\omega_\theta D/W_j$ that, as illustrated in the iso-contour plot at *Z/D*=3.5, are distributed along the azimuthal direction with wave number *k*=4, meaning of four pairs of counter-rotating streamwise vortices, which agrees with previous experiments (Violato and Scarano, 2011). Similarly to #1 and #2, modes #5 and #6 describe the motion of vortex rings after pairing together with travelling waves of $\omega_r D/W_j$ and $\omega_z D/W_j$ with a characteristic inclination of 40-45 degrees to the jet axis in the region 4<*Z/D*<6.5. However, compared to mode #1 and #2, they are rotated of $\pi/2$ around the jet axis and they also feature secondary Strouhal peak *St*=0.7. More three-dimensional features are identified by the pair of modes #8 and #9 which describe travelling "wave" of radial and axial vorticity filaments that also have a preferred orientation at 45 degrees to the jet axis in the region 4.5<Z/D<6 (related Strouhal peaks *St*=0.31 and 0.7).

The characteristic 45 degrees inclination of the radial and the axial vorticity that is observed in mode pairs #1-#2, #5-#6 and #8-#9 is associated with the process of vortex ring breakdown by axial ejection of vortex humps (Figure 5.12).

Pulsatile modes #7 and #10 (Figure 5.18) show four pairs of counter-rotating streamwise filaments of $\omega_r D/W_j$ and $\omega_z D/W_j$ that develop across the region of vortex breakdown between *Z/D*=3.5 and *Z/D*=8 and are respectively associated with Strouhal peak *St*=0.79 and *St*=0.15. These structures may be associated to the *propeller-like* vortex pattern already reported by Jung *et al.* (2004).

5.4.3 Decomposition based on Lamb vector

The POD analysis of the Lamb vector, which in Powell's aeroacoustic analogy accounts for the flow state (eq. (2.36)), shows the first 10 modes capturing 30.3% of the total *Lamb energy*. Travelling waves are described by the first 4 pairs of modes (#1 and #2, #3 and #4, #5 and #6, #7 and #8), illustrated in Figure 5.19. While in the vorticity modes toroidal vortices are described by the azimuthal vorticity component (Figure 5.17), in the Lamb vector modes the azimuthal coherence is described by the radial and the axial components $L_r D/W_j$ and $L_z D/W_j$. The development of a three-dimensional disturbance is instead described by the azimuthal component $L_\theta D/W_j$ (Figure 5.19 and Figure 5.20). Similarly to the velocity and vorticity decompositions, the first and the second mode of the Lamb vector describe the motion of toroidal vortices formed after pairing (*St*=0.36, Figure 5.21) and the presence of a three-dimensional disturbance (see isosurface $L_\theta D/W_j$) that develop across the end of the potential core. This disturbance grows with a characteristic 40-45 degrees inclination to the jet axis, similarly to the waves $\omega_r D/W_j$ and $\omega_z D/W_j$ observed in pairs #1-#2, #5-#6 and #8-#9 of the vorticity decomposition. In the region between *Z/D*=2.5 and 5, mode #3-#4 describes travelling toroidal vortices after shedding (*St*=0.72), as observed for the vorticity decomposition.

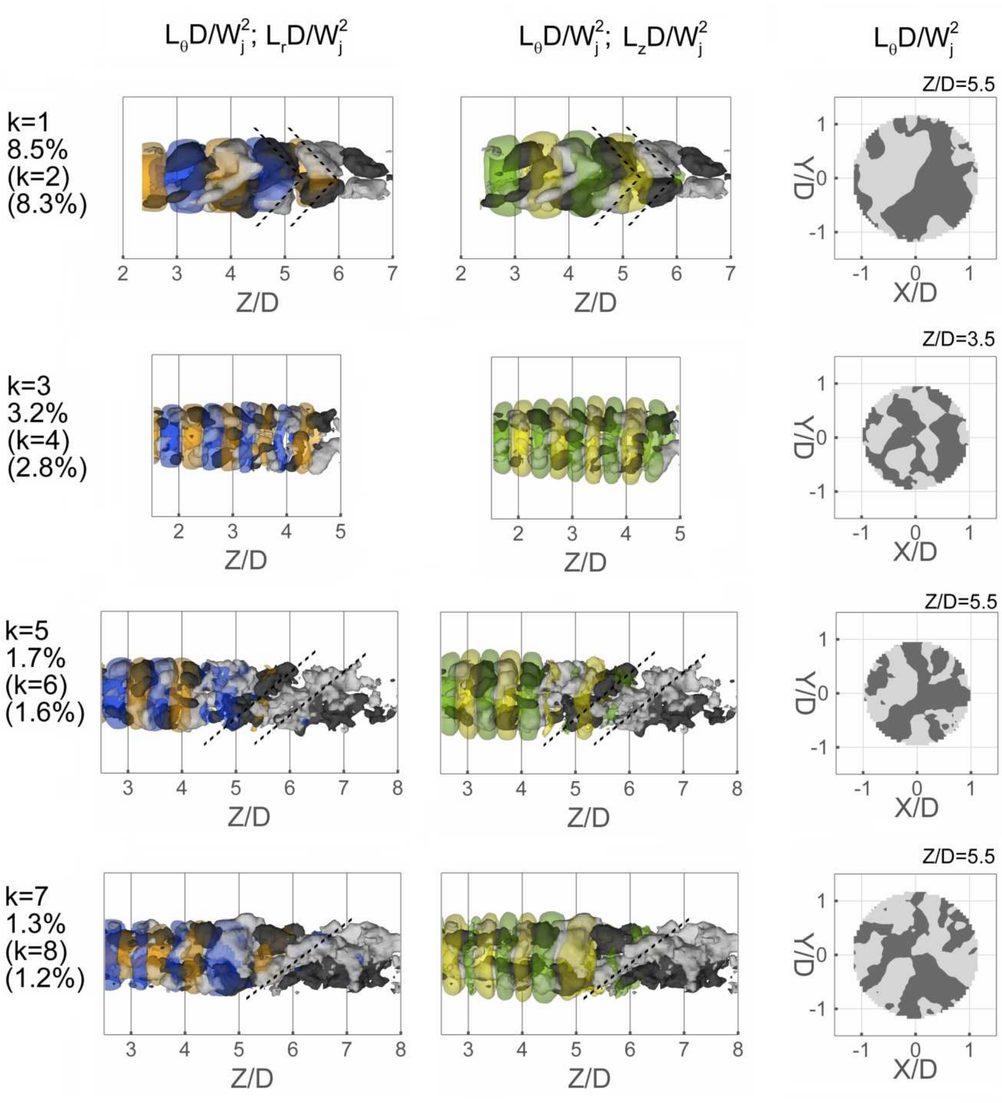
$L_\theta D/W_j^2$; $L_r D/W_j^2$
$L_\theta D/W_j^2$; $L_z D/W_j^2$
$L_\theta D/W_j^2$
k=1
8.5%
(k=2)
(8.3%)
k=3
3.2%
(k=4)
(2.8%)
k=5
1.7%
(k=6)
(1.6%)
k=7
1.3%
(k=8)
(1.2%)
Z/D
X/D
Y/D
Z/D=5.5
Z/D=3.5
Z/D=5.5
Z/D=5.5
2
3
4
5
6
7
8
-1
0
1

Figure 5.19 POD modes of Lamb vector describing travelling waves. Between brackets mode number and energy of the coupled mode. Left: iso-surfaces of $L_\theta D/W_j$ (positive in light grey; negative in dark grey) and $L_r D/W_j$ (positive in orange and negative in blue); centre: iso-surfaces of $L_\theta D/W_j$ (positive in light grey; negative in dark grey) and $L_z D/W_j$ (positive in yellow and negative in green); right: cross-sectional iso-contour of $L_\theta D/W_j$

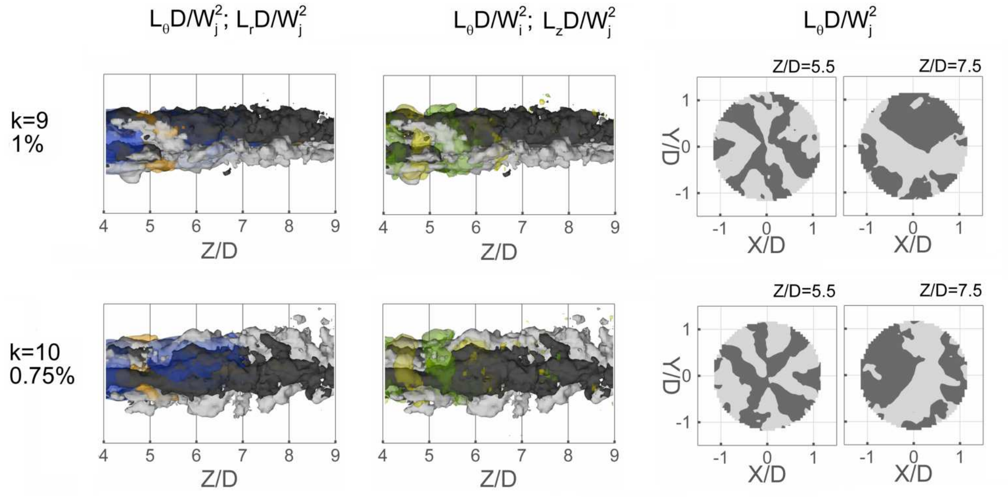

Figure 5.20 POD modes of Lamb vector describing pulsatile motions (refer to caption of Figure 5.19 for the legend)

The motion is combined with travelling wave of $L_\theta D/W_j$ showing an azimuthal distribution with a wave number *k*=4, as observed in mode #3-#4 for the radial and axial component of the vorticity (see cross-sectional plots at *Z/D*=3.5). Mode #5-#6, as well as mode #7-#8, describe the motion of vortices after shedding in the region between *Z/D*=2.5 and 5 (note that the related Strouhal is *St*=0.7, slightly slower than that of mode #3-#4). Further downstream, in the region across the end of the potential core (5<*Z/D*<7), filaments of $L_\theta D/W_j$ (see cross-sectional plots at Z/D=5.5) identify a travelling wave characterized by axial swirling with an angle of 40-45 degrees to the jet axis. Such motion is associated with *St*=0.93 for mode #5-#6 and *St*=0.6 for mode #7-#8.

Lamb vector pulsatile modes #9 and #10 (Figure 5.20) show 6 main pairs of streamwise filaments of $L_\theta D/W_j$ coherence that develop until the region of vortex breakdown (*Z/D*=5.5) and then merge into a main pair (*Z/D*=7.5). As shown in the cross-sectional contour plots of $L_\theta D/W_j$ at *Z/D*=7.5 (Figure 5.20), mode #10 is rotated of about π/2 around the jet axis with respect to mode #9. The related Strouhal peak is 0.64 for both modes.

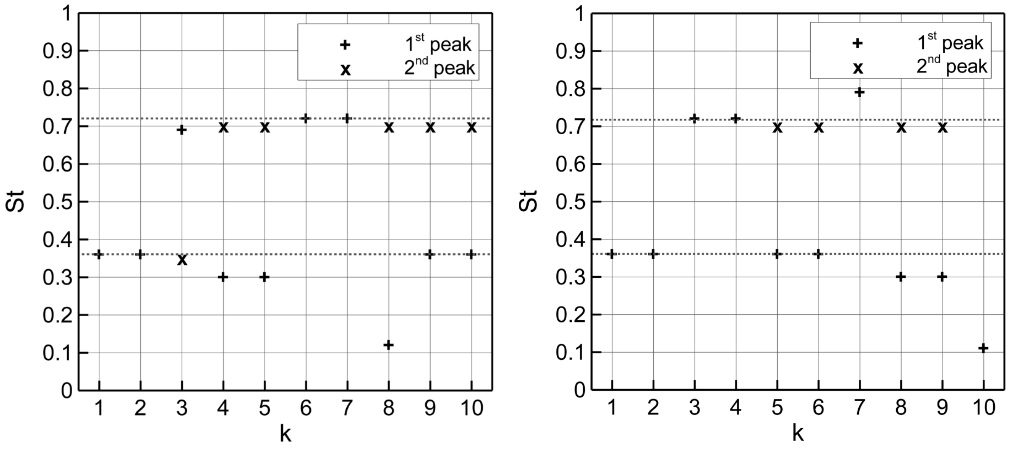

a) **V** modes b) **ω** modes

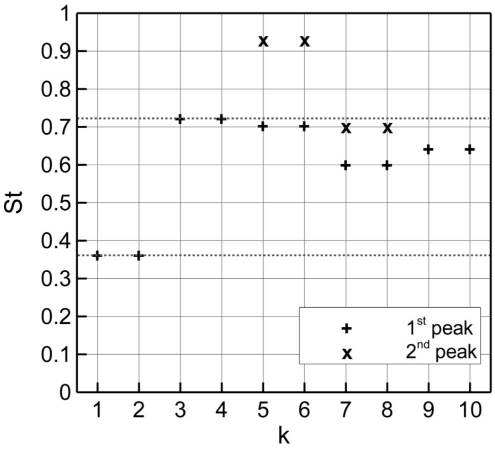

c) **L** modes

Figure 5.21 Spectrum peaks of POD mode time coefficients

5.5 The chevron jet

The early flow pattern of the chevron jet profoundly differs from the vortex ring shedding and pairing observed for the circular configuration. As shown in the temporal sequence of Figure 5.22, the axisymmetric ring-like coherence of the circular jet is replaced by streamwise flow structures of azimuthal (“SA”), axial (“ST”) and radial (“SR”) vorticity that are formed at the nozzle exit. Vortices “ST” and “SR” are organized in counter-rotating pairs (“STP” and “SRP”), which exhibit a rather stationary behavior. Despite the absence of vortex rings, between Z/D=1 and Z/D=3, the potential core of the chevron jet still exhibits some pulsatile motion with Strouhal number $0.56<St<0.85$, leading to instantaneous axial velocity fluctuations at jet axis of 0.12 at Z/D=2 and axial turbulence of 0.025 (Figure 4.19). Flow patches at axial velocity larger than W_j, as shown in Figure 5.22 by iso-surface W/W_j =1.05, alternates with ones at lower velocity in a range between 0.95 and 1.07.

The presence of counter-rotating pairs of vortices “STP” was observed in the lobe regions between chevrons at higher Reynolds number both experimentally (Bridges and Brown, 2004; Opalski *et al.*, 2005; Alkislar *et al.* 2007) and computationally (Xia *et al.*, 2009; Uzun and Hussaini, 2009). Bridges and Brown (2004) and Opalski *et al.* (2005) showed that, when chevrons penetrate the jet core, they induce axial vorticity, resulting in evident streamwise vortices at the chevron notches. Using time-averaged stereo-PIV data at several cross-sections, Alkislar *et al.* (2007) showed the three-dimensional axial development of the streamwise structures by iso-surface of axial mean vorticity. However, previous studies do not discuss the aspects related to the radial vorticity component “SR”, as they were conducted by planar PIV measurements at jet axis cross-sections, which only enable the evaluation of axial vorticity. The inspection of all vorticity components was given by Xia *et al.* (2008), who conducted LES computations and showed the pattern of the vorticity magnitude. However, the discussion of the contribution from each component is lacking, in relation to the different instability mechanisms. Also the study by Uzun and Hussaini (2009) focuses on the assessment of their LES simulation rather than on the flow behavior.

The cross-sectional contour plots of Figure 5.23 shows the instantaneous velocity pattern by iso-contours of axial velocity and X-Y projection of the velocity vector. At Z/D=1 and Z/D=2, circulatory patterns are observed at the chevron notch in a slightly staggered position. The coherence of these regions and the magnitude of the axial velocity in the jet core gradually decrease between Z/D=2 and Z/D=4, leading to the disappearance of the star-like pattern (Z/D=4).

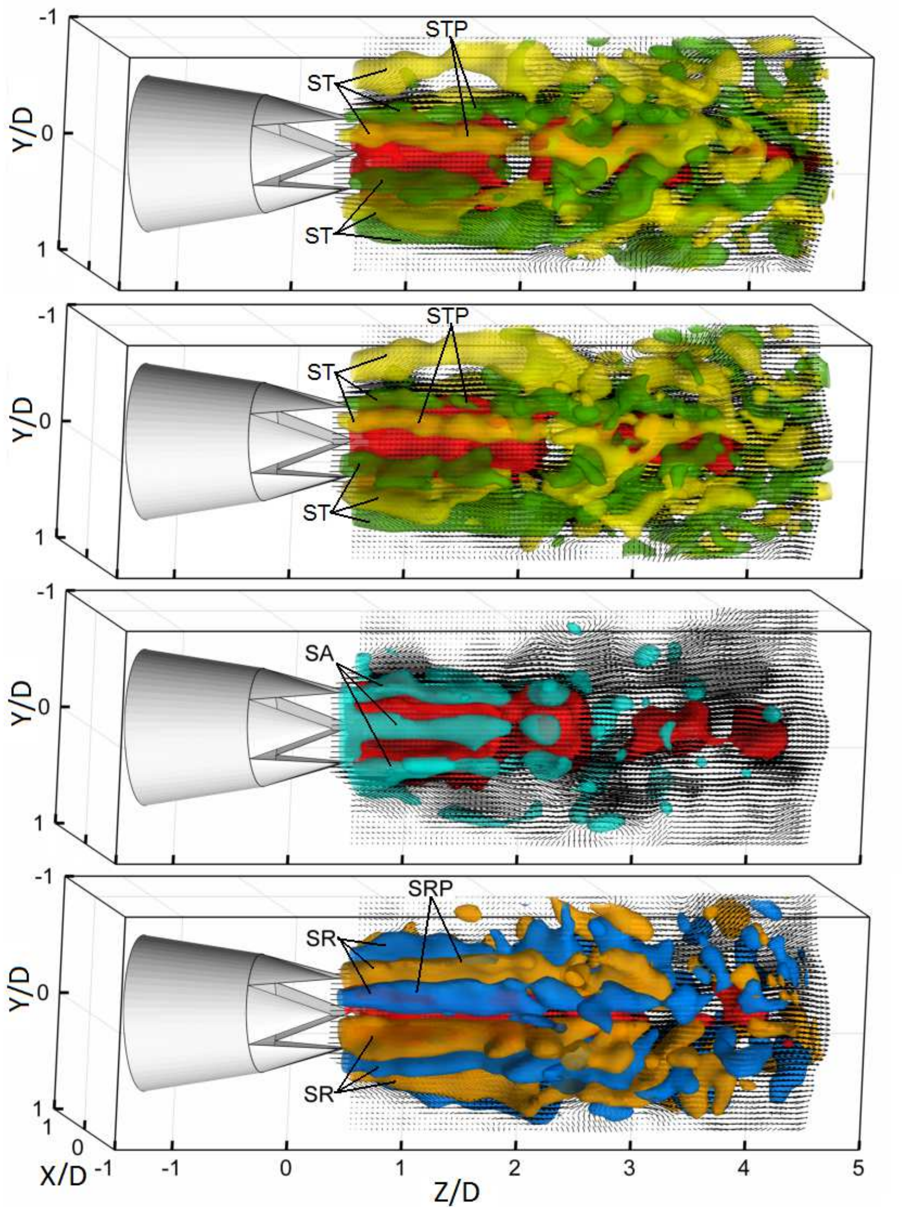

Figure 5.22 Time sequence visualization of the chevron jet. Velocity vector slice in the axial plane. Iso-surfaces of axial velocity W/W_j =1.05 (red). In the first two snapshots, iso-surfaces $\omega_z D/W_j$ =-1.2=-1.2 (green) and 1.2 (yellow); in the third snapshot iso-surfaces $\omega_\theta D/W_j$=4; in the fourth snapshot iso-surfaces $\omega_r D/W_j$=-1.2 (blue) and 1.2 (orange). Time separation between displayed images $\Delta t W_j/D$=0.61

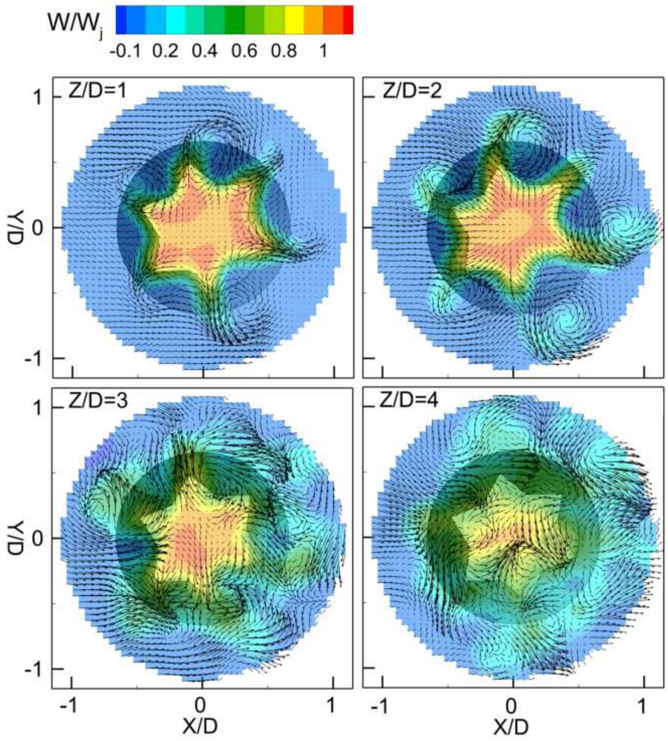

Figure 5.23 Cross-sectional iso-contours of W/W_j; X-Y projection of velocity vectors; tW_j/D=0.

5.5.1 Streamwise vortices

A detailed inspection of the vorticity patterns is given in Figure 5.24 and Figure 5.25, which show the cross-sectional contour plots of the vorticity components $\omega_\theta D/W_j$, $\omega_r D/W_j$, $\omega_z D/W_j$ and vorticity magnitude $|\boldsymbol{\omega}|D/W_j$. At Z/D=1, a total of 6 longitudinal structures of azimuthal vorticity ("SA"), the same ones depicted in the third snapshot of Figure 5.22, are located in correspondence to the chevron apices and show peaks of $\omega_\theta D/W_j$=5. Counter-rotating pairs of streamwise vortices of radial and axial vorticity, "SRP" and "STP" respectively, develop from the chevron notches, where they exhibit opposite sign and where the outward radial flow is one order of magnitude larger (V_r/W_j=0.2 and v_r'/W_j =0.03, Figure 4.20) than at the chevron apex. "SRP" instabilities show peak activity of radial vorticity $\omega_r D/W_j$=4, which is twice larger than the peaks of $\omega_z D/W_j$ associated with "STP" structures. Compared to those of the circular jet (Figure 5.8 and Figure 5.10), "SR" and "ST" instabilities are 50% stronger and 40% weaker, respectively. On the other hand, absolute vorticity at the chevron apex ($|\boldsymbol{\omega}|D/W_j$=6, Figure 5.25) is comparable to that observed in the circular jet for axisymmetric vortex-rings (vortex "3", Figure 5.3). A decrease in $|\boldsymbol{\omega}|D/W_j$ is instead observed at the chevron notches ($|\boldsymbol{\omega}|D/W_j<4$).

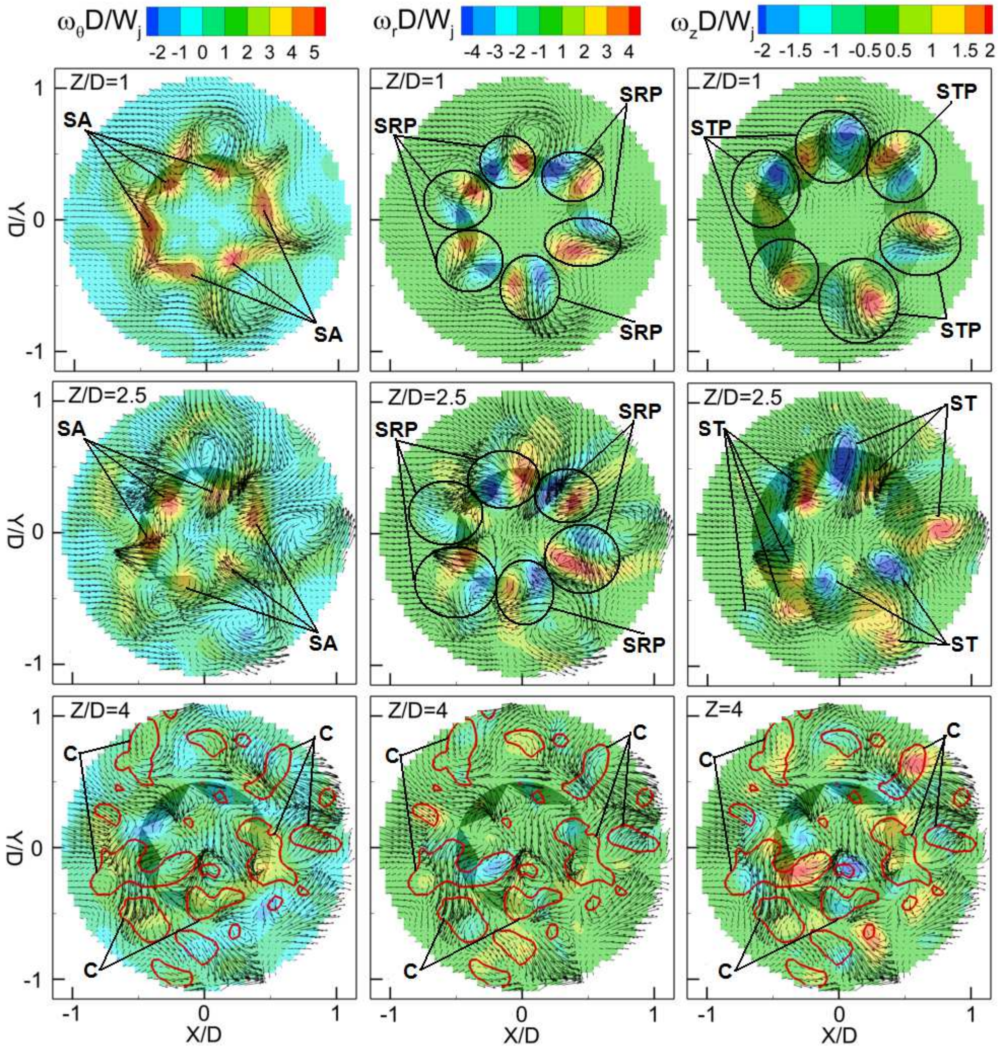

Figure 5.24 Cross-sectional iso-contour of $\omega_\theta D/W_j$, $\omega_r D/W_j$ and $\omega_z D/W_j$ with iso-line $\lambda_2 D/W_j$=-0.2; X-Y projection of velocity vectors; tW_j/D=0

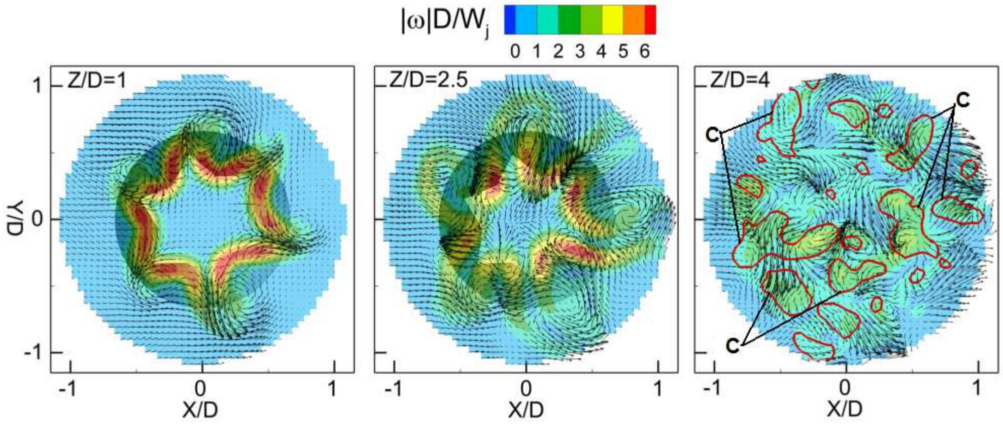

Figure 5.25 Cross-sectional iso-contour of $|\boldsymbol{\omega}|D/W_j$ with iso-line $\lambda_2 D/W_j$ =-0.2; X-Y projection of velocity vectors; tW_j/D=0

At Z/D=2.5, branches of higher axial velocity at the notch extends to R/D=0.75. Radial velocity V_r/W_j increases to 0.25 in regions corresponding both to the notch and to the apex, where axial and radial turbulence are comparable (w'/W_j =0.1 and v'_r/W_j =0.07, Figure 4.20). The increase of turbulent fluctuations amplitude is accompanied by the weakening of “SA” vortices and the movement of “ST” vortices from the notch regions, leading to the breakup of pairs. The coherence of $\omega_r D/W_j$ instead maintains the pair organization (“SRP”). The maximum absolute vorticity is concentrated at the chevron apex as seen at Z/D=1 (Figure 5.25).

At Z/D=4, the contour plot of axial velocity shows that the characteristic star-like pattern has disappeared in favor of a rather axisymmetric one (Figure 5.23; w'/W_j =0.07 and v'_r/W_j=0.05 in Figure 4.19) in which vortices “SA”, “SRP” and “ST” no longer exist. This loss of coherence is associated with a drop of vorticity magnitude $|\boldsymbol{\omega}|D/W_j$ of 30% in comparison with Z/D=1. As the identification of coherent pattern at Z/D=4 becomes difficult by the vorticity vector, the λ_2-*criterion* is adopted. Iso-lines $\lambda_2 D/W_j$ =-0.2 that are shown on the contour plots at Z/D=4 show that the transition region is characterized by coherent structures that will be referred as “C” vortices, discussed later in this section.

Bradshaw *et al*. (1963) suggested that lower sound emissions in jet flows could be achieved by increasing the loss of azimuthal coherence, such as for example by artificial augmentation of streamwise structures with lobed nozzle. For high Reynolds number jets, the chevron configuration was shown to yield a noise reduction by experimental studies based on microphone measurements (Bridges and Brown, 2004; Opalski *et al*., 2005; Alkislar *et al*. 2007) as well as by numerical simulations (Uzun and Hussaini, 2009; Xia *et al.*, 2009). However, the relation between the three-dimensional unsteady flow organization and the noise generation is still today a debated topic.

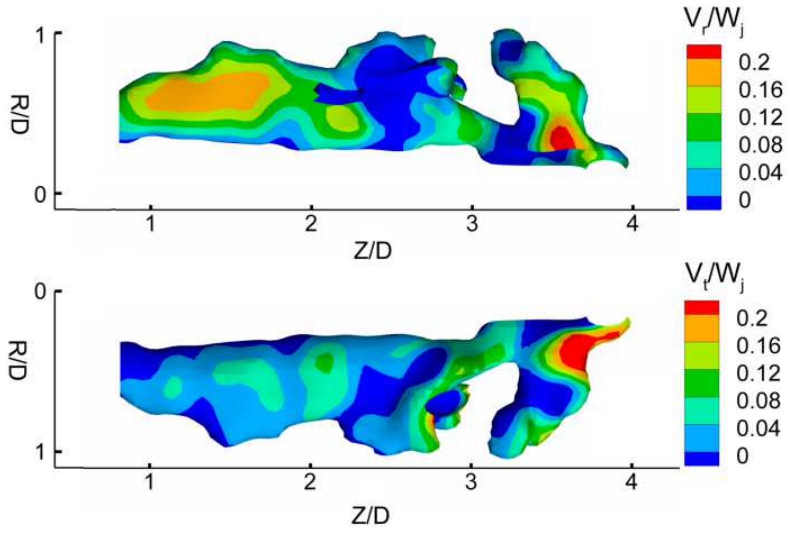

a) Iso-surface $\omega_r D/W_j=0.8$

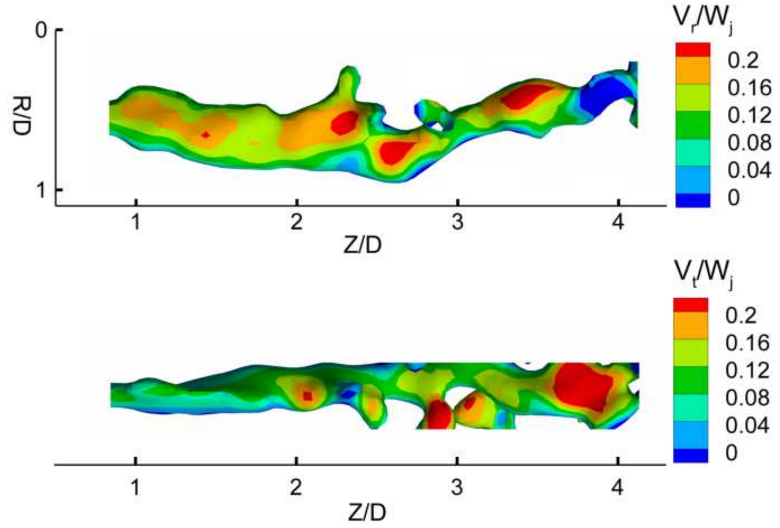

b) Iso-surface $\omega_z D/W_j=0.8$

Figure 5.26 Radial and tangential velocity field of streamwise vortices “SRP” and “STP” identified. Iso-surfaces color coded with V_r/W_j and V_t/W_j; $tW_j/D=0$

For a clearer insight in the three-dimensional development, the counter-rotating vortices “SRP” and “STP” (Figure 5.22), are extracted at $tW_j/D=0$ and, for each of the pair, the streamwise vortex with positive sign of the related vorticity component is illustrated in Figure 5.26. Vortex filament “ST” extends to 4 jet diameters downstream the nozzle and, at approximately $Z/D=2.5$, it bends inward towards the jet core with an angle of approximately 30 degrees to the axis. The core of the streamwise vortex is stretched in the radial direction, as shown at $Z/D=1$ in Figure 5.24, with dimension of the major and minor axis of 1/4*D* and 1/6D based on iso-surface $\omega_z D/W_j = 0.8$. Similar core size is observed for the “SR” structure, which develops up to $Z/D=2.8$ with a rather constant size of the core and gradually decays between $Z/D=2.5$ and 4. The velocity patterns related to the streamwise coherence are illustrated color-coding the iso-surface of the streamwise vortex with radial and tangential velocity components. For both “SR” and “ST”, the highest levels of V_r/W_j activity is observed on the side of the counter rotating vortex, with peaks of 0.2, whereas the tangential velocity V_t/W_j increases in the downstream direction reaching peaks of 0.2 at $Z/D>3$.

5.5.2 Flow coherence organization at transition

Transitional structures are characterized by a recurrent C-shape and are first observed where the streamwise vortices “ST” form approximately 30 degrees with the jet axis ($2.5<Z/D<3$, Figure 5.27). Here, a “C” vortex occupies a peripheral location in the shear layer ($0.5<R/D<1$) that is characterized by Reynolds stress $(w'v'_r)/W_j^2=0.0025$ at both the notch and the apex of the chevron. The “legs” of the vortex are immersed in the region of higher axial velocity and, consequently, they tend to be aligned along the jet axis. This is shown in Figure 5.28a illustrating a temporal sequence of a “C” vortex that is convected with a velocity of 0.25. At $tW_j/D=0$, the leg-to-axis angle is approximately 80 degrees and it reduces to 40 degrees at $tW_j/D=1.62$. Between $Z/D=2.5$ and 4, the characteristic “C” shape of the vortex is conserved for a time period of 2.3, after which it breaks down. The induced flow field of a “C” vortex engulfs fluid at the trailing side and ejects it at the leading side, as shown Figure 5.28b by the instantaneous iso-surface of radial and tangential velocity.

The normalized axial, radial and tangential flux associated with the “C” structure can be estimated by eq.(5.1), where S is the surface of the volume containing the structure. On average, it is found a net inward radial flux of 0.05, which is comparable to the axial flux in the upward direction. In the tangential direction, instead, the flux is one order of magnitude smaller. These observations show that the “C” vortices play a role in the entrainment of the outer flow, and that they may be responsible for the tilting of the streamwise structures towards the jet axis.

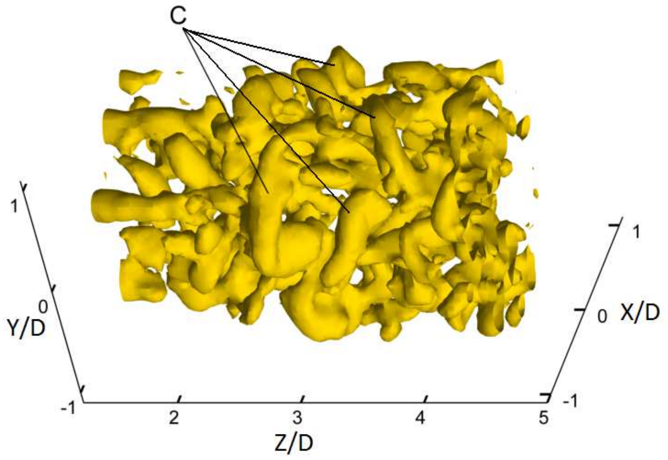
C
1
0
Y/D
-1
2
3
4
5
Z/D
1
0
X/D
-1

Figure 5.27 Chevron jet: ”C”-like flow structures shown by iso-surface of $\lambda_2 D/W_j$=-0.2; tW_j/D=0

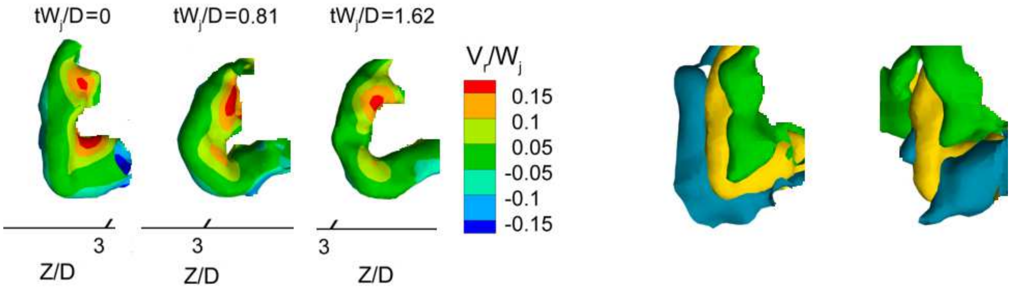
tW_j/D=0
tW_j/D=0.81
tW_j/D=1.62
V_r/W_j
0.15
0.1
0.05
-0.05
-0.1
-0.15
3
Z/D
3
Z/D
3
Z/D

a) b)

Figure 5.28 Velocity field associated with C-shaped structures. Left: temporal evolution of ”C” structure color-coded with V_r/W_j (Δt=0.81); right: iso-surface -0.05 (blue) and 0.05 (green) of V_r/W_j (left) and V_t/W_j (right)

5.6 Statistical distribution of vorticity components

An overview on the flow transition to three-dimensionality along the jet axis can be inferred from the axial distributions of the vorticity components, considering the average in time, along azimuthal and radial directions. For flow a generic space-time dependent flow variable $a(\mathbf{x},t)$ reads as

$$< a(\mathbf{x},t) >= \frac{1}{2\pi TR}\int_0^T\int_0^{2\pi}\int_0^{R^*} a(\mathbf{x},t)dRd\theta dt\,, \tag{5.2}$$

where T is the observation time and R^* is the radial position at the domain boundary. Equation (5.2) is applied to the absolute values of the azimuthal, the radial and the axial vorticity components, respectively $|\omega_\theta D/W_j|$, $|\omega_r D/W_j|$ and $|\omega_z D/W_j|$, between R/D=0 and R/D=1 and the corresponding axial distributions $<|\omega_\theta D/W_j|>$, $<|\omega_r D/W_j|>$ and $<|\omega_z D/W_j|>$are shown in Figure 5.29. Downstream the shedding and pairing of toroidal structures (Z/D>3.5), $<|\omega_r D/W_j|>$ and $<|\omega_z D/W_j|>$ increase as azimuthal instabilities and streamwise vortices grow. The azimuthal component $<|\omega_\theta D/W_j|>$ is still dominant, although it steadily decreases. In the region near the end of the potential core (5.5<Z/D<6.5), $<|\omega_z D/W_j|>$ reaches a peak (0.63 at Z/D=5.5) corresponding with the ejection and axial tilting of the "P" flow regions (Figure 5.12). In contrast, $<|\omega_r D/W_j|>$ steadily increases to 0.73 at Z/D=6.2, where the toroidal structures breakdown. Beyond the potential core (Z/D>6.5), the flow field shows an overall decrease of the vorticity components to values comparable to those in the region of growth of azimuthal instabilities and streamwise vortices formation (Z/D~4).

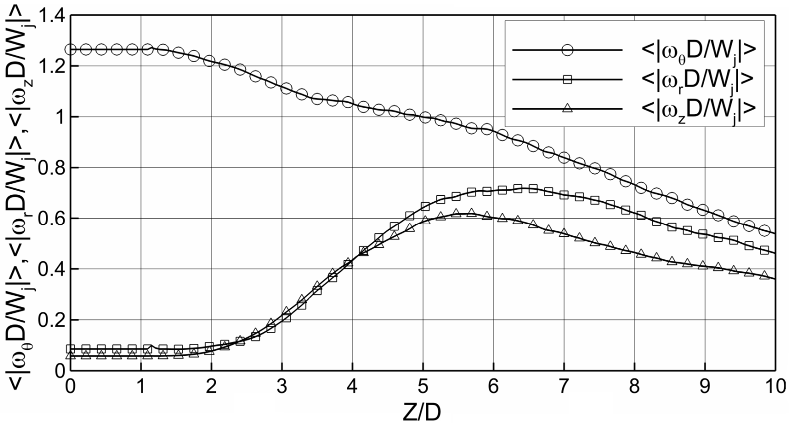

Figure 5.29 Axial distribution of $<|\omega_\theta D/W_j|>$, $<|\omega_r D/W_j|>$ and $<|\omega_z D/W_j|>$ in circular jet

The statistical axial distributions of vorticity in chevron and circular jets are compared in Figure 5.30, which illustrates the ratio between the radial and the azimuthal components $<|\omega_r|>/<|\omega_\theta|>$, and the ratio between the axial and the azimuthal components $<|\omega_z|>/<|\omega_\theta|>$. In the circular case, $<|\omega_r|>/<|\omega_\theta|>$ and $<|\omega_z|>/<|\omega_\theta|>$ show similar trends between Z/D=1.5 and 3.5, region dominated by azimuthally coherent ring vortices, with the former that is twice larger than the latter (0.07) (Figure 5.2). They both increase in the region of vortex pairing, azimuthal instabilities and streamwise vortices. By the end of the potential core, $<|\omega_z|>/<|\omega_\theta|>$ levels out 0.64, whereas $<|\omega_r|>/<|\omega_\theta|>$ increases beyond the end of the potential core (Z/D=7) where it levels out at 0.9.

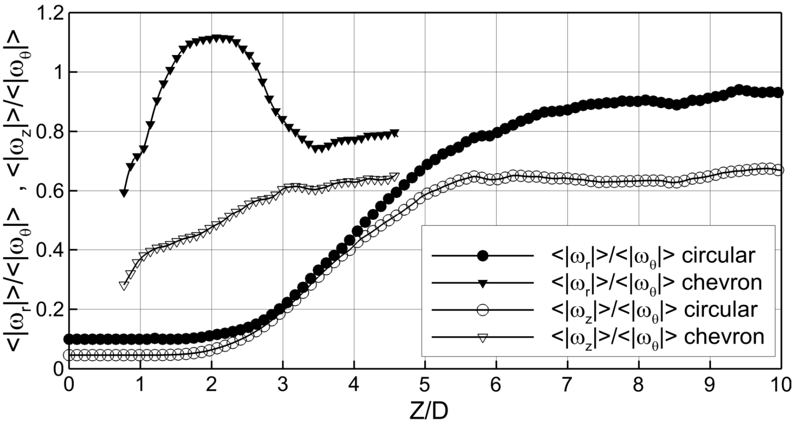

Figure 5.30 Axial distribution of $<|\omega_r|>/<|\omega_\theta|>$ and $<|\omega_z|>/<|\omega_\theta|>$ in the circular and chevron jets

In the chevron jet, $<|\omega_r|>/<|\omega_\theta|>$ and $<|\omega_z|>/<|\omega_\theta|>$ are larger than in the circular case, at any axial location between 1.5 and 4.8. At Z/D=1, where “SR” and “ST” structures are located at chevron notches (Figure 5.22, Figure 5.24 and Figure 5.25) $<|\omega_r|>/<|\omega_\theta|>$ is 0.72, approximately twice the value shown by $<|\omega_z|>/<|\omega_\theta|>$. While this grows steadily, $<|\omega_r|>/<|\omega_\theta|>$ steeply increases to 1.1 at Z/D=1.6, and then drops to 0.78 between Z/D=2.5 and 3.5, which is the region of streamwise coherence decay and “C” structure formation. More downstream, $<|\omega_r|>/<|\omega_\theta|>$ levels out at 0.78, whereas $<|\omega_z|>/<|\omega_\theta|>$ reaches a rather constant trend at 0.63.

5.7 Stretching and tilting of flow structures

The normalized vortex stretching-tilting $(\boldsymbol{\omega}\cdot\nabla)\mathbf{V}$ can be decoupled into a component of stretching

$$\mathbf{S}=\left((\boldsymbol{\omega}\cdot\nabla)\mathbf{V}\cdot\frac{\boldsymbol{\omega}}{|\boldsymbol{\omega}|}\right)\hat{\boldsymbol{\omega}}, \tag{5.3}$$

and a component of tilting

$$\mathbf{T}=\left((\boldsymbol{\omega}\cdot\nabla)\mathbf{V}\times\frac{\boldsymbol{\omega}}{|\boldsymbol{\omega}|}\right)\hat{\boldsymbol{\omega}}, \tag{5.4}$$

where $\hat{\boldsymbol{\omega}}$ is the unit vorticity vector.

The vortex stretching and tilting terms are evaluated at vortex locations, which allow determining their spatial distribution within the vortex rings.

5.7.1 The circular jet

In the circular jet, they increase on the vortex rings downstream of Z/D=3, especially after pairing, when azimuthal instabilities begin to grow. Figure 5.31 illustrates the example of vortex “3+4” (Figure 5.2). The absolute stretching $|\mathbf{S}|D^2/W_j^2$ reach peaks of 3 in correspondence to the azimuthal valley. By contrast, absolute tilting $|\mathbf{T}|D^2/W_j^2$ shows peaks of 2 with pattern that are hardly associable with the vortex azimuthal deformation. Axial tilting is typically twice larger compared to the x and y components. On the streamwise vortices “ST”, $|\mathbf{S}|D^2/W_j^2$ and $|\mathbf{T}|D^2/W_j^2$ are smaller than 1 on the leading side of the vortex ring, whereas they are maximum (3.5, Figure 5.32) on the longitudinal structures located within the vortex ring. On the trailing side of the vortex ring, instead, $|\mathbf{S}|D^2/W_j^2$ is 2.5 and $|\mathbf{T}|D^2/W_j^2$ is 1.5. Comparable peak values are observed for “SR” vortices, which are not illustrated.

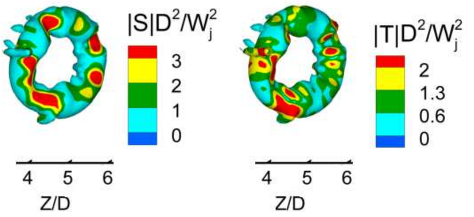

Figure 5.31 Circular jet: instantaneous stretching and tilting fields of vortex rings; iso-surface $\lambda_2 D/W_j$=-0.5 of vortex “3+4” color coded with $|\mathbf{S}|D^2/W_j^2$ (left) and $|\mathbf{T}|D^2/W_j^2$ (right) at tW_j/D=3.28

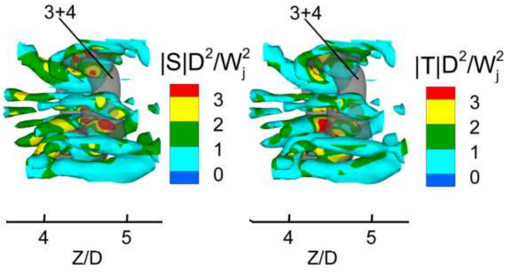

Figure 5.32 Circular jet: instantaneous stretching and tilting fields of streamwise vortices; iso-surface $\omega_z D/W_j$ =-1.2 and 1.2 color coded with $|\mathbf{S}|D^2/W_j^2$ (left) and $|\mathbf{T}|D^2/W_j^2$ (right); iso-surface of vortex “3+4” $\omega_\theta D/W_j$ =4 (grey); tW_j/D=4.1

As illustrated in Figure 5.33, similar peak magnitude of stretching and tilting fields $|\mathbf{S}|D^2/W_j^2$=3 and $|\mathbf{T}|D^2/W_j^2$=3 is observed when the periphery of the toroidal vortex disrupts into “C” structures and the inner portions of the vortex “P” are ejected (Figure 5.12). Beyond the end of the potential core, instead, stretching-tilting activity decrease to values of 1, which is typically observed in correspondence to the ”VF” structures as well as in the region closer to the jet axis where the coherence decays faster.

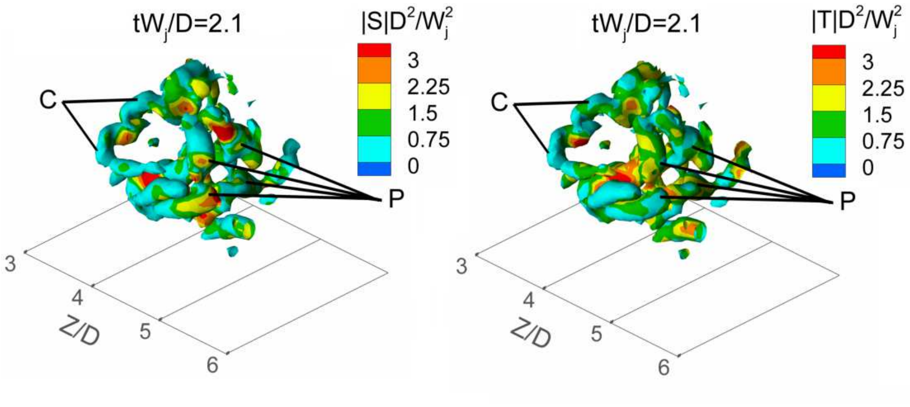
tW_j/D=2.1
$|S|D^2/W_j^2$
3
2.25
1.5
0.75
0
C
P
3
4
5
6
Z/D
tW_j/D=2.1
$|T|D^2/W_j^2$
3
2.25
1.5
0.75
0
C
P
3
4
5
6
Z/D

a) Vortex ring breakdown

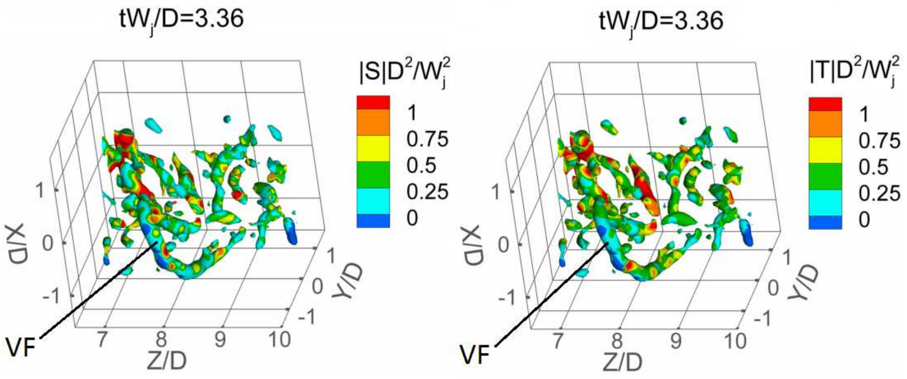
tW_j/D=3.36
$|S|D^2/W_j^2$
1
0.75
0.5
0.25
0
X/D
1
0
-1
Y/D
1
0
-1
Z/D
7
8
9
10
VF
tW_j/D=3.36
$|T|D^2/W_j^2$
1
0.75
0.5
0.25
0
X/D
1
0
-1
Y/D
1
0
-1
Z/D
7
8
9
10
VF

b) Vortex filaments advection

Figure 5.33 Circular jet: instantaneous stretching and tilting fields: a) vortex breakdown identified by iso-surfaces $\lambda_2 D/W_j$=-0.8; b) “VF” vortices identified by iso-surfaces $\lambda_2 D/W_j$=0.8; iso-surfaces are color coded with $|\mathbf{S}|D^2/W_j^2$ and $|\mathbf{T}|D^2/W_j^2$

5.7.2 The chevron jet

In the chevron jet, the streamwise structure “ST” are highly stretched and tilted on the side of the nozzle between Z/D=0.8 and Z/D=2, as depicted in Figure 5.34. $|\mathbf{S}|D^2/W_j^2$ and $|\mathbf{T}|D^2/W_j^2$ reach peak values of 3 and they substantially decrease in the downstream direction, with a drop of 30% in the regions corresponding to the “C” vortices. The upstream and downstream sides are characterized by $|\mathbf{S}|D^2/W_j^2$=2.2 and $|\mathbf{T}|D^2/W_j^2$=2.2 and a decrease to values smaller than 0.5 on the lateral side which is embedded in the region of lower axial velocity. Similar patterns are observed for the streamwise structures “SR”, which are not illustrated.

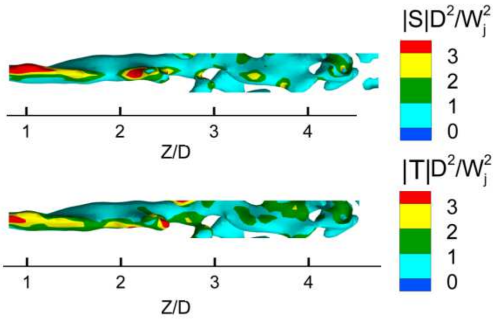

a) Streamwise vortex

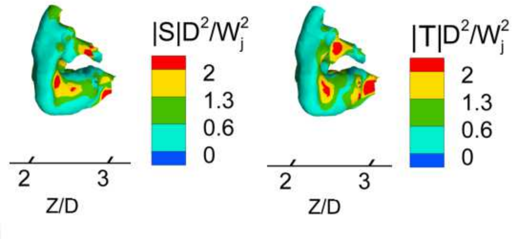

b) C-shaped vortex

Figure 5.34 Chevron jet: instantaneous stretching and tilting fields: a) iso-surfaces $\omega_z D/W_j=0.8$ of streamwise vortex; b) iso-surfaces λ_2=-0.2 of “C” vortex; iso-surfaces are color coded with $|\mathbf{S}|D^2/W_j^2$ (top) and $|\mathbf{T}|D^2/W_j^2$; tW_j/D=0

5.7.3 Statistical characterization

Stretching and tilting activities are statistically characterized along the jet axis. Equation (5.2) is applied to the absolute values of the stretching and tilting vectors, respectively $|\mathbf{S}|D^2/W_j^2$ and $|\mathbf{T}|D^2/W_j^2$, between R/D=0 and R/D=1 and the corresponding axial distributions, <|**S**|> and <|**T**|>, are shown in Figure 5.35.

In the chevron jet, between the nozzle exit and Z/D=2, <|**S**|> and <|**T**|> reach peaks of 0.28 and 0.24, respectively, which are approximately 5 times larger what observed for the circular configuration. In the chevron jet, peak activity of stretching and tilting (<|**S**|>=0.45 and <|**T**|>=0.57) is found at Z/D=2.8, where the streamwise vortices “ST” and “SR” begin to decay and “C” structures are formed. Further downstream, instead, they decrease of approximately 30% at Z/D=4.

In the circular case, <|**S**|> and <|**T**|> show a steep increase for $2<Z/D<5$, where the flow is characterized by vortex pairing and by fast growth of azimuthal instabilities and streamwise filaments. Between Z/D=5.5 and 6, where toroidal vortices undergo breakdown, <|**S**|> and <|**T**|> reach peak activity, although with maximum tilting (<|**T**|>=0.72 at Z/D=5.5) that is

20% larger than the peak of stretching. Further downstream (*Z/D*>6.5), in correspondence with the formation of “VF” structures and the coherence decay, <|**S**|> and <|**T**|> decrease to values that are comparable to those found for vortex pairing and early growth of azimuthal and streamwise vortices.

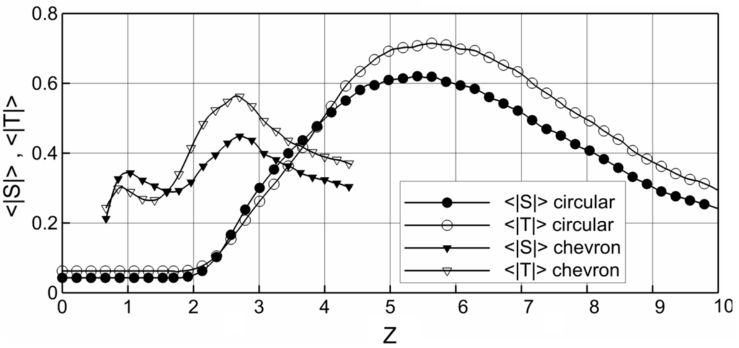

Figure 5.35 Axial distribution of space-time average of stretching and tilting vectors

5.8 Conclusions

The three-dimensional behavior of flow transition in circular and 6-chevron jets at *Re*=5000 has been investigated with time-resolved TOMO PIV. The vortex topological analysis using vorticity and λ_2-criterion shows differences in the large-scale flow organization between the circular and the chevron configuration.

In the circular case, the flow is characterized by a pulsatile motion leading to the shedding of vortex rings with a Strouhal number of 0.72. Between 2.75 and 3.5 jet diameters, vortex rings pair with a characteristic frequency of *St*=0.36. This process is characterized by peaks of axial and radial turbulence in the shear layer. The first and second pairing amplify the axial pulsatile motion in the jet column and lead to the axial strain, which induces the formation of three-dimensional patterns such as vortex-azimuthal instabilities and counter-rotating streamwise vortices of axial and radial vorticity (“ST” and “SR”, respectively). On average of 4 primary azimuthal waves grow on the vortex ring, leading to in-plane and out-of-plane deformation. Streamwise vortices “ST” and “SR” are distributed around the vortex rings with an angle of 30-40 degrees to the jet axis and they move with a characteristic inward-outward radial motion that is induced by the passage of the vortex rings. The axial vorticity peaks of “ST” are typically 50% larger than the radial ones of “SR”. At *Z/D*=3.2, a total of 11 streamwise vortex “ST” develop from the braid region and typically form 4 main streamwise pairs that interact with the vortex ring. The modal decomposition of axial vorticity shows that, in the azimuthal direction, the vortex rings and the streamwise vortices are characterized by energy peak at wave number *k*=4 with a phase shift of π. The axial vorticity induced by streamwise pairs on the vortex ring is staggered in phase opposition at the regions of interaction, where primary instabilities grow. With the growth of in-plane azimuthal instabilities, vortex ring humps are tilted and ejected along the axial direction as they are subjected to higher axial velocities. By the end of the potential core, this process culminates in the breakdown of the toroidal shape into streamwise filaments oriented at 30-45 degrees to the jet axis and peripheral structures of “C” shape. The latter re-organize as filaments oriented along the azimuthal direction in the region downstream of the potential core and, are largely responsible for the flow entrainment. In the vicinity of the jet axis, instead, vortex filaments show a scattered orientation.

The 3D flow organization is statistically investigated by applying the snapshot-POD technique to the velocity and vorticity fields. While the velocity decomposition is based on the kinetic energy, the vorticity one is referred to the flow enstrophy. The attention is focused on the description of the first 10 modes, which capture 27.5% of the total kinetic energy in the velocity decomposition and 20% of the total flow enstrophy in the vorticity decomposition. The first pair of velocity and vorticity modes, which are the most energetic ones, describe the presence of vortex rings travelling after pairing. In the velocity modes, the axial velocity component identifies a helical motion in the region across the end of the potential core and a flapping motion further downstream. It also shows a precession motion that develops downstream the end of the potential core. On the other hand, the radial and the azimuthal components respectively identifies wave-like and twisting motions between $Z/D=6$ and 10. In the vorticity decomposition, the first pair of modes shows that travelling vortex rings are characterized by the radial and axial vorticity fields developing across the end of the potential core with a characteristic 40-45 degree inclination to the jet axis. Such patterns, also observed in mode pairs at lower energy, are ascribable to the process of vortex ring breakdown.

Snaphot-POD analysis is also applied to the Lamb vector based on the L_2-norm of the fluctuating component. In Powell’s aeroacoustic analogy, the Lamb vector accounts for the flow state. The attention is focused on the description of first 10 modes, which capture 30.3% of the total *Lamb energy* content in the Lamb vector. The first pair of Lamb vector modes describe vortex ring travelling after pairing, where the characteristic azimuthal coherence of the rings is identified by the radial and the axial components of the Lamb vector and not by the azimuthal component as seen in the corresponding vorticity modes. In the region across the end of the potential core, the motion of the rings is accompanied by the development of a three-dimensional disturbance at 40-45 degree to the jet axis that is described by the azimuthal component. Travelling rings after shedding are identified by mode pairs at lower energy #3-#4, #5-#6 and #7-#8. In these last two, for $Z/D>5$, the azimuthal component describes a travelling wave with axial swirling at an angle of 40-45 degrees to the jet axis.

In the chevron jet, the column is characterized by a pulsatile motion ($0.56<St<0.85$) and the axisymmetric ring-like coherence observed for the circular jet is replaced by streamwise flow structures of azimuthal (“SA”), axial (“ST”) and radial (“SR”) vorticity that are formed at the nozzle exit. “SA” filaments develop from the nozzle apexes, while 6 counter-rotating pairs of streamwise vortices “STP” and “SRP” are formed at the nozzle exit in a position corresponding to the chevron notch, where the radial velocity is maximum, and they extend downstream up to *Z/D*=4. The maximum of radial vorticity associated with “SRP” structures is twice larger than that observed for the “STP” ones. Between *Z/D*=2.5 and 3, the shear layer is organized in “C” shaped vortices which, inducing inward radial flow, may be responsible for the tilting of the streamwise structures towards to the jet axis.

The stretching and tilting fields are analyzed in relation to the coherent structures. In the circular case, instantaneous activity is observed with the rise of three-dimensional patterns. It is associated with azimuthal instabilities and streamwise vortices and is maximum during the formation of “C” structures and the ejection of vortex humps. Beyond the end of the potential core, instead it drops of 60%. In the chevron jet, stretching and tilting peak activity corresponds to the region where “C” structures are formed, and interact with streamwise filaments.

Chapter 6

3D aeroacoustic source characterization and jet noise prediction

Violato D and Scarano F (2013), Three-dimensional vortex analysis and aeroacoustic source characterization of jet core breakdown, *Physics of Fluids*, 25, 015112, DOI 10.1063/1.4773444.

6.1 Introduction

Early experimental investigations on subsonic jet noise showed that the production of acoustic waves is mainly related to unsteady mechanisms involving large coherent flow structures (section 2.2.1), such as vortex rings in circular jets (Bradshaw *et al*. 1963; Crow and Champagne, 1971; Juvé *et al*., 1979).

Vortex rings generate sound by pairing **(**Bridges and Hussain, 1987; Laufer and Yen, 1983; Schram *et al.*, 2005), by azimuthal oscillations (Kopiev and Chernyshev, 1997; Kopiev *et al.*, 1999; Coiffet *et al.*, 2006) and by their disruption (Hussain and Zaman, 1981; Hussain, 1986). Noise emission are also generated by the collapse of the annular mixing-layer at the end of the potential core (Jordan and Gervais, 2008), by sudden decelerations due to the engulfment of fluid by toroidal structures (Juvé *et al.*, (1980) and the acceleration and stretch of vortical structures when moving towards the jet axial region (Bogey *et al*., 2003)

Michalke and Fuchs reported that the most radiating events in the Strouhal number range between 0.2 and 1, while Bradshaw *et al*. (1963) hypothesized that the loss of azimuthal coherence by artificial augmentation of streamwise structures, such as by lobed nozzles, could lead to lower sound emissions. This was also reported in later studies for chevron jets at high Reynolds number (Bridges and Brown, 2004; Opalski *et al.*, 2005; Alkislar *et al.* 2007; Uzun and Hussaini, 2009; Xia *et al.*, 2009).

The use PIV in combination with aeroacoustic analogies is a relatively recent strategy to investigate the sources of acoustic noise (see section 1.5.3 and 1.6). In a Mach 0.85 jet, Seiner *et al.* (1998) characterized the noise sources using two-point turbulence statistics to evaluate the Lighthill turbulent stress tensor and observed that the actual measurement of the Lighthill's acoustic tensor requires volumetric measurements with temporal resolution. In a subsonic and acoustically excited jet at low Reynolds number, Schram *et al.* (2005) investigated the mechanism of sound generation by vortex pairing with phase-locked planar PIV and a conservative formulation of vortex sound theory for axisymmetric flow, finding good agreement between the sound prediction and the sound measured by microphone at frequencies not contaminated by the acoustical excitation. The use of time-resolved experiments to determine the sound produced by the early transition stage due to vortex pairing (Schram et al, 2005) has been extended to the natural transition case by Violato *et al.* (2010).

6.2 Objectives

In this chapter, following Powell's analogy (1964), the acoustic source is associated with the second time derivative of the Lamb vector (see section 3.3.3). Although the current experiment does not enable to resolve all the spatial scales at which acoustic fluctuations are produced, the time-resolved TOMO PIV measurements (temporal resolution up to *St*=4) are employed to explore the role of coherent structures of circular jets, i.e. vortex rings, streamwise vortices, vortex filaments and C-structures, in the local activity of the instantaneous acoustic source. An analogous analysis is also proposed for chevron jet.

For the circular configuration, the analysis of the 3D pattern of the acoustic source is aided by the POD, which enables to identify more clearly some aspects of the flow large-scale organization, especially at core breakdown. Finally, acoustic predictions are performed by direct integration Powell's analogy using TR-TOMO PIV data.

6.3 Instantaneous patterns of the acoustic source

The relation between the large-scales structures and the local activity of acoustic sources in the region across the end of the potential core is explored recalling Powell's aeroacoustic analogy (1964). As discussed in section 3.3.3, the acoustic source can be mapped using the norm of the second time derivative of the Lamb vector ($\ddot{L} = \left| \left(d^2\mathbf{L} / dt^2 \right) \right| D^3 / W_j^4$) and can be discussed in relation with the coherent structures (described by the λ_2-criterion).

The instantaneous flow organization of the circular jet is compared with the corresponding acoustic source activity in Figure 6.1 by iso-surfaces and in Figure 6.2 by iso-contours on plane *Y/D*=0. The pattern yields evidence that the activity of $\ddot{L}$ is more intense for core breakdown than for the case of vortex pairing (Hussain and Zaman, 1981). The transient phenomenon of core breakdown, however, weakens rapidly and, beyond the end of the potential core, the region interested by $\ddot{L}$ activity collapses within 3 jet diameters. The peripheral region (0.8<*R/D*<1.6) exhibits "VF" structures (Figure 5.13) which are related with low sound production activity.

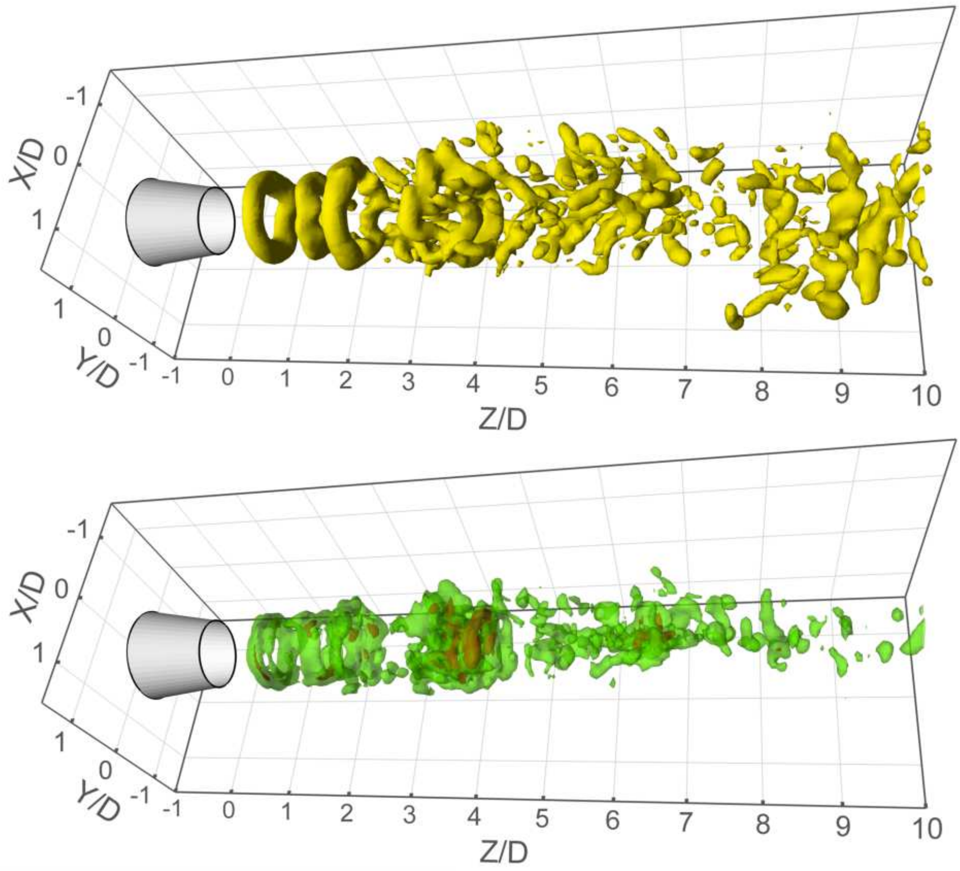

Figure 6.1 Circular jet: instantaneous vortex pattern (iso-surfaces $\lambda_2 D/W_j$ =-0.8 in yellow) and corresponding acoustic source (iso-surfaces $\ddot{L}$ =30 in green and $\ddot{L}$ =50 in red)

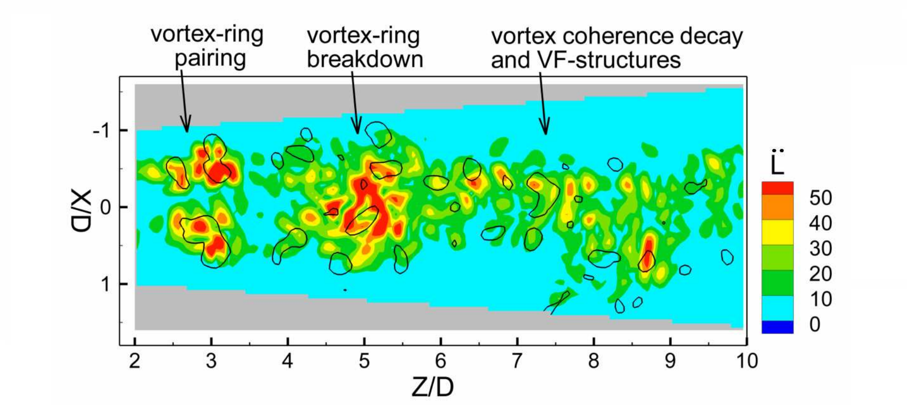

Figure 6.2 Instantaneous iso-contour plot of $\ddot{L}$ and iso-line $\lambda_2 D/W_j$ =-0.8 identifying coherent structures

The three dimensional acoustic source during the pairing of vortex “1” and “2” is illustrated in Figure 6.3. Production of $\ddot{L}$ =30 is observed downstream of Z/D=2.5 (see vortex “3”). Acoustic source peak activity $\ddot{L}$ =50 is observed associated with to the rise of azimuthal instabilities (“1” and “2”) and the streamwise structures vortices (“S”).

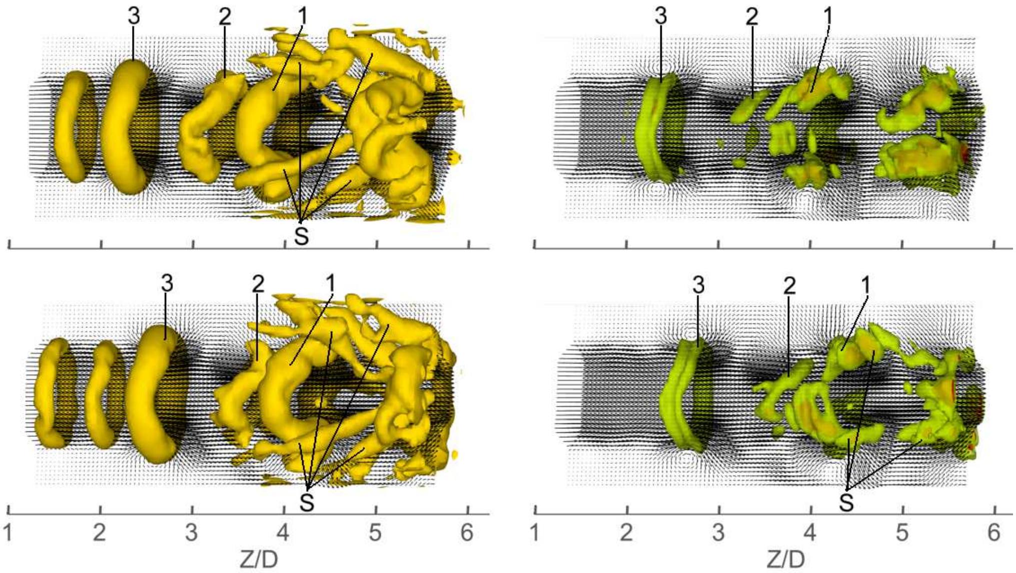

Figure 6.3 Circular jet: time sequence visualization of (left) flow structures (iso-surface $\lambda_2 D/W_j$ =-0.5) and (right) corresponding acoustic source (iso-surfaces $\ddot{L}$ =30 in green and $\ddot{L}$ =50 in red).; velocity vector slice in the axial plane; $\Delta t W_j/D$=0.61

6.3.1 Vortex ring breakdown as main acoustic source event

The vortex patterns evolution and the corresponding acoustic source field during the breakdown process of a toroidal structure is shown in the temporal sequence of Figure 6.4. Before breakdown (tW_j/D=0), the acoustic source shows a strongly distorted toroidal configuration corresponding to the vortex ring. Subsequently, during the loss of azimuthal coherence (0.84<tW_j/D<1.68), the acoustic source becomes more pronounced in the region closer to the jet axis, where portions "P" of the vortex ring (Figure 5.12) are tilted and ejected along the jet axis. On the other hand, the rupture of the vortex into "C" structures is not associated to significant activity in terms of $\ddot{L}$.

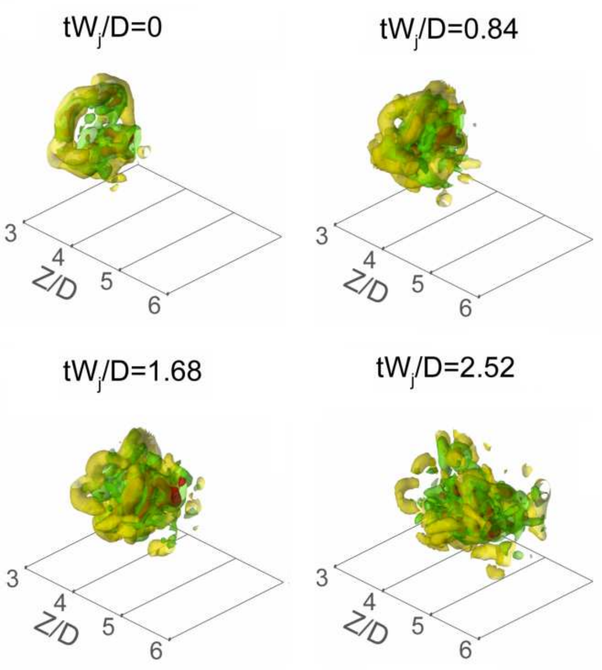

Figure 6.4 Time sequence visualization of vortex ring breakdown (iso-surfaces $\lambda_2 D/W_j$ =-0.8 in yellow) with acoustic source (iso-surfaces $\ddot{L}$ =30 in green and $\ddot{L}$ =50 in red)

6.3.2 The chevron jet

The acoustic source of the chevron jet is mapped and compared to the vortex patterns in Figure 6.5. The streamwise vortex pairs are not characterized by low source activity ($\ddot{L}$ <30). On the other hand, the acoustic source shows peaks of 50 in the region where the streamwise structures begin to decay and "C" vortices are formed (0<R<0.7, Z>2).

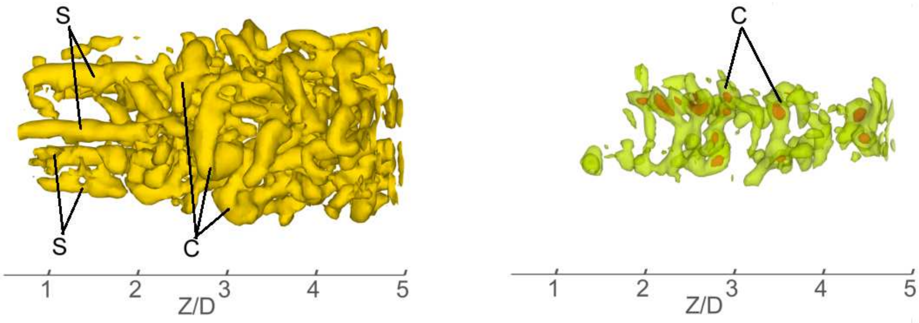

Figure 6.5 Chevron jet: instantaneous (left) flow structures (iso-surface $\lambda_2 D/W_j$ =-0.5) and (right) corresponding acoustic source (iso-surfaces $\ddot{L}$ =30 in green and $\ddot{L}$ =50 in red)

6.3.3 Statistical characterization of the acoustic source

The acoustic source activity is statistically characterized along the jet axis. Equation (5.2) is applied to $\ddot{L}$ between R/D=0 and R/D=1 and the corresponding axial distribution $\overline{\langle \ddot{L} \rangle}$ is shown in Figure 6.6.

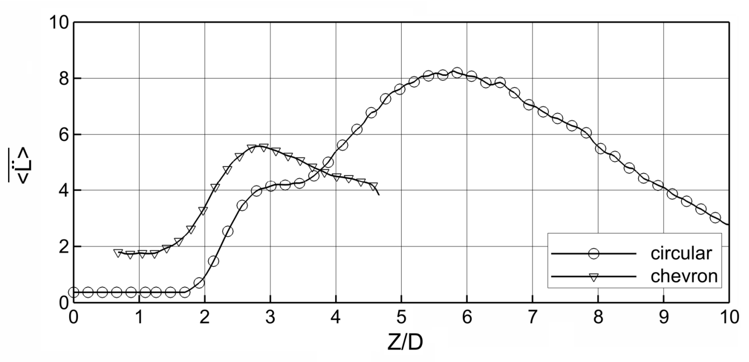

Figure 6.6 Space-time average of $\ddot{L}$

In the circular jet. the axial distribution of the source increases rapidly between 2 and 3 diameters due to the vortex pairing. A subsequent increase of comparable magnitude yields peak activity of $\overline{\langle \ddot{L} \rangle}$ between Z/D=5.5 and 6 where the portions “P” of vortex rings are stretched, tilted and then axially ejected yielding the disruption of the toroidal coherence

(Figure 5.12). Beyond the end of the potential core, $\overline{\langle \ddot{\mathrm{L}} \rangle}$ decays and at *Z/D*=10 the value is lower than that in the pairing region.

In the chevron jet, $\overline{\langle \ddot{\mathrm{L}} \rangle}$ shows a pronounced activity of 5.5 at *Z/D*=2.8, where “C” structure are formed and streamwise-vortex pairs (“S”) lose coherence. Compared to the value found at *Z/D*=0.8 (1.8), the peak activity is 3 times larger. For *Z/D*>2.8, $\overline{\langle \ddot{\mathrm{L}} \rangle}$ decreases with a 30% drop at *Z/D*=4.7.

6.4 3D modal decomposition

For the circular jet, $d^2\mathbf{L}/dt^2$ fields are analyzed by POD analysis to objectively inspect the three-dimensional features of the acoustic source. The decomposition is based a subset of snapshots that are extracted with a sampling rate of 100 Hz from the time-resolved sequence. A total of 190 snapshots are employed, which correspond to an observation length of 100 jet diameters that is shorter compared to the velocity, vorticity and Lamb vector ones (1000 jet diameters).

As shown in Figure 5.14, the modes of the first pair of the $d^2\mathbf{L}/dt^2$ decomposition are respectively associated with 7.01% and 6.81% of the total *acoustic* source energy (eq.(3.34)). The first 10 POD modes of the Lamb vector second time derivative ($d^2\mathbf{L}/dt^2$) capture 31.9% of the total *acoustic source energy* (eq. (3.34) and Figure 5.14). The first 5 pairs of modes (#1 and #2, #3 and #4, #5 and #6, #7 and #8, #9 and #10) identify travelling waves as shown in Figure 6.7. As seen in the Lamb vector modes, the azimuthal coherence is identified by the radial and the axial components ($\left(d^2L_r/dt^2\right)D^3/W_j^4$ and $\left(d^2L_z/dt^2\right)D^3/W_j^4$) which, in the region upstream of the end of the potential core, resemble a wave-packet organization (Cavalieri *et al.* 2011a and 2011b). On the other hand, the azimuthal component $\left(d^2L_\theta/dt^2\right)D^3/W_j^4$ typically identifies the development of three-dimensional disturbances.

The first pair of $d^2\mathbf{L}/dt^2$ modes describes the axisymmetric motion related to toroidal vortices after pairing (*St*=0.36, Figure 6.9). The vortices identified by $\left(d^2L_r/dt^2\right)D^3/W_j^4$ and $\left(d^2L_z/dt^2\right)D^3/W_j^4$ have spatial wavelength that is half of the pairing modes, as illustrated in Figure 6.7 where the iso-surfaces of mode *k*=1 are plotted together with the mid plane vector field of the velocity mode #1. On the other hand, by the end of the potential core (4.5<*Z/D*<6.5), where vortex rings disrupt (Figure 5.12) and the acoustic source is more pronounced (Figure 6.4 and Figure 6.6), the iso-surfaces of $\left(d^2L_r/dt^2\right)D^3/W_j^4$ and $\left(d^2L_z/dt^2\right)D^3/W_j^4$ show a gradual decay of the axisymmetric coherence.

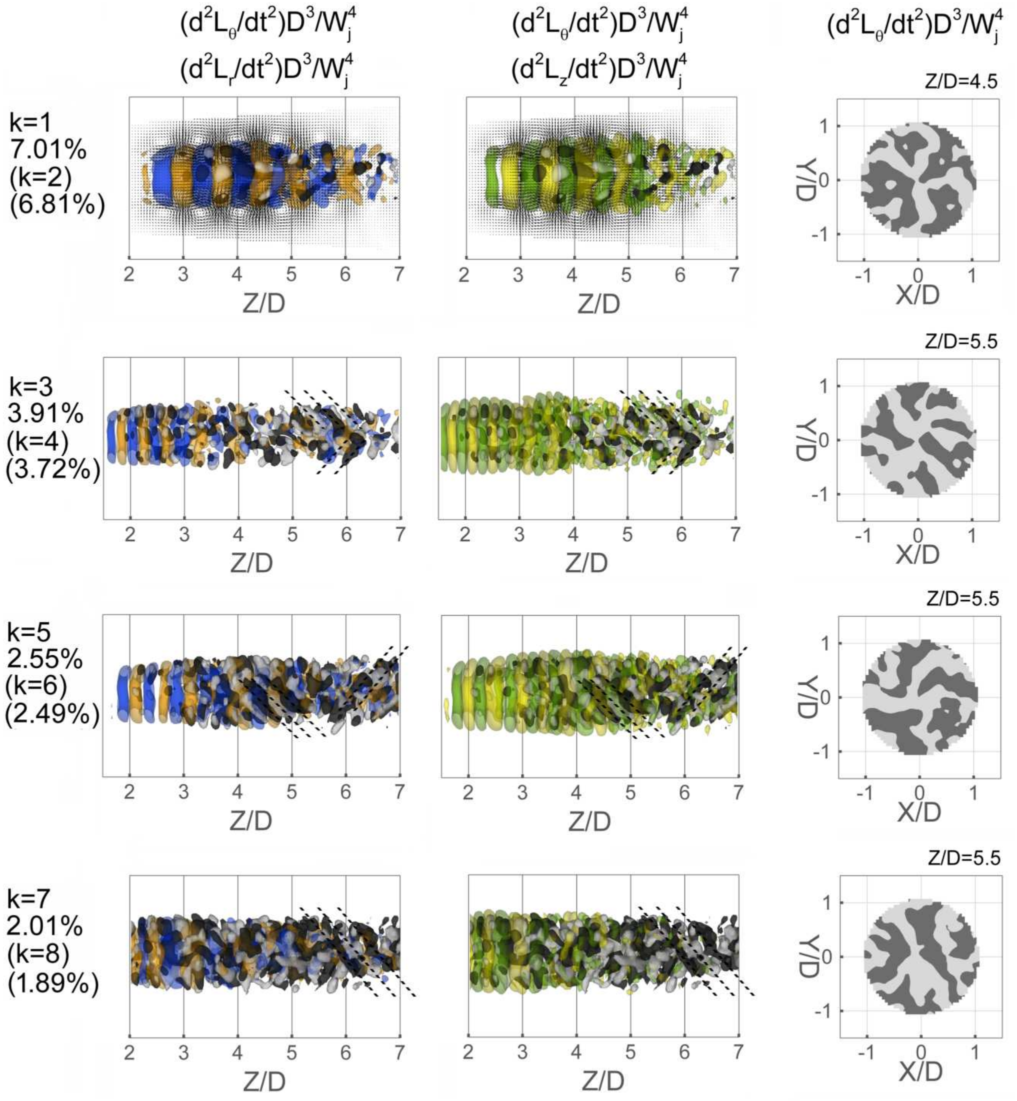

Figure 6.7 POD modes of the second time derivative of the Lamb vector describing travelling waves. Between brackets mode number and energy of the coupled mode. Left: iso-surfaces of $\left(d^2L_\theta/dt^2\right)D^3/W_j^4$ (positive in light grey; negative in dark grey) and $\left(d^2L_r/dt^2\right)D^3/W_j^4$ (positive in orange and negative in blue); center: iso-surfaces of $\left(d^2L_\theta/dt^2\right)D^3/W_j^4$ (positive in light grey; negative in dark grey) and $\left(d^2L_z/dt^2\right)D^3/W_j^4$ (positive in yellow and negative in green); right: cross-sectional iso-contour of $\left(d^2L_\theta/dt^2\right)D^3/W_j^4$

By color-coding these iso-surfaces with iso-contour of *Z/D* (Figure 6.8), it is possible to observe four humps (“Ps”), meaning of azimuthal instabilities with a wave number *k*=4. This wave number is also reported for the radial and the axial components of vorticity modes #3-#4 (Figure 5.17) and #10 (Figure 5.18), as well as for the azimuthal component of Lamb vector mode #3-#4 (Figure 5.19).

While in mode #1-#2 the iso-surfaces $\left(d^2L_\theta/dt^2\right)D^3/W_j^4$ do not exhibit any recurrent pattern, in mode #3-#4 they identify filaments at 40-45 degrees to the jet axis, as similarly reported for the vorticity and the Lamb vector modes (Figure 5.17, Figure 5.19). Such filaments describe travelling waves in the region by the end of the potential core (4.5<*Z/D*<6), where vortex rings disrupt (Figure 5.12) and the acoustic source becomes pronounced (Figure 6.4 and Figure 6.6). On the other hand, the radial and the axial components of mode #3-#4 describe travelling toroidal vortices that are related to the vortex shedding. Note that the spatial wavelength shown is half of the shedding modes observed in the velocity, vorticity and Lamb vector decomposition. Mode #3-#4 is associated with the shedding frequency (*St*=0.72) of ring vortices, and with a secondary frequency (*St*=1.9), that can instead be attributed to the three-dimensional travelling wave in the region by the end of the potential core. Patterns similar to mode #3-#4 are observed for mode pairs #5-#6, #7-#8 and #9-#10 also in the region across the end of the potential core (5<*Z/D*<7). For conciseness, Figure 6.7 does not show the latter pair.

While velocity, vorticity and Lamb vector modes are generally associated with values of the Strouhal number smaller than 1 (Figure 5.21), the modes of $d^2\mathbf{L}/dt^2$ are related to higher values (Figure 6.9), such as mode pair #3-#4 (*St*=1.9), mode pair #5-#6 (*St*=1.05), mode pair #7-#8 (*St*=1.15 and 1.42) and mode pair #9-#10 (*St*=1.28 and 1.48).

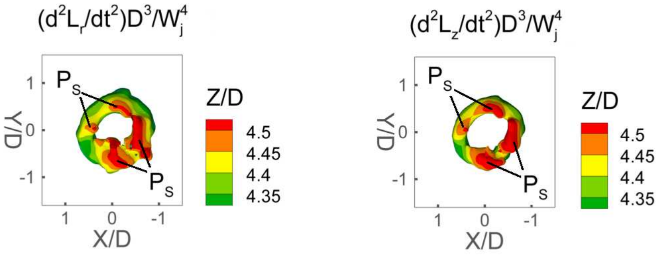

Figure 6.8 Detail of mode #1 of the second time derivative of the Lamb vector between *Z/D*=4.3 and 4.5. Positive iso-surfaces of $\left(d^2L_r/dt^2\right)D^3/W_j^4$ and $\left(d^2L_z/dt^2\right)D^3/W_j^4$ color coded with *Z/D*

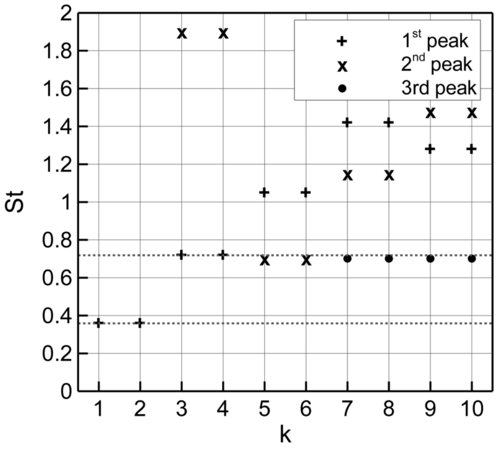

Figure 6.9 Spectrum peaks of POD $d^2\mathbf{L}/dt^2$ mode time coefficients

6.5 Noise prediction based on 4D PIV measurements

The phenomenological analysis given so far shows that the experiments are conducted at a resolution that enables to appreciate the details of the vortex interactions and their connection to the local pattern of the Lamb vector and its second temporal derivative. Following the work by Schram *et al.* (2005), it was shown that, under the assumption of axisymmetric flow, time-resolved planar PIV can be applied to predict the sound of pairing vortices by direct evaluation of Powell’s analogy (Violato *et al.* 2010). With DNS tailored on the TR-TOMO PIV jet experiment performed in this study, Moore *et al.* (2010) showed that, for the circular jet, the acoustic source can be localized by a domain that extends from the nozzle exit to 3-4 jet diameters beyond the end of the potential core. This is the case of the available measurements that, being performed over a jet axial extent that is sufficiently long (10 jet diameters), capture the large-scale events from the nozzle to 4 jet diameters beyond the end of the potential core (Figure 5.1).

When experimental data are concerned, the effective conservation of the flow impulse I (eq. (2.33)) and the kinetic energy T (eq. (2.35)) can be used as a-posteriori indicators of the suitability of the measurements for the sound prediction (section 2.3.2). Figure 6.10 shows the time history of axial and radial components of the flow impulse I and the kinetic energy T evaluated over the measurement domain during 2 periods of vortex pairing. The trend shows negligible fluctuations ascribed to the flux through the outflow boundary. The normalized *rms* fluctuations ($rmsI_r$=0.75; $rmsI_z$=0.53; $rmsT$=0. 24) are smaller than 15% of the corresponding mean value and they are comparable with those reported by Schram (2003).

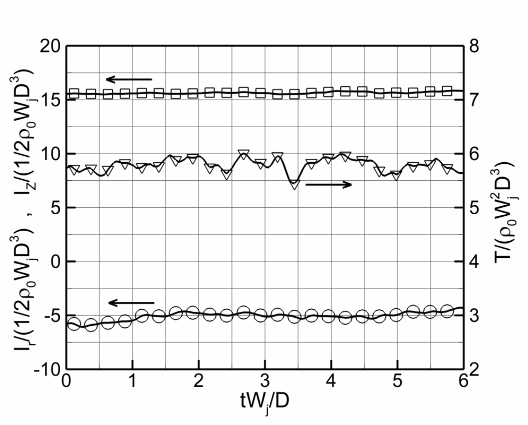

Figure 6.10 Impulse and kinetic energy time history during 2 period of vortex pairing. Axial impulse I_z (square symbol); radial symbol I_r (circular symbol); kinetic energy T (gradient symbol)

Acoustic predictions are performed based on Powell's analogy for a listener positioned at 90 degrees to the jet axis at a distance R_L. Thus, eq. (2.40) reduces to

$$p'(\mathbf{x},t) = -\frac{\rho_0}{4\pi c_0^2 R_L^3}\frac{\partial^2}{\partial t^2}\int_{Z_1}^{Z_2}\int_0^{2\pi}\int_0^{R_c(Z)} y_r\, L_r\big|_{t^*} \det(\mathbf{J})\, dR\, d\theta\, dZ\ . \tag{6.1}$$

where $R_c(Z) = 0.065Z + 1$ is the radius function of the conical domain and L_r is the radial component of the Lamb vector which is the only term accounting for the flow state.

The fluctuating component of L_r , $L_r' = L_r - \overline{L_r}$ (where $\overline{L_r}$ is the mean value) is damped at the domain boundaries using flat-Hann window function following Obrist and Kleiser (2007), who showed its benefits in limiting the effects of source spatial truncation.

Considering damping lengths at the inflow, outflow and radial boundary, respectively $\alpha\Delta Z$, $\beta\Delta Z$ (where $\Delta Z = Z_2 - Z_1$) and $\zeta R_C(Z)$ with $0 \le \alpha \le 1$, $0 \le \beta \le 1$ and $0 \le \zeta \le 1$, the flat-Hann window function along the axial direction reads as

$$h_z(Z) = \begin{cases} \dfrac{Z}{\alpha\Delta Z} - \dfrac{1}{2\pi}\sin\left[\dfrac{2\pi Z}{\alpha(\Delta Z)}\right] & Z_1 < Z < \alpha\Delta Z \\ 1 & \alpha\Delta Z \le Z \le (1-\beta)\Delta Z \\ \dfrac{(\Delta Z - Z)}{\beta\Delta Z} - \dfrac{1}{2\pi}\sin\left[\dfrac{2\pi(\Delta Z - Z)}{\beta\Delta Z}\right] & (1-\beta)\Delta Z \le Z \le Z_2 \\ 0 & elsewhere \end{cases} \tag{6.2}$$

while along the radial direction is

$$h_r(R) = \begin{cases} 1 & 0 \le R \le \zeta R_C(Z) \\ \dfrac{\left(R_C(Z)-R\right)}{\zeta R_C(Z)} - \dfrac{1}{2\pi}\sin\left[\dfrac{2\pi\left(R_C(Z)-R\right)}{\zeta R_C(Z)}\right] & (1-\zeta)R_C(Z) \le R \le R_C(Z) \\ 0 & elsewhere \end{cases} \tag{6.3}$$

Substituting equations (6.2) and (6.3) into equation (6.1) gives

$$p'(\mathbf{x},t) = -\frac{\rho_0}{4\pi c_0^2 R_L^3}\frac{\partial^2}{\partial t^2}\int_{Z_1}^{Z_2}\int_0^{2\pi}\int_0^{R_c(Z)} y_r\left(h_z h_r L'_r\big|_{t^*} + \overline{L_r}\right)\det(\mathbf{J})\,dR\,d\theta\,dZ\ . \tag{6.4}$$

Acoustic predictions are performed for a listener located at a distance $R_L=10^3$m, which satisfies the far-field assumption of ($R_L >> \lambda$[1]). The acoustic pressure spectrum illustrated in Figure 6.11 (black line) is obtained evaluating equation (6.4) with TR-TOMO PIV data between $Z_1/D=0$ and $Z_2/D=10$. It shows low-frequency peaks of sound pressure level SPL=-141.5 dB and -143.5 dB that, respectively, correspond to the vortex pairing (St=0.36) and shedding (St=0.72) frequencies, which is in agreement with Bridges and Hussain (1987). It is remarked here that hydrophone measurements of such acoustic waves are unfeasible as they should be conducted at a distance of 1 kilometer from the jet.

The spectrum also shows smaller peaks at higher frequency, which belong to a broader hump (1<St<2.75). To understand the importance of spatial domain truncation on the acoustic spectra, acoustic predictions are conducted for axial lengths of the domain varying between 6 to 10 jet diameters and the obtained spectra are compared in Figure 6.12. When the domain extends from Z_1/D =0 to $9 \le Z_2/D \le 10$, spectra show maximum variations of 2 dB for $St \le 2.25$. For shorter domains ($6 \le Z_2/D \le 8$), in contrast, they exhibit larger amplitude drop and profile variations. From the above discussion, the estimated values of SPL between St=0 and 2.25 can be reasonably considered to be associated with flow events rather than domain spatial truncation. Note that the frequencies associated with three-dimensional waves of $d^2\mathbf{L}/dt^2$ evolving by the end of the potential core (Figure 6.9; mode #3-#4: St=1.9; mode #5-#6: St=1.05; mode #7-#8: St=1.15 and 1.42; mode #9-#10: St=1.28 and 1.48) where vortex rings disrupt (Figure 5.12) and the acoustic source is more pronounced (Figure 6.6), lie in the range of the acoustic spectral hump (1<St<2.25).

Exploiting the linearity of the integral function (see equation (6.4)), the acoustic source can be mapped by the second time derivative of the radial component of the Lamb vector d^2L_r/dt^2. Temporal sequences of such quantity during vortex ring breakdown show the existence of characteristic frequencies that are between 3 to 7 times higher than the pairing frequency. An example of "life-cycle" of the source is given in Figure 6.13, which shows the evolution of region "A" in a period of time TW_j/D=0.45, corresponding to St=2.1, which agrees fairly well with the range of frequencies interested by the spectral hump (St=1 and 2.25) reported in Figure 6.11. This observation further confirms the dominant role of vortex ring disruption for acoustic production and collocates it in the frequency spectrum at values of the Strouhal more than two times larger than that of vortex shedding.

---

[1] $\lambda = c_0/f$, being λ the typical acoustic wavelength, c_0=1481m/s the speed of sound and f=15Hz the pairing frequency. Thus λ = 99m.

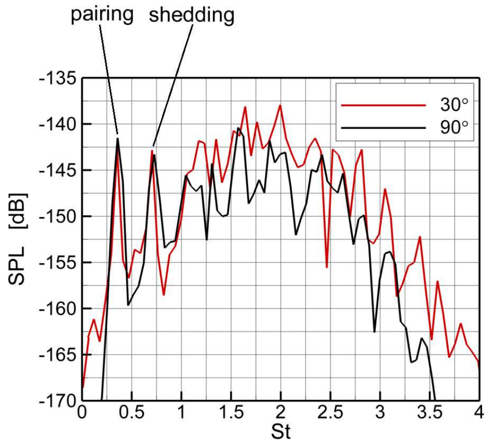

Figure 6.11 Predicted acoustic spectrum. Listener at 30 and 90 degrees to the jet axis; R_L= 10^3m (reference pressure: 20μPa)

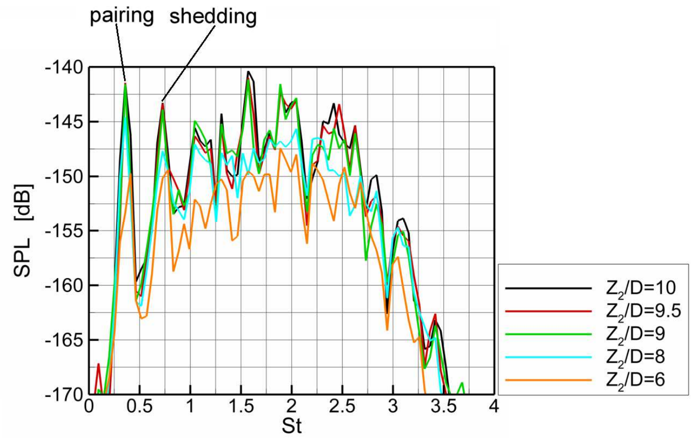

Figure 6.12 Predicted acoustic spectra obtained for different axial lengths Z_2/D of the domain (listener at 90 degrees to the jet axis; R_L= 10^3m; reference pressure 20μPa)

Finally, acoustic predictions are performed for a listener positioned at 30 degrees to the jet axis (R_L=10^3 m) using the data between Z_1/D=0 and Z_2/D=10. Similarly to eq. (6.4), the flat-Hann damping functions h_r (eq. (6.3)) and h_z (eq. (6.2)) are substituted in Powell analogy (eq. (2.40)) where they are applied to the fluctuating components of the Lamb vector $\mathbf{L}' = \mathbf{L} - \overline{\mathbf{L}}$ (where $\overline{\mathbf{L}}$ is the mean value). The equation that is then evaluated is

$$p'(\mathbf{x},t) = -\frac{\rho_0}{4\pi c_0^2 R_L^{\;3}} \frac{\partial^2}{\partial t^2} \int_{Z_1}^{Z_2} \int_0^{2\pi} \int_0^{R_c(Z)} \left(\mathbf{x}\cdot\mathbf{y}\right)\left[\mathbf{x}\cdot\left(h_r h_z \mathbf{L}'\big|_{t*} + \overline{\mathbf{L}}\right)\right] \det(\mathbf{J}) dR d\theta dZ \; . \qquad (6.5)$$

The resulting acoustic pressure spectrum (Figure 6.11, red line) shows peaks *SPL*=-143 dB and -141 dB that, respectively, correspond to the vortex pairing and shedding frequencies. This resembles the spectrum obtained at 90 degrees, despite discrepancies of about 1 dB. At 30 degrees, the acoustic spectrum is characterized by a broader hump (only the range $1 \le St \le 2.25$ is considered to be associated with flow events) featuring SPL levels typically 3 dB higher than those found at 90 degrees. This result is in agreement the jet noise directivity previously documented (Lush, 1971; Stromberg *et al.*, 1980; Bogey *et al.*, 2003)

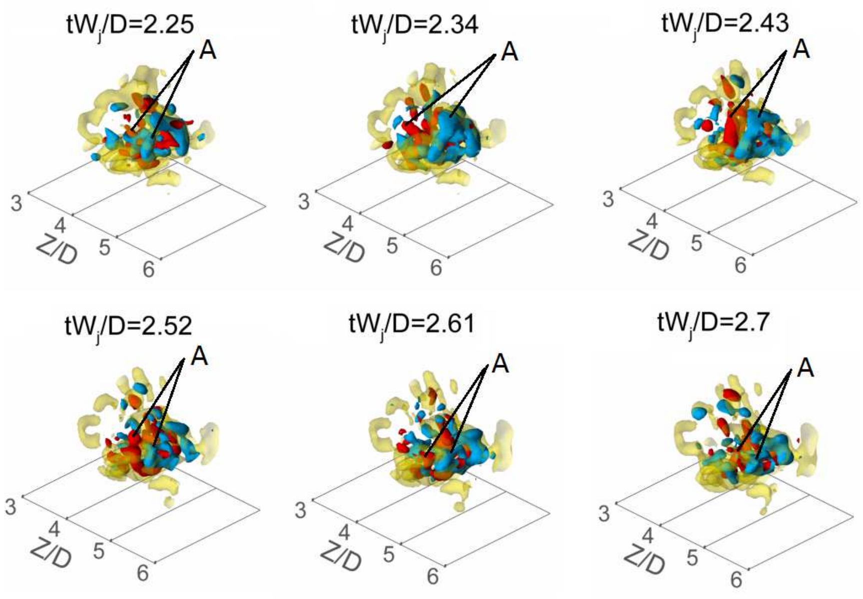

Figure 6.13 Time sequence visualization of acoustic source during vortex ring breakdown. Iso-surfaces $\left(d^2L_r/dt^2\right)D^3/W_j^4$ =-20 (blue) and 20 (red); iso-surfaces $\lambda_2 D/W_j$ =-0.8 (yellow)

6.6 Conclusions

The relation between coherent flow structures and the instantaneous acoustic source is investigated recalling Powell's analogy. The second time derivative of the Lamb vector is associated with the acoustic source. Its spatio-temporal evolution is visually compared to that of the vortices, which are detected by λ_2-criterion, to identify flow events involved in the acoustic generation. In the circular jet, high source activity is observed for the vortex pairing, azimuthal instabilities and streamwise filaments. However, the most intense source activity is observed by the end of the potential core when in-plane vortex ring humps are tilted and ejected leading to the vortex ring breakdown. During this process, the source is observed to lose the initial toroidal shape and to congregate in the proximity of the jet axis. In the chevron jet, peak activity is observed during the process of streamwise vortex decay and C structure formation (Z/D=2.8). At this location, a statistical characterization of the Lamb vector second time derivative shows a peak for the chevron, while for the circular configuration the highest activity is reported between Z/D=5.5 and 6, which corresponds to the region of vortex ring disruption by the ejection of in-plane humps.

For the circular jet, snapshot-POD analysis is applied to the second time derivative of the Lamb vector, which, following Powell's aeroacoustic analogy, is used to identify the acoustic source. The attention is focused on the description of first 10 modes, which capture 31.9% of the total *acoustic source energy*. The radial and axial components of the modes resemble a wave-packet organization with an axisymmetric pattern that gradually decays by the end of the potential core. Such pattern is particularly clear in the first mode pair, where the radial and the axial components identify a travelling wave related to vortex pairing, but with halved spatial wavelength, featuring the growth of four primary azimuthal waves. The other four mode pairs are instead associated with the vortex shedding although they are characterized by halved spatial wavelength. In the region by the end of the potential core, where vortex rings disrupt and the acoustic source is more pronounced, the azimuthal component of mode #3-#4 also describes the development of a three-dimensional disturbance at 40-45 degree to the jet axis. Similar disturbances are detected by mode #5-#6, #7-#8 and #9-#10 in the region across the end of the potential core.

Compared to velocity, vorticity and Lamb vector modes, which are typically associated with Strouhal numbers smaller than 0.9, the mode #3-#4, #5-#6, #7-#8 and #9-#10 of $d^2\mathbf{L}/dt^2$ are also related to higher values ($1.05 \leq St \leq 1.9$), which are attributed to the three-dimensional disturbances developing in the region across the end of the potential core.

Far-field acoustic predictions are performed by direct evaluation of Powell's analogy with TR-TOMO PIV data. For a far-field listener positioned at 90 degrees to the jet axis, the predicted acoustic spectrum shows peaks at the pairing and the shedding frequencies and several peaks belonging to a single broader hump in the frequency range $1 \leq St \leq 2.75$. Frequencies $St \leq 2.25$ are found to be unaffected by domain spatial truncation when the domain length is chosen to be greater than 9 diameters.

The frequencies that are related to the three-dimensional waves of the Lamb vector second time derivative modes (St=1.9, mode #3-#4; St=1.05, mode #5-#6; St=1.15 and 1.42, mode #7-#8; St=1.28 and 1.48, mode #9-#10) lie in the range of the acoustic spectral hump

($1 \leq St \leq 2.25$). This, by the visual inspection of the acoustic source, can be ascribed to the breakdown of ring vortices.

Finally, far-field acoustic predictions are performed for a far-field listener at 30 degrees to the jet axis. The related spectrum shows peaks at pairing and shedding frequencies and a broader hump that, compared with the 90 degrees spectrum, lies in the same frequency range and shows SPL levels that are typically 3 dB higher.

Chapter 7

Lagrangian and Eulerian evaluation of pressure field

Violato D, Moore P, Scarano F (2011), Lagrangian and Eulerian pressure field evaluation of rod-airfoil flow from time-resolved tomographic PIV, *Experiments in Fluids*, 50:1057-1070.

This work investigates the rod-airfoil air flow by time-resolved Tomographic Particle Image Velocimetry (TR-TOMO PIV) in thin-light volume configuration. Experiments are performed at the region close to the leading edge of a NACA0012 airfoil embedded in the von Karman wake of a cylindrical rod. The 3D velocity field measured at 5 kHz is used to evaluate the instantaneous planar pressure field by integration of the pressure gradient field. The experimental data are treated with a discretized model based on multiple velocity measurements. The time separation used to evaluate the Lagrangian derivative along a fluid parcel trajectory has to be taken into account to reduce precision error. By comparing Lagrangian and Eulerian approaches, the latter is restricted to shorter time separations and is found not applicable to evaluate pressure gradient field if a relative precision error lower than 10% is required. Finally, the pressure evaluated from tomographic velocity measurements is compared to that obtained from simulated planar ones to discuss the effect of 3D flow phenomena on the accuracy of the proposed technique.

7.1 Introduction

The knowledge of accurate methods to evaluate pressure fields from PIV measurements has become of high interest in many fluid dynamic investigations.

Aeroacoustic predictions of flows interacting with body surfaces (Haigermoser 2009; Koschatzky *et al.* 2010; Lorenzoni *et al.* 2009) is a recent field where the aforementioned methods are applied to time-resolved PIV to extract the body-surface pressure distribution which is used to predict the instantaneous far-field acoustic pressure by means of Curle's analogy (1955). Higher accuracy in the pressure evaluation from PIV would lead to more reliable PIV-based sound predictions to be used together with computational aeroacoustics CAA (Crighton 1993), sensors and microphone arrays (Brooks and Humphreys 2003). Liu and Katz (2006) developed a scheme to evaluate the instantaneous pressure distribution by integrating the material acceleration computed from four-exposure PIV data which enabled to map the instantaneous planar pressure field. Measurements of material acceleration in turbulent flows were also done earlier by Voth *et al*. (1998) and La Porta *et al.* (2000) using particle tracking technique. In the investigation of the instantaneous pressure field around a square-section cylinder by time-resolved stereo-PIV, de Kat *et al*. (2008) demonstrated the accuracy of the pressure determination scheme (Gurka *et al.* 1999) following an Eulerian approach.

The PIV technique was used for noise investigation by Seiner *et al.* (1999) who, in the study of jet noise, applied two-point velocity correlation to evaluate Lighthill turbulent stress tensor. Schroeder *et al*. (2004) investigated the noise producing flow structures in the wake of a flat plate with elliptic leading edge by space–time correlations of the fluctuating z-component of the vorticity field. The explicit use of acoustic analogies for sound prediction with time resolved PIV was done by Haigermoser (2009) for cavity noise studies and, later, by Koschatzky *et al.* (2010).

For the rod-airfoil benchmark configuration (Jacob *et al.* 2004), Henning *et al.* (2009) recently investigated the mechanism of sound generation by means of simultaneous planar PIV in the near-field and phased-microphone-array measurements in the far-field. Cross-correlation between the acoustic pressure and velocity or vorticity fluctuations (Henning *et al*. 2008) was applied to characterize flow structures involved in noise production. From the temporal evolution of the cross-correlation coefficient, the authors suggested that the source region was located by the leading edge of the airfoil. With a similar experimental approach, the far-field aeroacoustic of the rod-airfoil configuration was investigated by Lorenzoni *et al*. (2009) who reported a favorable comparison for the tonal component between microphone measurements and predictions based on Curle's acoustic analogy (1955) applied to time-resolved planar PIV (TR PIV).

A number of issues have emerged from some of the mentioned studies. Except for computational approaches, no account has been made of the 3-D features in the flow due to intrinsic limitation of the planar two- and three-component PIV technique. In the investigation of the rod-airfoil flow, Lorenzoni *et al.* (2009) stated that a noise prediction more accurate than that obtained assuming 2-D flow could be achieved if 3-D flow effects are taken into account. Also, in the same investigation, the low temporal resolution limited the accuracy of the evaluated instantaneous pressure, as well as of the pressure time rate of change, which is of prior importance for the evaluation of Curle's aeroacoustic analogy. Furthermore, the question of whether the pressure gradient should be estimated from either an Eulerian (Baur and Kongeter 1999) or a Lagrangian approach (Liu and Katz 2006) has not been fully answered and experimentally verified.

7.2 Objectives

By this work, tomographic particle image velocimetry technique (Elsinga *et al.* 2006; Schroeder *et al.* 2008), in thin-volume configuration, enabling to fully describe the velocity gradient tensor, is applied to study the 3-D flow pattern of a rod-airfoil system similar to that investigated by Lorenzoni *et al.* (2009). To discuss the 3-D flow effects neglected in the work by Lorenzoni *et al.* (2009), pressure and material acceleration on the measurement domain midplane are compared to those evaluated from planar PIV. Furthermore, the measurements are performed at high time resolution in order to apply a multi-step technique (Moore *et al.* 2010) based on Liu and Katz (2006) scheme for an accurate evaluation of Lagrangian derivatives.

The work includes a brief theoretical background of a Lagrangian approach to evaluate the instantaneous planar pressure distribution from TR-TOMO PIV. The relation between the time separation and the precision and the truncation errors is recalled. Furthermore, the Lagrangian approach for material derivative evaluation is compared to the Eulerian one in terms of precision error at different values of the time interval. A criterion restricting the relative precision error to 10% on the material velocity derivative is given and, under such conditions, the instantaneous planar pressure evaluated from tomographic velocity fields is compared to that obtained from synchronous planar PIV velocity fields to discuss 3-D flow effects in rod-airfoil flow. At present time, limiting the precision error on the material acceleration to a value of 10% represents a realistic estimate for well-controlled PIV experiments.

7.3 Theoretical background

7.3.1 Pressure field evaluation

Curle's aeroacoustic analogy (1955), an extension of Lighthill's theory (1952), accounts for the noise production from solid objects interacting with an unsteady flow. In the analytical formulation for low Mach number, the acoustic pressure fluctuation in the far-field region is a function of the time rate of change of the pressure fluctuation integral on the surface of the body caused by the interaction with the flow. This means that the surface pressure distribution has to be measured in time to evaluate the pressure fluctuation in the acoustic domain. The instantaneous pressure field p can be inferred from the measurement of the time-resolved velocity field according to the incompressible (ρ=const) Navier Stokes equations

$$\nabla p = -\rho\left(\frac{D\mathbf{V}}{Dt} + \nu\nabla^2\mathbf{V}\right), \tag{7.1}$$

where

$$\frac{D\mathbf{V}}{Dt}=\frac{\partial\mathbf{V}}{\partial t}+\left(\mathbf{V}\cdot\nabla\right)\mathbf{V} \tag{7.2}$$

is the material acceleration. This can be computed either by means of eq. (7.2) with an Eulerian approach, as proposed by Baur and Kongeter (1999), or with the Lagrangian approach (Liu and Katz 2006). The suitability of both schemes for the accurate evaluation of the pressure gradient distribution is currently under discussion (de Kat and van Oudheusden 2010), of which an experimental study is provided in the following sections.

Also, the pressure gradient spatial integration in a planar domain has been approached in different ways. Liu and Katz (2006) proposed an omni-directional virtual boundary integration algorithm, instead van Oudheusden *et al.* (2007) used a direct 2D integration technique based on the work of Baur and Kongeter (1999). Later, the same authors, referring to the work of Gurka *et al.* (1999), reverted to the use of Poisson equation,

$$\nabla^2 p=-\rho\nabla\cdot\left(\frac{D\mathbf{V}}{Dt}+\nu\nabla^2\mathbf{V}\right) \tag{7.3}$$

which has demonstrated superior accuracy and showed to be less prone to localized error propagation (de Kat et al. 2008). In the latter Neumann boundary conditions

$$\nabla p=-\rho\frac{D\mathbf{V}}{Dt} \tag{7.4}$$

are applied, whereas Dirichlet conditions are assigned where p is known either by a direct measurement or by invoking Bernoulli's equation in region of steady and irrotational flow:

$$p-p_{ref}=-\frac{1}{2}\rho\left(\left|\mathbf{V}_{\mathbf{ref}}\right|^2-\left|\mathbf{V}\right|^2\right) \tag{7.5}$$

The evaluation of the sound source integral of the Curle's analogy (1955) would require the measurement of the surface pressure distribution along the entire airfoil span. However, despite the fact that thin-volume TOMO PIV enables the velocity measurement over a limited airfoil span-wise, it is relevant to evaluate the effect of the 3D-flow features on the pressure field, which is obtained under the hypothesis of 2D flow if based on planar PIV measurements. Furthermore, the scheme used for the evaluation of the material velocity derivative is studied in relation to the measurement accuracy. Therefore, experiments need to be conducted at sufficiently high temporal resolution in order to be able to decouple the effects of the latter from the above ones.

The material derivative evaluation along a fluid particle trajectory can be performed only if the time evolution of three-component velocity vector is measured inside a volume, such as obtained by TR-TOMO PIV. In particular, between two time instants t_1 and t_2, the 3-D trajectory Γ (see Figure 7.1) can be reconstructed only between P$_2$ and P$_3$, that is inside the measurement domain $x_V \times y_V \times z_V$. On the other hand, the reconstruction of $\overset{\frown}{P_1P_2}$ and $\overset{\frown}{P_3P_4}$ is done respectively using the measurement performed on adjacent fluid particle trajectories Γ'' and Γ' that are inside the measurement volume when Γ is, respectively, still or already out (see trajectory projections Γ''_{XZ} and Γ'_{XZ}). Thus, for a planar measurement, the reconstruction of 3D-flow trajectories is not possible (Liu and Katz 2006).

Substituting eq. (7.2) in (7.1), it follows that the planar pressure gradient reads as

$$\frac{\partial p}{\partial x} = -\rho\left[\frac{\partial u}{\partial t} + u\frac{\partial u}{\partial x} + v\frac{\partial u}{\partial y} + w\frac{\partial u}{\partial z}\right] \tag{7.6}$$

$$\frac{\partial p}{\partial y} = -\rho\left[\frac{\partial v}{\partial t} + u\frac{\partial v}{\partial x} + v\frac{\partial v}{\partial y} + w\frac{\partial v}{\partial z}\right] \tag{7.7}$$

In the above equations, the viscous term is not included as commonly assumed in other studies at $Re > 10^3$ (Haigermoser 2009; de Kat *et al*. 2009; Koschatzky *et al*. 2010; Lorenzoni *et al*. 2009).

It is observed that planar measurements of 3D flow, providing two- or three-component velocity vector fields, result in an approximated evaluation of the planar pressure gradient distribution. On the contrary, tomographic ones return the complete velocity vector and the complete velocity gradient tensor, in turn enabling the determination of the pressure gradient under more general hypotheses.

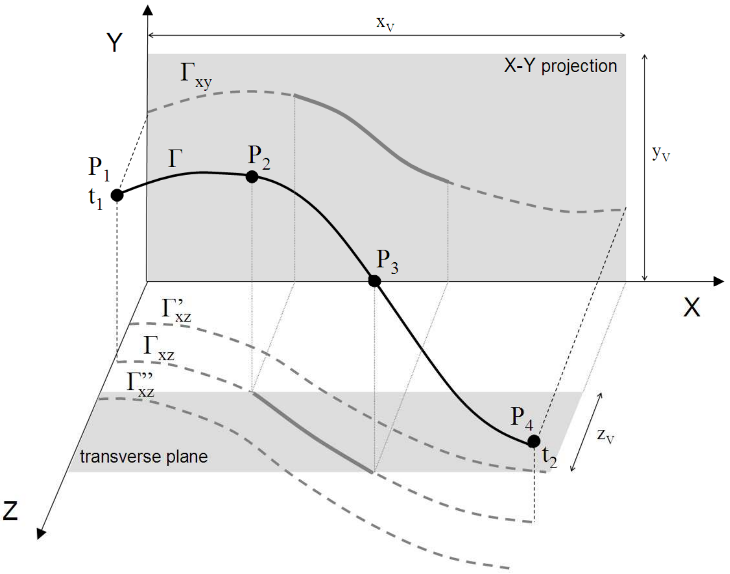

Figure 7.1 Three-dimensional fluid particle trajectory Γ (continuous black line) and its projections on plane *x-y* and *x-z*. In gray the domain of measurement

7.3.2 Material derivative evaluation

The Lagrangian approach

The Lagrangian evaluation of the material derivative along a fluid particle trajectory Γ is performed calculating the first order velocity difference:

$$\frac{D\mathbf{V}}{Dt}(\mathbf{x},t_0) \approx \frac{\mathbf{V}_2 - \mathbf{V}_1}{t_2 - t_1} = \frac{\Delta \mathbf{V}}{\Delta t} . \tag{7.8}$$

In the equation above, $\mathbf{V}_1 = \mathbf{V}(\mathbf{x}_1, t_1)$ and $\mathbf{V}_2 = \mathbf{V}(\mathbf{x}_2, t_2)$ are the fluid particle velocities at subsequent time instants and Δt is referred to as temporal separation.

The material derivative evaluation along a fluid particle trajectory is performed by two subsequent steps: the reconstruction of the fluid particle trajectory and the evaluation of velocity finite difference. Therefore, each of these two operations is a possible source of precision and truncation errors.

Figure 7.2a illustrates the effect of the time separation Δt between two subsequent velocity measurements on the trajectory reconstruction in terms of truncation error. Considering vector $\mathbf{V}_1$ and $\mathbf{V}_5$ to reconstruct the trajectory, then, according to the reconstruction by central scheme

$$\mathbf{x}_5 = \mathbf{x}_K + \mathbf{V}_3 \frac{\Delta t_{15}}{2} \tag{7.9}$$

$$\mathbf{x}_1 = \mathbf{x}_K - \mathbf{V}_3 \frac{\Delta t_{15}}{2} \tag{7.10}$$

the truncation error is $\overline{HK}\left(O\left(\Delta t^2\right)\right)$. When the time separation between velocity measurements is shorter, which is for example the case of $\mathbf{V}_2$ and $\mathbf{V}_4$, the truncation error reduces to $\overline{H'K}$.

In the same way, if a short temporal separation is employed, also the material derivative evaluation benefits of low truncation error.

Considering that PIV measurement uncertainty on the displacement field is μ =0.1 pixel (Willert and Gharib1999), the velocity uncertainty, indicated in Figure 7.2b with a circle, is given by

$$\varepsilon_V = \frac{\mu \cdot pxs}{\delta t} , \tag{7.11}$$

where *pxs* is the pixel or voxel size in physical units and δt is the pulse separation time.

The evaluation of the trajectory and the velocity variation will be affected by precision error. When the latter is computed with a short temporal separation, for example by means of $\mathbf{V}_2$ and $\mathbf{V}_4$, it is likely that its magnitude is comparable to the velocity uncertainty (see Figure 7.2c) therefore yielding high relative precision error in the material derivative. Higher temporal separations, instead, typically lead to larger velocity variations (see Figure 7.2d) and, consequently to more accurate evaluations of the Lagrangian acceleration.

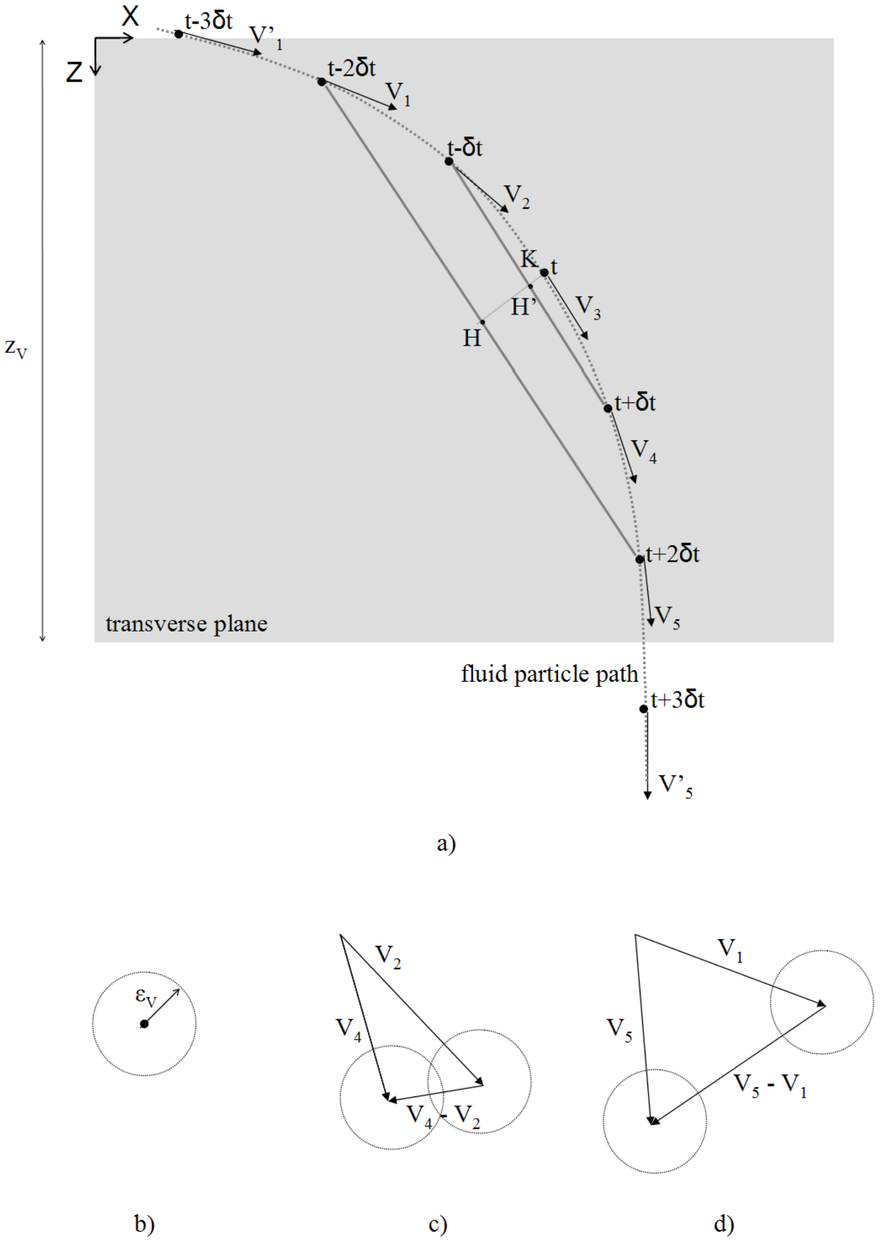
X
Z
t-3δt
V'1
t-2δt
V1
t-δt
V2
K
t
H'
V3
H
zV
t+δt
V4
t+2δt
V5
transverse plane
fluid particle path
t+3δt
V'5
εV
V2
V4
V4 - V2
V1
V5
V5 - V1

a)

b) c) d)

Figure 7.2 (a) Fluid particle traveling across the measurement domain (in gray); (b) uncertainty of velocity measurements; Lagrangian velocity variations: (c) $\Delta t=2\delta t$ and (d) $\Delta t=4\delta t$

The effect of the time separation on the precision and the truncation errors is inverse: to define the time separation to be used in practical application, it is now proposed a criterion limiting the total error affecting the material derivatives.

The total error on the material derivative is given by the sum of precision ε_p and truncation error ε_t. The precision error is defined by

$$\varepsilon_p = \left(\frac{D\mathbf{V}}{Dt}\right)_{measured} - \left(\frac{D\mathbf{V}}{Dt}\right)_{actual} . \tag{7.12}$$

In relative terms, the above reads as

$$\varepsilon_r = \frac{\left(\frac{D\mathbf{V}}{Dt}\right)_{measured} - \left(\frac{D\mathbf{V}}{Dt}\right)_{actual}}{\left(\frac{D\mathbf{V}}{Dt}\right)_{actual}} . \tag{7.13}$$

Recalling the velocity uncertainty ε_V, the relative precision error can be estimated as

$$\varepsilon_r = \frac{\varepsilon_V / \Delta t}{\left(D\mathbf{V}/Dt\right)_{ref}} , \tag{7.14}$$

where $\left(D\mathbf{V}/Dt\right)_{ref}$ is the value of reference for the material derivative.

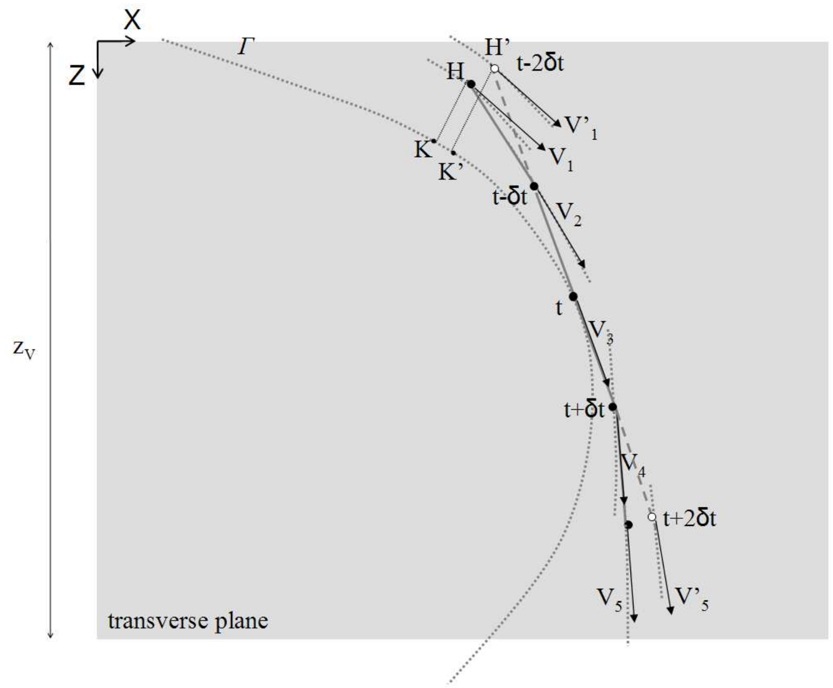

Figure 7.3 Comparison between single-step and multi-step method for trajectory evaluation

Considering that dominant flow structures are responsible for the largest pressure variation at the airfoil surface, from dimensional analysis, it is obtained that

$$D\mathbf{V}\big/ Dt = O\left(U_{\infty} f_{shed}\right) \tag{7.15}$$

where U_{∞} and f_{shed} are, respectively, the free-stream velocity and the shedding frequency of Karman vortices.

The criterion to employ on the material acceleration reads as

$$\varepsilon_r \leq 10\% \tag{7.16}$$

from which

$$\varepsilon_p \leq 0.1 U_{\infty} f_{shed} \,. \tag{7.17}$$

Recalling eq. (7.14), it is obtained the minimum time separation to evaluate the Lagrangian acceleration

$$\Delta t_{\min} = \frac{1}{0.1} \frac{\varepsilon_V}{U_{\infty} f_{shed}} \,. \tag{7.18}$$

A conservative estimate of ε_V for TOMO-PIV experiments can be inferred from the a-posteriori analysis by Scarano and Poelma (2009) who reported 0.1 voxels of error for *x* and *y* displacement, and 0.15 voxels for the *z* one.

On the other hand, the time separation must not be longer than a maximum value Δt_{max}, the time needed by a fluid particle to cross the measurement domain along the thickness z_V:

$$\Delta t_{\max} \approx \frac{z_V}{|w|} \tag{7.19}$$

where $|w|$ is the typical value of the out-of-plane velocity. A conservative estimate of $|w|$ is given in Lorenzoni *et al.* (2009) who found that *w* is 25% maximum of the free-stream velocity. When the time separation does not satisfy eq. (7.19), as, for example, in the case of $\Delta t=6\delta t$ (see vectors $\mathbf{V}'_1$ and $\mathbf{V}'_5$ in Figure 7.2), the Lagrangian tracking cannot be performed since the fluid particle exits the domain.

When the acquisition frequency is $f \geq 1\big/\Delta t_{\min}$, the method based on multiple velocity measurements (Moore *et al.* 2010) can be employed to reduce the truncation error in the trajectory evaluation as well as to take advantage of long time separation such to reduce the relative precision error in the material acceleration. In fact, if the material acceleration is for example computed with a time separation of $4\delta t$ (see Figure 7.3 where $\delta t= 1/f$), by the multi-step method, the trajectory is reconstructed using $\mathbf{V}_2$ and $\mathbf{V}_4$ in addition to $\mathbf{V}_1$ and $\mathbf{V}_5$. Hence, compared to the single-step approach, the truncation error is $\overline{HK}$ instead of $\overline{H'K'}$, which, in general terms means that, when $\Delta t = N\big/ f$, the use of the multistep approach reduces the truncation error of a factor *N*.

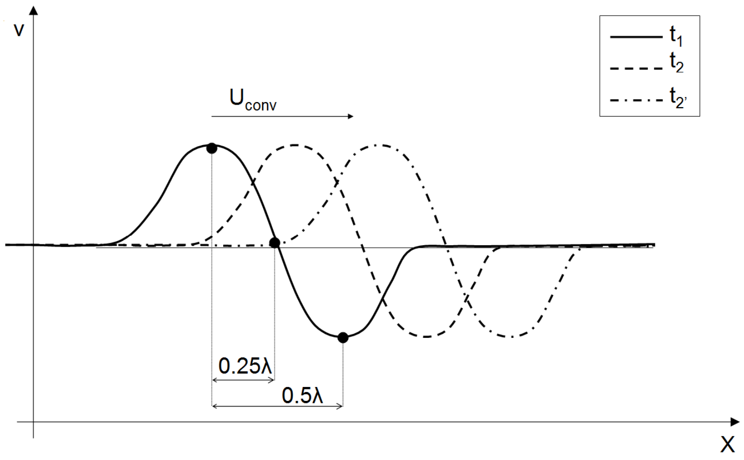

Figure 7.4 Convected vortex at three subsequent time instants

The Eulerian approach

The Eulerian evaluation of the material derivative through eq. (7.2) is subjected to a different treatment of the error propagation, and the criterion for an accurate measurement is here compared to that defined for the Lagrangian approach.

According to Nyquist–Shannon sampling theorem, the smallest flow scale of wavelength k that is resolved by PIV measurements is

$$\lambda \approx 2l \tag{7.20}$$

where l is the dimension of the smallest interrogation window employed for the cross correlation.

Considering also that the flow structures are convected by the mean flow U_{conv}, as illustrated in Figure 7.4, the material acceleration can be accurately evaluated if the time separation Δt is such that

$$\Delta t \approx C \frac{2l}{U_{conv}} . \tag{7.21}$$

In the above, the constant C must be chosen between 0 and 1 to ensure that both the Eulerian acceleration and the advection term of eq. (7.2) are evaluated on the same flow structure. In particular, in order to linearly approximate the velocity gradient with low truncation error $O(\Delta x)$, C must be smaller than 0.25 (see Figure 7.4). In many practical situations, however, the time requirement expressed in eq. (7.21) and the condition of velocity variation measurability of eq. (7.18) are conflicting and they cannot be respected at the same time.

7.4 Experimental set up

Experiments are carried out in the open test section of a low-speed wind tunnel (0.4 x 0.4m^2) at the Aerodynamic Laboratories of TU Delft Aerospace Engineering Department.

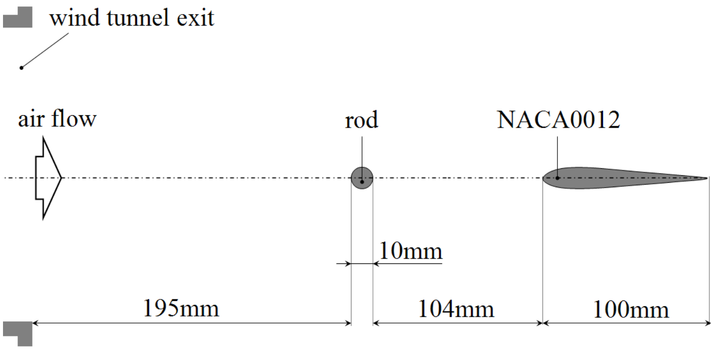

Figure 7.5 Sketch of the rod-airfoil configuration

A Plexiglas NACA0012 airfoil of 0.1m chord length *c* is horizontally placed at zero incidence 0.104 m in the wake of a cylindrical rod (d = 0.01 m), which is 0.195 m far from the wind tunnel exit (see Figure 7.5). The rod and the airfoil are in line with each other.

The configuration is tested for a nominal free-stream velocity of 5 m/s, yielding a Reynolds number of 3,500 on the rod diameter. The regime of flow motion past a rod is referred to as shear layer transition (Williamson 1996). Karman vortices are shed from the rod with a frequency of 100 Hz, which corresponds to a highly tonal noise generated by the interaction of the vortex on the airfoil leading edge (Table 7.1).

Table 7.1 Experimental conditions

Ambient pressure	p_a	1031 mbar
Ambient temperature	T_a	290 K
Nominal free-stream velocity	U_∞	5 m/s
Airfoil chord	c	0.1 m
Rod diameter	d	0.01 m
Reynolds number	Re_d	3500
Vortex shedding frequency	f_{shed}	100 Hz

Table 7.2 Experimental settings

Seeding material	Smoke particles ≈ 1 μm diameter concentration: 5 part/mm^3
Illumination	Quantronix *Darwin-Duo* Nd-YLF laser (2 x 25 mJ@1 kHz)
Recording device	4x Photron *Fast CAM SA1* cameras (1024 x 1024 pixels@5.4 kHz, 20 μm pixel pitch)
Recording method	Double frame/single exposure
Optical arrangement	Nikon objectives (f = 60 and 105 mm@ $f\#$ = 8); field of view = 50 x 50 mm^2; voxel size (pxs) 59 10^{-3} mm/vox
Acquisition frequency	5,000 Hz
Pulse separation (δt)	0.2 ms

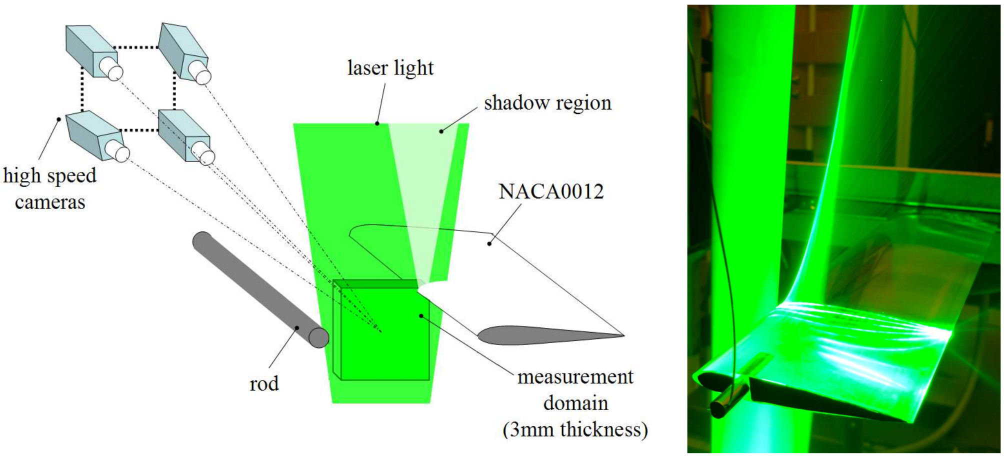
laser light
shadow region
high speed cameras
NACA0012
rod
measurement domain (3mm thickness)

Figure 7.6 (left) Sketch of rod-airfoil tomographic experiment set up and (right) detail of the illumination

The thin-light volume is formed at the leading edge of the quarter span section of the airfoil on the side of cameras, section still immersed in the inner core of the wind tunnel jet (see Figure 7.6). A knife-edge slit is added in the path of the laser light sheet to cut the low intensity lobes from the light profile and create a 3-mm-thickness sheet. The imaged particle concentration is 0.06 particles per pixel (*ppp*) corresponding to 5 particles/mm^3.

Four high-speed cameras, subtending a solid angle of 35 x 35 deg^2, record 12-bit images of tracer particles and the objective numerical aperture is set for a focal depth matching the light sheet thickness. Sheimpflug adapters are used to align the focal plane with the midplane of the illuminated volume. Sequences of 5,000 image quadruplets are acquired in continuous mode at 5 kHz, yielding a normalized sampling rate of $f^*=50$, where f^* is the ratio between acquisition and shed frequency (Table 7.2).

7.4.1 Tomographic reconstruction

The MART algorithm (Herrmann and Lent, 1976), which is implemented in LaVision *Davis* 7.4, is used to reconstruct the 3D-light intensity field. A total of 5 iterations of the algorithm are performed with a diffusion parameter of 0.5 for the first three.

Prior to the volume reconstruction, the 3D calibration function is corrected by the volume self-calibration to minimize the disparity fields, decreasing in the calibration error from a typical value of 0.5–0.1 pixel (Wieneke 2008). The accuracy of the reconstruction object is improved by means of image pre-processing with background intensity removal and non-linear subsliding minimum subtraction (11 x 11 kernel size).

Volumes of 50 x 50 x 3 mm^3 discretized with 831 x 831 x 50 voxels are then obtained applying a pixel to voxel ratio of 1. The resulting voxel size is 59 10^{-3} mm/vox.

The a-posteriori evaluation is made by means of the analysis of the reconstructed object intensity levels. The particle average peak intensity in a cross-section of the volume is displayed in Figure 7.7 (left) from which it can be deduced that light is concentrated within 50 voxels (≈ 3 mm) at a slight angle with respect to the calibration plane. The reconstructed region is sketched along the boundaries of the illuminated region. The peak intensity profile is extracted and normalized (Figure 7.7 right), yielding a signal-to- noise ratio (*SNR*) above 2 within a thickness of 30 voxels (1.8 mm) where, therefore, the measurement is considered reliable.

7.4.2 3D-Vector field computation

Three-dimensional particle field motion is computed by spatial cross-correlation of pairs of reconstructed volumes with VODIM software (Volume Deformation Iterative Multigrid, developed at TU Delft), an extension to volumetric intensity fields of the window deformation technique for planar cross-correlation (Scarano and Riethmuller 2000). Interrogation boxes of size decreasing from of 201 x 201 x 21 to 47 x 47 x 19 and 75% overlap between adjacent interrogation boxes produce a velocity field measured over a grid of 66 x 66 x 6 points. At the given particle concentration, an average of 50 particles are counted within the smallest interrogation box.

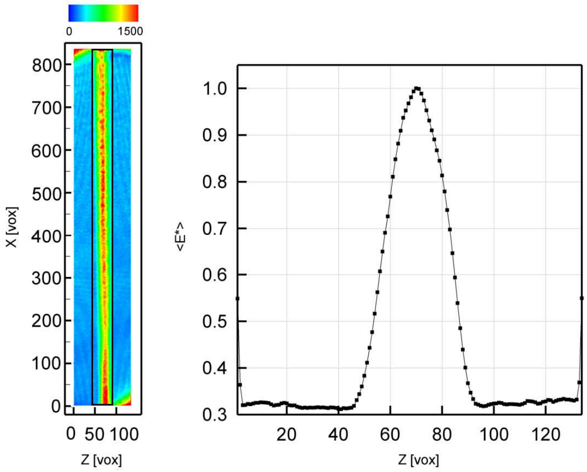

Figure 7.7 Left: reconstructed particle peak intensity distribution averaged along y-axis (*black box* indicates the reconstructed region); right: normalized particle peak intensity profile along z-axis to indicate the signal-to-noise ratio

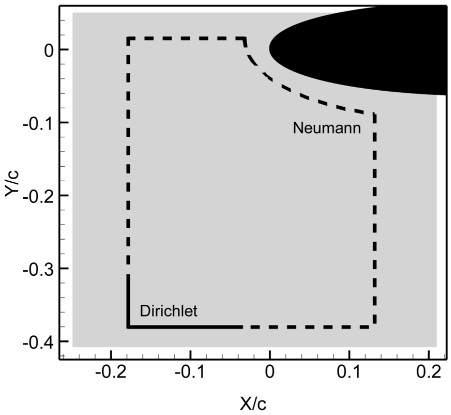

Figure 7.8 Boundary condition of Neumann (dashed line) and Dirichlet (solid line). In *gray* the measurement domain

Data processing is performed by in parallel with a dual quad-core Intel Xeon processors at 2.66 GHz with 8 GB RAM memory requiring 2 and 2.5 min for the reconstruction of a pair of objects and 3D cross-correlation, respectively. Noisy fluctuations of the velocity vectors are reduced by applying a space–time regression, a second order polynomial least-square fit over a kernel of 5 spatio-temporal samples (Scarano and Poelma 2009).

7.4.3 Pressure field determination

As the velocity domain is rather thin (just 6 measurement points along *z*-axis), the Lagrangian evaluation of the material derivative and, as consequence that of the pressure, is done on the mid z-plane of the domain where it is less likely that the fluid particles exit the domain at a given $\Delta t_{min}<\Delta t<\Delta t_{max}$ (see section 7.3.2). In particular, the integration is performed on the third *z*-plane where regions affected by measurement noise are avoided. In Figure 7.8, the integration domain is sketched and the Neumann and the Dirichlet boundary conditions are specified.

7.5 Results

A total of 100 shedding cycles are determined, each of which is described by 50 samples, ten times higher than the sampling rate used by Lorenzoni *et al.* (2009).

The spatial sampling rate of the velocity field, on the other hand, is 1.4 vectors/mm along *x* and *y*-direction and 3.4 vectors/mm along *z*, resulting from non-cubic interrogation boxes.

With respect to the reference velocity V_{ref} of 16 voxels at point (x/c= -0.24, y/c= -0.4), the velocity measurement uncertainty is 1%. In the following, V_{ref} will be referred to as U_∞.

7.5.1 Velocity field

In the region in front of the airfoil ($x/c \leq 0$; $0.04 \leq y/c \leq -0.08$, Figure 7.9), the mean flow is characterized by a decrease of u-velocity component leading to the stagnation point where the vertical velocity component rises in magnitude identifying a region of upward acceleration and one of downward. Flow symmetry is observed for the *w*-component which is affected by measurement errors not exceeding 1% of U_∞. From contours of turbulent kinetic energy,

$$k = \frac{1}{2}\left(\sqrt{\overline{u'^2}} + \sqrt{\overline{v'^2}} + \sqrt{\overline{w'^2}}\right) \tag{7.22}$$

(see Figure 7.9), intense turbulent motion is detected ahead of the airfoil in the region corresponding to the von Karman wake shed from the rod.

The wake is constituted by counter-rotating vortices which interact with the airfoil leading edge, as shown in the sequence of snapshots of Figure 7.13(first row) by contours of the out-of-plane vorticity component. Time instant *t* is normalized with respect to the shedding period *T* yielding $t^* = t/T$.

Measurements performed in the region corresponding to the laser shadow (in gray, see Figure 7.9) are not reliable and therefore are avoided from the analysis. Additionally, velocity derivatives are not performed near by the boundaries of the measurement domain since velocity vectors are typically affected by noise (in gray, see Figure 7.13).

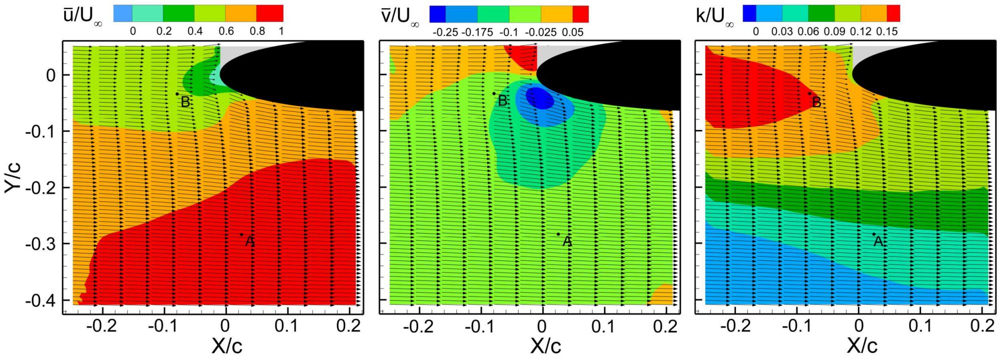

Figure 7.9 Mean velocity components and normalized turbulent kinetic energy on the midplane

7.5.2 Material velocity derivative

From dimensional analysis discussed in section 7.3, it results that, in order to limit the relative precision error to 10% maximum, ensuring that the z-displacement of the trajectory is shorter than z_v = 30 voxels, the time separation to be used for the Lagrangian evaluation of the material acceleration must be chosen between 0.6 and 1.5ms, according to eq. (7.18) and (7.19). In contrast, when the Eulerian approach is used, the time separation must not be larger than 0.3 ms. This conflicts with the condition of velocity measurability, $\Delta t \geq 0.6$ms (eq. (7.18)), and it leads to material acceleration affected by 20% in precision error.

Time separation constraints estimated for both the approaches are now verified by an a-posteriori analysis. Using the standard deviation $\sigma_{\Delta u}$ as an estimate of the typical velocity variation within Δt, $\left(\frac{D\mathbf{V}}{Dt}\right)_{ref}$ of eq. (7.14) can be rewritten as

$$\left(\frac{D\mathbf{V}}{Dt}\right)_{ref} = \frac{(\Delta\mathbf{V})_{ref}}{\Delta t} \approx \frac{\sigma_{\Delta u}}{\Delta t} \qquad (7.23)$$

In the above, velocity variations are evaluated along fluid particle trajectories when the approach is Lagrangian, or at fixed point when it is Eulerian.

Lagrangian approach: a-posteriori analysis

Considering point B (x/c = -0.077; y/c = -0.033) as representative of the region of intense turbulent motion (k/U_∞=0.15, Figure 7.9). In voxel units, the standard deviation evaluated within a time interval of 1/f=0.2 ms is 0.29 voxels. Therefore, it would result material acceleration affected by 34% of relative precision error. On the contrary, to restrict this to values not larger than 10%, according to eq. (7.14), where $\left(\frac{D\mathbf{V}}{Dt}\right)_{ref}$ is given by eq. (7.23), the time separation must be sufficiently large to have $\sigma_{\Delta u} \geq 1$ voxel. This is measured for $\Delta t \geq 0.8$ ms, which is in agreement with the estimation made a-priori by eq. (7.18).

Considering the Euclidean norm $|w'|$ of the mean and the fluctuating value of the w-velocity component,

$$|w'| = \sqrt{\overline{w}^2 + w'^2} \ , \tag{7.24}$$

as an estimate of the out-of-plane motion at point B. Typically, fluid particles move of 30 voxels along z-direction in a time interval of 3.4 ms. However, to avoid the evaluation of the trajectory by velocity vectors at domain border, as affected by noise, the maximum time separation is reduced to 1.5 ms, which leads to typical z-displacements of 15 voxels. In the legend of Figure 7.10 (top), standard deviation of velocity variation $\sigma_{\Delta u}$ and $|w'|$ are reported, in voxel unit, for each time separation.

In Figure 7.10 (top), the time history of x-component material velocity derivative at point B is plotted for time separation ranging between 0.2 and 3.2 ms. For Δt = 0.2ms and 0.4 ms, strong oscillations are exhibited because of $\sigma_{\Delta u}$ typically smaller than 1 voxel. On the other hand, when the time separation is larger than 0.8 ms, such as 1.2 ms, the Lagrangian derivative features trends gradually smoother meaning of a decreasing relative precision error. The effect of Δt on the trend of the Lagrangian velocity derivative can be also observed from the plot of probability density function: longer time separations leads to narrower Gaussian distributions as consequence of smoother trends.

For $\Delta t \geq 1.5$ ms, e.g. Δt = 2.4 and 3.2 ms which are not accepted because leading to z-displacement larger than $z_V/2$, rising truncation error is observed, for example, between 0 and 3 ms (see Figure 7.10 top).

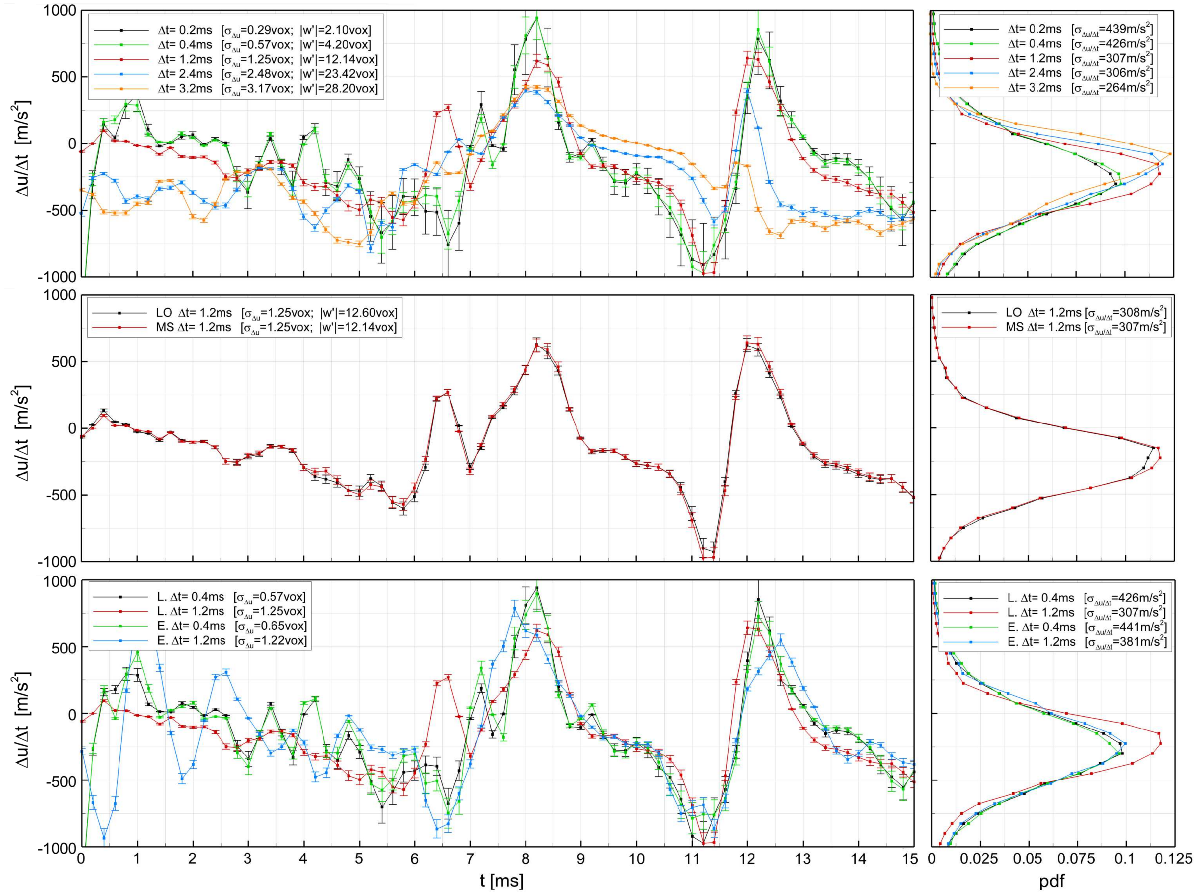

Figure 7.10 Time histories and corresponding probability density function of *x*-component of material velocity acceleration at point B using different time separation: (top) Lagrangian approach with MS scheme; (center) Lagrangian approach with LO and MS scheme; (bottom) comparison between the Lagrangian MS and the Eulerian approach.

For the present investigation, the time separation is chosen to be 1.2 ms, which, at point B, leads to a relative precision error of 8%. This, however, increases to 26% at point A (*x/c*=0.023; *y/c*=-0.028, $\sigma_{\Delta u}$ =0.38 vox), which is representative of the region out of the Karman wake and where the turbulent activity is 66% lower compared to that at point B (see Figure 7.9). In Figure 7.11, relative precision error at point A and B is plotted against time separation.

The time history of the Lagrangian velocity derivative computed by single-step scheme (LO) and by the multistep scheme (MS) proposed Moore *et al.* (2010) is illustrated in Figure 7.10(center). The two approaches lead to very similar results. This results from the velocity time resolution, which is sufficiently high that the use of the multi-step scheme does not lead to a reduction in the truncation error of the evaluated trajectories. Under such a condition, therefore, it is possible to decouple the investigation of the time separation on material derivative and pressure fields from that focused on the effects of flow three-dimensionality.

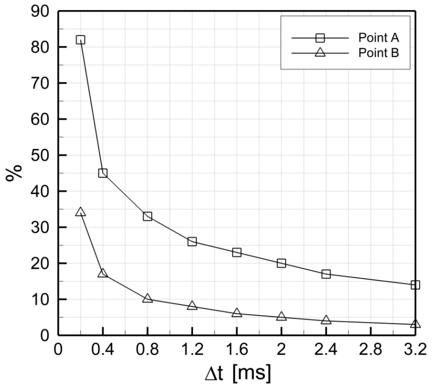

Figure 7.11 Relative precision error on the material derivative evaluated by the Lagrangian approach (MS)

Eulerian approach: a-posteriori analysis

By a-posteriori analysis of the time separation to employ in the Eulerian approach, the convection velocity U_{conv} (see eq. (7.21)) can be estimated by the local mean velocity component $\overline{u}$. This, at point B is, in voxel units, 10.5 voxels leading to a maximum time separation of 0.4 ms which confirms the a-priori estimation discussed in section 7.3.2. However, since the typical velocity variation measured within 0.4 ms is $\sigma_{\Delta u}$ =0.65 voxels, the material acceleration is affected by 15% precision error. To comply with the condition restricting the relative precision error to 10%, it would be requested to employ a separation time not smaller than 1ms, which is clearly in contrast to the condition stated by eq. (7.21).

Comparison

Compared with the minimum time separation allowed for the Lagrangian approach, that maximum for the Eulerian one is two times shorter yielding material acceleration with a relative precision error at point B 1.5 times larger than that estimated for the Lagrangian approach.

In Figure 7.10(bottom), the time history of the material acceleration at point B computed by both Eulerian and Lagrangian approach is plotted for time separation of 0.4 and 1.2 ms. Curves corresponding to the shortest Δt show a marked jigsaw-like behavior that are characterized by similar trend and statistical dispersion. When the material acceleration is calculated using Δt=1.2 ms, as condition eq. (7.21) is not satisfied, the Eulerian approach provides a noisy solution with standard deviation 25% larger than that corresponding to the Lagrangian one. Still, while in this case a decrease in $\sigma_{\Delta u / \Delta t}$ of 27% is observed when passing from a Δt=0.4 to 1.2 ms, for the Eulerian approach, the reduction is of 14%.

In Figure 7.13 (second and third row), a sequence of instantaneous contours of material acceleration is shown for both the Lagrangian and the Eulerian case. In the region of the Karman wake and in that by the leading edge, as already seen at point B (Figure 7.10 bottom), the Eulerian evaluation leads to noisy fields where, compared to the Lagrangian one, no flow-structure convection is detected.

7.5.3 Pressure field determination

The last step of the procedure consists in the spatial integration of eq. (7.3) on the mid z-plane. In Figure 7.14 (first row), the sequence of pressure fluctuation contours corresponding to those of vorticity is depicted to highlight the relation between cinematic and thermodynamic field. They are evaluated by means of the Lagrangian approach employing multi-step scheme with Δt =1.2 ms.

Compared to those obtained by the Lagrangian method, the pressure fields evaluated by means of the Eulerian approach with Δt = 0.4 ms, as illustrated in Figure 7.14(first and second row), show differences in the contour patterns, although less marked than those observed for the material derivative (Figure 7.13). To have a more quantitative understanding of the influence of the two approaches on the pressure field, the pressure time histories at point B corresponding to those of material acceleration of Figure 7.10(bottom) are plotted in Figure 7.12. Similarly to the material acceleration, when a time separation of 0.4 ms is employed, both the approaches lead to oscillating results with comparable values of standard deviation. In the Lagrangian approach, an increase in Δt from 0.4 to 1.2 ms leads to a reduction in standard deviation of the pressure signal of 30%, similarly to what observed for the material acceleration. By contrast, in case of the Eulerian approach, the drop is of 25%, which is approximately the double of the reduction observed for the corresponding material acceleration. This smoothing effect might be due to the integration method, on which no further investigation has been conducted within this thesis.

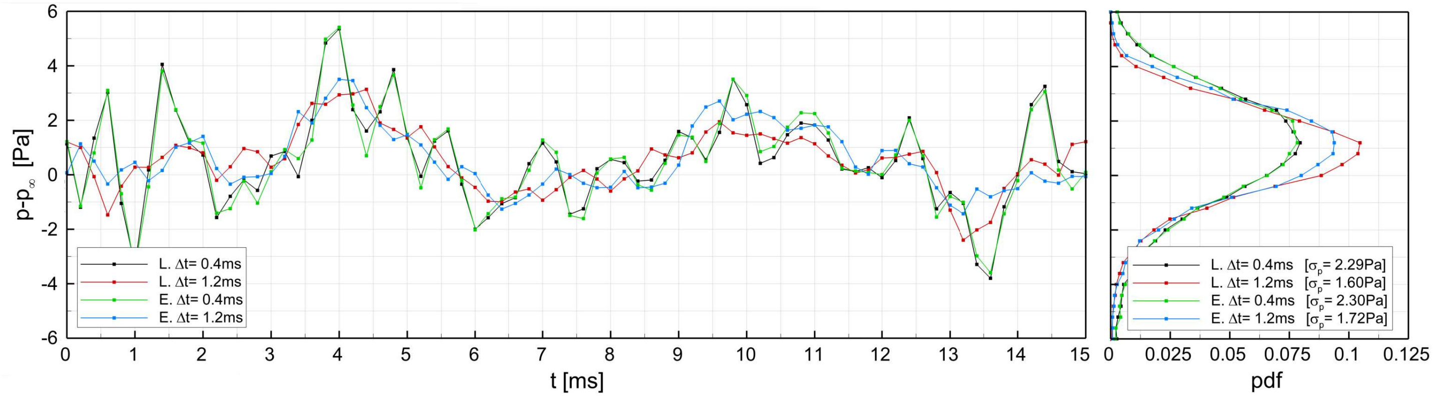

Figure 7.12 Time histories and corresponding probability density function of pressure fluctuation at point B resulting form the Lagrangian (MS) and the Eulerian approach

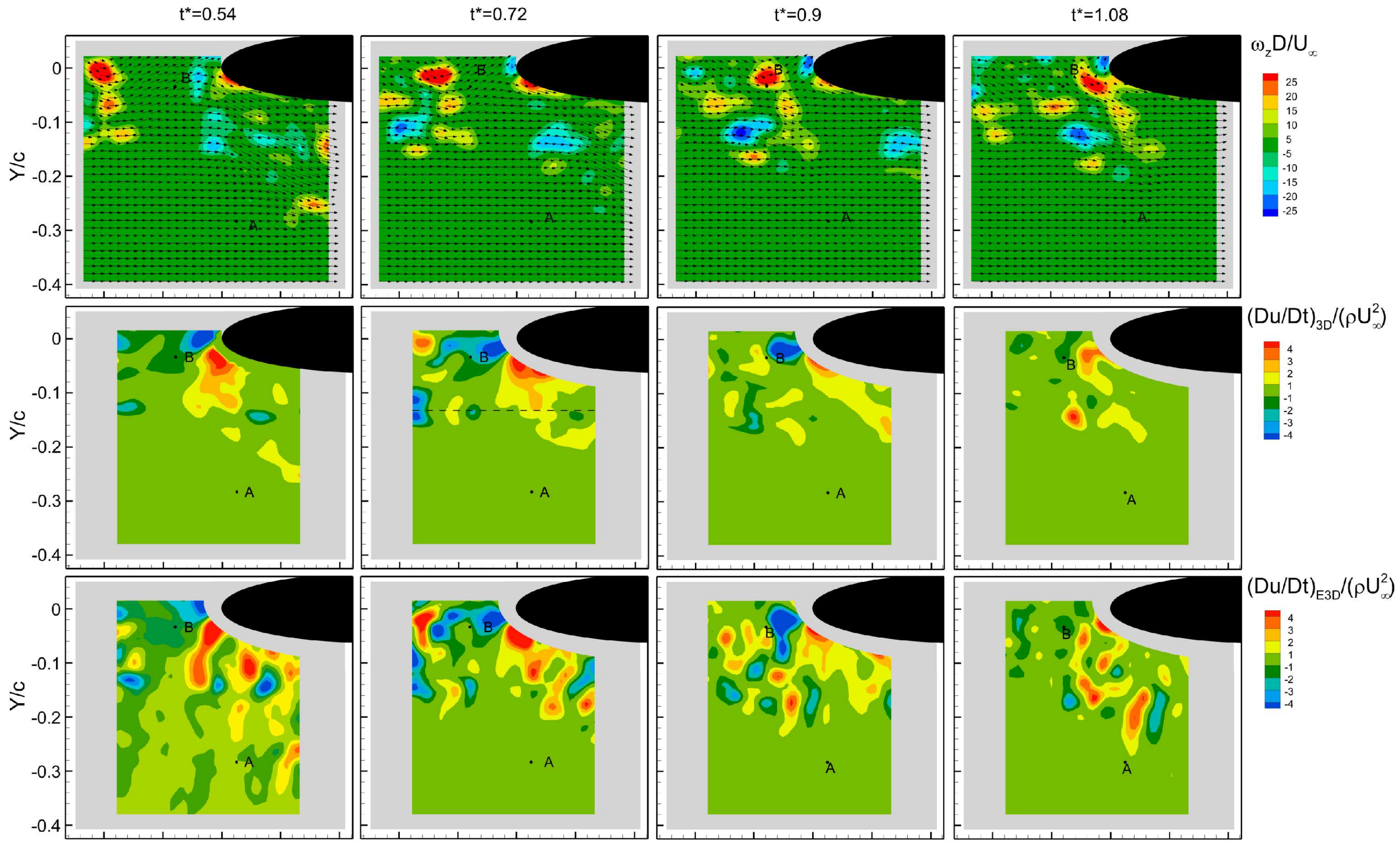

Figure 7.13 Sequence of instantaneous out-of-plane vorticity component contours with velocity vectors in a convective frame of reference $u = 0.2U_\infty$ (first row); contours of material acceleration inferred from 3D velocity field by means of the Lagrangian approach@ Δt =1.2 ms (second row) and the Eulerian approach @ Δt = 0.4 ms (third row)

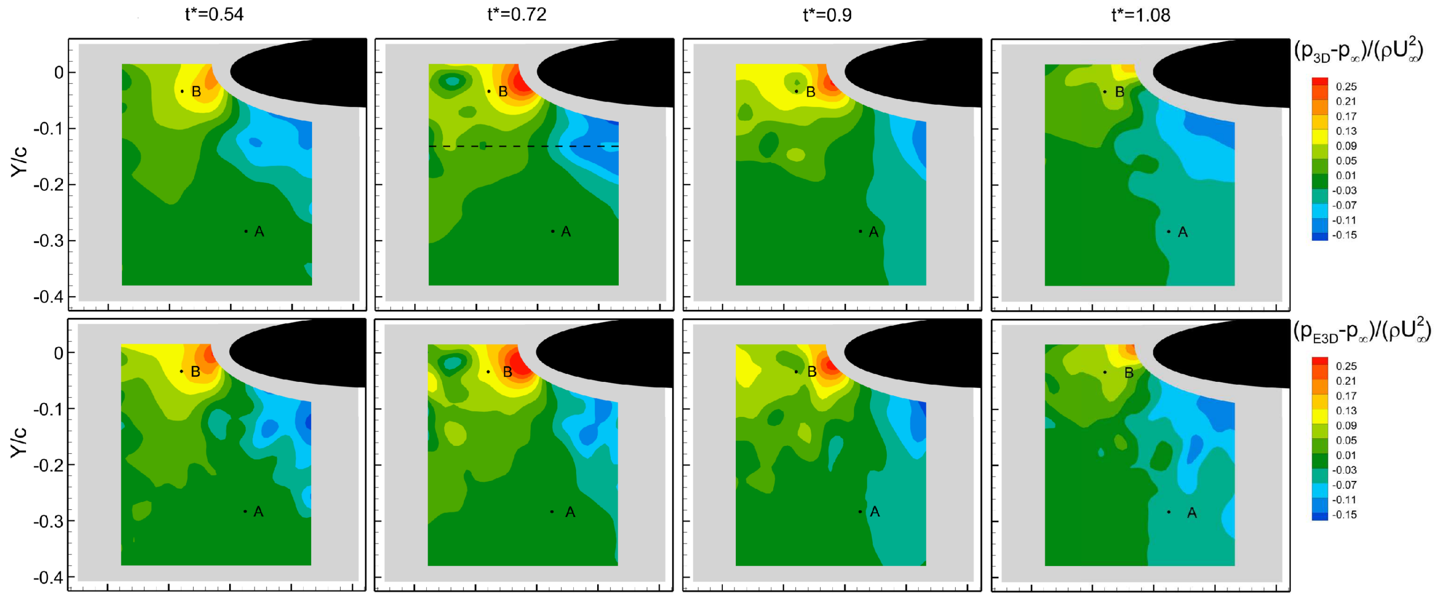

Figure 7.14 Sequence of instantaneous pressure fluctuation contours inferred from 3D velocity field by means of the Lagrangian approach@ Δt =1.2 ms (first row) and the Eulerian approach@ Δt =0.4 ms (second row)

7.5.4 3-D flow effects

A synchronous planar and tomographic PIV measurement is simulated in order to evaluate 3D flow effects on the pressure field. Volumes of 831 x 831 x 17 voxels, corresponding to 50 x 50 x 1mm^3 are extracted from the central z-position of the reconstructed tomographic objects. The imaged particle intensity levels are summed along *z* in a Gaussian way and are cross-correlated with interrogation windows of size identical to the *x-y* dimensions of the interrogation boxes (see section 7.4.2). An average of 50 particles is counted in the smallest interrogation window.

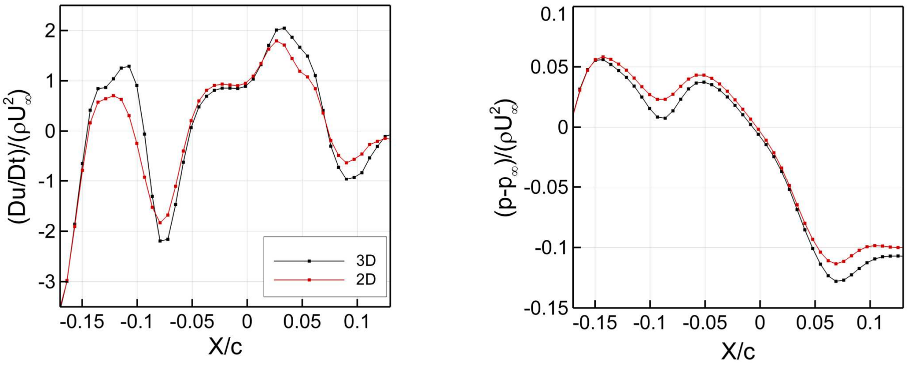

Figure 7.15 Material acceleration (left) and pressure fluctuation (right) inferred from 3D and 2D velocity field at *y/c*=-0.125

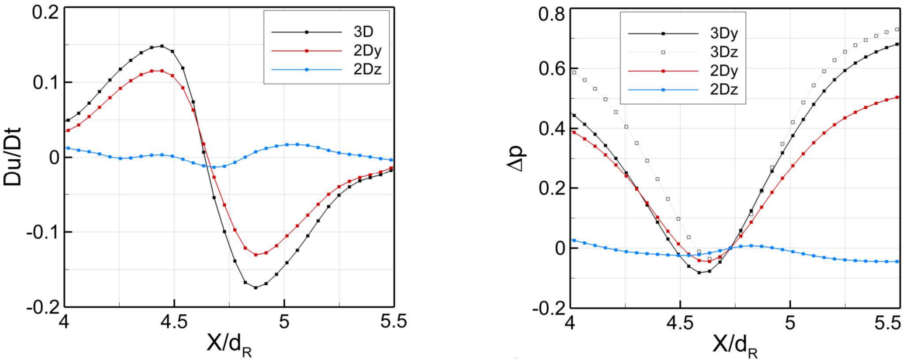

Figure 7.16 Cylinder wake vortex: *3D*- and *2D*-based material acceleration (left) and pressure (right) along streamwise direction

A Lagrangian approach is used to evaluate the material acceleration. This, however, is evaluated along the projection of particle trajectories on the measurement plane, as only two velocity components can be measured by planar PIV.

Three- and two-dimensional-based material acceleration and pressure fluctuation show similar pattern, as illustrated in Figure 7.15 where the flow quantities are plotted along y/c=-0.125 at t^* = 0.72 (see Figure 7.13 and Figure 7.14). In general, the similarity is observed at each point of the integration plane and for all the time instants.

To further investigate the effect of flow three dimensionality on the Lagrangian approach, tomographic PIV data of a cylinder wake at Re = 540 are used. The attention is focused upon a subregion of 61 x 48 x 27 measurement points containing a vortex, which is located 5 cylinder diameters (d_R) downstream. Details of the experiment are given in Scarano and Poelma (2009).

Compared to TOMO-PIV measurements obtained in thin-light volume configuration, the ones performed on the cylinder wake enable the evaluation of the pressure field also on planes which are not aligned with the dominant flow direction. As each shedding cycle is sampled approximately 9 times, the evaluation of the material acceleration is performed by single-step scheme (LO) without any substantial rise in truncation error (see section 7.5.2).

The pressure field is integrated on the planes y/d_R=5 and z/d_R = 0 using the corresponding planar subsets of two-component velocity (respectively called as *2Dy* and *2Dz*) and the tomographic data (3D). *2Dy*-, *2Dz*- and *3D*-based material acceleration and pressure field are compared along the intersection of the aforementioned planes (see Figure 7.16). In case of *2Dy* subset, errors are typically smaller than 20% similarly to what observed for the rod-airfoil flow. In contrast, if the planar subset is not parallel with the y-plane, which is the dominant direction of flow, the error increases, meaning of a larger influence of the out-of-plane velocity component on the trajectory reconstruction. On plane z/d_R =0, for example, the 2D-based evaluation lead to an error of 100%. Similar behavior is observed for the pressure field which is integrated assigning boundary condition of Dirichlet Δp=0 at point (x/ d_R = 4.71, y/d_R =5, z/d_R =0) and Neumann along the domain boundaries. Moreover, 3D-based pressure fluctuation evaluated on plane y/d_R = 5 and on plane z/d_R =0 (respectively *3Dy* and *3Dz*, see Figure 7.16 right) show small differences, as a result of the error introduced by the pressure integration method.

7.6 Conclusions

This chapter describes an experiment performed on a rod-airfoil flow by means of TR-TOMO PIV in thin-light volume configuration. Being a 3-D measurement technique, TR-TOMO PIV, when performed at time rate of sampling sufficiently high, enables the detection of the unsteady and the 3-D nature of the turbulent flow motions typical of the rod-airfoil configuration. In fact, unlike planar measurements where only two velocity components are available, it provides all the velocity information for the Lagrangian evaluation of the instantaneous pressure field.

A criterion restricting the relative precision error to 10% on the Lagrangian velocity derivative is proposed to determine the time separation in which performing the evaluation along the particle trajectories. The effect of Δt on the material derivative is analyzed in terms of relative precision error, and 1.2 ms is finally chosen. On the other hand, when an Eulerian approach is employed, the time separation is limited to 0.4 ms in order to evaluate the Eulerian acceleration and the advection term on the same flow scales. Under such a condition, the method yields a relative precision error of 15%.

Material velocity derivative and pressure fluctuation evaluated from tomographic measurements in a Lagrangian manner feature patterns similar to those obtained from planar ones as long as the measurement plane is aligned with the dominant flow direction. Instead, if the condition of alignment is no longer satisfied, which means that the out-of-plane velocity component becomes not negligible with respect to the others, the Lagrangian approach based on planar measurements leads to an erroneous evaluation of the material acceleration and the pressure field.

Further investigations are needed to quantify the effects of the pressure integration method.

In the present study, noise predictions by means of Curle’s analogy are not performed because flow velocity measurements are available on a limited portion of the airfoil surface. Nevertheless, the demonstration of the necessary steps for a Lagrangian evaluation of the pressure fluctuation field based on TR-TOMO PIV velocity data suggests that further investigations are needed to extend the process up to the determination of the source term of Curle’s analogy. This combined with TR-TOMO PIV has the potential to be a powerful tool to predict noise, to identify the source of sound and to understand the noise generation mechanism.

Chapter 8

Conclusions

This chapter is dedicated to summarize the main results and conclusions of the thesis.

8.1 3D organization and dynamics of subsonic jets

Time-resolved tomographic PIV experiments are conducted on circular and 6-chevron jets (*Re*=5,000) in a tailored-water jet facility. Compared to planar (2D2C and 2D3C) and single point measurement techniques, a full 3D approach enables unambiguous descriptions of the vortex topology, based on the full vorticity vector or the λ_2-criterion. Moreover, temporal resolution allows addressing the growth and development of the coherent flow structures along with their mutual interaction. In this context, 4D measurements (3D time-dependent) of the flow pattern represents a necessary milestone in the development of a novel experimental method that uses PIV measurements in combination with aeroacoustic analogies.

8.1.1 Circular jet

The flow is characterized by a pulsatile motion leading to vortex ring shedding (*St*=0.72) and, further downstream, to vortex ring pairing (*St*=0.36). While this process shows an axisymmetric pattern, the flow axial strain gradually leads to the formation of three-dimensional patterns such as vortex-azimuthal instabilities and counter-rotating streamwise vortices. On average of 4 primary azimuthal waves grow on the vortex ring, leading to in-plane and out-of-plane deformation. Streamwise vortices are characterized by both axial and radial vorticity, respectively, “ST” and “SR”. Typically 4 main streamwise pairs are distributed around the vortex rings at an angle of 30-40 degrees to the jet axis and move with a characteristic inward-outward radial motion induced by the passage of the vortex rings.

To ascertained the influence between streamwise structures and vortex rings, not reported in previous studies by planar PIV (Liepman and Gharib, 1992; Ghanapathisubramani *et al*, 2002), spatial mode analysis is performed along the circumference corresponding to the vortex ring core and along the one corresponding to the cores of the streamwise structure. Both spectra show high energy content at wave number k=4 (with a phase shift of π), which indicates the preferred mode of influence of streamwise vortices on vortex rings, with the axial vorticity induced by streamwise pairs on the vortex ring that is staggered in phase opposition at the regions of interaction, where primary instabilities grow.

With the growth of in-plane azimuthal instabilities, vortex ring humps are tilted and ejected along the axial direction as they are subjected to higher axial velocities. By the end of the potential core, this process culminates in the breakdown of the toroidal shape into streamwise filaments oriented at 30-45 degrees to the jet axis and peripheral structures of "C" shape. These re-organize as filaments oriented along the azimuthal direction in the region downstream of the potential core and are largely responsible for the flow entrainment. In the vicinity of the jet axis, instead, vortex filaments show a scattered orientation.

The analysis of the 3D patterns in the region of transition from the axisymmetric to the three-dimensional regime is aided by applying POD analysis to velocity, vorticity and Lamb-vector fields, with the latter that accounts for the flow state in Powell's aeroacoustic analogy. The first pair of velocity and vorticity modes describes the presence of vortex rings travelling after pairing. In the velocity modes, the axial velocity identifies a helical motion in the region across the end of the potential core and, downstream, a flapping motion. It also shows a precession motion that develops downstream the end of the potential core where the radial and the azimuthal components respectively identify wave-like and twisting motions. In the vorticity decomposition, the first pair of modes shows that travelling vortex rings are characterized by the radial and axial vorticity fields developing across the end of the potential core with a characteristic 40-45 degree inclination to the jet axis. Such patterns, also observed in mode pairs at lower energy, are ascribed to the process of vortex ring breakdown. The first pair of Lamb vector modes describes vortex ring travelling after pairing, where the characteristic azimuthal coherence of the rings is identified by the radial and the axial components of the Lamb vector and not by the azimuthal component as observed in the vorticity modes. In the region across the end of the potential core, the azimuthal component identifies the development of a three-dimensional disturbance at 40-45 degree to the jet axis. In all the above decompositions, travelling rings after shedding are identified by mode pairs at lower energy.

The stretching and tilting fields are analyzed in relation to the coherent structures. In the circular case, instantaneous activity is observed with the rise of three-dimensional patterns. It is associated with azimuthal instabilities and streamwise vortices and is maximum during the formation of "C" structures and the ejection of vortex humps. Beyond the end of the potential core, instead, it drops of 60%.

8.1.2 Chevron jet

In the chevron jet, although the column is characterized by a pulsatile motion, the axisymmetric ring-like coherence observed in the circular jet is replaced by streamwise flow structures. These are formed at the nozzle exit and are constituted by azimuthal (“SA”), axial (“ST”) and radial (“SR”) vorticity. While “SA” filaments develop from the nozzle apexes, 6 counter-rotating pairs of streamwise vortices “STP” and “SRP” are generated at the nozzle exit in a position corresponding to the chevron notch. The decay of streamwise vortices is accompanied by the formation of C-shaped structures, which, inducing inward radial flow, may be responsible for the tilting of the streamwise structures towards to the jet axis.

The stretching and tilting fields are analyzed in relation to the coherent structures. In the chevron jet, stretching and tilting peak activity corresponds to the region where “C” structures are formed and interact with streamwise filaments.

8.2 The implication of coherent structures in the aeroacoustic generation

The relation between coherent flow structures and the instantaneous acoustic source is investigated recalling Powell’s aeroacoustic analogy. Within this formulation, the second time derivative of the Lamb vector is associated with the acoustic source. Its spatio-temporal evolution is mapped and is compared to that of the vortices, to visually detect flow events involved in the acoustic generation.

In the circular jet, pronounced source activity is observed in correspondence to vortex pairing, azimuthal instabilities and streamwise filaments. However, the largest aeroacoustic generation is found by the end of the potential core during the vortex ring breakdown process. In the chevron jet, instead, the peak activity is reported during the process of streamwise vortex decay and C structure formation.

For the circular jet, POD analysis is applied to the second time derivative of the Lamb vector to analyze the source 3D patterns. The radial and axial components of the modes resemble a toroidal pattern that gradually decays by the end of the potential core. Such pattern is particularly clear in the first mode pair, where the radial and the axial components identify a travelling wave related to vortex pairing (but with halved spatial wavelength) with four primary azimuthal waves. The mode pairs at lower energy are instead associated with the vortex shedding, while in the region by the end of the potential core, the azimuthal component shows the development of a three-dimensional disturbance at 40-45 degree to the jet axis. While POD modes of velocity, vorticity and Lamb vector fields are associated with Strouhal numbers smaller than 0.9, the modes of the acoustic source also features higher Strouhal numbers ($1.05 \leq St \leq 1.9$), which are attributed to the three-dimensional disturbances by the end of the potential core.

8.2.1 Noise prediction based on 4D PIV measurements

The use of 4D PIV measurements to perform unbiased acoustic predictions of the jet noise is a challenging task, especially due to the constraints on the extent of the instantaneous measurement domain and on the required spatio-temporal resolution. For this reason, acoustic analyses have been so far afforded using DNS or LES techniques, which provide to obtain accurate descriptions of the flow field.

In this thesis, the available TR TOMO PIV measurements are performed at spatial and temporal resolution (up to Strouhal of 4) that enables to appreciate the details of the vortex interactions and their connection to the local pattern of the Lamb vector second time derivative. Moreover, they are conducted over a jet axial extent that is sufficiently long (10 jet diameters) to capture the large-scale events from the nozzle to 4 jet diameters beyond the end of the potential core. The above reasons motivate the challenge of using TR-TOMO PIV data to perform far-field acoustic predictions by direct evaluation of Powell’s analogy (section 6.5). The spectrum of the acoustic pressure perceived by listener at 90 degrees to the jet axis shows peaks at the pairing and the shedding frequencies and a broader hump ($1 \leq St \leq 2.75$), with frequencies $St \leq 2.25$ that are unaffected by domain spatial truncation. Such hump is ascribed to the breakdown of ring vortices, after inspecting the acoustic source and having observed that the frequencies ($1.05 \leq St \leq 1.9$) associated with the 3D waves of the acoustic source modes lie in the frequency range of the acoustic spectral hump ($1 \leq St \leq 2.25$). Finally, far-field acoustic predictions at 30 degrees to the jet axis shows SPL levels higher than at 90 degrees, in agreement with the jet noise directivity.

8.3 Lagrangian and Eulerian evaluation of pressure field

An experimental investigation is conducted on a rod-airfoil flow by means of TR-TOMO PIV in thin-light volume configuration. Unlike planar measurements where only two velocity components are available, TR-TOMO PIV provides all the velocity information for the Lagrangian evaluation of the instantaneous pressure field.

A criterion restricting the relative precision error to 10% on the Lagrangian velocity derivative is proposed to determine the time separation at which performing the evaluation along the particle trajectories. The effect of Δt on the material derivative is analyzed in terms of relative precision error, and 1.2 ms is finally chosen. In contrast, when an Eulerian approach is employed, the time separation is limited to 0.4 ms in order to evaluate the Eulerian acceleration and the advection term on the same flow scales. Under such a condition, the method yields a relative precision error of 15%.

Material velocity derivative and pressure fluctuation evaluated from tomographic measurements in a Lagrangian manner feature patterns similar to those obtained from planar ones as long as the measurement plane is aligned with the dominant flow direction. Instead, if the condition of alignment is no longer satisfied, which means that the out-of-plane velocity component becomes not negligible with respect to the others, the Lagrangian approach based on planar measurements leads to an erroneous evaluation (up to 100%) of the material acceleration and the pressure field.

Chapter 9

Outlook on 3D organization of compressible jets

To conclude the manuscript, it is presented the on-going investigation on 3D flow organization in compressible jets that is conducted in collaboration with NLR (National Aerospace Laboratory of the Netherlands) within the research framework of the ORINOCO project.

9.1 The ORINOCO project

ORINOCO, which is the acronym for "cOoperation with Russia in the field of advanced engIne NOise COntrol based on plasma actuators", is a collaborative project funded by the European Community’s Seventh Framework Program, involving 6 Russian and 7 European partners. ORINOCO is addressing specifically the field of advanced engine-noise control based on plasma actuators.

The application of plasma technology for jet noise reduction is a novel concept that requires fundamental approaches to understand the interaction mechanisms with the main jet and the resulting radiated sound. The main topic of ORINOCO concerns theoretical, numerical and experimental investigations for the efficient implementation of plasma actuators for jet noise reduction.

A primary objective of ORINOCO is to understand the organization of large-scale turbulence, as this is generally recognized as important noise source in high-speed subsonic and supersonic jets. Part of the experimental investigation is conducted by TOMO PIV which, being a fully 3D velocimetry technique, enables unambiguous interpretation of the large-scale features compared to planar and single point ones.

9.1.1 Jet flow facility

The experiments are conducted in the jet tomography facility the Aerodynamic Laboratories of TU Delft in the Aerospace Engineering Department. Contoured shaped nozzle (Figure 9.1) with exit diameter D=22 mm and contraction ratio of 4.4:1 are installed at the bottom of the octagonal tank described in section 4.1. The nozzle is connected to a support, which is divided in a settling chamber (*a*) and a pressure chamber (*c*) by a choke plate (*b*) with diameter of 100 mm. In the pressure chamber, the total pressure P_0 and the total temperature T_0 are measured by means of a static pressure tube and a thermocouple, respectively. The maximum pressure allowed in this chamber is approximately of 30 bar. The high pressure system provides stabilized air supply with mass flow rate up to 0.18 Kg/s and pressure of approximately 3 bar in the pressure chamber. The pressure drops due to the filters and choking plate are found to be about 1 bar at Mach number 0.9. A wooden extension is applied on the Plexiglas tank, as shown in Figure 9.2. At top of the extension, a Plexiglas window enables the access of the laser light. About 10 cm upstream of the window, a crossjet of air is placed to avoid the deposit of impurities (mainly PIV seeding particles).

The measurements are performed at Mach numbers of 0.3, 0.9 and 1.1 at the exit of the nozzle. The exit velocity W_j are, respectively, 100 m/s, 270 m/s and 340 m/s, corresponding to Reynolds numbers of 160,000, 400,000 and 600,000. Note that these are the characteristic regimes of actual operating turbojets. The experimental conditions are summarized in Table 1.

Table 9.1 Experimental conditions

Mach	T_0 [C]	P_{amb} [Pa]	P_0 [Pa]
0.3	16.9	101044	106011
0.9	15.4	101073	169900
1.1	14.5	101120	217593

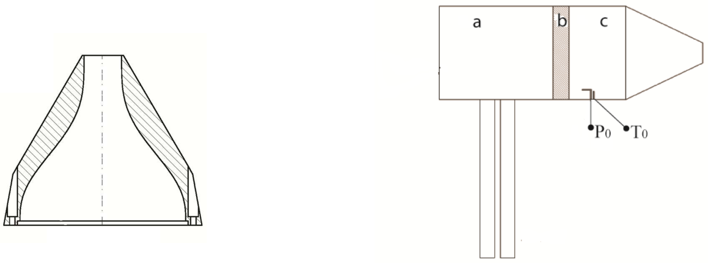

Figure 9.1 Left: contoured nozzle; right: schematic of the nozzle mount

9.1.2 Tomographic PIV measurements

The flow is seeded with DEHS particles (particle diameter of 1 micron) in a concentration of 0.86 particles/mm^3. After a transmission distance of approximately 4 m, the laser beam features a diameter of 6 mm and is further expanded through a beam expander to a diameter of 35mm.

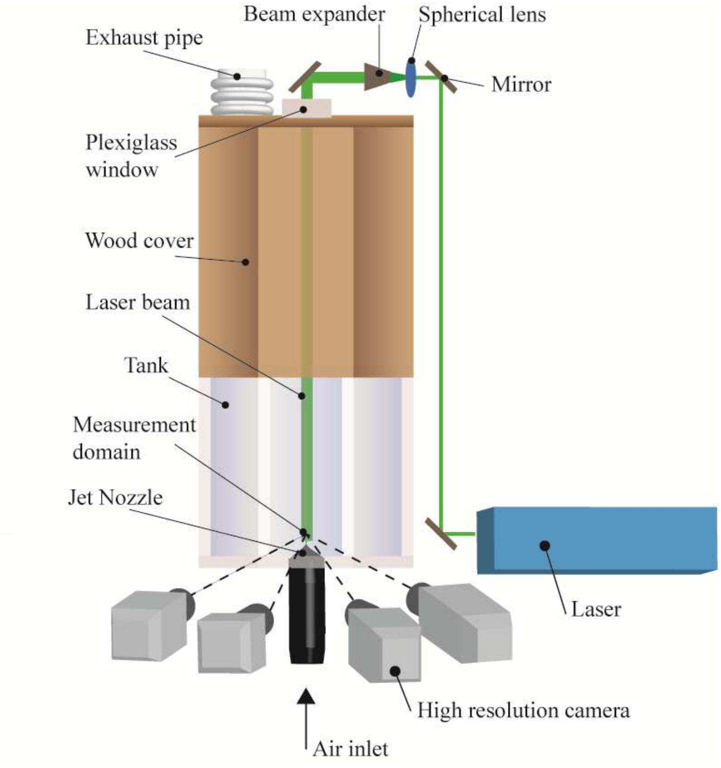
Beam expander
Spherical lens
Exhaust pipe
Mirror
Plexiglass window
Wood cover
Laser beam
Tank
Measurement domain
Jet Nozzle
Laser
High resolution camera
Air inlet

Figure 9.2 Schematic view experimental arrangement for tomographic PIV measurements

The illumination is provided by a *Quanta Ray* double cavity Nd:Yag laser from Spectra-Physics with a maximum pulse energy of 400mJ and a maximum pulse frequency of 10 Hz. The light scattered by the particles is recorded by a tomographic system composed of four LaVision Imager Pro LX 16M (4872x3248 pixels resolution at 3Hz, pixel pitch 7.4µm, 12 bit) at frequency of 1.7 Hz. The cameras are arranged horizontally with azimuthal aperture of 90 degrees (Figure 9.2). The shape of the illuminated volume with a beam of cylindrical cross section eliminates the need for camera-lens tilt mechanism to comply with the

Scheimpflug condition. Nikon objectives of 105mm focal length are set with a numerical aperture *f#*=16 to allow focused imaging of the illuminated particles. For the chosen imaging configuration and for the selected particle concentration, the particle image density attains a maximum of 0.04particles/pixel at the jet axis and decreases towards the edge of the illuminated volume. The separation time between the two exposures is set to obtain a maximum displacement of approximately 12 pixels along the jet axis exit (5µs @ *M*=0.3; 1.5µs @ *M*=0.9; 1µs @ *M*=1.1). The field of view is of 35x190mm^2 with a digital resolution of 25 pixels/mm. The measurement domain extends from 2.5 diameters off the nozzle up to 10.5 diameters.

The volumetric light intensity reconstruction is performed combining the MLOS technique with the SMART algorithm by the LaVision software *Davis* 8. This method allows to reduce the time of 3D light intensity reconstruction by factor 5 compared to the standard MART technique. A three-dimensional mapping function from image-space to physical object-space is generated by imaging a calibration target. The initial experimental errors due to system calibration are approximately 0.5 pixels as estimated from the disparity vector field. The misalignment is reduced to less than 0.05 pixels making use of the *3D self-calibration* technique (Wieneke, 2008). The raw images are pre-processed with subtraction of the minimum intensity at each pixel for the entire sequence, followed by a subtraction of the local minimum over a kernel of 31x31 pixels. The SMART algorithm is applied with five iterations, without compromising the reconstruction accuracy in comparison to MART. The illuminated volume is discretized with 1135 x 4731 x 1141 voxels.

The three-dimensional particle field motion is computed with volume cross-correlation technique by the LaVision software *Davis* 8. A final interrogation volume of 80x80x80 voxels (2x2x2 mm3) with an overlap between adjacent interrogation boxes of 75% produce a velocity field measured over a grid of 57 x 57 x 237 points (vector pitch of 0.5 mm). At the given particle concentration, 9 particles are counted, on average, within the interrogation box.

Data processing is performed on a 48-core Intel *Xeon* processor at 2.20 GHz with 132 GB RAM memory. Reconstruction of a pair of objects and the 3D cross-correlation requires 40 minutes and 20 minutes respectively.

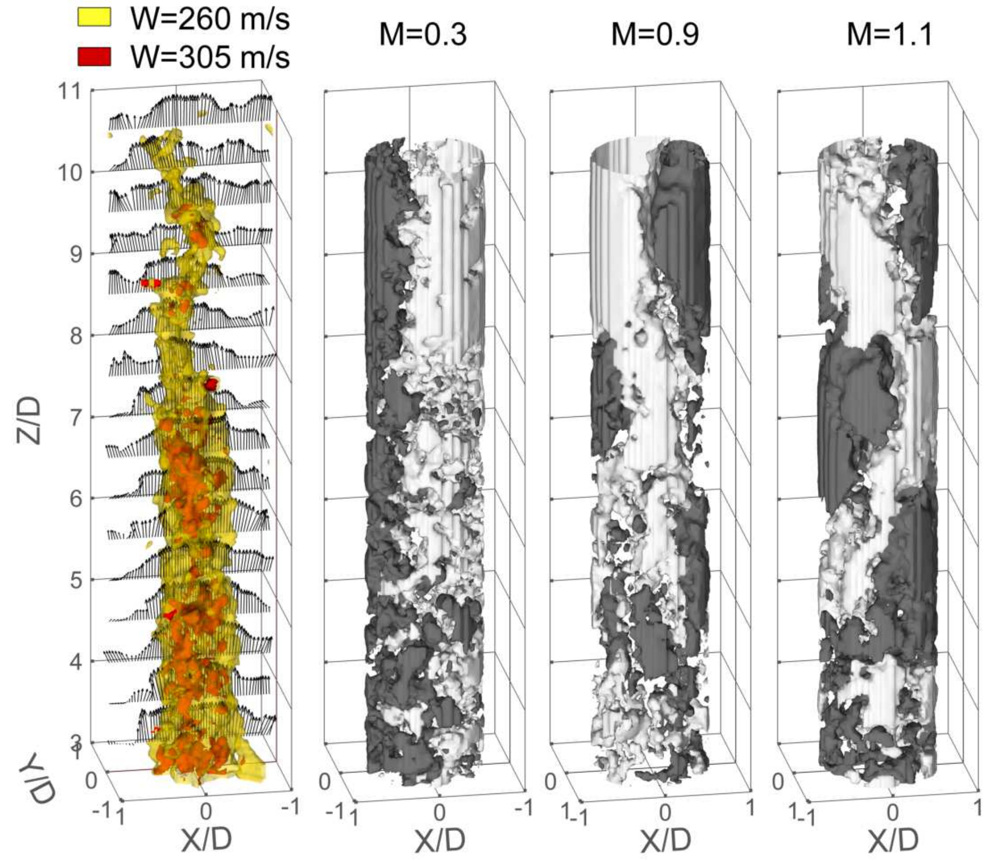

a) b) c) d)

Figure 9.3 a) Instantaneous iso-surfaces of axial velocity of jet at *M*=0.9, with vector shown on plane *Y*=0 (1 every 15 along *Z* direction); first POD mode of axial velocity (positive iso-surfaces of W/W_j in light grey and negative in dark grey); (b) *M*=0.3, (c) *M*=0.9 and (d) *M*=1.1

9.1.3 3D organization by modal decomposition

The axial development of jet at Mach 0.9 is shown in Figure 9.3, which depicts the instantaneous iso-surfaces of axial velocity. Visualization of the instantaneous iso-contours of axial velocity at M=0.3, 0.9 and 1.1 are reported in the appendix where planar PIV experiments are presented.

Snapshot-POD (Sirovich, 1987; see section 3.3.4) is applied to the axial component of the velocity vector **V** to inspect the large-scale structures developing in the jet. The decomposition of velocity is based on a sequence of 100 uncorrelated snapshots. The distribution of energy across the three-dimensional POD modes and the cumulative energy distributions are illustrated in Figure 9.4 for each Mach number. The first pair of modes, which is the only analyzed in this section (see Figure 9.3), is less energetic at M=0.3.

At M=0.3, the first pair is phase shifted of approximately 90 degrees about the jet axis, describing a precession motion. This was also reported for mode pair #9-#10 in the *Re*=5,000 jet (section 5.4.1; Violato and Scarano, 2013).

At M=0.9 and 1.1, the first pair is phase shifted of π/2 in the axial direction, describing travelling waves. The intertwining between the region of positive and negative W indicates a helical motion (Iqbal and Thomas, 2007; Lynch and Thurow, 2009). For Z/D>8, instead the first pair identifies a flapping motion (Lynch and Thurow, 2009). These observations reported seem to agree with what seen in mode pair #4-#5 for the incompressible jet at Re=5,000 (section 5.4.1).

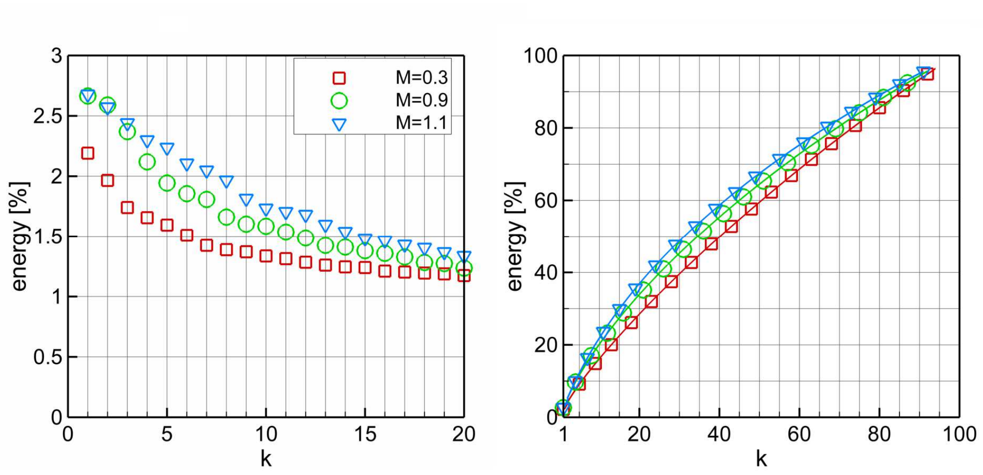

Figure 9.4 Left: energy distributions across first 20 modes of velocity; right: cumulative energy distributions (symbols are shown 1 every 5)

9.2 Towards time-resolved TOMO PIV for high speed flows

Enabling the measurement of the temporal and spatial features of 3D flow structures, time-resolved tomographic PIV technique can play an important role in the experimental investigation of flow events that generate noise. This potential has been acknowledged by Tinney *et al.* (2008b) and in the review article on PIV for aeroacoustics by Morris (2011).

The impact of TOMO PIV in the field of jet aeroacoustics is recently confirmed by the successful application of the technique, within the ORINOCO project, to investigate the 3D organization in high-speed compressible jets (section 9.1).

At high-speed flow regimes, the evaluation of temporal spectra is not affordable with the current kHz-based-rate tomographic systems.

On the other hand, information on the temporal evolution can be retrieved using burst TOMO PIV systems, which is currently being developed at the Aerodynamics Department of Delft University of Technology in the state-of-the-art experiment on high-speed separated flows. Three 4-cameras tomographic sets (Figure 9.5) are employed with 2 lasers to perform 4-pulses PIV. This enables the measurement of 2 (or 3 depending on the time separation between the second and third pulses) subsequent 3D velocity fields, from which acceleration can be evaluated.

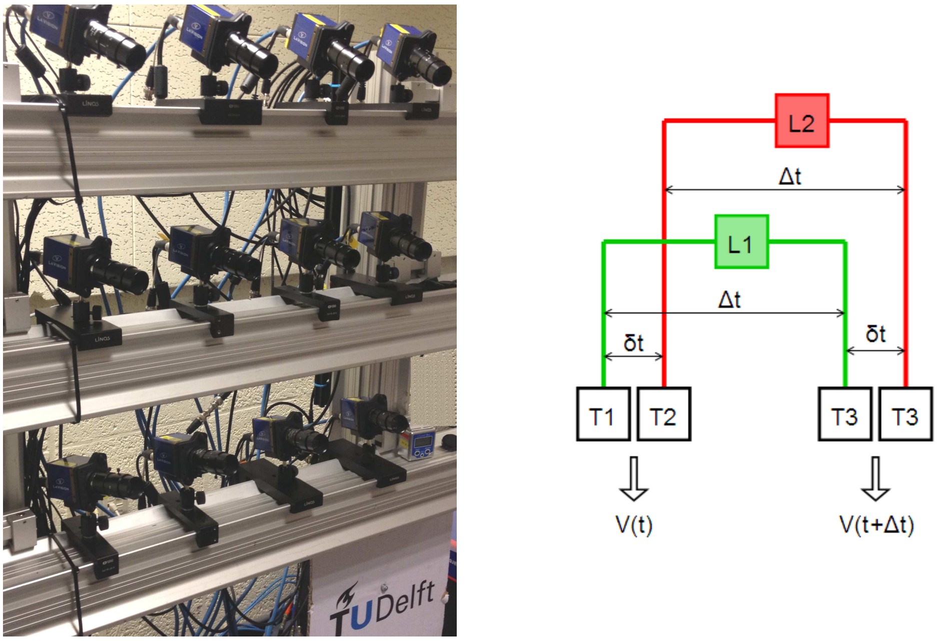

Figure 9.5 4-pulses TOMO PIV; left) imaging system used in the experiment on high speed separated flows (courtesy of K. Lynch); (right) sketch of the acquisition process using tomographic systems T1, T2 and T3 and lasers L1 and L2

Appendix A

High resolution PIV measurements on compressible jets

Planar PIV experiments are conducted on the compressible jets investigated for the ORINOCO project (see chapter 9) for statistical characterization and for flow visualization purposes.

A schematic view of the experimental arrangement is shown in Figure A 1. The illumination is provided by the same equipment used for tomographic PIV (see section 9.1.1). The flow is seeded with DEHS particles with a concentration of 86.7 particles/mm^3. A light sheet of 1.5mm thickness is formed. Sequences of 500 image pairs of the tracer particles are recorded at a frequency of 0.8Hz by two LaVision *Imager Pro* LX 16M CCD cameras (4872 x 3248 pixels @ 3Hz,12bit intensity resolution). Both cameras are arranged with the largest dimension of the sensor aligned with the jet axis in order to maximize the spatial resolution. *Nikon* objectives of 105mm focal length are mounted and the numerical aperture $f_\#$ is set at 4 to maximize the light intensity. The field of view (FOV) of each camera is 69.5mm x 104.2mm, with a digital resolution of 46.8pixels/mm. The two cameras are combined to cover a measurement domain is of 69.5mm x 208.4 mm, corresponding to about 8.5 diameters along the jet axis. The time delay between image pairs is such to obtain a maximum particle image displacements of approximately 12 pixels at the jet exit (3µs @ M=0.3; 1µs @ M=0.9; 0.8µs @ M=1.1).

The quality of the image is improved by historical background intensity removal. The vector calculation is performed by using a sequential cross-correlation with a multi-grid multi-pass algorithm. The interrogation window size decreases from 64 x 64 pixels (1.4 x 1.4 mm^2) to 32 x 32 pixels with 75% overlap, leading to a vector pitch of 0.17mm (129 vector points per jet diameter).

Instantaneous velocity fields

The spatial development of the jets at M=0.3, 0.9 and 1.1 is illustrated, respectively, in Figure A 2, Figure A 3 and Figure A 4, which shows the iso-contour of instantaneous axial velocity W. Note regions of compression and expansion in M=1.1 jet.

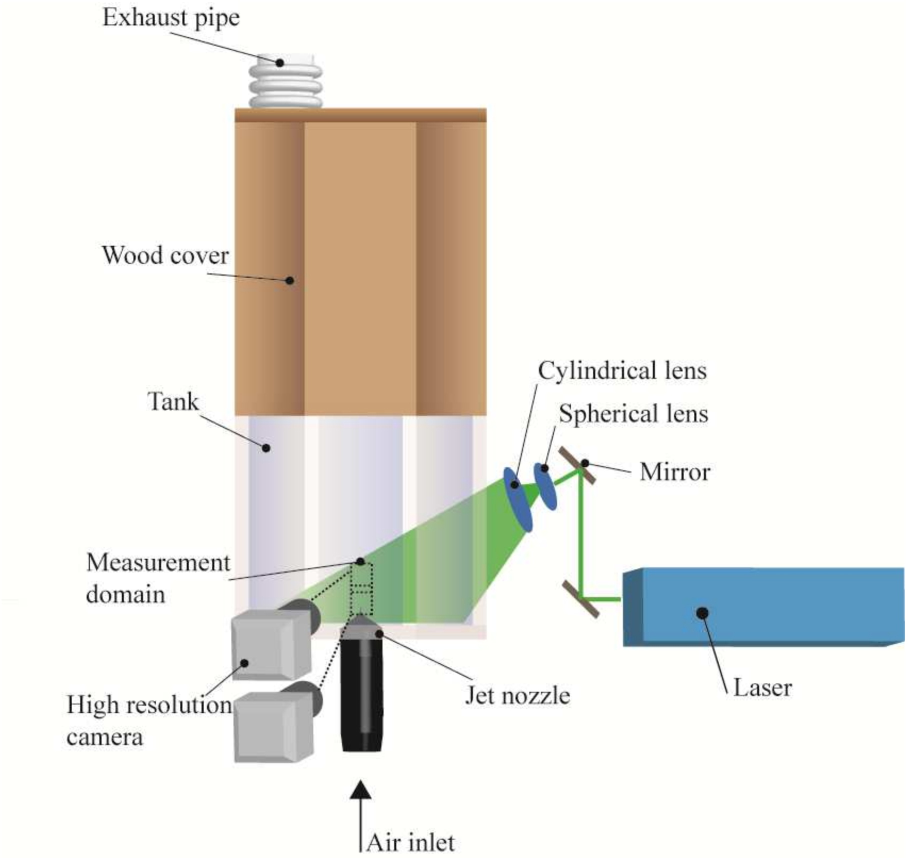
Exhaust pipe
Wood cover
Tank
Cylindrical lens
Spherical lens
Mirror
Measurement domain
High resolution camera
Jet nozzle
Laser
Air inlet

Figure A 1 Schematic view experimental arrangement for planar PIV measurements

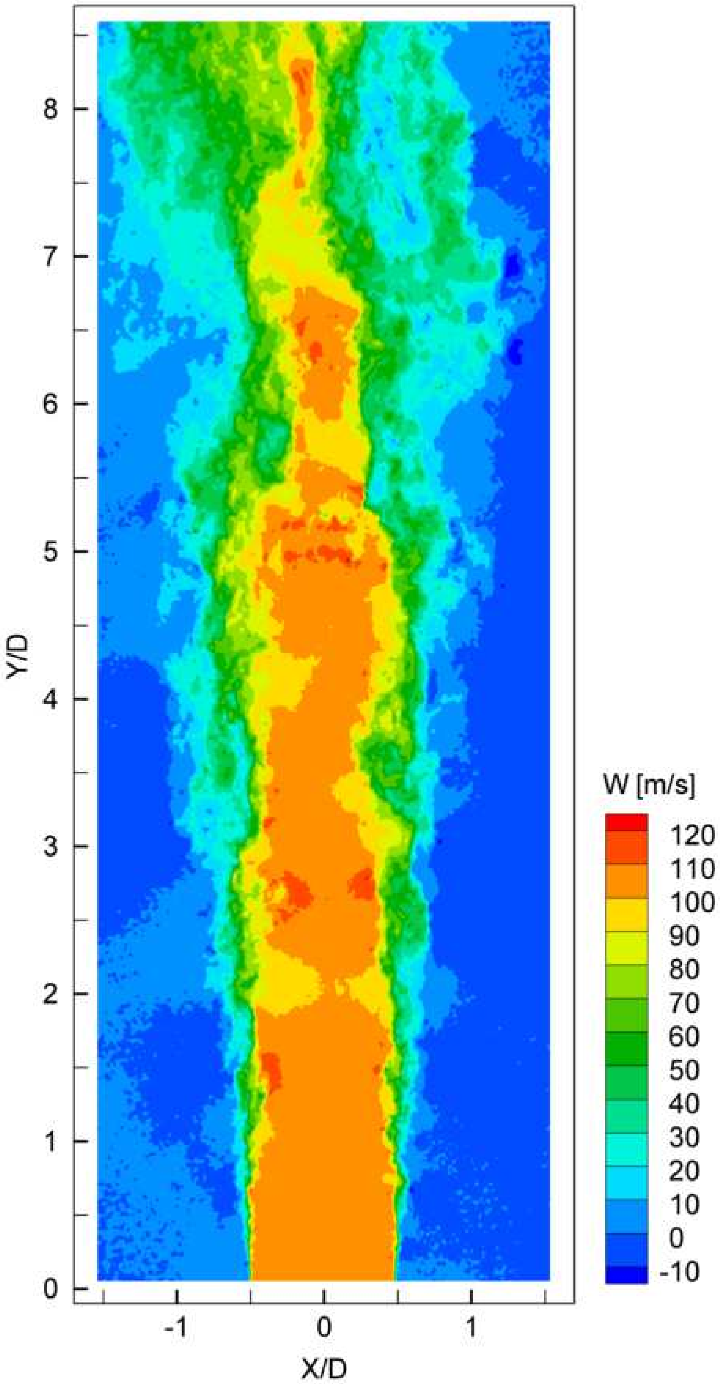

Figure A 2 Iso-contours of instantaneous streamwise velocity field of the contoured nozzle at M=0.3; normalized momentum thickness θ/D=0.0018 at Y/D=0.1

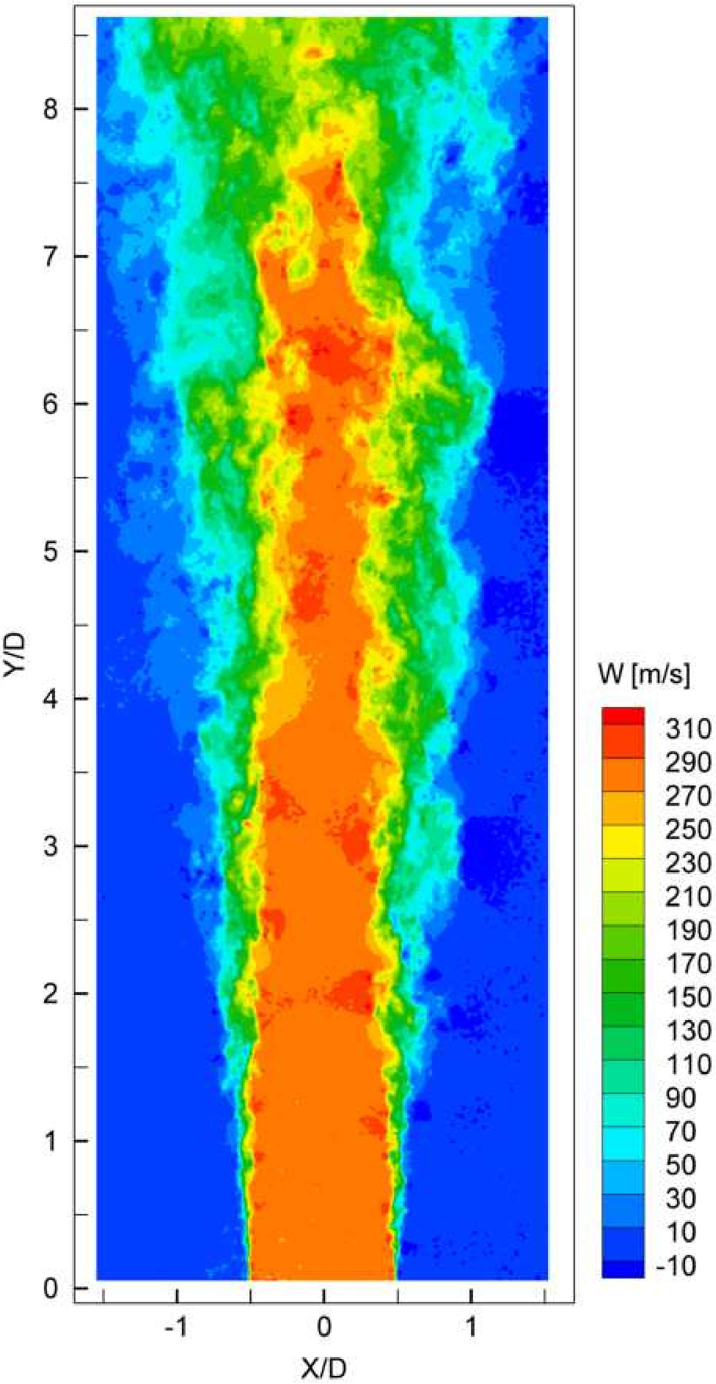

Figure A 3 Iso-contours of instantaneous streamwise velocity field of the contoured nozzle at *M*=0.9; normalized momentum thickness at the jet exit *θ/D*=0.00196 at *Y/D*=0.1

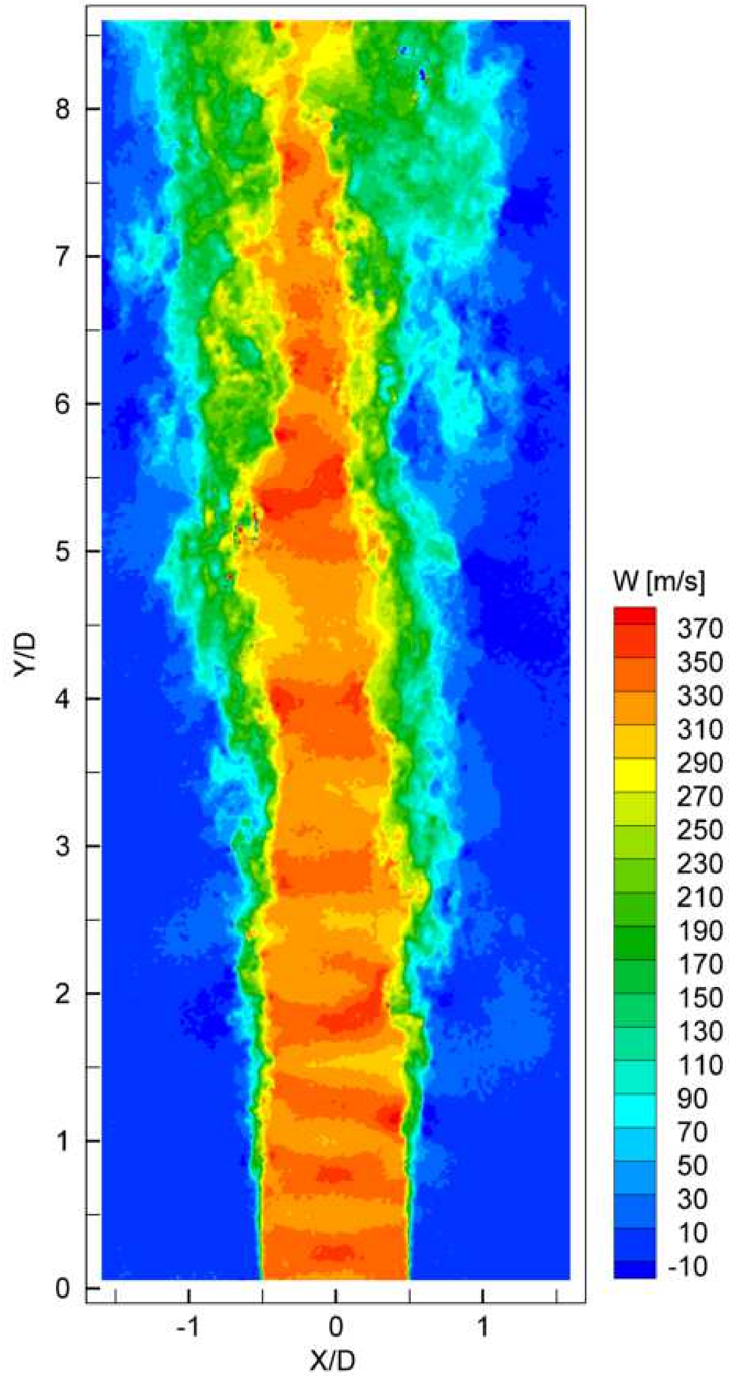

Figure A 4 Iso-contours of instantaneous *W* of the contoured nozzle at *M*=1.1; normalized momentum thickness *θ/D*=0.008 at *Y/D*=0.1

Appendix B

Sound and its human perception

Sound is constituted by local pressure fluctuations of the medium, liquid or gaseous, that propagates as isentropic energy-carrying waves. Humans perceive sound waves only within a frequency range from 20 Hz to 20,000 Hz and amplitudes that are usually very small. The minimum audible level, which is nine orders of magnitude smaller than the ambient pressure, varies with the frequency and typically increases with the age. The value of reference is 2×10^{-5} Pa, which is commonly referred to as threshold of hearing.

The loudness perceived by the humans changes logarithmically with the root-mean square of the pressure variation and is quantified in terms of sound pressure level (SPL)

$$\mathrm{SPL} = 20\log_{10}\left(\frac{p_{rms}}{p_{ref}}\right),$$

where p_{rms} is the root mean square of the acoustic pressure and p_{ref} is the threshold of hearing. The sound pressure level is measured in decibels (dB).

Based on SPL scale, an increase of 20dB corresponds to approximately to a doubling in the perceived loudness of sound, although this may differ from individual to individual and also with the frequency of the sound. A few examples of noise sources that are common in one’s everyday life are given in Table B 1.

Table B 1 Examples noise sources with sound pressure and sound pressure levels

	Sound pressure [Pa]	*SPL [dB]*
Jet engine at 30 m	6.32×10^{2}	150
Threshold of pain	6.32×10	130
Hearing damage	6.32×10^{0}	110
Jet engine at 100 m	6.32×10^{0}	110
Car at 10 m	2×10^{-1}	60
Conversation at 1 m	2×10^{-3}	40
Quiet room	6.32×10^{-4}	30
Breathing	6.35×10^{-5}	10
Threshold of hearing	2×10^{-5}	0

Bibliography

Abramowitz M, Stegun IA (1965), Handbook of mathematical functions, *Dover Publications*.

Adrian RJ (1977), On the role of conditional averages in turbulence theory, In Turbulence in Liquids, *Proceeding of the 4th Biennal Symposium Missouri*, USA (A77-40426 18-34), Princeton, USA, 323–332, Science Press.

Adrian RJ, (1991), Particle-imaging techniques for experimental fluid mechanics, *Annual Review of Fluid Mechanics*, 23, 1: 261-304.

Adrian RJ, (2005), Twenty years of particle image velocimetry, *Experiments in Fluids*, 39:159-169.

Adrian RJ, Yao CS (1985), Pulsed technique application to liquid and gaseous flows and the scattering power of seed materials, *Applied Optics*, 24:1.

Alkislar MB, Krothapalli A, Butler GW (2007), The effect of streamwise vortices on the aeroacoustics of a Mach 0.9, *Journal of Fluid Mechanics*, 578:139–169.

Alkislar MB, Krothapalli A, Lourenço LM (2003), Structure of a screeching rectangular jet: a stereoscopic PIV study, *Journal of Fluid Mechanics*, 489:121–154.

Atkinson CH, Soria J (2009), An efficient simultaneous reconstruction technique for tomographic particle image velocimetry, *Experiments in Fluids*, 47:553-568.

Batchelor BK (1967), An Introduction to fluid dynamics, *Cambridge University Press*, Cambridge, 1967.

Baur X, Kongeter J (1999), PIV with high temporal resolution for the determination of local pressure reductions from coherent turbulent phenomena, *PIV'99*, Santa Barbara, USA.

Becker HA, Massaro TA (1968), Vortex evolution in a round jet, *Journal of Fluid Mechanics* 31:435–448.

Berkooz, G, Holmes P, Lumley JL (1993), The proper orthogonal decomposition in the analysis of turbulent flows, *Annual Review of Fluid Mechanics*, 25:539-575.

Bernal LP, Roshko A (1986), Orderly structure in jet turbulence, *Journal of Fluid Mechanics*, 170:499–525.

Bi W, Sugii Y, Okamoto K, Madarame H (2003), Time-resolved proper orthogonal decomposition of the near-field flow of a round jet measured by dynamic particle image velocimetry, *Measurement Science and Technology*, 14 L1-L5.

Birch SF, Lyubimov DA, Maslov VP, Secundov AN (2006), Noise prediction for chevron nozzle flows, *12th AIAA/CEAS Aeroacoustics Conference*, Cambridge, Massachusetts.

Blevis RD (1984), Review of sound induced by vortex shedding from cylinders, *Journal of Sound and Vibration*, 92(4):455-470.

Bodony D, Lele SK (2004), Jet noise prediction of cold and hot subsonic jets using large-eddy simulation, *AIAA Paper* 2004-3022.

Boersma BJ (2005), Large Eddy Simulation of the sound field of a round turbulent jet, *Theoretical Computational Fluid Dynamics*, 19:161-170.

Bogey C, Bailly C, Juve´ D (2003), Noise investigation of a high subsonic, moderate Reynolds number jet using a compressible LES, *Journal of Theoretical and Computational Fluid Dynamics*, 16(4):273–297.

Bradshaw P, Ferriss DH, Johnson RF (1964), Turbulence in the noise producing region of a circular jet, *Journal of Fluid Mechanics*, 19: 591-624.

Bridges J, Brown CA (2004), Parametric testing of chevrons on single flow hot jets, Technical Report No. 213107, NASA.

Bridges JE, Hussain AKMF (1987), Roles of initial condition and vortex pairing in jet noise, *Journal of Sound and Vibration*, 117:289-311.

Brooks TF, Humphreys Jr. WM (2006), A deconvolution approach for the mapping of acoustic sources (DAMAS) determined from phased microphone array, *Journal of Sound and Vibration*, 294(4-5):856–879.

Brown GB (1935), On vortex motion in gaseous jets and the origin of their sensitivity to sound, *Proceeding of the Physical Society*, 47: 703.

Brücker C (1995), Digital-particle-image-velocimetry (DPIV) in a scanning light sheet: 3D starting flow around a short cylinder, *Experiments in Fluids*, 19:255-263.

Cabana M, Fortuné V, Jordan P (2008), Identifying the radiating core of Lighthill’s source term, *Theoretical and Computational Fluid Dynamics*, 22: 87-106.

Camussi R, Guj G (1999), Experimental analysis of intermittent coherent structures in the near field of a high Re turbulent flow, *Physics of Fluids*, 11:423.

Cantwell BJ (1981), Organized motion in turbulent flow, *Annual review of Fluid Mechanics*, 13(1): 457-515.

Cavalieri A, Daviller G, Comte P, Jordan P, Tadmor G, Gervais Y (2011a), Using large eddy simulation to explore sound-source mechanisms in jets, *Journal of Sound and Vibration* doi:10.1016/j.jsv.2011.04.018.

Cavalieri A, Jordan P, Agarwal A, Gervais Y (2011b), Jittering wave-packet models for subsonic jet noise, *Journal of Sound and Vibration*, doi:10.1016/j.jsv.2011.04.007.

Cavalieri A, Violato D, Rodrıguez D, Jordan P, Scarano F, Colonius T, Gervais Y (2012), Low-speed jet dynamics and sound radiation, *18th AIAA/CEAS Aeroacoustics Conference*, Colorado Spring, USA.

Cintriniti JH, George WK (2000), Reconstruction of the global velocity field in the axisymmetric mixing layer utilizing the proper orthogonal decomposition, *Journal of Fluid Mechanics*, 418:137–166.

Clarke JP (2003), The role of advances air traffic management in reducing the impact of aircraft noise and enabling aviation growth, *Journal of Air Transport Management*, 161-165.

Coiffet F, Jordan P, Delville J, Gervais Y, Ricaud F (2006), Coherent structures in subsonic jets: a quasi irrotational source mechanism? *International Journal of Aeroacoustics*, 5:67–89.

Colonius T, Lele SK (2004), Computational aeroacoustics: progress on nonlinear problems of sound generation, *Progress in Aerospace*, 40:315-416.

Crighton DG (1975), Basic principles of aerodynamic noise generation, *Progress in aerospace sciences*, 16-1:31-96.

Crighton DG (1993), Computational aeroacoustic for low Mach number flows, *Computational Aeroacoustics Springer*, Berlin.

Crow S, Champagne F (1971), Orderly structure in jet turbulence, *Journal of Fluid Mechanics*, 48:547–591.

Crow SC (1970), Aerodynamic sound emission as a singular perturbation problem, *Studies in Applied Mathematics*, 49:21–44.

Crow SC, (1972), Acoustic gain of a turbulent jet, *Physiological Society Meeting*, Vol.6, University of Colorado, *Boulder*, Paper IE.

Curle N (1955), The influence of solid boundaries upon aerodynamic sound, *Proceedings of the Royal Society of London*, A 231:505–514.

Dahan C, Elias G, Maulard J, Perulli M (1978), Coherent structures in the mixing zone of a subsonic hot free jet, *Journal of Sound and Vibration*, 59(3):313–333.

de Kat R, van Oudheusden BW (2010), Instantaneous planar pressure from PIV: analytic and experimental test-cases, *15th International Symposium on Applications of Laser Techniques for Fluid Mechanics*, Lisbon, Portugal.

de Kat R, van Oudheusden BW, Scarano F (2008), Instantaneous planar pressure field determination around a square-section cylinder based on time-resolved stereo-PIV, *14th International Symposium on Applications of Laser Techniques for Fluid Mechanics*, Lisbon, Portugal.

de Kat R, van Oudheusden BW, Scarano F (2009), Instantaneous pressure field determination in a 3d flow using time resolved thin volume tomographic-PIV, *8th international symposium on particle image velocimetry—PIV09*, Melbourne, Australia.

Di Florio D, Di Felice F, Romano GP (2002), Windowing, re-shaping and re-orientation interrogation windows in particle image velocimetry for the investigation of shear flows, *Measurement Science and Technology*, doi:10.1088/0957-0233/13/7/301.

Dimotakis PE, Miake-Lye RC, Papantoiou DA (1983), Structure dynamics of round turbulent jets, *Physics of Fluids*, 26:3185-3192.

Discetti S, Astarita T (2010), Acceleration of Tomo-PIV by multigrid reconstruction schemes, *15th International Symposium on Applications of Laser Techniques for Fluid Mechanics*, Lisbon, Portugal.

Discetti S, Astarita T (2012), Fast 3D PIV with direct sparse cross- correlation, *Experiments in Fluids*, DOI 10.1007/s00348-012-1370-9.

El Hassan M, Meslem A (2010), Time-resolved stereoscopic particle image velocimetry investigation of the entrainment in the near field of circular and daisy shaped orifice jets, *Physics of Fluids*, 22:035,107.

El Hassan M, Meslem A, Abed-Meraim K (2011), Experimental investigation of the flow in the near-field of a cross-shaped orifice jet, *Physics of Fluids*, DOI:10.1063/1.3562841.

Elsinga GE, Adrian RJ, van Oudheusden BW, Scarano F (2010), Three-dimensional vortex organization in a high-Reynolds-number supersonic turbulent boundary layer, *Journal of Fluid Mechanics*, 644: 35-60.

Elsinga GE, Scarano F, Wieneke B, van Oudheusden BW (2006), Tomographic particle image velocimetry, *Experiments in Fluids*, 41:933–947.

Elsinga GE, Westerweel J, Scarano F, Novara, M (2011), On the velocity of ghost particles and bias errors in Tomographic-PIV, *Experiments in Fluids*, 50:825-838.

Enrich RJ (1981), Methods of experimental physics, part 1, p.6, *Fluid Dynamics Academic*, New York.

Eriksson C, Rosenlund M, Pershagen G, Hilding A, Ostenson CG, Bluhm G (2007), Aircraft noise and incidence of hypertension, *Epidemiology*, 18(6):716-21.

Ffowcs JE, Hawkings DL (1969), Sound generation by turbulence and surfaces in arbitrary motion, *Proceeding of the Royal Society of London*, A 264:321–342.

Ffowcs Williams JE (1977), Aeroaocoustics, *Annual Review of Fluid Mechanics*, 9:447-68.

Fleury V, Bailly C, Jondeau E, Michard M, Juvé D (2008), Space-time correlation in two subsonic jets using dual Particle Image Velocimetry, *AIAA Journal*, 46, n10.

Franssen EAM, van Wiechen CMAG, Nagelkerke NJD, Lebret E (2002), Aircraft noise around a large international airport and its impact on general health and medication use, *Occupational Environmental Medicine*, 61:405-413.

Freund JB (2001), Noise sources in a low-Reynolds-number turbulent jet at Mach 0.9, *Journal of Fluid Mechanics*, 438:277-305.

Ganapathisubramani B, Longmire KE, Marusic I (2002), Investigation of three dimensionality in the near field of a round jet using stereo PIV, *Journal of Turbulence*, DOI: 10.1088/1468-5248/3/1/016.

Geers LFG, Tummers MJ, Bueninck TJ, Hanjalic K (2008), Heat transfer correlation for hexagonal and in-line arrays of impinging jets, *International Journal Heat and Mass transfer*. doi:10.1016/j.ijheatmasstransfer.2008.01.035.

Geers LFG, Tummers MJ, Hanjalic K (2005), Particle imaging velocimetry-based identification of coherent structures in normally impinging multiple jets, *Physics of Fluids*, Vol 17 055105.

Ghaemi S, Ragni D, Scarano F (2012), PIV-based pressure fluctuation in the turbulent boundary layer, *Experiments in Fluids*, DOI 10.1007/s00348-012-1391-4.

Goldstein ME (1976), Aeroacoustics, *McGraw-Hill*, New York.

Goldstein ME (1984), Aeroacoustics of turbulent shear flows, *Annual Review of Fluid Mechanics,* 16 263-85.

Goldstein ME (2003), A generalized aeroacoustic analogy, *Journal of Fluid Mechanics* 488:315-333.

Grizzi S, Camussi R (2012), Wavelet analysis of near-field pressure fluctuations generated by a subsonic jet, *Journal of Fluid Mechanics*, 698:92-124.

Guj G, Carley M, Camussi R, Ragni A (2003), Acoustic identification of coherent structures in a turbulent jet, *Journal of Sound and Vibration*, 259:1037-1065.

Gurka R, Liberzon A, Hefetz D, Rubinstein D, Shavit U (1999), Computation of pressure distribution using PIV velocity data, *Proceedings of the 3rd International Workshop on Particle Image Velocimetry—PIV'99,* Santa Barbara, USA.

Haigermoser C (2009), Application of an acoustic analogy to PIV data from rectangular cavity flow, *Experiments in Fluids*, 47:145–157.

Hain R, Kähler CJ, Michaelis D (2008), Tomographic and time resolved PIV measurements on a finite cylinder mounted on a flat plate, *Experiments in Fluids,* 45:715-724.

Harper-Bourne M (2010), Jet noise measurements: past and present, *International Journal of Aeroacoustics* 9:559–88.

Henning A, Kaepernick K, Ehrenfried K, Koop L, Dillmann A (2008), Investigation of aeroacoustic noise generation by simultaneous particle image velocimetry and microphone measurements, *Experiments in Fluids*, 45:1073–1085.

Henning A, Koop L, Ehrenfried K, Lauterbach A, Kroeber S (2009), Simultaneous multiplane PIV and microphone array measurements on a rod-airfoil configuration, *15th AIAA/CEAS Aeroacoustics Conference*, Miami, USA AIAA-2009-3184.

Henning A, Schroeder A, Krebs I, Agocs J (2010), Aeroacoustic Investigations on a Cold Jet by Means of Simultaneous PIV and Microphone Measurements. *15th International Symposium on Applications of Laser Techniques to Fluid Mechanics,* Lisbon, Portugal.

Herrmann GT, Lent A (1976), Iterative reconstruction algorithm, *Computers in Biology and Medicine Journal*, 6:273 294.

Hileman JI, Thurow BS, Caraballo EJ and Sammy M (2005), Large-scale structure evolution and sound emission in high-speed jets: real-time visualization with simultaneous acoustic measurements, *Journal of Fluid Mechanics*, 544: 277-307.

Hinsch KD (2002), Holographic particle image velocimetry, *Measurement Science and Technology*, 13:R61-R72.

Ho CM, Gutmark EJ (1987), Vortex induction and mass entrainment in a small aspect-ratio elliptic jet, *Journal of Fluid Mechanics*, 179:383.

Hori T, Sakakibara J (2004), High-speed scanning stereoscopic PIV for 3D vorticity measurement in liquids, *Measurement Science and Technology*, 15:1067–1078.

Howe MS (1975), The generation of sound by aerodynamic sources in inhomogeneous steady flow, *Journal of Fluid Mechanics*, 67:597-610.

Howe MS (2003), Theory of vortex sound, *Cambridge University Press*, Cambridge, UK.

Huang HT, Fielder HF, Wang JJ (1993a), Limitation and improvement of PIV, Part I. Limitation of conventional techniques due to deformation of particle image patterns, *Experiments in Fluids*, 15:168-174.

Huang HT, Fielder HF, Wang JJ (1993b), Limitation and improvement of PIV Part II. Particle image distortion, a novel technique, *Experiments in Fluids*, 15: 263-273.

Humble RA, Elsinga GE, Scarano F, van Oudheusden BW (2009), Three-dimensional instantaneous structure of a shock wave/turbulent boundary layer interaction, *Journal of Fluid Mechanics*, 622:33–62.

Hussain AKMF (1983), Coherent structures reality and mith, *Physics of Fluids*, 26:2816-2850.

Hussain AKMF (1986), Coherent structures and turbulence, *Journal of Fluid Mechanics*. 173:303-356.

Hussain AKMF, Zaman KBMQ (1981), The preferred mode of the axisymmetric jet, *Journal of Fluid Mechanics*, 110, 39.

Iqbal MO, Thomas FO (2007), Coherent structure in a turbulent jet via a vector implementation of the proper orthogonal decomposition, *Journal of Fluid Mechanics*, 571: 281-326.

Ising H, Kruppa B (2004), Health effects caused by noise: Evidence in the literature from the past 25 years, *Noise and Health*, 6:5-13.

Jacob MC, Boudet J, Casalino D, Michard M (2004), A rod-airfoil experiment as benchmark for broadband noise modeling, *Theoretical and Computational Fluid Dynamics*, 19:171–196.

Jambunathan K, Lai E, Moss MA, Button BL (1992), A review of heat transfer data for single circular jet impingement, *International Journal of Heat and Fluid Flow*, 13:2.

Jeong J, Hussain F (1995), On the identification of a vortex, *Journal of Fluid Mechanics*, 285:69–94.

Jordan P, Colonius T (2013), Wave packets and turbulent jet noise, *Annual Review of Fluid Mechanics*, 45:173-95.

Jordan P, Gervais Y (2008), Subsonic jet aeroacoustics: associating experiment, modeling and simulation. *Experiments in Fluids*, DOI 10.1007/s00348-007-0395-y.

Jordan P, Schlegel M, Noack BR, Tinney CE, (2007), Indentifying noisy and quiet modes in a jet, *13th AIAA/CEAS Aeroacoustic Conference*, Rome, Italy.

Jung D, Gamard S, George WK (2004), Downstream evolution of the most energetic modes in a turbulent axisymmetric jet at high Reynolds number. Part 1. The near-field region, *Journal of Fluid Mechanics*, 514: 173-204.

Juvé D, Sunyach M, Comte-Bellot G (1980), Intermittency of the noise emission in subsonic cold jets, *Journal of Sound and Vibration*, 71(3):319–332.

Kataoka M, Suguro H, Degawa K, Maruo I, Mihata (1987), The effect of surface renewal on jet impingement heat transfer, *International Journal of Heat and Mass Transfer*, 30 559–567.

Katz J, Sheng J (2010), Applications of Holography in Fluid Mechanics and Particle Dynamics, *Annual Review of Fluid Mechanics*, 42:531-555.

Keane RD, Adrian RJ (1992), Theory of cross-correlation analysis of PIV images, *Applied Scientific Research*, 49:191-215.

Khashehchi M, Elsinga GE, Ooi A, Soria J, Marusic I (2010), Studying invariants of the velocity gradient tensor of a round turbulent jet across the turbulent/nonturbulent interface using tomo PIV, *15th International Symposium on Applications of Laser Techniques to Fluid Mechanics*, Lisbon, Portugal.

Kinzie KW, Schein DB, Solomon WD (2002), Experiments and analyses of distributed exhaust nozzles. *8th AIAA/CEAS Aeroacoustics Conference, 2555*.

Kopiev VF, Chernyshev SA (1997) Vortex ring eigen-oscillations as a source of sound. *Journal of Fluid Mechanics* 341:19–57

Kopiev VF, Zaitsev MY, Chernyshev SA, Kotova AN (1999), The role of large-scale vortex in a turbulent jet noise, *Proceedings of the 5th AIAA/CEAS Aeroacoustics Conference*, AIAA-99-1839, Washington, USA.

Koschatzky V, Moore PD, Westerweel J, Scarano F, Boersma BJ (2010), High speed PIV applied to aerodynamic noise investigation, *Experiments in Fluids*. DOI:10.1007/s00348-010-0935-8.

Kostas J, Soria J, Chong MS (2005), A comparison between snapshot POD analysis of PIV velocity and vorticity data, *Experiments in Fluids*, 38:146-160.

Kroo IM (2003), Aircraft design: synthesis and analysis, http://adg.staford.edu/aa241/AircraftDesign.html.

Kryter K D (1994), The handbook of hearing and the effects of noise: physiology, psychology and public health, *Boston Academic Press*.

Kyle DM, Shreenivasan KR (1993), The instability and breakdown of a round variable-density jet, *Journal of Fluid Mechanics*, 249:619-664.

La Porta A, Voth GA, Crawford JA, Alexander J, Bodenschatz E (2000), Fluid particle accelerations in fully developed turbulence, *Nature*, 409:1017–1019.

Lamb H (1878), On the conditions for steady motion of a fluid, *Proceedings London Mathematical Society*, 9:91.

Lau JC, Fisher MJ, Fuchs HV (1972), The intrinsic structure of turbulent jets, *Journal of Sound and Vibration*, 22(4):379–406.

Lau JC, Morris PJ, Fisher MJ (1979), Measurements in subsonic and supersonic free jets using a laser velocimeter, *Journal of Fluid Mech*anics, 93:1-27.

Laufer J, Yen T-C (1983), Noise generation by a low-Mach-number jet, *Journal of Fluid Mech*anics, 134:1–31.

Leonard A (1985), Computing three-dimensional incompressible flows with vortex elements, *Annual Review of Journal of Fluid Mechanics*, 17, 523.

Lepicovsky J (1989), The role of nozzle-exit boundary layer velocity gradient in mixing enhancement of free jets, *Proceeding 3rd Joint ASCE/ASME Mechanics Conference*, San Diego, USA.

Liepmann D, Gharib M (1992), The role of streamwise vorticity in the near field entrainment of round jets, *Journal of Fluid Mechanics*, 245:643–668.

Lighthill MJ (1952), On sound generated aerodynamically, Part 1: general theory, *Proceedings of the Royal Society of London*, A 211:564–587.

Lilley GM (1974), On the noise from air jets, *Noise Mechanisms*, AGARD CP 131, 13.1-13.12.

List EJ (1982), Turbulent jets and plumes, *Annual Review of Fluid Mechanics*, 14:189-212.

Liu X, Katz J (2006), Instantaneous pressure and material acceleration measurements using a four-exposure PIV system. *Experiments in Fluids*, 41:227–240.

Lorenzoni V, Tuinstra M, Moore P, Scarano F (2009), Aeroacoustic analysis of rod-airfoil flow by means of time resolved PIV, *Proceedings of the 15th AIAA/CEAS aeroacoustics conference*, Miami, USA.

Lorenzoni V, Tuinstra M, Scarano F (2012), On the use of time-resolved particle image velocimetry for the investigation of rod-airfoil aeroacoustics, *Journal of Sound and Vibration*, 331:5012-5027.

Lumley JL (1981), Coherent structures in turbulence, *In Transition and turbulence*, R. E. Meyer 215-242, Academic.

Lush PA (1971), Measurements of subsonic jet noise and comparison with theory, *Journal of Fluid Mechanics*, 46-3:477-500.

Lynch KP, Thurow BS (2009), POD analysis of 3d-flow visualization images of a circular jet with Reynolds number 9500, *39th AIAA Fluid Dynamics Conference,* San Antonio, USA.

Maas HG, Gruen A, Papantoniou D (1993), Particle tracking velocimetry in three-dimensional flows, *Experiments in Fluids*, 15:133-146.

Martin JE, Meiburg E (1991), Numerical investigation of three-dimensionally evolving jet subject to axisymmetric and azimuthal perturbations, *Journal of Fluid Mechanics,* 230 27.

Matsuda T, Sakakibara J (2005), On the vortical structure in a round jet, *Physics of Fluids*, 17:025,106.

Maynard JD, Williams EG, Lee Y, (1985), Near field acoustic holography: Theory of generalized holography and development of NAH, *Journal of the Acoustical Society of America*, 78 1395–1413.

Meinhart CD, Wereley ST, Santiago JG (2000), A PIV algorithm for estimating time-averaged velocity fields, *Journal of Fluids Engineering*, 122:285.

Melling A (1997), Tracer particles and seeding for particle image velocimetry, *Measurement Science and Technology*, 8: 1406-1416.

Meyer KE, Pedersen JM, Ozcan O (2007), A turbulent jet in crossflow analysed with proper orthogonal decomposition, *Journal of Fluid Mechanics*, 583:199-227.

Michalke A, Fuchs HV (1975), On turbulence and noise of an axisymmetric shear flow, *Journal of Fluid Mechanics*, 70:179–205.

Mitchell BE, Lele SK, Moin P (1999), Direct computation of the sound generated by vortex pairing in an axisymmetric jet, *Journal of Fluid Mechanics*, 383:113–142.

Moehring W (1978), On vortex sound at low Mach number, *Journal of Fluid Mechanics*, 85:685.

Mollo-Christensen (1967), Jet noise and shear flow instability seen from an experimenter's viewpoint (Similarity laws for jet noise and shear flow instability as suggested by experiments), *Journal of Applied Mechanics*, 34:17.

Moore CJ (1977), The role of shear layer instability waves in jet exhaust noise, *Journal of Fluid Mechanics*, 80:321–367.

Moore P, Lorenzoni V, Scarano F (2010), Two techniques for PIV based aeroacoustic prediction and their application to a rod-airfoil experiment, *Experiments in Fluids*, Doi:10.1007/s00348-010-0932-y.

Moore P, Violato D, Bryon K, Scarano F (2010), On the suitability of direct application of acoustic theory to time-resolved tomographic PIV tested by DNS for low Mach number jet flows, *16th AIAA/CEAS Aeroacoustic Conference*, Stockholm, Sweden.

Morfey CL (1984), Sound radiation due to unsteady dissipation in turbulent flows, *Journal of Sound and Vibration*, 48:95–111.

Moroni M, Cushman JH, Cenedese A (2003), A 3D-PTV two-projection study of pre-asymptotic dispersion in porous media which are heterogeneous on the bench scale, *International Journal of Engineering Science*, 41:337–70.

Morris PJ, Farassat F (2002), Acoustic analogy and alternative theories for jet noise prediction. *AIAA Journal*, 40(4):671–680.

Morris SC (2011), Shear layer instabilities: particle image velocimetry measurements and implications for acoustics, *Annual Review of Fluid Mechanics*, 43: 529-550.

Nogueira J, Lecuona A, Rodriguez PA (1999), Local field correction PIV: on the increase of accuracy of digital PIV systems, *Experiments in Fluids*, 27:107-116.

Novara M and Scarano F (2012), Performances of motion tracking enhanced Tomo-PIV on turbulent shear flows, *Experiments in Fluids*, 52:1027-1041.

Novara M, Batemburg KJ, Scarano F (2012), Motion tracking-enhanced MART for tomographic PIV, *Measurement Science and Technology*, 21:035401.

Novara M, Ianiro A, Scarano F (2012), Adaptive interrogation for 3D-PIV, *Measurement Science and Technology*, accepted for publication.

Obermeier F (1985), Aerodynamic sound generation caused by viscous processes. *Journal of Sound and Vibration*, 99:111–120.

Obrist D, Kleiser L (2007), The influence of spatial domain truncation on the prediction of acoustic far-fields, *13th AIAA/CEAS Aeroacoustic Conference*, Rome, Italy.

Oldenhof E, Tummers MJ, van Veen EH, Roekaerts DJEM (2010), Ignition kernel formation and lift-off behavior of jet-in-hot-coflow flames, *Combustion and Flame*, doi:10.1016/j.combustflame.2010.01.002.

Opalski AB, Wernet MP, Bridges JE (2005), Chevron nozzle performance characterization using stereoscopic DPIV, *AIAA Journal*, 444.

Paschereit CO, Oster D, Long TA, Fiedler HE, Wygnaski I (1992), Flow visualization of interactions among large coherent structures in an axisymmetric jet, *Experiments in Fluids*, 12:189-199.

Paterson RW (1984), Turbofan forced mixer nozzle flow field: a benchmark experimental study, *ASME Journal of Engineering for Gas Turbines and Power*, 106:692.

Patte-Rouland B, Lalizel G, Moreau J, Rouland E (2001), Flow analysis of an annular jet by particle image velocimetry and proper orthogonal decomposition, *Measurement Science and Technology*, 12 1404-1412.

Percin M, Hu Y, Van Oudheusden BW, Remes B, Scarano F (2012), Wing Flexibility Effects in Clap-and-Fling, *International Journal of Micro Air Vehicles*, 3:217-228.

Petersen RA (1978), Influence of wave dispersion on vortex pairing in a jet, *Journal of Fluid Mechanics*, 89:469.

Phillips OM (1960), On the generation of sound by supersonic turbulent shear layers, *Journal of Fluid Mechanics,* 9:1-28.

Powell A (1964), Theory of vortex sound, *Journal of Acoustic Society of America*, 36:177.

Proebsting S, Scarano F, Bernardini M, Pirozzoli S (2012), A comparative study of turbulent boundary layer wall pressure fluctuations obtained from high-speed tomographic PIV and DNS, *Proceedings of the 16th International Symposium on Applications of Laser Techniques to Fluid Mechanics*, Lisbon, Portugal

Raffel M, Willert CE, Kompenhans J (1998), Particle image velocimetry – A practical guide, *Springer,* New York.

Raffel M, Willert CE, Wereley ST, Kompenhans J (2007). Particle image velocimetry – a practical guide, *Springer*, New York.

Ragni D, Schrijer FFJ, van Oudheusden BW, Scarano F (2010), Particle tracer response across shocks measured by PIV, *Experiments in Fluids*, 50:53-64.

Rajaratnam N (1976), Turbulent Jets, *Elsevier*, New York.

Rousseaux G, Seifer S, Steinberg V, Wiebel A (2006), On the Lamb vector and the hydrodynamic charge, *Experiments in Fluids*, 42:291-299.

Saffman PG (1992), Vortex Dynamics, *Cambridge University Press,* Cambridge.

Scarano F (2003), Theory of non-isotropic spatial resolution in PIV, *Experiments in Fluids*, 35: 268-277.

Scarano F (2008), Overview of PIV in Supersonic Flows. Particle Image Velocimetry, New developments and recent applications, 112: 445-463, *Springer*, New York.

Scarano F (2013), Tomographic PIV: principle and practice. Measurement Science and Technology, 23, R1-R28.

Scarano F and Riethmuller ML (1999), Iterative multigrid approach in PIV image processing with discrete window offset, *Experiments in Fluids*, 26:513-523.

Scarano F, Poelma C (2009), Three-dimensional vorticity patterns of cylinder wakes, *Experiment Fluids*, 47:69–83.

Scarano F, Poelma C, Westerweel J (2007), Towards four-dimensional particle image velocimetry, *7th International Symposium PIV*, Rome, Italy.

Scarano F, Riethmuller ML (2000), Advances in iterative multigrid PIV image processing, *Experiments in Fluids*, 29:S51–S60.

Scarano F, Sciacchitano A (2011), Robust elimination of light reflections in PIV, *9th International Symposium PIV*, Kobe, Japan.

Schetz JA, Fush AE (1999), Fundamentals of fluid mechanics, *Wiley*.

Schmid JP, Violato D, Scarano F (2012), Decomposition of time-resolved tomographic PIV, *Experiments in Fluids*, DOI 10.1007/s00348-012-1266-8.

Schmid PJ (2010), Dynamic mode decomposition of numerical and experimental data. *Journal of Fluid Mechanics*, 656:5–28.

Schram C (2003) Aeroacoustic of subsonic jets: Prediction of the sound produced by vortex pairing based on particle image velocimetry, *PhD Thesis Eindhoven University*, the Netherlands, http://web.phys.tue.nl/nl/de_faculteit/capaciteitsgroepen/transportfysica/fluid_dynamics_lab/publications/gdy/.

Schram C, Hirschberg A (2003), Application of vortex sound theory to vortex-pairing noise: sensitivity to errors in flow data, *Journal of Sound and Vibration*, 266-5: 1079–1098.

Schram C, Hirschberg A, Verzicco R (2004), Sound produced by vortex pairing: prediction based on particle image velocimetry, *AIAA Journal*, 42-11: 2234-2244.

Schram K, Taubitz S, Anthoine J, Hirschberg A (2005), Theoretical/empirical prediction and measurement of the sound produced by vortex pairing in a low Mach number jet, *Journal of Sound and Vibration*, 281:171–187.

Schrijer F, Scarano F (2008), Effect of predictor–corrector filtering on the stability and spatial resolution of iterative PIV interrogation, *Experiments in Fluids*, 45:927–941.

Schroeder A, Geisler R, Elsinga GE, Scarano F, Dierksheide U (2008), Investigation of a turbulent spot and a tripped turbulent boundary layer flow using time-resolved tomographic PIV, *Experiments in Fluids*, 44, 305–316.

Schroeder A, R. Geisler R, Staack K, Henning A, Wieneke B, Elsinga GE, Scarano F, Poelma C, Westerweel J. (2010), Eulerian and Lagrangian views of a turbulent boundary layer flow using time-resolved tomographic PIV, *Experiments in Fluids*, DOI 10.1007/s00348-010-1014-x.

Schroeder W, Dierksheide U, Wolf J, Herr M, Kompenhans J (2004), Investigation on trailing-edge noise sources by means of high speed PIV, *Proceedings of the 12th International Symposium on Applications of Laser Techniques to Fluid Mechanics*, Lisbon, Portugal.

Sciacchitano A, Scarano F, Wieneke B (2012), Multi-frame pyramid correlation for time-resolved PIV, *Experiments in Fluids*, DOI 10.1007/s00348-012-1345-x.

Seiner JM, Ukeiley L, Poton MK (1999), Jet noise source measurements using PIV, *5th AIAA/CEAS Aeroacoustic Conference*, Bellevue, USA.

Sheng J, Malkiel E, Katz J (2008), Using digital holographic microscopy for simultaneous measurements of 3D near wall velocity and wall shear stress in a turbulent boundary layer, *Experiments in Fluids*, 45:1023-1035.

Shinneeb AM, Balachandar R, Bugg JD (2008), Analysis of Coherent Structures in the Far-Field Region of an Axisymmetric Free Jet Identified Using Particle Image Velocimetry and Proper Orthogonal Decomposition, *Journal of Fluid Engineering*, Vol 130.

Sirovich L (1987), Turbulence and the dynamics of coherent structures. Part 1: Coherent structures, Quarterly of Applied Mathematics, Vol. XLV, 561-571.

Smith, MJT (1989), Aircraft noise, *Cambridge University Press*.

Soria J (1996), An investigation of the near wake of a circular cylinder using a video-based cross-correlation particle image velocimetry technique, *Experimental Thermal Fluid Science Journal*, 12:221-233.

Staack K, Geisler R, Schr¨oder A, Michaelis D (2010), 3D3C coherent structure measurement in a free turbulent jet, *15th International Symposium on Applications of Laser Techniques to Fluid Mechanics*, Lisbon, Portugal.

Stromberg JL, McLaughlin DK, Troutt TR (1980), Flow field and acoustic properties of a Mach number 0.9 jet at low Reynolds number, *Journal of Sound and Vibration*, 72, 159-176.

Tam CKW (1998), Jet noise: since 1952, *Theoretical and Computational Fluid Dynamics*, 10: 393-405.

Tam CKW, Morris PJ (1980), The radiation of sound by the instability waves of a compressible plane turbulent shear layer, *Journal of Fluid Mechanics* 98 (2):349–381.

Tam CKW, Zaman KBMQ (2000), Subsonic jet noise from non-axisymmetric and tabbed nozzles, *AIAA Journal*, 38, 4:592599.

Tennekes H, Lumley JL (1972), A first course in turbulence. *The MIT Press*.

Theunissen R, Scarano F, Riethmuller ML (2007), An adaptive sampling and windowing interrogation method in PIV, Measurement Science Technology, 18: 275–287.

Theunissen R, Scarano F, Riethmuller ML (2010), Spatially adaptive PIV interrogation based on data ensemble, *Experiments in Fluids*, 48:875-887.

Thomas R, Kinzie K, Pao S (2001), Computational analysis of a Pylon-Chevron core nozzle interaction, *7th AIAA/CEAS Aeroacoustics Conference*, Maastricht, the Netherlands.

Thurow B, Satija A, (2007), Further development of a high speed three-dimensional flow visualization system, *AIAA Paper* 2007-1060.

Tinney CE, Coiffet F, Delville J, Hall A, Jordan P, Glauser M (2006), On spectral linear stochastic estimation, *Experiments in Fluids*, 41:763–75.

Tinney CE, Glauser MN, Ukeiley LS (2008a), Low-dimensional characteristic of a transonic jet. Part 1. Proper orthogonal decomposition, *Journal of Fluid Mechanics*, 612:107-141.

Tinney CE, Ukeiley LS, Glauser MN (2008b), Low-dimensional characteristics of a transonic jet. Part 2. Estimate and far-field prediction, *Journal of Fluid Mechanics*, 615:53-92.

Traffic review 2011, *Amsterdam Airport Schiphol*, http://www.schiphol.nl/SchipholGroup/Company1/Statistics/TrafficReview.htm.

Tristanto I (2004), Towards hybrid mesh large eddy simulation for jet aeroacoustics, *10th AIAA/CEAS Aeroacoustics Conference*, Manchester, UK.

Tummers MJ, Hubner AW, van Veen EH, Hanjalic K, van der Meer ThH (2009), Hysteresis and transition in swirling non premixed flames, *Combustions and Flames*, Doi:10.1016/j.combustflame.2008.10.027.

Tummers MJ, Jacobse J, Voorbrood SGJ (2011), Turbulent flow in the near field of a round impinging jet, *International Journal Heat and Mass Transfer*, doi:10.1016/j.ijheatmasstransfer.2011.07.007.

Ukeiley L, Tinney CE, Mann R, Glauser M (2007), Spatial correlations in a transonic jet, *AIAA Journal*, 45,6.

Uzun A, Hussaini MY (2009), Simulation of noise generation in near-nozzle region of a chevron nozzle jet, *AIAA Journal*, DOI: 10.2514/1.36659.

van Oudheusden (2013), PIV-based pressure measurement, *Measurement Science and Technology* (to appear).

van Oudheusden B, Scarano F, Roosenboom EWM, Casimiri EWF, Souverein LJ (2007), Evaluation of integral forces and pressure fields from planar velocimetry data for incompressible and compressible flows, *Experiments in Fluids*, 43:153–162.

Verzicco R, Iafrati A, Riccardi G, Fatica M (1997), Analysis of the sound generated by the pairing of two axisymmetric co-rotating vortex rings, *Journal of Sound and Vibration*, 200(3):347–358.

Verzicco R, Orlandi P (1994), Direct simulations of the transitional regime of a circular jet, *Physics of Fluids*, 6:751.

Violato D, Ianiro A, Cardone G, Scarano F (2012), Three-dimensional vortex dynamics and convective heat transfer in circular and chevron impinging jets, *International Journal of Heat and Fluid Flow*, 37:22-36.

Violato D, Moore P, Scarano F (2011). Lagrangian and Eulerian pressure field evaluation of rod-airfoil flow from time-resolved tomographic PIV. *Experiments in Fluids*, *Experiments in Fluids*, 50:1057-1070.

Violato D, Moore P, Bryon K, Scarano F (2010), Application of Powell’s analogy for the prediction of vortex pairing sound in a low-mach number jet based on time resolved planar and tomographic PIV, *16th AIAA/CEAS Aeroacoustic Conference*, Stockholm, Sweden.

Violato D, Scarano F (2011), Three-dimensional evolution of flow structures in transitional circular and chevron jets, *Physics of Fluids*, DOI: 10.1063/1.3665141.

Violato D, Scarano F (2013), Three-dimensional vortex analysis and aeroacoustic source characterization of jet core breakdown, *Physics of Fluids*, 25, 015112, DOI 10.1063/1.4773444.

Viswanathan K (2004), Aeroacoustics of hot jets, *Journal of Fluid Mechanics,* 516:39–82.

Voth GA, Satyanarayan K, Bodenschatz E (1998), Lagrangian acceleration measurements at large Reynolds numbers. *Physics of Fluids*, 10:2268–2280.

Wang M, Freund JB, Lele SK (2006), Computational prediction of flow-generated sound, *Annual Review of Fluid Mechanics*, 18:483-512.

Wernet MP (1998), Digital PIV measurements in the diffuser of a high speed centrifugal compressor, *AIAA Paper,* 98-2777.

Wernet MP (2005), Characterization of the tip clearance flow in an axial compressor using 3D digital PIV, *Experiments in Fluids*, 39: 743–753.

Wernet MP (2007), Temporally resolved PIV for space–time correlations in both cold and hot jet flows, *Measurement Science and Technology*, 18:1387-1403.

Westerweel J (1993), Digital Particle Image Velocimetry, *Delft University Press*.

Westerweel J (1997), Fundamentals of digital particle image velocimetry, *Measurement Science and Technology*, 8:1379-1392.

Westerweel J (2000), Theoretical analysis of the measurement precision in particle image velocimetry, *Experiments in Fluids*, DOI 10.1007/s003480070002.

Westerweel J, Elsinga GE, Adrian RJ (2013), Particle image velocimetry for complex and turbulent flows, *Annual Review of Fluid Mechanics*, 45:409-436.

Westerweel J, Scarano F (2005), Universal outlier detection for PIV data, *Experiments in Fluids*, 39:1096-1100.

Widnall SE, Sullivan JP (1973), On the stability of vortex rings, *Proceedings of the Royal Society of London*, 332:335-353.

Wieneke B (2008), Volume self-calibration for 3D particle image velocimetry, *Experiments Fluids*, 45:549–556.

Willert (1997), Stereoscopic digital particle image velocimetry for application in wind tunnel flows. *Measurement Science and Technology*, 8:1465–1479.

Willert C, Stasicki B, Klinner J, Moessner S (2010), Pulsed operation of high-power light emitting diodes for imaging flow velocimetry, *Measurement Science of Technology*, 21:075402.

Willert CE, Gharib M (1991), Digital particle image velocimetry, Experiments in Fluids, 10:181–193.

Williamson CHK (1996), Vortex dynamics in the cylinder wake, *Annual Review of Fluid Mechanics*, 28:477–539.

Winant CD, Browand FK (1974), Vortex pairing: the mechanism of turbulent mixing layer growth at moderate Reynolds number, *Journal of Fluid Mechanics*, 63: 237-255.

Wright C, Blaisdell G, Lyrintzis A (2004), Using RANS to predict the performance of mixers in reducing jet noise, *42nd AIAA Aerospace Sciences Meeting and Exhibit*, 1274.

Wu H, Tan D, Miorini RL, Katz J (2011), Three-dimensional flow structures and associated turbulence in the tip region of a waterjet pump rotor blade, *Experiments in Fluids*, 51:1721-1737.

Xia H, Tucker PG, Eastwood S (2009), Large-eddy simulations of chevron jet flows with noise predictions, *International Journal of Heat and Fluid Flow*, 30: 1067–1079.

Yule AJ (1978), Large structure in the mixing layer of a round jet, *Journal Fluid Mechanics*, 89:413-432.

Zaman KBMQ, Hussain AKMF (1980), Vortex pairing in a circular jet under controlled excitation. Part 1: General jet response, *Journal of Fluid Mechanics*, 101:449–491.

Zaman KBMQ, Raman G (1997), Reversal in spreading of a tabbed circular jet under controlled excitation, *Physics of Fluids*, 9:3733.

Zaman KBMQ (2011), Effect of nozzle exit conditions on subsonic jet noise, *17th AIAA/CEAS Aeroacoustic Conference*, Portland, USA, AIAA Pap. 2011-2704.

Zhang J, Tao B, Katz J (1997), Turbulent flow measurement in a square duct with hybrid holographic PIV, *Experiments in Fluids*, 285:69–94.

List of publications

Journal articles

Violato D, Scarano F (2013), Three-dimensional vortex analysis and aeroacoustic source characterization of jet core breakdown, *Physics of Fluids*, 25, 015112, DOI 10.1063/1.4773444.

Violato D, Ianiro A, Cardone G, Scarano F (2012), Three-dimensional vortex dynamics and convective heat transfer in circular and chevron impinging jets, *International Journal of Heat and Fluid Flow*. 37:22-36.

Schmid JP, Violato D, Scarano F (2012), Decomposition of time-resolved tomographic PIV, *Experiments in Fluids*, 52:1567-1579.

Violato D, Scarano F (2011), Three-dimensional evolution of flow structures in transitional circular and chevron jets, *Physics of Fluids*, 23, 124104, DOI 10.1063/1.3665141.

Violato D, Moore P, Scarano F (2011), Lagrangian and Eulerian pressure field evaluation of rod-airfoil flow from time-resolved tomographic PIV, *Experiments in Fluids*, 50:1057-1070.

Conference proceedings

Violato D, Scarano F (2012), Visualization of hydrodynamic field and aeroacoustic source in transitional jet by TR-TOMO PIV, *15th International Symposium on Fluid Visualization*, Minsk, Belarus.

Ianiro A, Violato D , Cardone G, Scarano F (2012), Three-dimensional features in swirling impinging jets. *15th International Symposium on Fluid Visualization*, Minsk, Belarus.

Cavalieri A, Violato D, Rodrıguez D, Jordan P, Scarano F, Colonius T, Gervais Y (2012), Low-speed jet dynamics and sound radiation, *18th AIAA/CEAS Aeroacoustics Conference*, Colorado Spring, USA.

Violato D, Ianiro A, Cardone G, Scarano F (2011), Investigation on circular and chevron impinging jets by IR thermography and time-resolved tomographic PIV, *ASME Joint Fluids Engineering Conference*, Hamamatsu, Japan.

Scarano F, Violato D (2011), Visualization and characterization of vortical structures in 3 and 4 dimensions by PIV. *14ème Congrès Français de Visualisation et de Traitement d'Images en Mécanique des Fluides* Lille, France.

Violato D, Moore P, Bryon K, Scarano F (2010), Application of Powell's analogy for the prediction of vortex pairing sound in a low-mach number jet based on time resolved planar and tomographic PIV, *16th AIAA/CEAS Aeroacoustic Conference*, Stockholm, Sweden.

Moore P, Violato D, Bryon K, Scarano F (2010), On the suitability of direct application of acoustic theory to time-resolved tomographic PIV tested by DNS for low Mach number jet flows, *16th AIAA/CEAS Aeroacoustic Conference*, Stockholm, Sweden.

Lorenzoni V, Violato D, Scarano F (2010), Characterization of noise sources in a rod-airfoil configuration by means of Time-Resolved Tomographic PIV, *16th AIAA/CEAS Aeroacoustic Conference*, Stockholm, Sweden.

Schmid PJ, Violato D, Pust O, Scarano F (2010), Decomposition of time-resolved tomographic PIV, *15th International Symposium on Applications of Laser Techniques for Fluid Mechanics*., Lisbon, Portugal.

Scarano F, Bryon K, Violato D (2010), Time-resolved analysis of circular and chevron jets transition by Tomo-PIV, *15th International Symposium on Applications of Laser Techniques for Fluid Mechanics*, Lisbon, Portugal.

Violato D, Moore P, Scarano F (2009), Rod-airfoil investigation by time–resolved TOMO PIV for aeroacoustics, 8th *International Symposium on Particle Image Velocimetry PIV-09*, Melbourne, Australia.

Talks

Violato D, Scarano F (2012), 3D flow organization and dynamics in subsonic jets – aeroacoustic source analysis by tomographic particle image velocimetry, *University of California Berkeley*, USA.

Violato D, Scarano F (2012).Three-dimensional vortex analysis and aeroacoustic source characterization of jet core breakdown. *65rd Annual Meeting APS Division Fluid Dynamics*, San Diego, USA.

Violato D, Scarano F (2012). Jet flow diagnostics by TR-TOMO PIV - towards aeroacoustic source detection. *International Workshop on the Application of Particle Image Velocimetry for Aeroacoustics and Noise*, Delft, the Netherlands.

Violato D, Scarano F (2012), Incompressible jets acoustics by time-resolved TOMO PIV, *Burgersdag 2012 J.M.Burgerscentrum*, Eindhoven, the Netherlands.

Violato D, Scarano F (2011), Jet flow diagnostics by TR-TOMO PIV - towards aeroacoustic source detection. *International Conference on Applications for Image based Measurements*, Ulm, Germany.

Schmid PJ, Violato D, Scarano F (2010), Analysis of time-resolved tomographic PIV data of a transitional jet, *63rd Annual Meeting APS Division Fluid Dynamics*, Long Beach, USA.

Violato D, Scarano F (2010), Time-resolved tomographic PIV investigation of transitional jet for aeroacoustics, *Burgersdag 2010 J.M. Burgerscentrum*, Twente, the Netherlands.

Curriculum Vitae

Daniele Violato was born on September 5, 1982, in Pinerolo, Italy. He graduated *cum laude* in aerospace engineering at Politecnico di Torino, Italy, with a M.Sc. thesis titled "Vascular geometry reconstruction from Magnetic Resonance Imaging (MRI) for computational blood flow modeling". This work was conducted at the Aeronautics Department of Imperial College London under the supervision of Prof. S. Sherwin and Prof. D. D'Ambrosio.

In October 2008, after a year experience in Turbocare S.p.A. (Siemens group) as project engineer, Daniele started the Ph.D. research at the Aerodynamics Section of TU Delft, with the supervision of Prof. F. Scarano. Conducted within the FLOVIST project (funded by the European Research Council), his Ph.D. research focused on the development of a novel methodology based on tomographic PIV to investigate jet aeroacoustics, results of which are discussed in the present manuscript. During his research, Daniele collaborated with Dr. P. Jordan and Dr. A. Cavalieri from Université de Poitiers (France), Prof. G. Cardone and Dr. A. Ianiro from Università Federico II di Napoli (Italy) and Prof. P. Schmid from Ecole Polytechnique du Paris (France). Since May 2012, he has been the delegated scientist for the ORINOCO project (funded by the European Community's Seventh Framework Program), for which, in collaboration with the National Aerospace Laboratory of the Netherlands (NLR), he has investigated high-speed compressible jets with tomographic PIV.

Daniele can be contacted by email at daniele.violato@gmail.com.